Journal of
Ocean Engineering
and Technology

한국해양공학회지

KSOE

www.joet.org

KSOE The Korean Society of Ocean Engineers

Journal of Ocean Engineering and Technology
한국해양공학회지

CONTENTS

GENERAL INFORMATION

"Journal of Ocean Engineering and Technology" is the official journal published by "The Korean Society of Ocean Engineers (KSOE)". The ISO abbreviation is "J. Ocean Eng. Technol." and acronym is "**JOET**". It contains original research articles, technical articles, review articles, and brief communications on technical issues.

JOET published the first issue in 1987 and has been publishing bimonthly since 2002. JOET is ranked the most influential journal with the longest history and largest membership around 1,000 people in the field of ocean engineering in Korea. **JOET** covers all topics in ocean engineering fields, and has five major research areas including ships/offshore platforms, coastal civil engineering, marine materials, ocean renewable energy platforms, marine robots, etc.

Ships and offshore platforms: Design of marine structures; Resistance and propulsion; Seekeeping and maneuvering; Experimental and computational fluid dynamics; Ocean wave mechanics; Fatigue strength; Plasticity; Optimization and reliability; Arctic technology and extreme mechanics; Noise, vibration, and acoustics; Concrete engineering; Thermodynamics and heat transfer; Hydraulics and pneumatics;
Coastal civil engineering: Coastal structures; Port and harbor structures; Soil mechanics; Drilling and exploration; Hydraulics of estuary; Seismic engineering; Coastal disaster prevention engineering;
Marine materials: Metallic materials; Organic materials; Ceramics; Composite materials; Materials properties; Corrosion and Anti-corrosion; Tribology;
Ocean renewable energy platforms: Offshore wind turbines; Wave energy platforms; Tidal current energy platforms; Floating photovoltaic energy platforms;
Marine robots: Robot sensor system; Autonomous navigation; Robot equipments; Spatial information and communications; Underwater network; Design of underwater vehicles;
Common areas: Design for safety; IT-based design; IT-based production engineering; Welding mechanics; Control engineering; GPS and GIS; Inspection and sensor; Port and logistics; Leisure boat and deep see water; Offshore process systems engineering;

JOET is an open access journal currently published online. Therefore, all ocean engineers and researchers around the world can easily access all journal articles via the journal homepage (http://www.joet.org) and download the PDF-based original texts or view the web-based XML texts for free. Offline annual subscription fee is 100USD. **JOET** has a system where two or more peer reviewers must review each submitted paper and it is operated very strictly.

Full text is freely available from http://www.joet.org and http://www.ksoe.or.kr without sign-in. **JOET** is being indexed in some prominent database such as Korean Citatation Index (KCI), Google Scholar, and Directory of Open Access Journals (DOAJ).

For correspondences concerning business matters, author needs to contact KSOE Secretariat by email or phone (e-mail: ksoehj@ksoe.or.kr or Tel: +82 51 759 0656). Correspondences for publication matters can be asked via email to the Editor-in-Chief (email: heroeswise2@gmail.com).

Original Research Article

Current Status of the 2nd Generation of Intact Stability: Investigation of the Pure Loss of Stability and Parametric Roll Mode

Jaeho Chung [1], Dong Min Shin [2], Won-Don Kim [3] and Byung Young Moon [4]

[1]Research Professor, Security Convergence Institute, Korea Advanced Institute of Science and Technology (KAIST), Daejeon, Korea
[2]Research Professor, Shipbuilding & Ocean Equipment Industry Empowerment Center, Kunsan National University, Gunsan, Korea
[3]President, Marine Tech-In Co.,Ltd., Busan, Korea
[4]Professor, Shipbuilding & Ocean Equipment Industry Empowerment Center, Kunsan National University, Gunsan, Korea

ABSTRACT: *A review of the 2nd generation of intact stability by the International Maritime Organization is performed. The main issues with the new stability criteria are reviewed. In particular, the physical background and related mathematical formulations of the pure loss of stability and parametric roll are summarized. Based on a literature review, benchmark calculation results for 17 different types of ships are discussed, and the final results are in excellent agreement with our physical expectations. Some relatively serious design problems are found in the application of the new stability criteria to sample ships built in Korea, and possible technical solutions are proposed, which have to be improved in the coming years.*

1. Introduction

1.1 Background of study

The behavior of ships in waves is a very important issue related to the safety of ships, and the International Maritime Organization (IMO) is working to ensure safer maritime movements by establishing intact stability criteria for the safe operation of vessels and applying them to all vessels. As part of this effort, the IMO has been developing the Second Generation Intact Stability Criteria (SGISC) and preparing to apply them to all vessels for over a decade. The IMO is known to be in the final development stages for new stability criteria, with the aim of implementing these criteria after 2020 (Belenky et al., 2011; Peters et al., 2011; Chouliaras, 2014).

The first intact stability criteria were introduced by the Maritime Safety Committee (MSC) as the Intact Stability (IS) code (2008) and came into force in 2010. This first generation intact stability criteria were based on Rahola's work (1939), and a weather criterion was added to the criteria in the 1950s. The SGISC were launched in 2002 by the subcommittee on Stability and Load Lines and on Fishing Vessels Safety (SLF) under IMO, but the practical application began in 2005.

The most fundamental reason for the development of new stability criteria is that accidents also occur on ships that meet existing stability

criteria. The accident that affected an American President Lines (APL) ship in 1998, as shown in Fig. 1, is a typical example. Countermeasures to these accidents (ABS, 2004) were discussed separately before the discussion of the IMO second generation intact stability criteria. However, because these accidents do not occur frequently, it seems impossible to find their causes and develop countermeasures based on experience. Thus, it seems reasonable to think about more quantitative and systematic countermeasures. In particular, as the rapidly changing shipping industry has begun to buildships of previously non-existent size, problems that cannot be
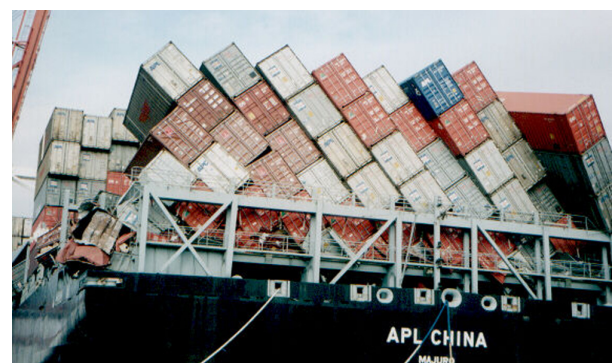

Fig. 1 APL China accident, 1998

solved empirically have arisen. For this reason, the IMO has formed a group of experts from around the world to develop new stability criteria, and much debate has taken place over the last decade.

When new stability criteria are implemented, new ships are more likely to have reduced onboard cargo volumes in comparison to existing ships. In the case of existing ships, there is a great possibility that they will be forced to decrease their onboard cargo volume or operating speed, which is expected to have a large impact on future ship operations. Because the shipbuilding industry accounts for a large portion of the Korean economy, and the Korean shipbuilding industry accounts for a very large share of the world's shipbuilding industry, it is necessary to pay attention to the design changes that will occur when the new stability criteria come into effect. However, to date, there has been no full-scale research on the intact stability criteria in Korea. When new stability criteria with greater safety are put in force, they are expected to be more restrictive in terms of the speed and loading conditions than the current ship criteria, which means that more ships will need to be built than at present. As a result, it seems to be very positive. In particular, among the large ships, the types of ships most affected by the reinforcement of the stability criteria at present are considered to be container ships, RoRo ships, RoPax, and cruise ships with a relatively high center of gravity. From the Korean shipbuilder's perspective, more careful consideration should be given to whether or not to change the design of large container ships, which have secured international competitiveness for Korean shipbuilders.

This paper introduces the SGISC being developed by IMO and illustrates their mathematical modeling and solution method. In addition, the new design environment or design methods are discussed, including the technical limitations that occur when actually applied to ships. Finally, the operational constraints of the existing ships and the possibility of design changes are discussed by applying the new criteria to the small and medium-sized container chips actually being constructed in Korea in order to provide actual technical discussions based on the new criteria.

1.2 Current status of IMO Second Generation Intact Stability Criteria study

As seen in Uzunoglu (2011), Peters et al. (2011), Umeda (2013), Krüger et al. (2013), and Grinnaert (2017), the SGISC that have been discussed so far consist of a three-stage verification process and one operation guide, as shown in Fig. 2. This verification test is also expected to be applied to the ship stability criteria (IS 2008) currently in force, and it is known that any ship that does not pass this process will not be able to operate. Therefore, the new stability criteria should be satisfied for the operation of ships.

The SGISC include a multi-stage verification process to minimize the cost required for the calculations needed to apply the criteria. The SGISC currently under development are intended for ships longer than 24 m in length. If a very detailed calculation criterion is provided for a large number of ships, it is expected that performing the calculation for the criterion application will be impossible within a practical time
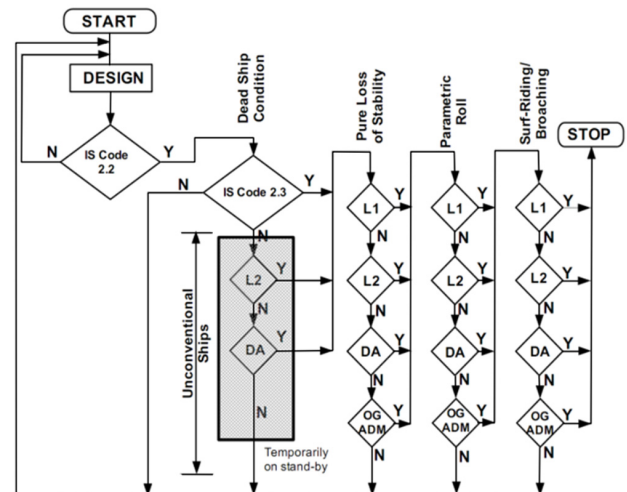
Fig. 2 Second Generation Intact Stability Criteria (SGISC) diagram

limit because the number of target ships is very large. A multi-stage application criterion was introduced to actually reduce the calculation demand for applying the criterion by using a method that does not perform a detailed calculation again when the margin of stability has been established through a simple calculation.

The first two stages of the ongoing 3 + 1 stage structure of the SGISC are called the "vulnerability assessment" stages, which are based on a simple empirical formula. The vulnerability decision at this stage is not conclusive, but it means that the ship is likely to lose stability in the sea, and that the ship has weak stability in the sea. In fact, the largest logical difficulty in establishing the stability criteria lies in the problem of the rarity of ship accidents related to stability. Thus, it is considered to be reasonable to approach the stability criteria probabilistically. As shown in Fig. 2, the implementation of the SGISC does not abolish the existing Stability Criteria (IS 2008 2.3), but involves the concept of adding additional criteria to the existing criteria. Thus, the existing stability criteria do not disappear. Therefore, all of the data related to the existing stability calculations will be meaningful and will not be discarded. The newly added part of the stability criteria consists of a structure that authenticates the stability of the ship when the criteria in each mode are passed after applying multi-layered criteria for each independent inspection mode.

Because such existing methods often report logically contradictory results, efforts have been made to solve this problem. For example, satisfying the level-1 criteria means satisfying the level-2 criteria as well, but, in the case of verification through actual calculations, sometimes contradictory results may be obtained. As a result, efforts to find realistic measures to solve this logical contradiction have continued. Until now, most of the research and discussions related to stability have been focused on levels 1 and 2, and the opinions about the criteria have significantly coincided. Thus, the final work is proceeding with the aim of finalizing the criteria in 2020. The most complex level of verification is level 3, where the stability calculation is performed at the most complex level. This is called a "direct stability assessment" (DSA), which is also closely related to the

development of the ship's own operational guidance.

Performing model experiments in the DSA part is a very expensive task. In general, conducting model experiments is unrealistic, and the demand for direct stability assessment by computer simulation is expected to increase. Therefore, it is considered that active measures for these problems are required.

Because the IMO's criteria for second generation intact stability have not been established, the criteria discussed in this paper are not exhaustive regulations and may be changed later. Accordingly, the conclusions presented here may vary. However, when looking at the discussion so far, the stability criteria are based on physical phenomena and established through mathematical modeling and rational simplification. As a result, their fundamental structures do not appear to change, but the criteria are likely to be strengthened or mitigated by changing certain criteria values. In addition, the errors that may occur in the application of the simplified reference equation can be corrected when the high-level direct evaluation method is implemented even if the low-level provisions of the vulnerability standard are unreasonable.

2. Vulnerability to stability loss mode

When a hull is assumed to be a rigid body, its motion has six degrees of freedom. In ships with a typical shape, most of the movement displacement is very small compared to the length of the hull, but the rolling value should not be underestimated. Because the overturning of a ship in waves is usually caused by a large rolling value, the most important element of a ship's movement is its roll. Therefore, most ship stability assessments focus on the calculation of the roll. The IMO defines the vulnerable stability status for the following five modes, and levels 1 and 2 of each mode are defined in Table 1.

The activities of the SGISC development committee lasted for more than a decade, and because of characteristics that reflect the interests of specific countries, the discussion on which particular phenomena would be included in the new stability criteria was continued. In addition to the pure loss stability, parametric roll, and surf-riding/ broaching modes included in the draft, the excessive acceleration and dead ship modes were added later. Because of the different positions of the experts, there were many conflicting discussions about the prerequisites, especially the definition of incident waves, to establish the criteria for the individual modes. These discussions are still not completely unified and remain as concurrently applicable options, which can be sources of confusion. In some cases, the criteria values for determining the vulnerability have been changed for one criterion.

Therefore, appropriate care should be taken. In particular, the criteria presented in the references have also changed over time, and the application criteria can be changed or deleted, requiring careful attention to a literature search. The history of the regulation discussions can be confirmed in official papers such as IMO (2009a), IMO (2009b), IMO (2012), IMO (2013), IMO (2016a), and IMO (2016b), and this study was also performed by following the criteria provided in these papers.

Among the vulnerable stability modes included so far, the typical vulnerability modes directly related to large ships affecting the shipbuilding industry in Korea are the pure loss of stability and parametric roll modes. The remaining three vulnerable stability modes are excluded from the application target in the case of large ships or are barely related to the Korean shipbuilding industry. Thus, a discussion of these modes is omitted and the above two vulnerable stability modes are covered in this paper.

2.1 Pure loss of stability

When a ship in service encounters a wave with a wavelength similar to the length of the ship, and the midship position of the hull is the same as the wavelength, the stability of the hull decreases more rapidly than when the ship is in constant water. The decrease of the stability in this hogging situation in still water is called the pure loss of stability. In sagging, where the center of the hull is located at the wave hollow due to the movement of the wave, the stability increases sharply. However, if a situation in which the stability is repeatedly reduced in the hogging state lasts for a long time, the stability of the hull may be vulnerable.

Modern ships, especially container ships and cruise ships, have design conditions that require a large deck area to load many containers or accommodate cabins. In this case, because the change in the water plane according to the height is very large, the shape of the water plane according to the position of the wave is also greatly changed, which causes a pure loss of stability.

2.1.1 Vulnerability criteria in pure loss of stability (level 1)

There are two ways to calculate the risk of the pure loss of stability mode. The most basic method is to calculate the metacentric height (GM) value when the hull encounters a steep wave with the same length as the hull. In this method, the GM value is calculated when a wave with $\lambda = L_{PP}$ and $h = \lambda \cdot S_W$ ($S_W = 0.0334$) values is located at 10 positions before and after the center point of the hull. Then, it is considered safe when the minimum GM value is greater than and equal to the reference value (R_{PLA}).

Table 1 SGISC reference documents

	Pure loss of stability	Parametric roll	Broaching	Dead ship condition	Excessive acceleration
Definition of criteria (L-1, 2)	SDC 2/WP.4 Annex 1	SDC 2/WP.4 Annex 2	SDC 2/WP.4 Annex 3	SDC 2/WP.5 Annex 1	SDC 2/WP.5 Annex 2
Explanatory notes	SDC 2/WP.5 Annex 3	SDC 2/WP.5 Annex 4	SDC 2/WP.5 Annex 5	SDC 2/WP.5 Annex 6	SDC 2/WP.5 Annex 7
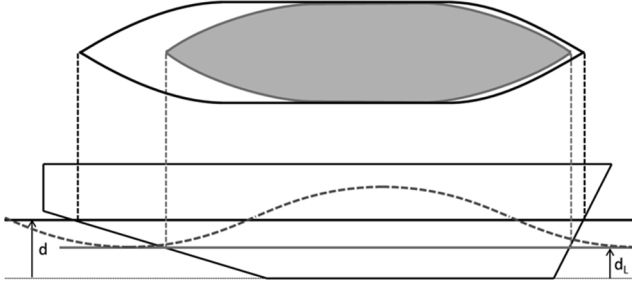
Fig. 3 Definition of drafts for pure loss of stability criteria (d: draft amidship corresponding to loading condition under consideration, d_L: $d - \delta d_L$)

$$GM_{MIN} > R_{PLA} \tag{1}$$

Here, the R_{PLA} value is the minimum value of GM, which is a criterion for satisfying level 1, and is defined as 0.05 (m) in the IMO regulation (IMO, 2016b). Another approach is to avoid the complexity of finding the GM value for each wave position and taking into account the trim and settlement in that state. In this method, the ratio between the change in the GM value of the hull and the GM value in still water is calculated. Complexity can be avoided because only the draft at each wave position needs to be considered. In level 1, the change in the GM value is calculated through a simple hull geometric calculation.

$$\frac{GM_a}{GM_0} \geq 0.12, \quad GM_a = \frac{I_{up} - I_{low}}{2V} \tag{2}$$

Here, the moment of inertia at any point (d) above the surface based on the water surface of Fig. 3 is defined as I_{up}, and the moment of inertia at point (d_L) below the water surface is defined as I_{low}.

The draft required for this is defined in Fig. 3 .

2.1.2 Vulnerability criteria in pure loss of stability (level 2)

As in other modes, level 2 is a calculation performed only if the level-1 criteria are not met. The calculation is made more realistic and the complexity of the calculation increases. The assessment approach determines the sum of probabilistic risks in waves of various components as the extent of the final vulnerability. According to the existing research results to date, there are two methods for calculating level 2 (option A and option B). Option A uses the stability angle (loll angle) ϕ_S, and option B uses the original power loss angle (angle of vanishing stability) ϕ_ν. Because option B is less frequently used than option A as a result of the complexity of the calculation, option A is used in this paper.

In the case of option A, the criteria are represented as $CR1$ and $CR2$, and a method is used where a ship is determined to be safe when both of the risk values calculated based on the two criteria are 0.06 or less. This is expressed as follows:

$$\max(CR1, CR2) < 0.06$$

$$CR1 = \sum_{i=1}^{N} W_i C1_i \quad C1 = \begin{cases} 0 \ (\phi_\nu > 30^\circ) \\ 1 \ (\phi_\nu < 30^\circ) \end{cases} \tag{3}$$

$$CR2 = \sum_{i=1}^{N} W_i C2_i \quad C2 = \begin{cases} 0 \ (\phi_S > 25^\circ \text{ or } 15^\circ) \\ 1 \ (\phi_S < 25^\circ \text{ or } 15^\circ) \end{cases} \tag{4}$$

where W_i is a weighted factor depending on the significant wave factor (Hs) and wave period (Tz) and is provided in IMO regulation.

The criteria in level 2 of the pure resilience mode are to estimate the hull risk of each probabilistic ocean component as an index of 1 or 0, multiply the probability value by the risk factor for each component, express the final risk as $CR1$ and $CR2$, and determine whether the magnitude of the risk is above a certain value.

$$C2_i = \begin{cases} 1 & \phi_s > R_{PL2a} = 15^\circ \text{ or } \phi_{loll} > R_{PL2b} = 25^\circ \\ 0 & otherwise \end{cases} \tag{5}$$

This probabilistic assessment necessarily requires a definition of the wave distribution, which covers 16 wave periods and 17 wave heights recommended by the International Association of Classification Societies (IACS) and judges the stability criteria with the stability loss risks in 197 waves that can actually occur. The detailed information on this definition is defined by the IMO (2009a).

Belenky et al. (2011) reported the results of applying the above

Fig. 4 Calculation result for pure loss of stability ($CR1$, level 1)

Fig. 5 Calculation result for pure loss of stability ($CR2$, level 2)

Table 2 Example of calculating vulnerability of representative vessels for pure loss of stability (S: satisfied, U: unsatisfied)

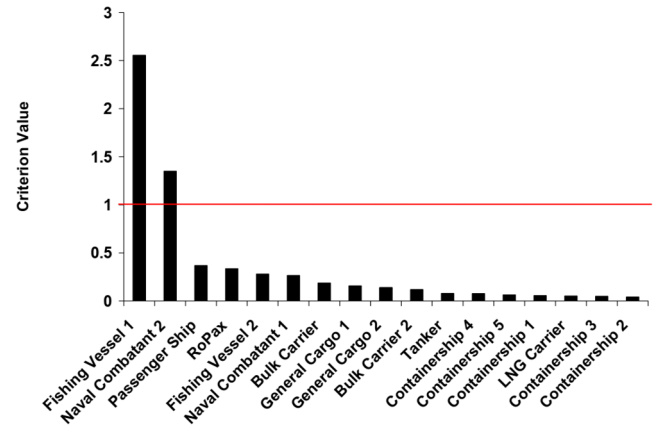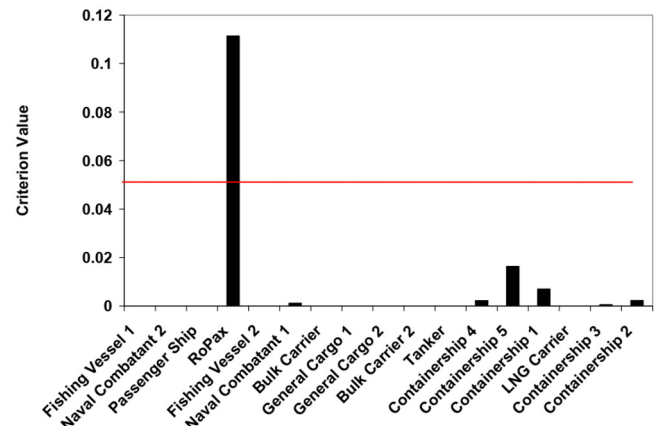| Type	L	GM	Vs	CR1	Vulnerability (CR1)	CR2	Vulnerability (CR2)
Fishing vessel 1 (ITTC A2)	34.5	1.97	15	2.56	U	0.00	-
Naval combatant 2 (ONR TH)	150	1.16	15	1.35	U	0.00	-
Passenger ship	276.4	3.42	15	0.37	S	0.00	-
RoPax	137	0.36	15	0.34	S	0.11	U
Fishing vessel 2	21.56	0.51	15	0.28	S	0.00	-
Naval combatant 1 (ONR FL)	150	0.20	15	0.27	S	0.00	S
Bulk carrier	275	4.19	15	0.19	S	0.00	-
General cargo 1 (S60)	121.9	0.15	15	0.16	S	0.00	-
General cargo 2 (C4)	161.2	0.15	15	0.14	S	0.00	-
Bulk carrier 2	145	0.15	15	0.12	S	0.00	-
Tanker	320	1.72	15	0.08	S	0.00	-
Containership 4	283.2	0.15	15	0.08	S	0.00	S
Containership 5 (C11)	262	0.15	15	0.06	S	0.02	S
Containership 1	322.6	0.15	15	0.06	S	0.01	S
LNG carrier	267.8	0.15	15	0.05	S	0.00	-
Containership 3	330	0.15	15	0.05	S	0.00	S
Containership 2	376	0.15	15	0.04	S	0.00	S

vulnerability criteria of pure loss of stability to 17 representative ship models. The results are shown in Table 2, Fig. 4, and Fig. 5.

According to these results, the values of two factors, CR1 and CR2, significantly change with the target ship, and thus the vulnerability in each mode can be determined with clear criteria. Except for fishing vessel 1 and a battleship, which are special kinds of ships, the CR1 values of common merchant ships are evenly distributed. Thus, the difference between the values is not very large, and their distribution is very dichotomous compared to CR2, so that it is easy to see whether or not the criteria are satisfied. In addition, the results also show that the risks of RoPax and container ships are higher than those of other ships, as is generally expected.

2.2. Parametric roll

Parametric vibration is a vibration phenomenon that occurs when two vibromotive forces are applied during one vibration cycle (like swinging), and it is a common phenomenon in our daily lives. The parametric roll of a ship is a resonance phenomenon that occurs when the period of the wave incident on the hull is 1/2 of the resonance period of the general roll, which is distinguished from the common roll resonance. Unlike the roll generated in a ship during beam sea runs, it should be noted that parametric rolls may occur when a wave meets one half of the roll resonant period in longitudinal waves.

The resonant frequency of a beam sea occurs at a specific frequency irrespective of wave steepness, but the magnitude of the rolling angle varies with the wave steepness, and parametric roll may occur at twice this frequency. The frequency of the parametric roll has a value twice that of the rolling resonance frequency of the wave, but is also affected by the wave steepness. In particular, a higher wave height tends to

widen the frequency at which parametric rolls can occur, which is a good indication that a high wave height increases the likelihood of parametric roll at sea.

In recent years, it is common for the roll resonance period to increase with the size of the vessel. Here, because large resonances can be generated even when large vessels encounter waves with half the resonance period and not reach a very large resonance frequency, it is difficult to occur. For example, the 8000 TEU class container ship "APL China" experienced an accident involving parametric roll, which caused the loss of most of its containers in October of 1998. After this accident, extensive research on the parametric roll phenomenon was conducted, along with extensive research on how to detect signs of parametric roll in advance (ABS, 2004).

The kinematic equation for roll is generally complex with other modes of motion, but the IMO currently recommends interpreting a single degree of freedom motion that only considers roll for parametric rolls. The roll equation of the hull, including the rotational moment of inertia (I_x) of the hull relative to the roll angle (ϕ), and the corresponding additional mass (A_{44}), damping coefficient (B_{44}), and stability (W) generated during the motion can be expressed as follows:

$$(I_x + A_{44})\ddot{\phi} + B_{44}\dot{\phi} + W \cdot GZ(\phi, t) = 0 \tag{6}$$

With appropriate assumptions, this equation can be expressed as follows. The mathematical development process for this equation is described in detail in Uzunoglu (2011) and Umeda (2013).

$$\ddot{\phi} + 2\delta\dot{\phi} + \left(\omega_m^2 + \omega_a^2 \cos(\omega_c t)\right) \cdot \phi = 0 \tag{7}$$

$$\omega_m = \sqrt{\frac{\Delta \cdot GM_m}{I_x + A_{44}}} \; ; \; \omega_a = \sqrt{\frac{\Delta \cdot GM_a}{I_x + A_{44}}} \; ; \; \delta = \frac{1}{2}\frac{B_{44}}{I_x + A_{44}} \qquad (8)$$

where ω_e is defined as the encounter frequencies ω_m, ω_a and δ is defined as in Eq. (8). In Eq. (8), Δ is the hull displacement, GM_m is the mean of the GM values, and GM_a is the amplitude of the GM change in the wave.

The roll equation can be expressed by substituting the well-known Mathieu equation as follows:

$$\frac{d^2 x}{d\tau^2} + (p + q\cos(\tau)) \cdot x = 0 \qquad (9)$$

$$p = \left(\overline{w^2}_m - \mu^2\right); \; q = \overline{w^2}_m \qquad (10)$$

The behavior of the solution of this nonlinear equation is well known, where the divergence and convergence are very nonlinear, depending on the values of parameter p and q, and the behavior of the solution varies significantly even with small parameter changes. This is shown schematically in Fig. 6. The figure illustrates the Ince-Strutt diagram and shows the diverging and non-diverging areas according to the parameter values. It is not easy to predict the diverging area. In the actual calculation of the roll, the roll angle diverges according to a given parameter in some cases. This situation physically corresponds to a situation where a parametric roll occurs and, consequently, a large roll motion occurs.

Another difficulty in predicting parametric roll is the effect of damping. Rolling is dampened by a variety of causes, but it is very difficult to accurately predict each of these factors. Ikeda (2004) conducted a study to systematically analyze the causes of roll damping and developed a practical formula to mathematically express its rough magnitude. Fig. 7 shows an example where the values of the roll are different when the damping is considered and when the damping is not considered. In this figure, it can be seen that the solution considering the nonlinear damping can be stable even though the solution of the linear equation diverges. This result shows that the simplified model has more design margins. Thus, the assessment of the roll tends to be more conservative. It can be seen that applying a more realistic model can be expected to reduce the design margins because the behavior of the solution can be more exactly estimated even though the construction of the mathematical model is complex. Thus, it can be inferred that a more optimized solution can be obtained in the actual design.
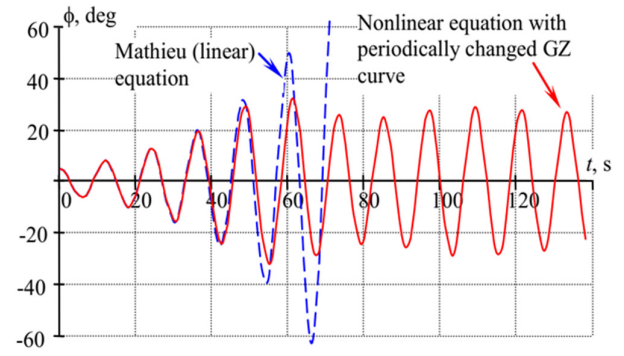
Fig. 7 Effect of nonlinearity on the solution (─: nonlinear equation, - -: Mathieu (linear) equation)

2.2.1 Acceptance equation of parametric roll stability (level 1)

Belenky et al. (2011) proposed the following simple acceptance equation through some assumptions about the behavior of the above equations.

$$\frac{\Delta GM}{GM} \le R_{PR} \qquad (11)$$

$$\Delta GM = \frac{I_H - I_L}{2V}, \; \text{only if} \; \frac{V_D - V}{A_W(D-d)} \ge 1.0 \qquad (12)$$

Here, there are various proposals for the size of R_{PR} for the shape of each ship, which is mainly defined as a value based on the central section coefficient (C_m). I is the moment of inertia, V_D is the volume, A_W is the waterline area, and d is the draft. For specific definitions, see Table 3, Table 4 and IMO Regulations (IMO, 2016b).

Fig. 8 shows the level-1 calculation results for parametric rolls. When the criteria value for the assessment is set to 0.49, 10 ship models are judged to be vulnerable, indicating that they do not pass the level-1 criteria at a fairly high rate. The ships in this category have high ship speed characteristics, and most ships judged as vulnerable have a ship speed of 9.26 m/s or more. Exceptionally, it is considered that general cargo ships with a ship speed of 8.23m/s were judged to be vulnerable because of the height of the center of gravity. Liquefied

Fig. 6 Ince-Strutt diagram

Fig. 8 Parametric roll (level 1)

Table 3 Principle dimension of sample ships

Dimensions		Unit	1000 TEU	1040 TEU	22000 RoPax
LengthOverall: Abt.		m	146.3	143.9	160
LengthBetweenPerpendiculars:		m	136.1	134.7	148
Breadth(Mld.):		m	22.6	22.6	24.8
Depth (Mld.) :		m	11.2	11.2	14
Draft (D.L.W.L,Mld.):		m	7.4	7.4	5.8
Draft (S.L.W.L,Mld.):		m	8.2	8.2	
Complements:		p	20	20	48
Full load displacement:		t	17,773.1	17,981.8	12,422.6
Light ship weight:		t	4,838	4,543	8,621
Gross tonnage (international): Abt.		t	-	9,930	22,000
AK : B. Keel area		m^2	13.9	13.9	60
LWL		m	136.1	134.7	148
B (ext)		m	22.6	22.6	24.8
Btm shell thick =		m	0.014	0.014	0.014
Speed	max	m/s			
Speed	service	m/s	9.26	9.26	10.29
Power	MCR	kW	8280	8280	13920
Power	NCR	kW	7452		
Dia of propeller	m	m	5.6	5.4	4.3
La	m	m	2.55	2.725	3
hs	m	m	0.2	0.2	0.05

Table 4 1040 TEU CV pure loss of stability and parametric roll (Level-1)

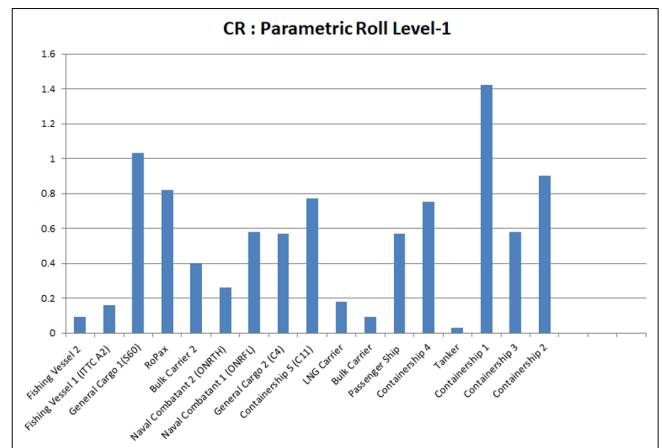|										
	Draft	5.238	5.029	4.860	8.214	8.115	8.134	8.214	8.157	8.134
	only if, $(V_D-V)/A_W(D-d) \geq 1.0$	1.17	1.18	1.19	1.06	1.06	1.06	1.06	1.06	1.06
V_D	Displacement volume (m^3)	25501	25501	25501	25501	25501	25501	25501	25501	25501
A_W	Area of water plane (m^2)	2238.0	2213.0	2194.0	2675.7	2661.7	2664.5	2675.7	2667.9	2664.5
$I_L=$	Second Moment of the water plane at the draft d_L (m^4)	62284	61146	59961	82869	82364	82574	82794	82596	82501
KB	Center of buoyancy in height direction	2.827	2.707	2.819	4.497	4.439	4.451	4.497	4.464	4.451
$GM_{min}=$	$=KB+(I_L/V)-VCG$ $=KB+(I_L/(C_b \times L_{PP} \times B \times d))-VCG$	3.292	3.451	3.684	-0.044	-0.021	0.015	-0.059	0.013	-0.001
criteriaR_{PLA}	$R_{PLA}=[min(1.83d(Fn)^2, 0.05]m$	0.05	0.05	0.05	0.05	0.05	0.05	0.05	0.05	0.05
	$1.83d(Fn)^2=$	0.622	0.597	0.577	0.975	0.963	0.966	0.975	0.968	0.966
$GMmin>R_{PLA}$	Result (Pure loss of stability L-1)	Safe	Safe	Safe	Danger	Danger	Danger	Danger	Danger	Danger
	$\Delta GM/GM$ is calculated as follows:	5.514	5.463	5.379	0.991	0.982	0.998	0.98	1.022	0.987
	$\Delta GM=(I_H-I_L)/(2V)$ $=(I_H-I_L)/(2 \times C_b \times L_{pp} \times B \times d)$	1.676	1.732	1.796	0.923	0.938	0.932	0.925	0.931	0.934
	$\Delta GM/GM=$		0.317	0.334	0.931	0.956	0.934	0.944	0.911	0.947
	Result (Parametric Roll L-1)		Safe	Safe	Danger	Danger	Danger	Danger	Danger	Danger

natural gas (LNG) carriers with a relatively high speed (9.26 m/s) are considered to be stable because of their low center of gravity, based on the nature of the cargo.

2.2.2 Acceptance equation of parametric roll stability (level 2)

Like the pure loss of stability mode, the vulnerability of parametric rolls can also be found using the probabilistic approach, and the calculation procedures are not different from those of level 1. However, in the case of level 2 for parametric rolls, very fine calculations are required to avoid the large design margins caused by excessive conservation. It should be noted that two methods (level 2A and level 2B) are jointly used because of different opinions between experts on how to evaluate parametric roll. To date, a ship has been recognized as passing the stability criteria if it passes one of these two methods. Thus, level 2B is executed only if level 2A fails. As a result, it has the same effect as setting two levels again inside level 2.

In level 2, the same calculation as in level 1 is performed. In practice, however, the degree of risk for each wave at a given sea level is calculated and the weight of the wave is multiplied by this value. After that, the final degree of vulnerability, C1, is calculated to judge whether or not this value is above the criteria value.

$$C1 = \sum_{I=1}^{n} W_i C_i' \le R_{PR0} \quad (13)$$

$$GM(H_i, \lambda_i) > 0, \quad \frac{\Delta GM(H_i, \lambda_i)}{GM(H_i, \lambda_i)} < R_{PR} \quad (14)$$

The level-2B approach for parametric roll evaluates the risk by averaging the values in each of the seven directions, taking into account the risk elements along the wave direction.

$$C2 = \left[\sum_{i=1}^{3} C2(Fn_i, \beta_h) + C2(0, \beta_h) + \sum_{i=1}^{3} C2(Fn_i, \beta_f) \right] / 7 \quad (15)$$

The detailed wave information on this method is defined by the IMO (2009a).

In this paper, the main dimensions of ships designed and built by Korea Maritime Services (KMS) are listed in Table 3, and the parametric roll calculation results for the target ships are listed in Table 4, Table 5, and Table 6. The results of this assessment can be clearly seen by plotting the results (Fig. 9). In the case of the level-2B method, the integral process of the differential equations is essential. In this process, different results are reported depending on whether the nonlinear terms are taken into account. In this paper, the results of each of the two methods applied are displayed and compared.

The calculation results show that the size of the roll angle is always small when the nonlinear terms are considered. This result means that more detailed calculations are a means to eliminate excessive conservatism. The calculated linear/nonlinear results show that

high-speed ships with high centers of gravity such as container ships, RoPax, and passenger ships tend to be significantly vulnerable to parametric rolls.

It should be noted that, through levels 1 and 2, the vulnerability to parametric roll is generally greater than the vulnerability to pure loss of stability. Accordingly, it is necessary for shipbuilders to recognize that parametric roll is the most important mode to check during design. At the same time, in the eyes of ship operators such as shipping companies, the capacity of the cargo to be loaded on new ships should be reduced because of the vulnerability to parametric roll in order to reduce the ship's operating speed or lower the center of gravity compared to the current ships in accordance with the new stability criteria.
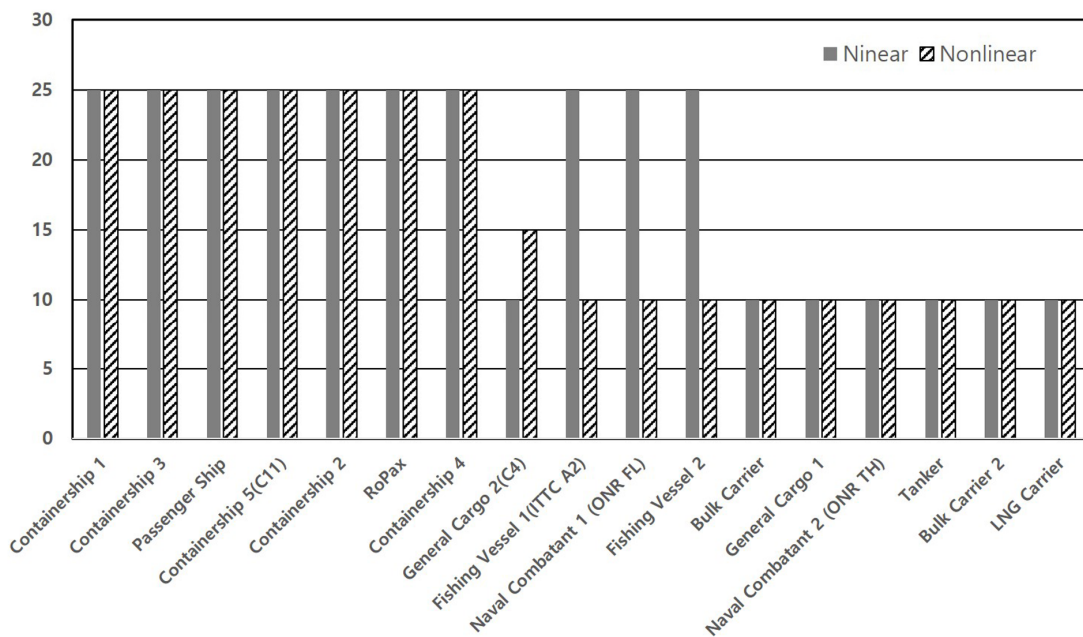

Fig. 9 Parametric roll angle (Level-2)

Table 5 1000 TEU CV pure loss of stability and parametric roll (Level-1)

	Draft	13.9	13.9	13.9	13.9	13.9	13.9	13.9	13.9	13.9
	only if, $(V_D-V)/A_W(D-d) \geq 1.0$	1.17	1.18	1.18	1.05	1.06	1.05	1.05	1.06	1.05
V_D	Displacement volume (m^3)	25851.1	25851.1	25851.1	25851.1	25851.1	25851.1	25851.1	25851.1	25851.1
A_W	Area of water plane (m^2)	2273.0	2260.4	2250.1	2706.8	2704.4	2705.2	2706.9	2703.4	2707.9
$R_L=$	Second Moment of the water plane at the draft d_L (m^4)	63354	62929	62465	84260	84275	84245	84120	84150	84393
RB	Center of buoyancy in height direction	2.842	2.783	2.732	4.490	4.479	4.483	4.491	4.475	4.494
$GM_{min}=$	$=KB+(I_L/V)-VCG$ $=KB+(I_L/(C_b \times L_{PP} \times B \times d)-VCG$	2.806	2.997	3.118	-0.007	0.106	0.162	0.090	0.206	0.319
criteriaR_{PLA}	$R_{PL}A=[\min(1.83d(Fn)^2, 0.05]$m	0.05	0.05	0.05	0.05	0.05	0.05	0.05	0.05	0.05
	$1.83d(Fn)^2=$	0.621	0.608	0.597	0.965	0.963	0.963	0.965	0.962	0.965
$GM_{min}>R_{PLA}$	Result (Pure loss of stability L-1)	Safe	Safe	Safe	Danger	Safe	Safe	Safe	Safe	Safe
	$\Delta GM/GM$ is calculated as follows:	5.292	5.309	5.285	0.943	1.038	1.094	0.797	1.131	1.223
	$\Delta GM=(I_H-I_L)/(2V)$ $=(I_H-I_L)/(2 \times C_b \times L_{pp} \times B \times d)$	1.673	1.694	1.717	0.911	0.911	0.912	0.915	0.915	0.907
	$\Delta GM/GM=$	0.316	0.319	0.325	0.966	0.878	0.833	1.148	0.809	0.742
	Result (Parametric Roll L-1)	Safe	Safe	Safe	Danger	Danger	Danger	Danger	Danger	Danger

Table 6 GT 22,000 Ton class RoPax pure loss of stability and parametric roll (Level-1)

	Draft	1.26	1.28	1.29	1.13	1.17	1.17	1.26	1.28	1.28
	only if, $(V_D-V)/A_W(D-d) \geq 1.0$	41043.9	41043.9	41043.9	41043.9	41043.9	41043.9	41043.9	41043.9	41043.9
V_D	Displacement volume (m^3)	2723.9	2676.4	2631.2	3079.2	2966.5	2966.5	2720.7	2667.2	2667.2
A_W	Area of water plane (m^2)	74837.88	73570.96	71293.18	88414.44	87548.38	87548.38	77499.16	76183.94	76183.94
$I_L=$	Second Moment of the water plane at the draft d_L (m^4)	2.834	2.730	2.624	3.240	3.128	3.128	2.826	2.708	2.708
KB	Center of buoyancy in height direction	-0.430	-0.610	-0.895	-0.379	-0.523	-0.604	-0.374	-0.560	-0.657
$GM_{min}=$	$=KB+(I_L/V)-VCG$ $=KB+(IL/(C_b \times L_{PP} \times B \times d)-VCG$	0.05	0.05	0.05	0.05	0.05	0.05	0.05	0.05	0.05
criteriaR_{PLA}	$R_{PL}A=[\min(1.83d(Fn)^2, 0.05]$m	0.672	0.648	0.623	0.762	0.738	0.738	0.670	0.643	0.643
	$1.83d(Fn)^2=$	Danger	Danger	Danger	Danger	Danger	Danger	Danger	Danger	Danger
$GM_{min}>R_{PLA}$	Result (Pure loss of stability L-1)	Safe	Safe	Safe	Danger	Safe	Safe	Safe	Safe	Safe
	$\Delta GM/GM$ is calculated as follows:	3.245	3.107	2.915	3.074	2.969	2.888	3.121	3.01	2.868
	$\Delta GM=(I_H-I_L)/(2V)$ $=(I_H-I_L)/(2 \times C_b \times L_{pp} \times B \times d)$	3.807	3.992	4.247	2.829	2.950	2.950	3.685	3.883	3.883
	$\Delta GM/GM=$	1.173	1.285	1.457	0.920	0.994	1.021	1.181	1.290	1.354
	Result (Parametric Roll L-1)	Danger	Danger	Danger	anger	Danger	Danger	Danger	Danger	Danger

3. Example of Korean Ship Stability Vulnerability Mode Calculation

The achievements of global researchers on 2nd generation stability are enormous, but because there are many types of ships with a wide range of sizes, there is a limit to the use of these results by Korean shipbuilding officials. It is considered that looking at the results for previous ships in relation to second generation stability will be of practical help to those in Korea.

The results of level-1 calculations for the pure loss of stability and parametric roll modes are listed in Table 4, Table 5, and Table 6. Because of the characteristics of container ships, they have various

loading conditions. However, this paper covers typical loading conditions. In particular, the draft is calculated by taking into account the weight difference between departure and arrival, including changes in draft according to the operation of the hull. In this research, it was found that the assessment of the vulnerability of pure stability occurred at level 2 under the conditions that the load and draft both increased. Each linear parameter is estimated using linearized interpolation, but the results show very reasonable results. In the case of container ships, because the change in the up and down direction of the bow of a full ship is large, and the shape of the water plane significantly changes according to the draft, there is a high possibility of a pure loss of stability. Based on these calculations, it is possible to consider how to reduce the ship's operating speed and Froude number in order to improve the vulnerability of the pure loss of stability mode from the hull design point of view. First, let us consider a method that increases the hull in order to reduce the Froude number. If the length of the ship is increased from 134.7 m to 153.5 m, with the speed fixed at 9.26 m/s, the Froude number will be reduced from 0.255 to 0.239, which will pass the vulnerability test at level 1. However, it is not realistic to increase the length of the hull. In contrast, let us consider that the ship's operating speed is reduced in order to reduce the Froude number. If the ship speed is reduced from 9.26 m/s to 8.23 m/s, with the length of the ship fixed at 134.7 m, the Froude number can be reduced to the desired level. Therefore, this is a more realistic alternative. As a solution from the operation side, we can think of a method to lower the center of gravity by approximately 10 cm. It might be possible to accomplish this by reducing the container capacity. When considering the movement of the desired center of gravity, it is necessary to sacrifice the first stage of the container loading layer. Because reducing the container loading capacity is a very important problem for the ship owner, it is conceivable to move the center of gravity downward by loading all of the empty containers on top as a solution that does not reduce the container loading capacity. However, this method should be considered with great care because it acts as a factor that greatly affects the unloading order. Finally, the center of gravity can be moved downward with the ballast water. This method can also be considered as a secondary solution because it can only be linked to the total container load capacity and requires careful calculation, and the distance to move the center of gravity is limited.

Three ships were found to be vulnerable to parametric roll, which was expected to some extent. In the case of container ships and RoPax ships, a considerably high center of gravity is inevitable because of the presence of structures such as cargo or cabins on the upper deck. Because of the nature of the ship, if the center of gravity is made extremely low, its movement will be limited because an increase in the roll acceleration is expected to damage the cargo or adversely affect the health of the crew. As a way to improve the vulnerability to parametric roll, reducing the change in the water plane configuration subject to the change in the draft is a basic method to reduce the difference in the moment of inertia $(I_H - I_L)$. However, it is very difficult to introduce such a cylindrical ship model when considering the resistance/propulsion performance. It is locally possible to consider increasing the bilge-kill area, but this is considered to be a limited solution because of the limited bilge-kill space.

In this study, negative results were obtained in most cases when assessing vulnerabilities applying level 1 criteria, but these results mean that more detailed research is needed through level 2, and more realistic assessments can be expected from level-2 research. In the case of parametric rolls, however, it is considered that significant changes are required for all three ship models, along with more careful calculations, including a three-step direct assessment method.

4. Summary and conclusion

This paper examined the current international research trends for the second generation of stability criteria and briefly summarized the physical background of each mode and the mathematical modeling procedure. In particular, in view of the fact that Korean shipbuilders mainly build large ships, this paper discussed the pure loss of stability mode and parametric roll mode, which are very relevant for Korean shipbuilders, leaving out the modes that are very unlikely to occur in large ships or that are already excluded from the calculation in the regulations themselves.

In the case of the pure loss of stability mode, it has been shown that the ships in question are often not large problems even if they are designed according to the current criteria, but in the case of parametric roll, the ships may often fail to meet the vulnerability criteria. In particular, container ships, which represent one of the most important ship models in the Korean shipbuilding industry, have frequently been found to fail to meet the vulnerabilities of the parametric roll mode depending on the loading conditions. Consequently, appropriate measures are considered to be required. The conclusions are summarized as follows:

(1) In order to prevent the loss of life and cargo due to the occurrence of various marine accidents, the IMO is developing the second generation of stability criteria to improve the stability of ships, which will ensure that a ship has sufficient stability even in waves. The new stability criteria are in addition to the existing stability criteria, which will remain in effect even after the new stability criteria are put in place.

(2) Regarding the stability in waves, the criteria for five modes are being developed. The inspection structure is composed of a multi-layer structure to minimize the calculations used to verify whether or not the stability criteria are satisfied. The calculations to verify the criteria have been minimized. That is, at a low level, the criteria are verified by simple calculations, and as the level becomes higher, more complicated and detailed verification is performed. If the criteria are satisfied at the low level, the calculation for the next level is not performed. In general, because the lower level involves a greater design margin, vulnerabilities are conservatively assessed and the assessment results are unfavorable for optimization.

(3) At level 1, which is the lowest level, the stability is assessed in a

very simple way. However, at level 2, a more complex method is introduced to assess the stability by determining the probabilistic vulnerability.

(4) Level 3 performs very detailed calculations by performing direct simulations, but this level requires a program with a high level of calculation. The specifications for this calculation program are under discussion. However, in general, a reasonable computer program requires a relatively long calculation time, and thus the development of a technique for determining the stability of a ship within a practical time is required.

(5) When reviewing the results of applying the second generation of stability criteria to the previous ships built in Korea in various cases, it seems that the ships built under the current criteria do not meet the stability criteria in many cases and there is no choice but to operate the ships in a state where the ship speed, dead weight capacity, and other factors are limited. Therefore, it is considered that appropriate design changes are needed to meet the new stability criteria.

Acknowledgments

References

American Bureau of Shipping (ABS). (2004). Guide for the Assessment of Parametric Roll Resonance in the Design Of Container Carriers. Houston, USA; American Bureau of Shipping.

Belenky, V., Bassler, C.G., & Spyrou, K.J. (2011). Development of Second Generation Intact Stability Criteria (NSWCCD-50-TR-2011/065). Naval Surface Warfare Center Carderock Division, US Navy.

Chouliaras, S. (2014). Evaluation of IMO'S Second Generation Intact Stability Criteria (M.S. Thesis). National Technical University of Athens, Athens, Greece.

Grinnaert, F. (2017). Analysis and Implementation of Second Generation Criteria in a Stability Computer Code (Ph.D. Thesis). Université de Bretagne Occidentale (UBO), Brest, France.

Ikeda, Y. (2004). Prediction Methods of Roll Damping of Ships and Their Application to Determine Optimum Stabilization Devices. Marine Technology, 41(2), 89-93.

International Maritime Organization (IMO). (2009a). International Code of Intact Stability. Development of Second Generation Intact Stability Criteria, London.

International Maritime Organization (IMO). (2009b). Information Collected by the Intersessional Correspondence Group on Intact Stability. SLF 52/INF.2, Submitted by USA, London, England.

International Maritime Organization (IMO). (2012). Proposal of Revision of Updated Draft Vulnerability Criteria of Levels 1 and 2 for the Failure Modes of Pure Loss of Stability and Prametric Rll. SLF ISCG 54/19, Submitted by Japan, London, England.

International Maritime Organization (IMO). (2013). Information Cllected by the Correspondence Group on Intact Stability Rgarding the Scond Gneration Itact Sability Citeria Dvelopment, SDC 1/INF.8, Submitted by Japan, London, England.

International Maritime Organization (IMO). (2016a). Finalization of Second Generation Intact Stability Criteria, Amendments to Part B of the 2008 IS Code on Towing, Lifting and Anchor Handling Operations. SDC 3/WP.5, 3rd Session.

International Maritime Organization(IMO). (2016b). Observations Rgarding the Fasibility of the Crrent Vrsion of the Lvel 2 Citerion for Parametric roll in the Second Generation Intact Stability Citeria. Submitted by Sweden, London England.

Krüger S., Hatecke H., Billerbeck H., Bruns A., & Kluwe F. (2013). Investigation of the 2nd Generation of Intact Stability Criteria for Ships Vulnerable to Parametric Rolling in Following Seas. Proceedings of ASME 2013 32nd International Conference on Ocean, Offshore and Arctic Engineering, Nantes France, 10353-10363. https://doi.org/10.1115/OMAE2013-10353

Peters, W., Belenky, V., Bassler, C., Spyrou, K.J., Umeda, N., Bulian, G., & Altmayer, B. (2011). The Second Generation Intact Stability Criteria: An Overview of Development. Proceedings of SNAME Annual Meeting and Expo - Society of Naval Architects and Marine Engineers, Houston, USA.

Rahola, J. (1939). The Judging of the Stability of Ships and the Determination of the Minimum Amount of Stability Especially Considering the Vessels Navigating Finnish Water (Ph.D. Thesis). Technical University of Finland, Helsinki Finland.

Umeda, N. (2013). Current Status of Second Generation Intact Stability Criteria Development and Some Recent Efforts. Proceedings of the 13th International Ship Stability Workshop, Brest, France, 138-157.

Uzunoglu, C.E. (2011). Numerical and Experimental Study of Parametric Rolling of a Container Ship in Waves (Master's Thesis). Technical University of Lisbon, Lisbon, Portugal.

Author ORCIDs and Contributions

Author name	ORCID	Contributions
Chung, Jaeho	0000-0003-1975-3435	①②③④⑤
Shin, Dong Min	0000-0002-9287-9803	③④
Kim, Won-Don	0000-0002-8892-064X	②
Moon, Byung Young	0000-0002-3935-504X	⑤

① Conceived of the presented idea or developed the theory
② Carried out the experiment or collected the data
③ Performed the analytic calculations or numerical simulations
④ Wrote the manuscript
⑤ Supervised the findings of this study

Original Research Article

Numerical Study on the Improvement of the Motion Performance of a Light Buoy

Bo-Hun Son[1] and Se-Min Jeong[2]

[1]*Graduate Student, Department of Naval Architecture and Ocean Engineering, Chosun University, Gwangju, Korea*
[2]*Professor, Department of Naval Architecture and Ocean Engineering, Chosun University, Gwangju, Korea*

ABSTRACT: *A light buoy is equipped with lighting functions and navigation signs. Its shape and colors indicate the route to vessels sailing nearby in the daytime, with its lights providing this information at night. It also plays a role in notifying the presence of obstacles such as reefs and shallows. When a light buoy operates in the ocean, the visibility and angle of light from the lantern installed on the buoy changes, which may cause them to function improperly. Therefore, it is necessary for the buoy to have stable and minimal motions under given environmental conditions, mainly waves. In this study, motion analyses for a newly developed lightweight light-buoy in waves were performed to predict the motion performance and determine the effect of the developed appendages for improving the motion performance. First, free decay tests, including benchmark cases, were performed using computational fluid dynamics (CFD) to estimate the viscous damping coefficients, which could not be obtained using potential-based simulations. A comparison was made of the results from potential-based simulations with and without considering viscous damping coefficients, which were estimated using CFD. It was confirmed that the pitch and heave motions of the buoy became smaller when the developed appendages were adopted.*

1. Introduction

A light buoy is generally moored in a port, inland waterway, or coastal area to provide route information to ships sailing nearby based on its shape, color, and installed lanterns, and to provide information about hazards such as the presence of reefs or shallow water. Because conventional light buoys are made of iron materials, they are heavy, susceptible to corrosion and erosion, difficult to maintain, and have reported problems such as collisions with ships resulting in human injuries. To improve these problems, light buoys that adopt eco-friendly and lightweight materials have been developed (Jeong et al., 2017). The motions of floating offshore structures, as well as the light buoys, which are the subject of this study, are particularly affected by external environmental loads (esp., waves). To secure the motion and structural stability, the difference between the natural frequency of the structure and the frequency of the primary wave in the installation area should be increased or appendages should be developed and/or applied to improve the motion performance. In the case of light buoy, it is necessary to secure the performance of the pitch and roll motions because it is important to secure the visibility of the installed lantern even during these motions. In addition, if excessive heave occurs, it may cause structural damage to the mooring system. Son et al. (2018) estimated the wind and current loads acting on a light buoy subject to changes in the wind direction, wind speed, and current direction at various sea states using computational fluid dynamics (CFD) and analyzed the potential-based motion analysis of a single-moored light buoy by applying the estimated load. As a result of the analysis, it was predicted that the pitch and roll would show large values that did not satisfy the design target under certain sea status. One of the reasons was that viscous damping effect was not considered, which will be described later.

In general, experimental methods and numerical methods based on potential theory are widely used to estimate the motion performances of ships and floating bodies. Among these, it is difficult for potential-based motion analysis to accurately estimate motions that exhibit relatively strong viscous effects and non-linearities. In order to compensate for this problem, studies are in progress in which a viscous damping coefficient calculated through a free decay test or forced

oscillation test is applied to a potential-based motion analysis. Bhattacharyya (1978), Journée and Massie (2001), and Kim et al. (2015) proposed methods to calculate the damping coefficient from free decay tests. Koh and Cho (2016) performed numerical analyses of the characteristics of the heave of a circular cylinder according to the number, size, and relative position of the damping plate using the viscous damping coefficient calculated by performing the free decay test. In a study related to the motion performance of a light buoy, Hong et al. (2001) conducted a model test to estimate the dynamic behavior of the light buoy and the tension force of mooring lines under an extreme environment. In addition to the experimental methods that have been conventionally performed, studies performing free decay tests using CFD have been actively conducted in recent years. Suk et al. (2016) performed a free decay test using CFD, and then estimated the motion performance of a platform supply vessel using Maxsurf Motion, which is commercial motion analysis software, along with the calculated damping coefficient. In addition, Ko et al. (2018a), Ko et al. (2018b), and Kim et al. (2019) performed free decay tests using experiments and CFD to estimate the motion responses of floating bodies in regular waves, and analyzed the motion characteristics.

The current study examined the effects of appendages developed to improve the pitch and heave performances of lightweight light buoys through numerical simulation. After performing the verification simulation for the free decay test using STAR-CCM+, the commercial CFD software made by Siemens, and confirming the accuracy of the used computational methods and schemes, free decay tests were performed on light buoys with/without appendages and the viscous damping coefficient was estimated from the results. In addition, the motion performance was analyzed by applying Aqwa, which is potential-based motion analysis software made by ANSYS Inc., to the estimated viscous damping coefficient, and the effect of the appendages was evaluated by comparing the pitch and heave response amplitude operators (RAOs) of the light buoy with and without appendages (Fig. 1).
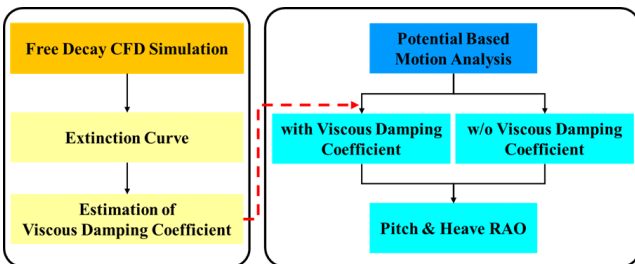

Fig. 1 Schematic flow chart of present study

2. Calculation of damping coefficient

The six degree of freedom motion equation for floating bodies in waves can be expressed by Eq. (1).

$$\left(M_{ij}+a_{ij}\right)\ddot{x}_j+B_{ij}\dot{x}_j+C_{ij}x_j=F_j \qquad i,j=1\sim6 \tag{1}$$

where M_{ij} is the mass or mass moment of inertia of the floating body, x_j is the displacement of the j directional motion, a_{ij} is the i directional added mass or added mass moment of inertia due to the j directional motion, B_{ij} is the j directional damping coefficient due to the i directional motion, C_{ij} is the j directional restoring coefficient due to the i directional motion, and F_j is the wave excitation force matrix.

When performing a free decay test to calculate the viscous damping coefficients of the heave and pitch, only a single degree of freedom motion is considered, as shown in Eqs. (2) and (3).

$$\left(M_{33}+a_{33}\right)\ddot{x}_3+B_{33}\dot{x}_3+C_{33}x_3=F_3 \tag{2}$$

$$\left(M_{55}+a_{55}\right)\ddot{x}_5+B_{55}\dot{x}_5+C_{55}x_5=F_5 \tag{3}$$

Eqs. (4)-(6) were used to calculate the heave and pitch damping coefficients B_{33} and B_{55}, respectively.

$$B_{ii}=2\zeta_{ii}\sqrt{\left(M_{ii}+a_{ii}\right)C_{ii}} \qquad\qquad i=3,5 \tag{4}$$

$$C_{33}=\rho g A \tag{5}$$

$$C_{55}=\rho g \nabla GM \tag{6}$$

where ζ is a non-dimensional damping coefficient, ρ is the density, g is the acceleration of gravity, A is the waterplane area, ∇ is the displacement volume, and GM is the metacenter height.

Non-dimensional damping coefficient ζ is calculated using the method proposed by Journée and Massie (2001), and viscous damping coefficient $b_{ii,vis}$ is calculated using Eq. (7), which was proposed by Koh and Cho (2016).

$$b_{ii,vis}=B_{ii}-r_{ii}(\omega_o) \qquad i=3,5 \tag{7}$$

where $r_{ii}(\omega_o)$ is the radiation damping coefficient at the natural frequency.

3. Estimation of viscous damping coefficient using CFD

3.1 Governing equation

The continuity equation and Reynolds-Averaged Navier-Stokes (RANS) equations were used as the governing equations for the unsteady and incompressible turbulent flows, which are shown in Eqs. (8) and (9), respectively.

$$\frac{\partial u_i}{\partial x_i}=0 \tag{8}$$

$$\frac{\partial u_i}{\partial t}+\frac{\partial(u_iu_j)}{\partial x_j}=-\frac{1}{\rho}\frac{\partial p}{\partial x_i}+\frac{\partial}{\partial x_j}\left\{(\nu+\nu_t)\frac{\partial u_i}{\partial x_j}\right\}+f_i \tag{9}$$

where u is the velocity vector, x is the coordinate, t is the time, p is the pressure, ν is the kinematic viscosity, ν_t is the eddy viscosity, and f is the external force.

## 3.2 Numerical simulation method

STAR-CCM + 11.04 was used as the CFD analysis program, and the Realizable k- ε model was used as the turbulence model. The volume of fluid (VOF) method was used to capture the free-surface, and the overset grid and dynamic fluid body interaction (DFBI) techniques were applied to simulate the motion of the floating body.

3.3 Verification simulation of free decay of circular cylinder

This simulation was performed under the same conditions as the free decay test and CFD simulation of the pitch and heave of a circular cylinder performed by Palm et al. (2016), and the results were compared. The diameter of the cylinder was 0.515 m, and the center of gravity in the vertical direction at the initial draft of 0.173 m was located 0.0758 m from the bottom of the cylinder. The horizontal axis moment was 0.9 kg·m². The initial angle and displacement of the circular cylinder in the free decay test were 8.898° and 0.075 m, respectively.

First, a simulation to check the grid convergence was performed with three grid systems: a medium grid with the base size, coarse grid
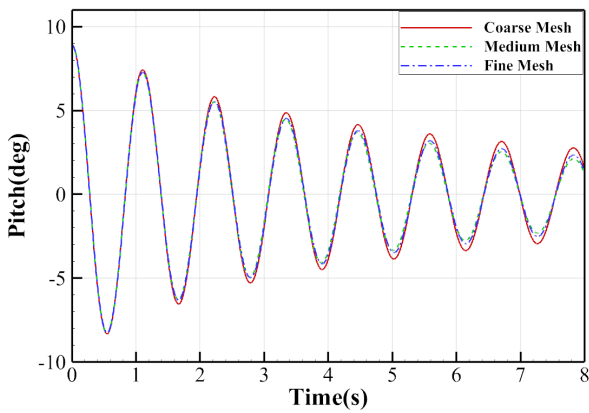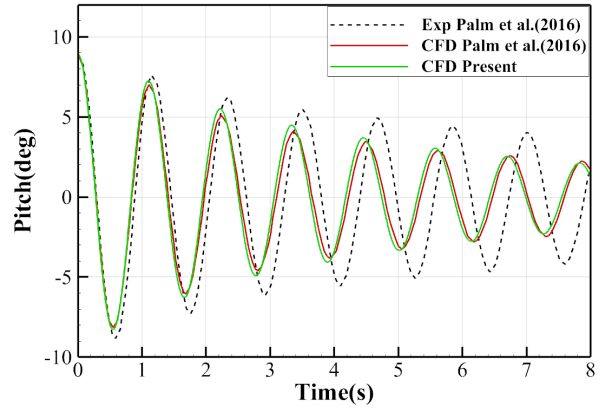

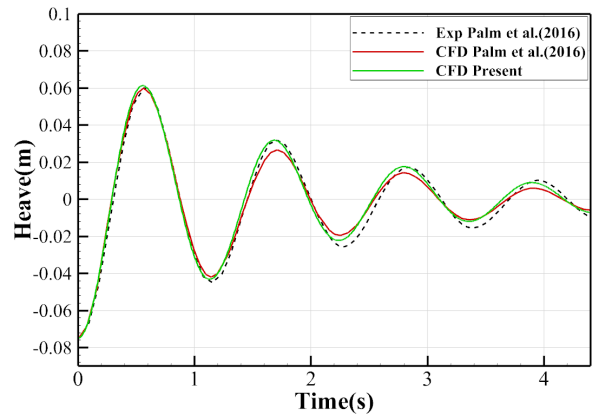(a) Pitch decay curves for cylinder
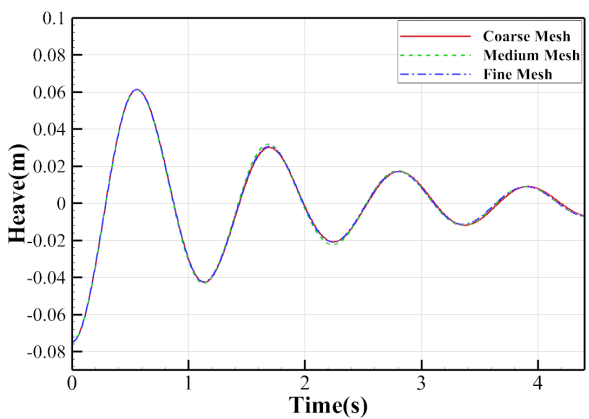
(b) Heave decay curves for cylinder

Fig. 2 Free decay curves for grid convergence test

(a) Pitch decay curves for cylinder

(b) Heave decay curves for cylinder

Fig. 3 Comparison of free decay curves between present CFD results and those of reference (Palm et al., 2016)

with a size 14% larger than the base size, and fine grid with a size 14% smaller than the base size. At this time, the numbers of grids were 711,139, 961,867, and 1,389,682 in the coarse, medium, and fine grid systems, respectively. As shown in Fig. 2, there was no significant difference in the results for the medium and fine grids.

Fig. 3 shows the time history of the pitch and heave of the circular cylinder obtained through the CFD simulation of this study compared to the experimental and CFD results obtained by Palm et al. (2016), and it can be seen that they are relatively coincident with each other. For a quantitative evaluation, natural frequency and non-dimension damping coefficients were calculated from the results of the free decay test and are shown in Table 1. The pitch natural frequency had significant differences of 2.68% and -1.40% compared to the results of the experiment and CFD analysis conducted by Palm et al. (2016), respectively. As described by Palm et al. (2016), these differences were caused by the significant influence on the pitch due to the center of gravity, moment of inertia, and draft, which are difficult to set and measure accurately in small-scale experiments.

The heave natural frequency respectively showed differences of 2.48% and 1.42% compared to the results of the experiment and CFD analysis conducted by Palm et al. (2016). It was considered to be a good match. To more accurately compare the attenuation of the pitch

Table 1 Comparison of natural frequencies and non-dimensional damping coefficients between present CFD results and those of reference (Palm et al., 2016)

	Natural frequency, ω (rad/s)			Non-dimensional damping coefficient, ζ (-)		
	Exp Palm et al. (2016)	CFD Palm et al. (2016)	CFD Present	Exp Palm et al. (2016)	CFD Palm et al. (2016)	CFD Present
Pitch	5.370	5.595	5.518	0.028	0.042	0.038
Heave	5.650	5.712	5.794	0.090	0.108	0.095

and heave, the damping coefficient was calculated and compared using the method proposed by Journée and Massie (2001). The pitch damping coefficient respectively showed differences of about 25.19% and -11.61% from the experiment conducted by Palm et al. (2016) and the CFD analysis. The heave damping coefficient respectively showed differences of about 5.8819% and -13.08% from the experiment conducted by Palm et al. (2016) and the CFD analysis. These values were closer to those of the experiment.

3.4 Free decay simulation of light buoy

3.4.1 Target model

The recently developed LL-24 type of lightweight light buoy (Jeong et al., 2017) was targeted (Fig. 4). The height of the analysis model was 4.086 m, and the diameter of the buoyant body was 2.40 m. To improve the motion performance of the light buoy, two types of appendages were installed at the lower part of the light buoy. An appendage created based on the heave damping plate was installed on the lower center part of the buoy, and a conical structure created based on the bilge keel of the vessel was installed on the lower part of the buoyant body of the buoy (Fig. 5). Koh et al. (2013) conducted a study on the reduction of the circular cylinder's heave according to the presence or absence of a damping plate with changing the porosity of the damping plate through a free decay test. The porous damping plate

showed a higher damping coefficient than that of the non-porous damping plate. Therefore, the effect of porosity for each appendage was also investigated in this study. For the sake of convenience, the base model without an appendage was denoted as the base, and the
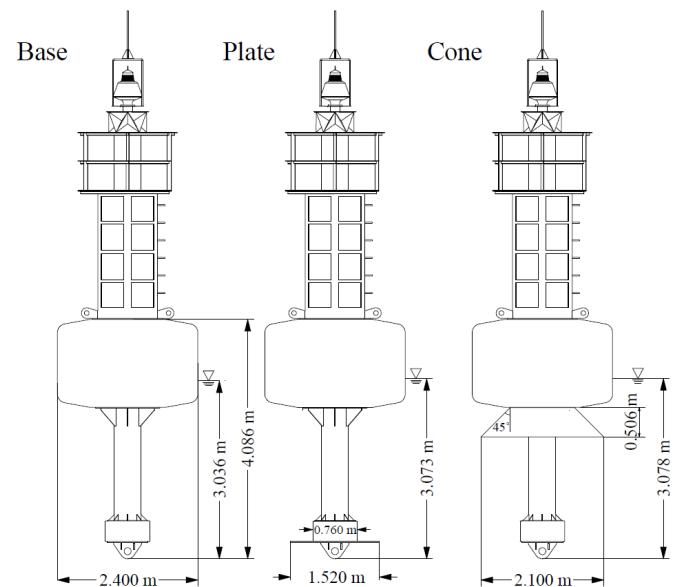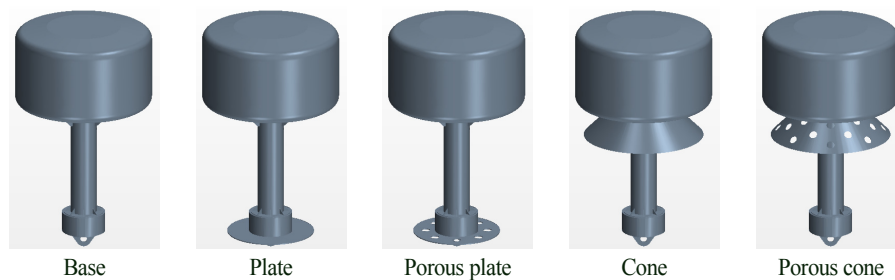

Fig. 4 Geometries of target light-buoys without and with developed appendage

Fig. 5 Geometries of simplified light-buoys without and with developed appendage

Table 2 Main particulars and hydrostatic properties of light buoys without and with appendages

	Base	Plate	Porous plate	Cone	Porous cone
Mass (kg)	2,423	2,596	2,579	2,617	2,597
Diameter (m)			2.40		
Draft (m)	3.036	3.073	3.069	3.078	3.073
Center of gravity (m)	2.136	2.009	2.021	2.150	2.149
GM (m)	1.052	1.144	1.137	1.018	1.021
Mass moment of inertia (kg·m^2)	10,902	11,490	11,435	10,965	10,958

models with a heave damping plate, porous heave damping plate, conical structure, and porous conical structure were respectively denoted as the plate, porous plate, cone, and porous cone. The main specifications of the light buoy and light buoy with a appendages installed are listed in Table 2. When the appendage was installed, the mass of the light buoy increased by about 7% compared to the base model, and the changes in the center of gravity and draft were considered in the numerical simulation.

3.4.2 Computational domain, boundary conditions, and grid system

The computational domain and boundary conditions are illustrated in Fig. 6. The size of the computational domain was set to 25 m in the depth direction below the free water surface, and 30.0 D (=72.00 m) was set based on the diameter D (=2.40 m) of the buoyant body in the length and width directions. As the boundary conditions, a no-slip wall was applied to the bottom boundary surface, a symmetry plane condition was used for the upper surface of the computational domain, and a pressure outlet boundary condition was applied for other boundaries. In order to suppress the generation of reflected waves, the numerical damping of the wave was applied to a section corresponding to about 1/3 of the entire computational domain length from the end of the entire computational domain.

The grid systems were created using a surface remesher, trimmer mesh, and prism layer mesh. The grids were densely positioned to capture the complex flow around the light buoy and free surface (Fig.
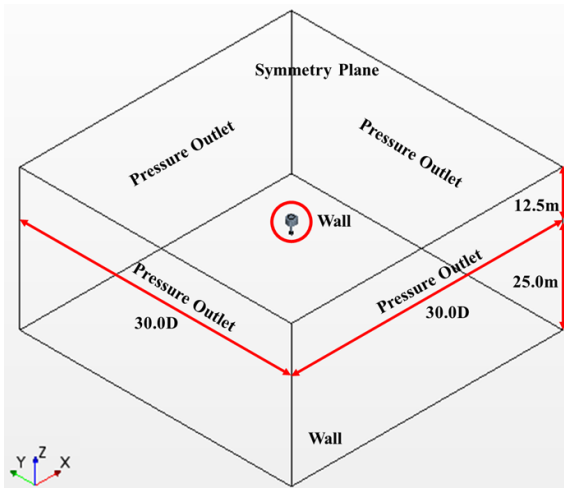
7). On the basis of the pitch, 127 grids per wavelength and 51 grids per wave height were used. On the basis of the heave, 26 grids per wavelength and 10 grids per wave height were used. The total number of the grids was about 2.35 million in the base model, and about 2.9 million in most other cases depending on the type of appendage.

A degree of freedom was allowed the pitch, heave, and surge motions, and the initial angle and displacement of the light buoy were set to 10° for the pitch and 0.40 m below the draft in the vertical direction for the heave.

3.4.3 Result of numerical simulation

The pitch time history of the light buoys with and without appendages is illustrated in Fig. 8. The models with the appendage installed show faster damping than the base model and have smaller peaks when the plate and porous plate are installed compared to those when the cone and porous cone appendages are installed. The damping coefficients were estimated to compare the motion damping effects of the appendages in more detail and are listed in Table 3. It can be seen that the plate type appendages have the highest damping coefficients, and the damping coefficient increases in the same appendage with porosity. Depending on the porosity of the appendage, it was confirmed that the porous appendage had a relatively more significant damping effect than the non-porous appendage, as presented in the research of Koh et al. (2013). In addition, the pitch natural frequency was estimated to be higher than that of the base model when an appendage was installed. The natural frequency increased when the
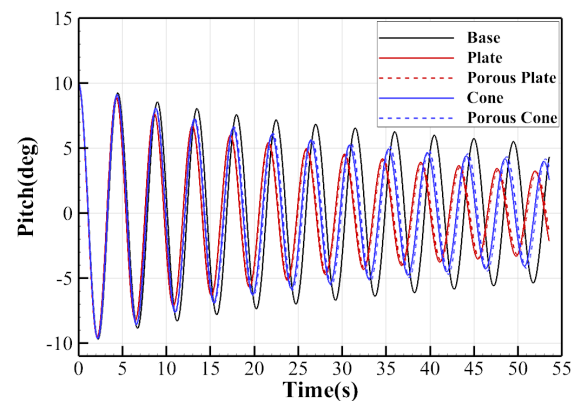

Fig. 6 Computational domain and boundary conditions

Fig. 7 Grid system for free decay test of light buoys

Fig. 8 Comparison of pitch decay curves of light buoys without and with appendages

Table 3 Predicted non-dimensional pitch damping coefficients and natural frequencies of buoys without and with appendages

	ζ (-)	Relative increment of ζ (%)	ω (rad/s)
Base	0.0135	-	1.397
Plate	0.0209	54.89	1.452
Porous plate	0.0219	62.37	1.447
Cone	0.0167	23.44	1.425
Porous cone	0.0172	27.31	1.418

appendage was installed. This was because the GM and draft increased and the restoring moment coefficient also increased as a result of the installation of the appendage.

Fig. 9 shows the vorticity distribution at each peak position (phase) when the light buoy proceeds with pitch free decay. It can be seen that a complex and strong vortex is formed around the appendage. Therefore, the viscous damping coefficient increases due to the energy loss caused by the vortex generation, strong viscous effect, and interaction with the light buoy.

Fig. 10 shows the wave elevation around the light buoy at each peak position (phase) when the light buoy proceeds with pitch free decay. Looking at the first peak, it can be seen that a relatively high wave is generated around the model when an appendage is installed. It seems that the increase in the amount of energy dissipation due to wave

generation results in an increase in the damping coefficient.

The heave time history of the light buoys with and without appendages is illustrated in Fig. 11. As with the said pitch, the models with the appendage installed show faster damping than the base model and have smaller peaks when the plate and porous plate are installed than when the cone and porous cone appendages are installed. The damping coefficients were estimated to compare the motion damping effects of the appendages in more detail and are listed in Table 4. It was estimated that the plate-type appendages had the highest damping coefficients, and the damping coefficient increased for the same appendage with porosity. When the appendage was installed, the natural frequency was estimated to be smaller than that of the base model. The natural frequency varied depending on the model. It was thought that this was because the mass and/or added mass was changed
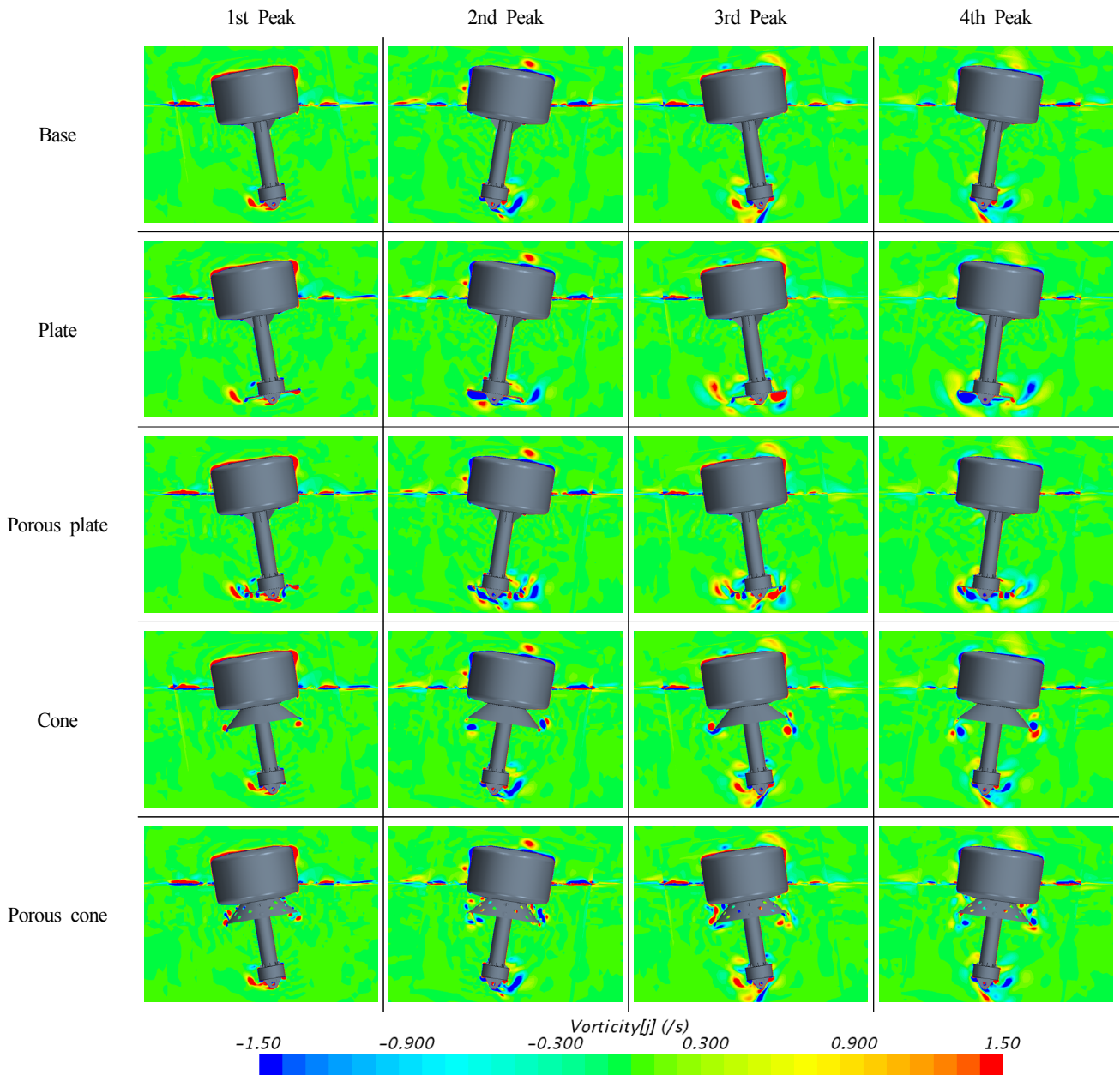

Fig. 9 Comparison of vorticity around light buoys without and with appendages during pitch free decay test

	1st Peak	2nd Peak	3rd Peak	4th Peak
Base				
Plate				
Porous plate				
Cone				
Porous cone				

Position in Cartesian 1[Z] (m)

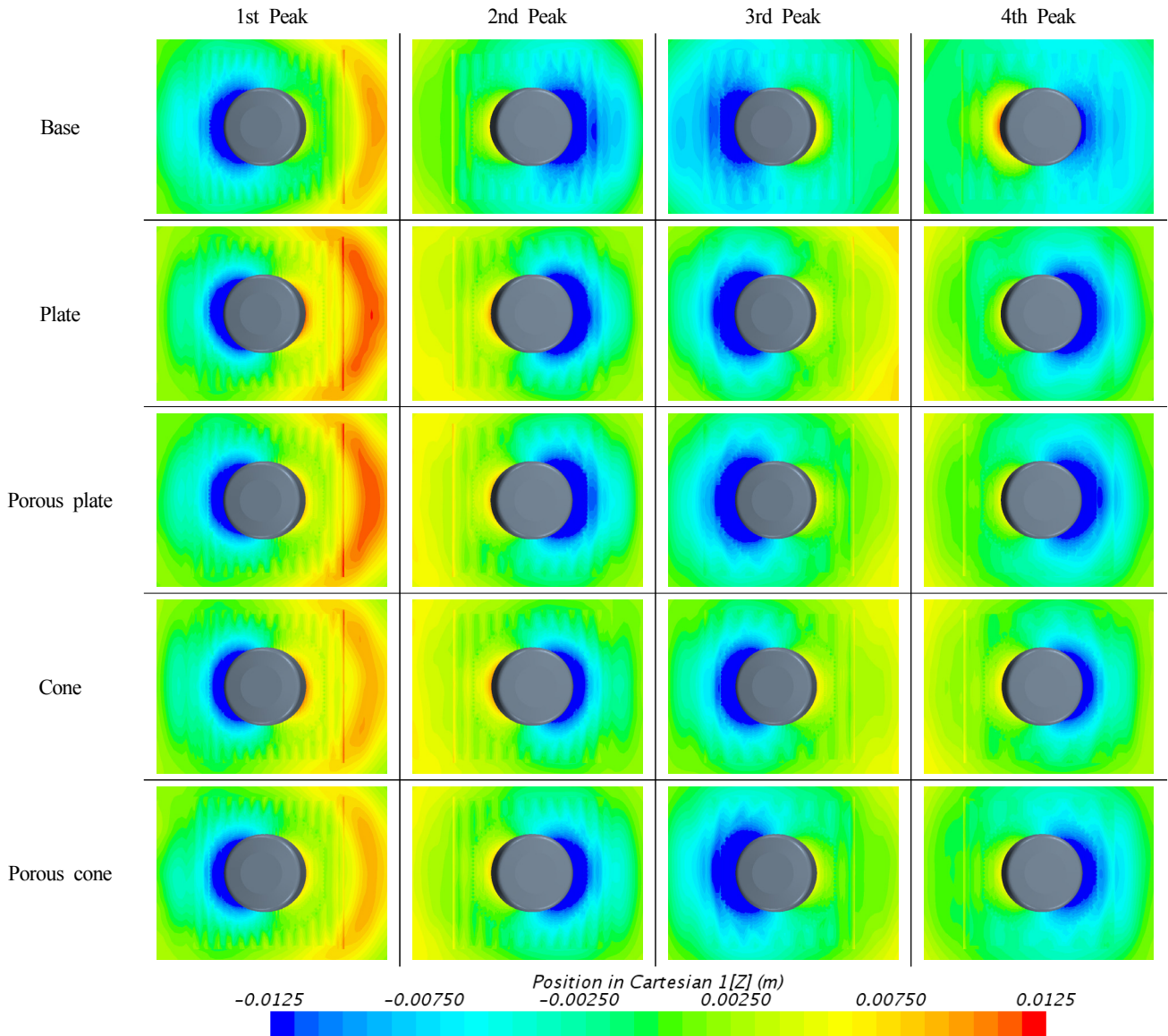−0.0125   −0.00750   −0.00250   0.00250   0.00750   0.0125

Fig. 10 Comparisons of wave elevation around light buoys without and with appendages during pitch free decay test

by the installation of the appendage, and the damping coefficient increased as a result of radiation and viscosity.
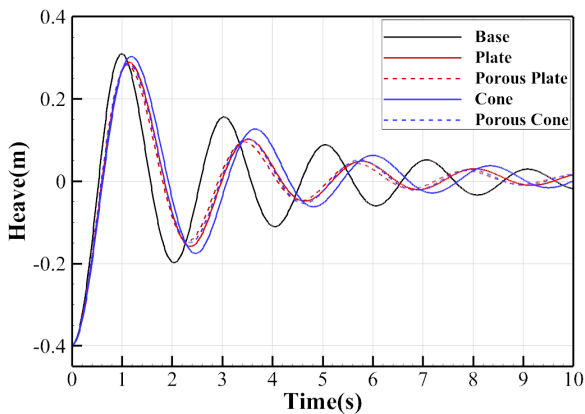

Fig. 11 Comparison of heave decay curves of light buoys without and with appendages

Table 4 Predicted non-dimensional heave damping coefficients and natural frequencies of buoys without and with appendages

	ζ (-)	Relative increment of ζ (%)	ω (rad/s)
Base	0.1107	-	3.107
Plate	0.1550	39.97	2.748
Porous plate	0.1660	49.99	2.813
Cone	0.1344	21.37	2.649
Porous cone	0.1587	43.37	2.795

Fig. 12 shows the vorticity distribution at each peak position (phase) when the light buoy proceeds with heave free decay. As with the pitch, a complex and strong vortex is formed around appendages in heave, and, in particular, it is clearly created in the plate modes.

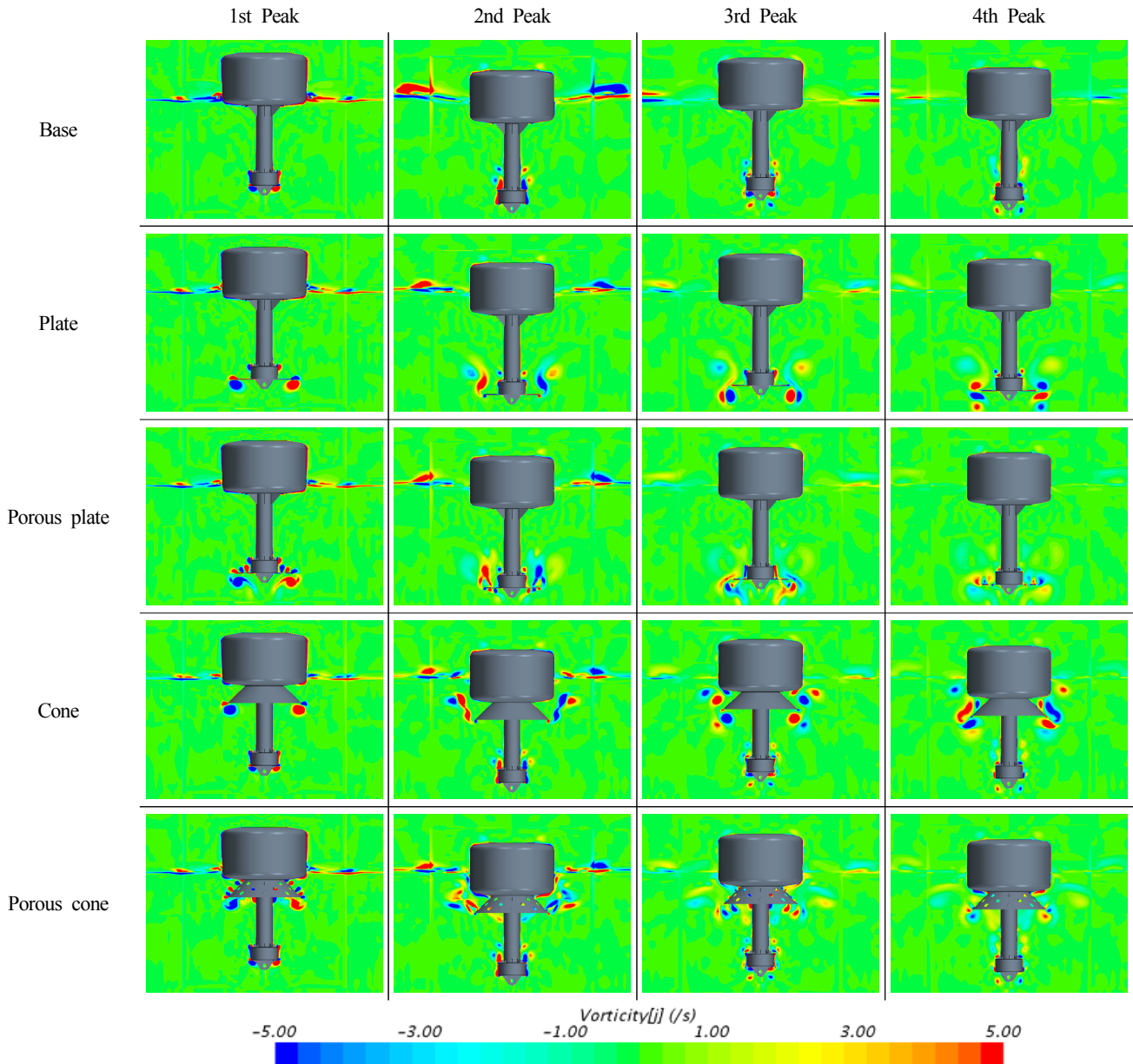Fig. 13 shows the wave elevation around the light buoy at each peak

| | 1st Peak | 2nd Peak | 3rd Peak | 4th Peak |

Fig. 12 Comparison of vorticity contours around light buoys without and with appendages during heave free decay test

position (phase) in heave free decay. When looking at the first and second peaks, the models with appendages installed produce lower waves than the base model. This is because the heave becomes smaller as a result of the installation of the appendage.

4. Estimation of motion performance

The potential-based motion analysis was performed using ANSYS Aqwa with applying the viscous damping coefficient, which was estimated through the CFD simulations of the free decay tests and dealt as a linear damping.

4.1 Estimated result of motion performance

Table 5 lists the added mass moment of inertia, radiation damping

coefficient, viscous damping coefficient, and ratio of the viscous damping to the entire damping coefficient in the pitch motion at natural frequencies calculated through the potential-based motion analysis. The installation of appendages caused increases in the mass moment of inertia and viscous damping coefficient. In addition, the radiation damping coefficient accounted for a very small portion of the entire damping coefficient, whereas the viscous damping coefficient accounted for a significant portion. The estimated viscous coefficients are placed in descending order of the porous plate, plate, porous cone, cone and base.

Fig. 14(a) and Fig. 14(b) respectively show the pitch RAOs when the viscous damping coefficient is not considered and when it is considered. When the viscosity was not considered, it was confirmed that a very large motion occurred regardless of whether or not an appendage was installed near the natural frequency (1.397 rad/s) of the
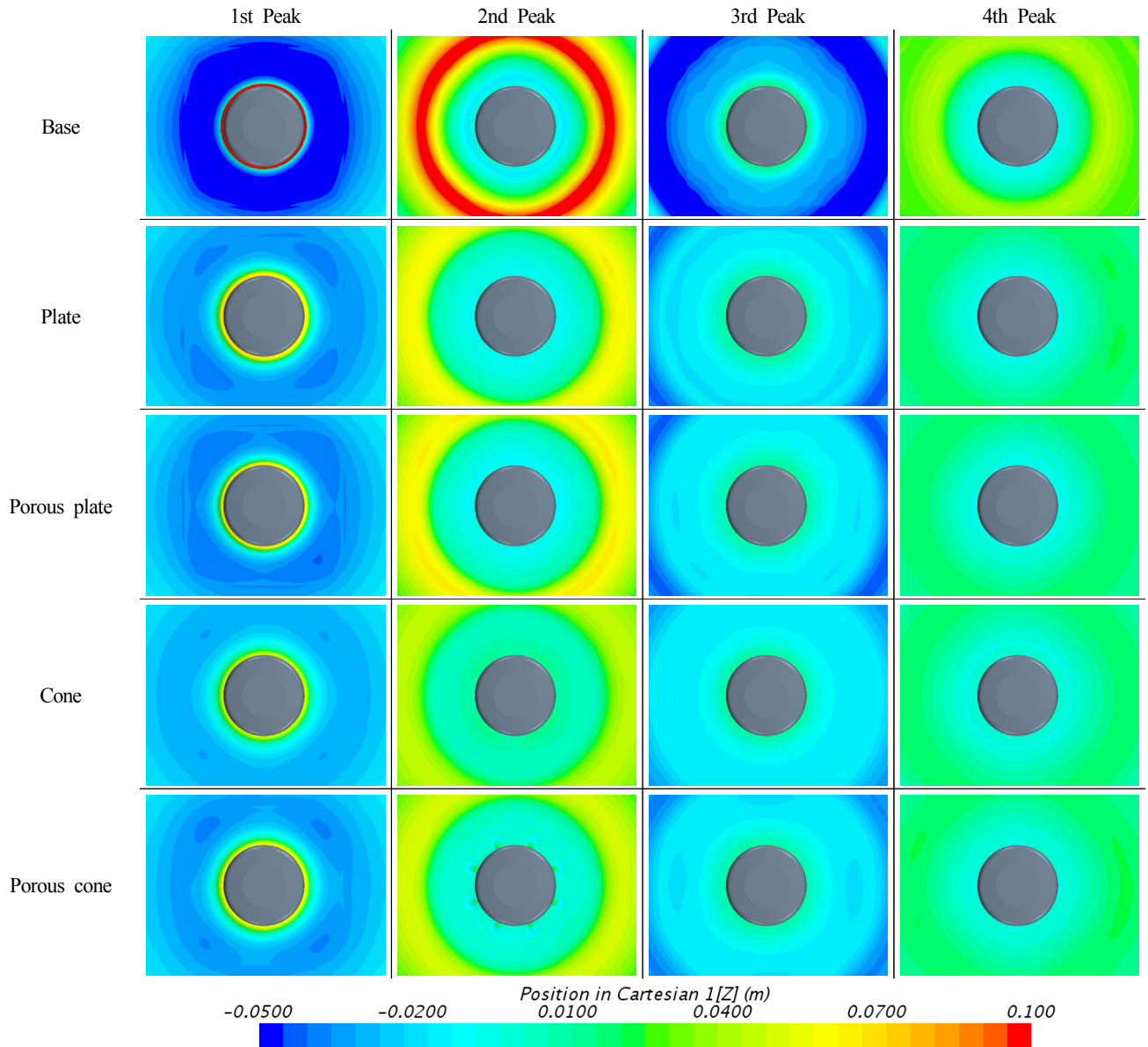
Fig. 13 Comparison of wave elevations around light buoys without and with appendages during heave free decay test

Table 5 Coefficients of added mass moment of inertia, viscous and radiation damping, and ratio of viscous damping to whole damping for pitch motion at natural frequencies of buoys

	a_{55} (kg·m²)	$b_{55,vis}$ (kg·m²/s)	$r_{55}(\omega_o)$ (kg·m²/s)	$\dfrac{b_{55,vis}}{B_{55}}$ (-)
Base	1,968	63.359	0.488	0.9924
Plate	2,435	109.952	0.884	0.9920
Porous plate	2,556	114.261	0.842	0.9927
Cone	2,145	80.067	0.656	0.9919
Porous cone	2,116	82.690	0.610	0.9927

base model. This was because the viscous damping. which accounted for a significant portion of the damping coefficient of the pitch motion, was ignored. Considering the viscous damping coefficient, it was

shown that the RAO was significantly reduced in Fig 14(b). The maximum values of the pitch RAO were placed in the ascending order of the porous plate, plate, porous cone, cone, and base.

Table 6 lists the added mass, radiation damping coefficient, viscous damping coefficient, and ratio of viscous damping to the entire damping coefficient for the pitch motion at natural frequencies calculated through the potential-based motion analysis. With the exception of the cone model, the models had radiation damping coefficients that were larger than the viscous damping coefficient. The ratio of the viscous damping coefficient to the entire damping coefficient was smaller than the pitch motion. This was because the wave elevation caused by the heave of a circular cylinder type floating body was higher than that caused by the pitch motion. In addition, the ratio of the radiation damping coefficient to the entire damping coefficient decreased when the appendages were installed because the maximum motion displacement and velocity were reduced as a result
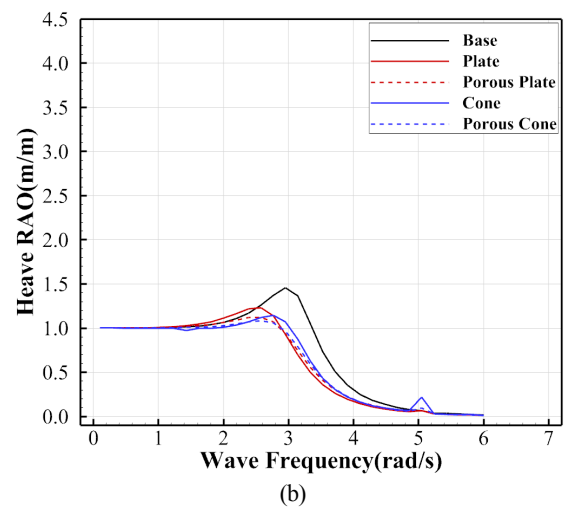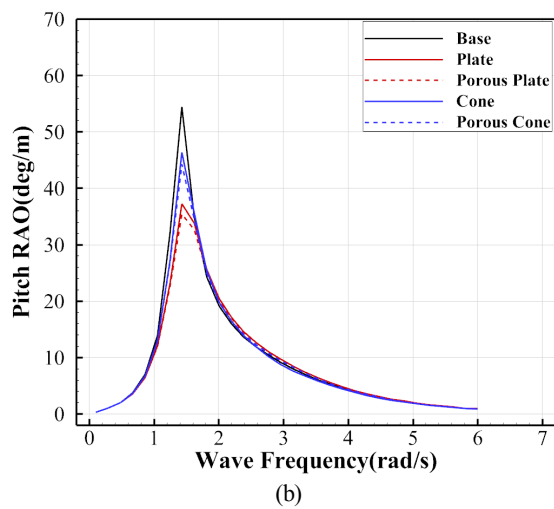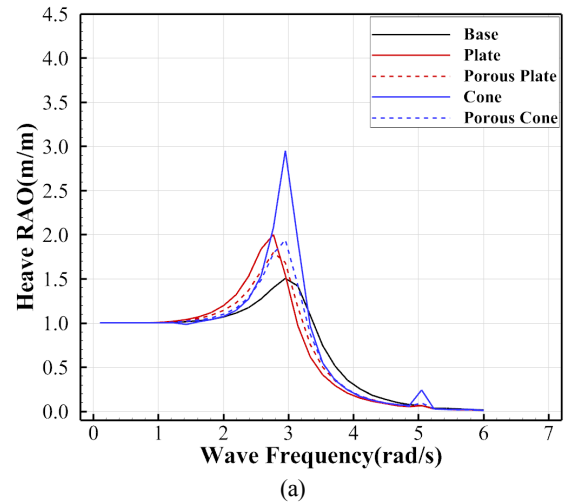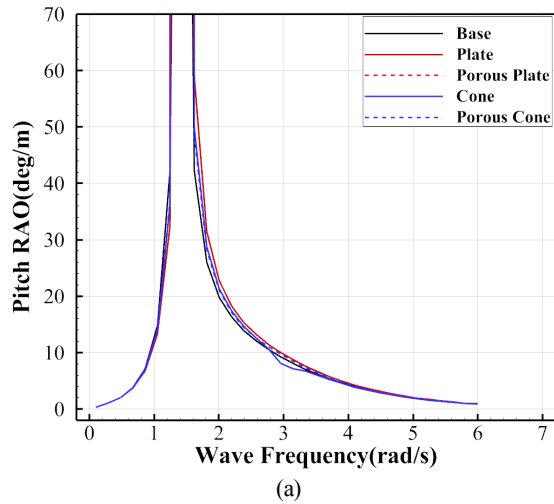
(a)

(b)

Fig. 14 Pitch RAOs of light buoys (a) without and (b) with considering viscous damping

(a)

(b)

Fig. 15 Heave RAOs of light buoys (a) without and (b) with considering viscous damping

Table 6 Coefficients of added mass, viscous and radiation damping, and ratio of viscous damping to whole damping for heave motion at natural frequencies of buoys

	a_{33} (kg)	$b_{33,vis}$ (kg/s)	$r_{33}(\omega_o)$ (kg/s)	$\dfrac{b_{33,vis}}{B_{33}}$ (-)
Base	2,254	136	3,107	0.0419
Plate	2,874	2,243	2,890	0.4368
Porous plate	3,166	2,387	2,987	0.4441
Cone	2,549	2,907	1,710	0.6295
Porous cone	2,609	2,570	2,600	0.4970

of the installation of appendages. The estimated viscous damping coefficients were placed in the descending order of the cone, porous cone, porous plate, plate, and base.

Fig. 15(a) and Fig. 15(b) respectively show the heave RAOs estimated through the analysis of the potential-based motion when the viscous damping coefficient is not considered and when it is considered. The difference in the RAO values when the viscous

damping coefficient is considered and when it is not considered at the natural frequency (3.107 rad/s) of the base model is smaller than that in the pitch motion because the ratio of the viscous damping coefficient to the heave damping coefficient is relatively small. When the viscosity was not considered, the base model was estimated to have the greatest reduction in motion in the vicinity of the natural frequency, but when the viscosity was considered, the motion of the light buoy with appendage decreased. The maximum values of the heave RAO were placed in the ascending order of the porous cone, porus plate, cone, plate, and base. As with the pitch motion, the maximum value of the heave RAO was estimated to be reduced in all the models with appendages installed.

5. Conclusion

This study examined the effect of reducing the pitch and heave motions of the appendages developed to improve the motion of a light buoy through numerical analyses. In addition, the motion performance of the light buoy was examined in relation to the installation and type

of appendage by performing analyses of the potential-based motion while applying the viscous damping coefficient estimated through a free decay test using CFD.

(1) For validation, a CFD simulation of the circular cylinder's pitch and heave free decay was performed. The results were compared to the experimental results and other CFD results and were in good agreement with them.

(2) A CFD simulation of the free decay of the pitch and heave was performed for the base model without any appendage and for the plate, porous plate, cone, and porous cone models with the appendages installed, and each viscous damping coefficient was calculated. The damping coefficient was estimated to be increased by the installation of the appendage. The viscous damping coefficient accounted for most of the pitch damping coefficient, and the viscous damping and radiation coefficients were estimated to be at equivalent levels in the heave damping coefficient.

(3) Potential-based motion analyses of cases with and without considering the viscous damping coefficient calculated by CFD were performed, and the results were compared. When considering the viscous damping coefficient, the RAO was significantly reduced near the natural frequency of each model.

(4) The motion analysis of each model considering the viscous damping coefficient showed that the motion was reduced by the installation of the appendage. The maximum RAO values were estimated to have an ascending order of the porous plate, plate, porous cone, cone, and base for the pitch, and the ascending order of the porous cone, porous plate, cone, plate, and base for the heave.

The results of this study are expected to be used as basic data for analyses of the motion performances of marine structures such as spar platforms (circular cylinder type) and wave energy converters (WECs) as well as light buoys. The results will be compared to the results obtained from CFD single simulations in the future.

References

Bhattacharyya, R. (1978). Dynamics of Marine Vehicles. New York: Wiley.

Hong, K.Y., Yang, C.K., & Choi, H.S. (2001). An Experimental Method for Analysis of the Dynamic Behavior of Buoys in Extreme Environment. Journal of Ocean Engineering and Technology, 15(3), 134-141.

Jeong, D.S., Jeong, S.M., Jeong, S.S., & Yang J.H. (2017). Stability Evaluation of a LL-24-type Lightweight Light-Buoy Adopting EPP. Journal of Advanced Engineering and Technology, 10(2), 297-303.

Journée, J.M.J. & Massie, W.W. (2001). Offshore Hydromechanics. Lecture notes. Netherlands: Delft University of Technology.

Kim, M.G., Jung, K.H., Park, S.B., Lee, G.N., Park, I.R. & Suh, S.B. (2019). Study on Roll Motion Characteristics of a Rectangular Floating Structure in Regular Wave. Journal of Ocean Engineering and Technology, 33(2), 131-138. https://doi.org/ 10.26748/KSOE.2019.009

Kim, N.W., Kim, Y.J., & Ha, Y.R. (2015). Experimental Study of the Free Roll Decay Test for the Evaluation of Roll Damping Coefficients. Journal of the Society of Naval Architects of Korea, 52(6), 460-470. https://doi.org/10.3744/SNAK.2015.52.6.460

Ko, H.S., Bae, Y.H. & Cho, I.H. (2018a). Dynamic Analysis of a Floating Structures Using OpenFOAM. Journal of Computational Fluids Engineering, 23(1), 101-112.

Ko, H.S., Cho, I.H. & Bae, Y.H. (2018b). Non-linear Dynamic Analysis of an Eccentrical Cylinder-type Wave Energy Converter Using OpenFOAM. Journal of Computational Fluids Engineering, 23(3), 18-26. https://doi.org/10.6112/kscfe. 2018.23.3.018

Koh, H.J. & Cho, I.H. (2016). Heave Motion Response of a Circular Cylinder with the Dual Damping Plates. Ocean Engineering, 125, 95-102. https://doi.org/10.1016/j.oceaneng.2016.07.037

Koh, H.J., Kim, J.R. & Cho, I.H. (2013). Model Test for Heave Motion Reduction of a Circular Cylinder by a Damping Plate. Journal of Ocean Engineering and Technology, 27(4), 76-82. https://doi.org/10.5574/KSOE.2013.27.4.076

Palm, J., Eskilsson, C., Paredes, G.M., & Bergdahl, L. (2016). Coupled Mooring Analysis for Floating Wave Energy Converters using CFD: Formulation and Validation. International Journal of Marine Energy, 16, 83-99. https://doi.org/10.1016/j.ijome.2016.05.003

Son, B.H., Ko, S.W., Yang, J.H., & Jeong, S.M. (2018). Motion Analysis of Light Buoys Combined with 7 Nautical Mile Self-Contained Lantern. Journal of the Korean Society of Marine Environment & Safety, 24(5), 628-636. https://doi.org/10.7837/kosomes.2018.24.5.628

Suk, J., Kim S.Y., Yang, Y.J., Jin, S.H., & Park. J.C. (2016). A Study for Roll Damping Performance of a Platform Supply Vessel with or without Bilge Keel Using CFD. Journal of the Korean Society of Marine Engineering, 40(9), 791-798. https://doi.org/10.5916/jkosme.2016.40.9.791

Author ORCIDs and Contributions

Author name	ORCID	Contributions
Son, Bo-Hun	0000-0001-8635-3787	②③
Jeong, Se-Min	0000-0001-9252-1273	①④⑤

① Conceived of the presented idea or developed the theory
② Carried out the experiment or collected the data
③ Performed the analytic calculations or numerical simulations
④ Wrote the manuscript
⑤ Supervised the findings of this study

Numerical Study on Characteristics and Control of Heading Angle of Floating LNG Bunkering Terminal for Improvement of Loading and Off-loading Performance

Seunghoon Oh[1], Dong-Woo Jung[2], Yun-Ho Kim[1], Hyun-Uk Kwak[2], Jae-Hwan Jung[1],
Sung-Jun Jung[1], Byeongwon Park[1], Seok-Kyu Cho[3], Dongho Jung[3] and Hong Gun Sung[3]

[1]Senior Researcher, Korea Research Institute of Ships and Ocean Engineering, Daejon, Korea
[2]Senior Engineer, Korea Research Institute of Ships and Ocean Engineering, Daejon, Korea
[3]Principal Researcher, Korea Research Institute of Ships and Ocean Engineering, Daejon, Korea

ABSTRACT: *In this study, heading characteristics and heading control performances were evaluated to achieve the wave shield effect. The wave shield effect originating from heading control reduces the relative motions of moored vessels in a floating liquefied natural gas bunkering terminal (FLBT). Therefore, loading and off-loading performances are improved through reduced relative motion. For the objective of this study and efficiency of the analysis, a simplified model was used that assuming no relative motion of the moored vessels in the FLBT. The simplified model involved modeling the environmental loads and inertia of several floating bodies, including FLBT, into the environmental loads and inertia of a single vessel. The simplified model was validated through comparisons with model tests. With the simplified model, heading characteristics and heading control simulations were performed using low-frequency planar motion equations. The heading characteristics and heading control performances of FLBT were analyzed through the results of simulations under the expected environmental conditions. The capacity of the tunnel thrust for the heading control performance was confirmed to be adequate for improvement of the loading and off-loading performances using the wave shielding effects under the operation conditions.*

1. Introduction

Owing to the regulation of exhaust gas emissions from vessels, liquefied natural gas (LNG) has been garnering attention as an alternative eco-friendly fuel for vessels. LNG is considered as one of the most realistic alternatives to satisfy SOx and NOx regulations. Such social awareness is accelerating the development of LNG-powered vessels. It is necessary to expand the LNG bunkering infrastructure to supply LNG to vessels with LNG propulsion for their smooth operation. Relevant studies have been actively conducted both nationally and globally, and their feasibility has been reviewed.

The Korea Research Institute of Ships & Ocean Engineering (KRISO) has been conducting studies on an offshore floating LNG bunkering system and has reviewed the system in terms of the design, equipment, and rules for offshore floating bunkering infrastructure. A floating LNG bunkering terminal (FLBT) unloads LNG from an LNG

carrier and supplies LNG to the vessel with an LNG propulsion vessel through an LNG bunkering shuttle (LNG-BS). As the loading and off-loading operations of the FLBT are undertaken on the sea, it is essential to evaluate its operational stability in the marine environment. As 5K and 30K LNG-BSs have a relatively small displacement compared with FLBT, the work performance was observed to be degraded due to the marine environment under the operating conditions in the numerical analysis and model tests (Kim et al., 2017; Kim et al., 2018; Jung et al., 2018; Jung, 2019). Therefore, shielding the FLBT from ocean waves is essential for improving its loading and off-loading performances. A stern tunnel thruster was considered to control the heading angle of the FLBT to a constant value, to use the shielding effect for the FLBT. Numerical (Oh et al., 2019) and experimental (Park et al., 2019) studies have been conducted on the characteristics and control methods of the heading angle for the FLBT-only case using a stern tunnel thruster. However,

as the loading and off-loading operations are generally performed in the environment where one or more floating bodies are moored in the FLBT, evaluation of the heading angle characteristics and control performance of the FLBT with multiple floating bodies is required.

In this study, heading angle control was numerically analyzed to evaluate the heading angle characteristics and control performance of the FLBT with multiple moored vessels. Environmental loads on the off-loading vessels, including the FLBT, were calculated through verified model tests and numerical analysis. As the mooring line of the vessel moored at the FLBT is taut, the amplitude of relative motion is small in terms of heading angle control. The relative motion of a vessel moored using the taut mooring can be ignored. Therefore, the heading angle characteristics and control performance were analyzed using a simplified model, in which the vessels moored at the FLBT were considered as a part of the FLBT. The environmental loads (wind, current, and wave) and inertia (mass, moment of inertia, and added mass) acting on the multiple vessels were replaced by the loads and inertia of a single vessel to construct a simplified model. Model tests and comparative studies were conducted to confirm the validity of the simplified model. Low-frequency planar motion simulation of the FLBT was performed using the simplified model that was validated under the environmental conditions of the expected FLBT installation

position, and the heading angle characteristics of the FLBT were identified. Finally, the heading angle control performance, which is essential for the ocean wave shielding effect to improve the loading and off-loading performances, was evaluated. Proportional-derivative (PD) control was used for the heading angle control, and the Lagrange multiplier method was used as the thrust allocation algorithm. Through the performance evaluation of the heading angle control, the range of the controllable heading angles was verified, and the result can be used as a guide for the operating procedure.

2. Simplified Model for Loading and Off-loading Scenarios and Evaluation of Heading Angle Control Performance

2.1 Off-loading Scenario

The FLBT receives LNG from LNG carriers and supplies the received LNG to the vessels with LNG propulsion systems through the LNG-BS. The FLBT developed in this study is shown in Fig. 1. It was designed to receive LNG from a 170K LNG carrier and unload the LNG to 30K and 5K LNG-BSs simultaneously. According to a study on the operating procedure of the developed FLBT, it can dock up to three vessels simultaneously, and the total operation time when three
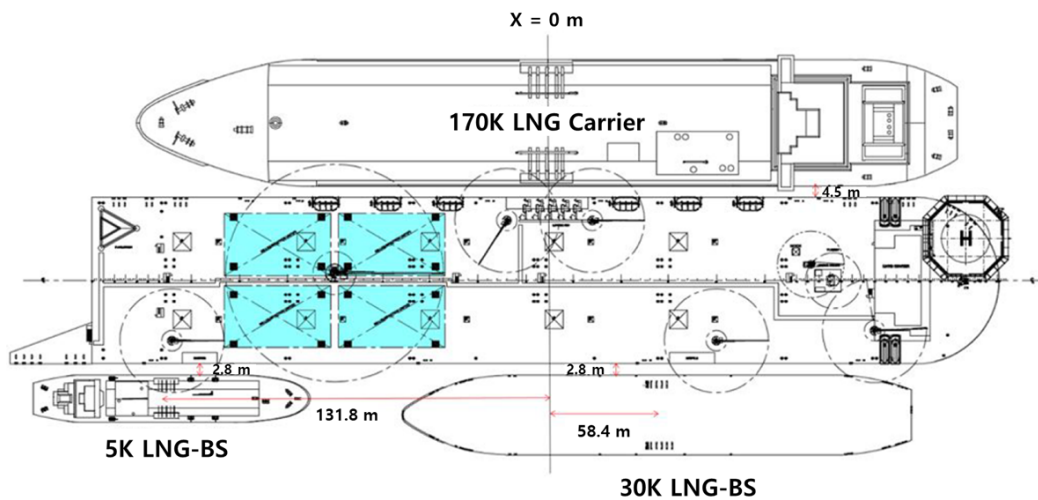

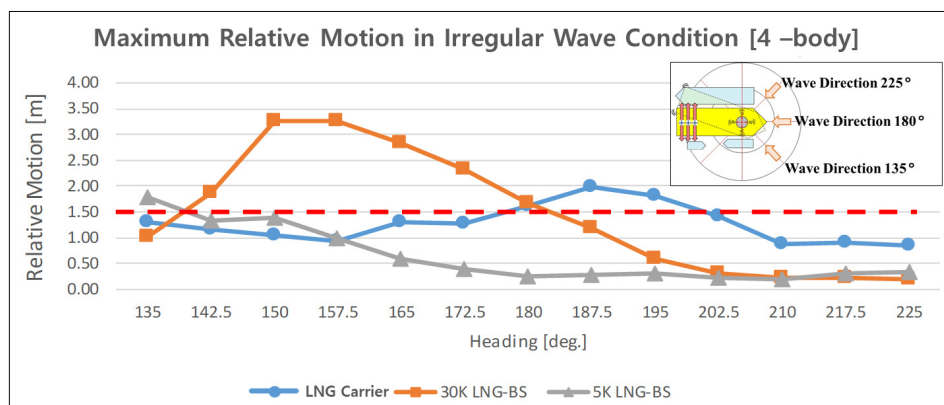**Fig. 1** Arrangement by the scenario of loading and off-loading operations

Fig. 2 Maximum relative motion response in irregular wave conditions (Jung, 2019)

vessels are docked in the FLBT for off-loading was analyzed to be significantly short compared with the entire off-loading operation time. However, to determine the range of loading and off-loading, the operating conditions when the maximum number of vessels is docked should be considered.

Kim et al. (2017), Kim et al. (2018), Jung et al. (2018), and Jung (2019) conducted model tests and numerical analysis of the relative motion of docked vessels in an FLBT during operation to examine the loading and off-loading performances of the FLBT. They confirmed that it is necessary to have the shielding effect from the sea waves and maintain the heading angle to improve the loading and off-loading performances of the 5K LNG-BS. The results of the study conducted by Jung (2019) confirmed that all the vessels docked in the FLBT with the heading angles ranging from 202.5° to 225° were capable of stable loading and off-loading as shown in Fig. 2. In this study, based on studies on the operating procedure of the FLBT and the loading and off-loading performances (Kim et al., 2017; Kim et al., 2018; Jung et al., 2018; Jung, 2019), the heading angle characteristics and heading angle control performance will be evaluated to improve the loading and off-loading performances.

2.2 Environmental Conditions

Based on the data survey on the environmental load, the wave deformation and seawater flow were numerically analyzed in the estimated installation area to evaluate the design conditions according to the frequency. As shown in Table 1, it was assumed the operating condition, under which docking, loading, and off-loading are performed, with a one-year return period.

The environmental conditions were determined by selecting the expected installation area, as shown in Fig. 3, to evaluate the design conditions of the FLBT.
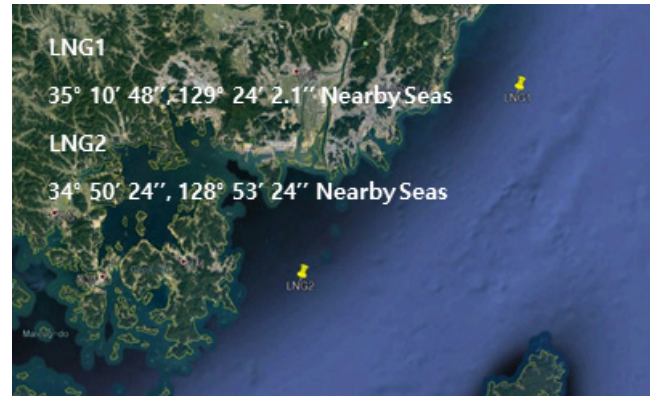

Fig. 3 Proposed sites for FLBT operation

Table 1 Operation conditions (1-year return period)

		Operation condition
Current speed Vc (m/s)		1.23
Wind speed Vw (m/s)		9.58
Wave	Hs (m)	1.98
	Tp (s)	6.48

2.3 Simplified Model for Evaluation of Heading Angle Control Performance

The vessels under test in the LNG loading and off-loading scenarios are a 170K LNG carrier, 30K LNG-BS, and 5K LNG-BS including the FLBT. The principal dimensions of these vessels are shown in Table 2.

As shown in Fig. 4, the FLBT is moored through the heading turret to maintain its position, and three tunnel thrusters are installed at the stern for the heading angle control, which is advantageous for berthing, loading, and off-loading. Each thruster is designed through advanced static analysis and has a capacity of 561 kN (Oh et al., 2019).
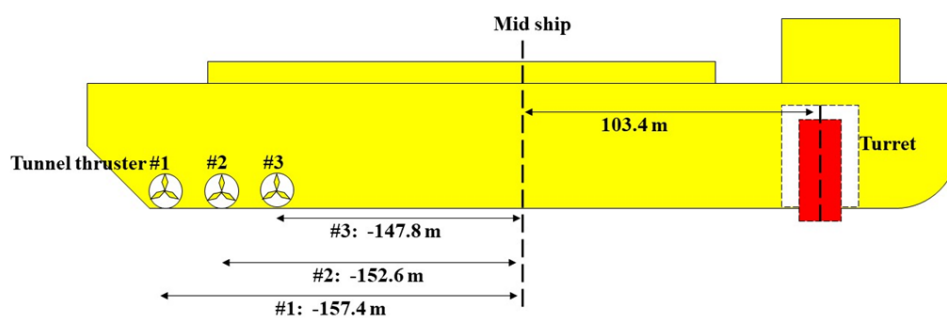

Fig. 4 Location of tunnel thruster and turret

Table 2 Principal dimensions of operating vessels

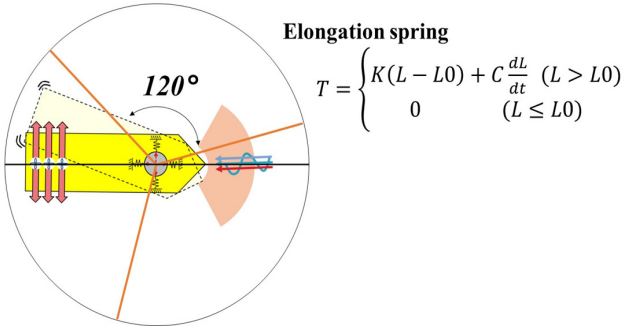|	FLBT	170K LNG Carrier	30K LNG-BS	5K LNG-BS
Loading condition (-)	Design condition	Design condition	Ballast condition	Ballast condition
Length (m)	326.0	282.2	162.0	91.2
Breadth (m)	60.0	45.5	26.5	17.0
Depth (m)	32.7	26.0	15.0	10.0
Draft (m)	13.5	12.0	5.08	4.3
Displacement (t)	2.39×10^5	1.11×10^5	1.69×10^4	4.75×10^3

Fig. 5 Schematic for simplified mooring model

The FLBT is designed to maintain its position by using 15 mooring lines connected to the turret. Five mooring lines form a cluster and the angle between clusters is 120°. In this study, the mooring system was simplified to a simple tensile model as shown in Fig. 5. As three simple elongation springs are attached to the center of the turret, the turret is modeled in the simulation to have free rotation without a resistance force against rotation. This simplification process is considered suitable for accomplishing the objective of this study i.e., to understand the characteristics of the heading angle of the FLBT. In the modeling, the modeled spring constant was similar to that of the recovery curve of the mooring system (Oh et al., 2019).

An LNG carrier, 30K LNG-BS, and 5K LNG-BS are deployed in relative positions, as shown in Table 3, via taut mooring on the FLBT, as shown in Fig. 1.

Table 3 Relative positions of vessels

	X (m)	Y (m)	Heading (deg.)
FLBT	0.0	0.00	180.0
170K LNG Carrier	0.0	57.25	0.0
30K LNG-BS	58.40	-46.05	0.0
5K LNG-BS	-131.80	-41.55	180.0

In this study, it was assumed that the vessel, which was moored on the FLBT, does not show any relative motion in the heading angle control. According to the previously conducted review studies on loading and off-loading performances (Kim et al., 2017; Kim et al., 2018; Jung et al., 2018; Jung, 2019), this assumption is reasonable because the maximum relative motion of the vessel was 3.27 m and most relative motions were 1.5 m or smaller. As it was assumed that there is no relative motion between floating bodies, four vessels can be simplified into one rigid body. For simplicity, the load and inertia acting on each floating body are replaced by the FLBT single-hull loading.

The mass and moment of inertia can be simply substituted with Eqs. (1)-(2).

$$M_{total} = M_{FLBT} + M_{170K} + M_{30K} + M_{5K} \tag{1}$$

$$\begin{aligned} I_{zz,total} &= I_{zz,FLBT} + I_{zz,170K} + I_{zz,30K} + I_{zz,5K} \\ &\quad + M_{FLBT} \cdot r_{FLBT}^2 + M_{170K} \cdot r_{170K}^2 \\ &\quad + M_{30K} \cdot r_{30K}^2 + M_{5K} \cdot r_{5K}^2 \end{aligned} \tag{2}$$

where M_{total}, M_{FLBT}, M_{170K}, M_{30K} and M_{5K} indicate the substituted mass, and the masses of the FLBT, 170K LNG carrier, 30K LNG-BS, and 5K LNG-BS, respectively. $I_{zz,total}$, $I_{zz,FLBT}$, $I_{zz,170K}$, $I_{zz,30K}$ and $I_{zz,5K}$ indicate the substituted yawing moment of inertia, and the yawing moments of inertia of the FLBT, 170K LNG carrier, 30K LNG-BS, and 5K LNG-BS calculated at each center of gravity, respectively. r_{FLBT}, r_{170K}, r_{30K}, and r_{5K} indicate the distances from the single center of gravity of all the four floating bodies to the center of gravity of the corresponding floating body.

The added mass should also be replaced with a part of the hull of the FLBT. As the heading angle simulation simulates the long-period motion, the added mass at zero frequency was calculated and used. If the frequency is assumed to be zero, then the free surface boundary condition for horizontal motion becomes a rigid wall condition. Therefore, it is defined as a double body problem. The boundary element method was used to solve the boundary value for the double body problem. This method uses the basic solution, $G(\vec{x}, \vec{\xi})$,, which is represented by Eq. (3), and the boundary integral in Eq. (4).

$$G(\vec{x}, \vec{\xi}) = -\frac{1}{4\pi}\left(\frac{1}{r} + \frac{1}{r'}\right) \tag{3}$$

where

$$\begin{cases} r = \sqrt{(x-\xi_1)^2 + (y-\xi_2)^2 + (z-\xi_3)^2} \\ r' = \sqrt{(x-\xi_1)^2 + (y-\xi_2)^2 + (z+\xi_3)^2} \end{cases}$$

$$\phi_j(\vec{x}) = \int_S \sigma(\vec{\xi}) G(\vec{x}, \vec{\xi}) dS(\vec{\xi}) \tag{4}$$

where $\vec{x}$ and $\vec{\xi}$ are the field and source points, respectively, and the density function, $\sigma(\vec{\xi})$, is an unknown value determined only by the boundary conditions. The density function, σ, can be determined through a system of equations derived from the boundary conditions of an object. The surface potential of the object, ϕ, can be calculated using the determined density function, σ, and Eq. (4). The calculated mass, a_{ij}, can be obtained by substituting the calculated potential, ϕ, into Eq. (5).

$$a_{ij} = \rho \int_{S_B} \phi_i n_j dS \tag{5}$$

where ρ is the seawater density and $n_j (j = 1,2,6)$ represents the normal vectors of the body surface. The panel mesh applied to the calculation is shown in Fig. 6 and the displacement error was within 0.065% in the modeling. The calculated added mass is summarized in Table 4.
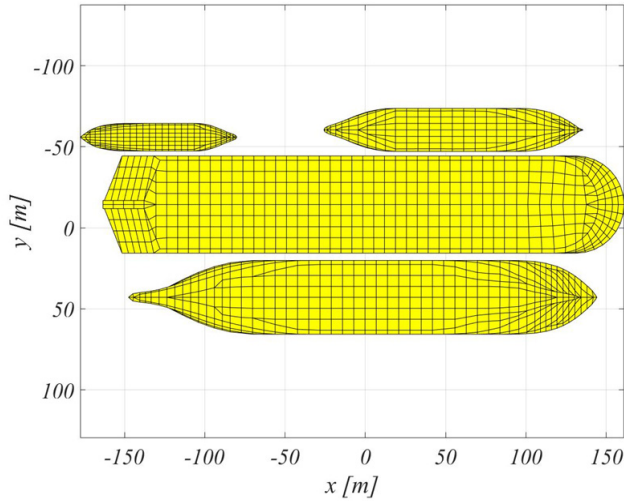
Fig. 6 Panel mesh for the added mass of 1-body simplification (4-body)

Table 4 Added mass of 1-body simplification (4-body)

	Value
A11 (t)	24,094
A22 (t)	140,078
A66 (t·m^2)	816,722,570

The load acting on each floating body was composed of wind load, current load, and wave drift load. For the wind load, the result of the wind tunnel test conducted in the study by Park et al. (2017) was used. The wind tunnel test was conducted in Force Technology in Denmark, as shown in Fig. 7. The model ship was made of high-density polyurethane foam and was used for the test by separating the top part of the ship under test from the repair surface and below.

The current load was calculated based on the study conducted by Jung et al. (2017), in which computational fluid dynamics calculations were performed and the current load coefficient was calculated. Based on the computational analysis, which was systematically performed by Jung et al. (2017), the current load coefficient was measured in the wind tunnel test, and it was confirmed that the coefficient was affected
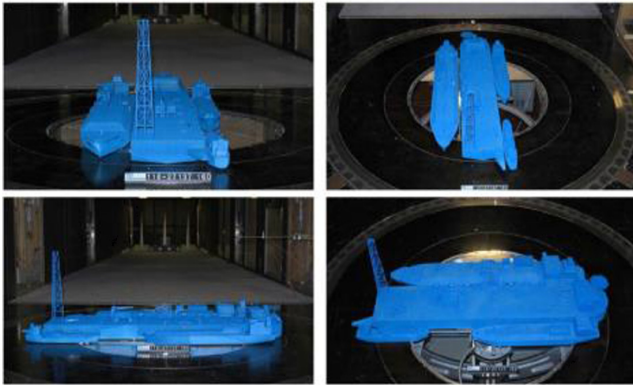

Fig. 7 Wind load test for 4-body operation (Park et al., 2017)
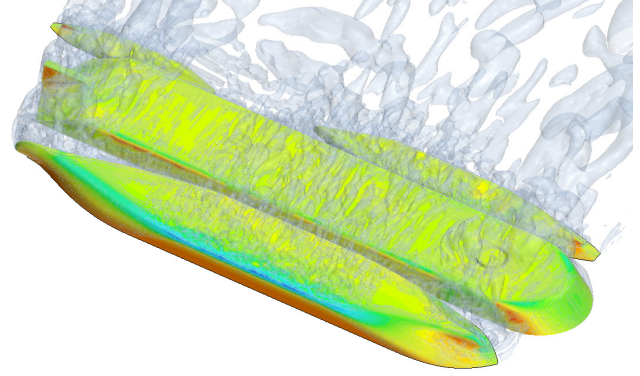

Fig. 8 Current load calculation for 4-body operation

by the experimental environment of the wind tunnel. Furthermore, the analysis indicated that Boundary conditions for unbounded flow were not satisfied. Based on the study by Jung et al. (2017), the docked current loads of four floating bodies were calculated in this study as shown in Fig. 8.

The wave drift load was calculated based on a study by Kim et al. (2018). To calculate the wave drift load, a high-order boundary element method based on the free-surface green function (Choi and Hong 2002) was used, and a gap flow damping term was applied to reduce the non-physical resonance of the gap of the floating body. Detailed calculations can be found in the study by Kim et al. (2018).

For the calculated environmental load, the load acting on each floating body was also simplified to a single FLBT hull load. The individual loads of the floating bodies were replaced with a single load using Eqs. (6)-(8).

$$F_{x,total} = F_{x,FLBT} + F_{x,170K} + F_{x,30K} + F_{x,5K} \qquad (6)$$

$$F_{y,total} = F_{y,FLBT} + F_{y,170K} + F_{y,30K} + F_{y,5K} \qquad (7)$$

$$M_{z,total} = M_{z,FLBT} + M_{z,170K} + M_{z,30K} + M_{z,5K} \qquad (8)$$
$$+ \vec{F}_{FLBT} \times \vec{r}_{FLBT} + F_{170K} \times \vec{r}_{170K} + F_{30K} \times \vec{r}_{30K} + F_{5K} \times \vec{r}_{5K}$$

where $\vec{F}_{total}$, $\vec{F}_{FLBT}$, $\vec{F}_{170K}$, $\vec{F}_{30K}$ and $\vec{F}_{5K}$ are the substituted horizontal load, and the horizontal loads of the FLBT, 170K LNG carrier, 30K LNG-BS, and 5K LNG-BS, respectively. $M_{z,total}$, $M_{z,FLBT}$, $M_{z,170K}$, $M_{z,30K}$ and $M_{z,5K}$ are the substituted yawing load moment, and the yawing load moments of the FLBT, 170K LNG carrier, 30K LNG-BS, and 5K LNG-BS, respectively. $\vec{r}_{FLBT}$, $\vec{r}_{170K}$, $\vec{r}_{30K}$, and $\vec{r}_{5K}$ are the distance vectors from the center of gravity of all the four floating bodies to the center of gravity of the corresponding floating body. The substituted wind and current loads are shown in Figs. 9 and 10. For the wave drift load, the load response amplitude operator (RAO) was regenerated by the wave height of the incident wave and shown in Fig. 11.
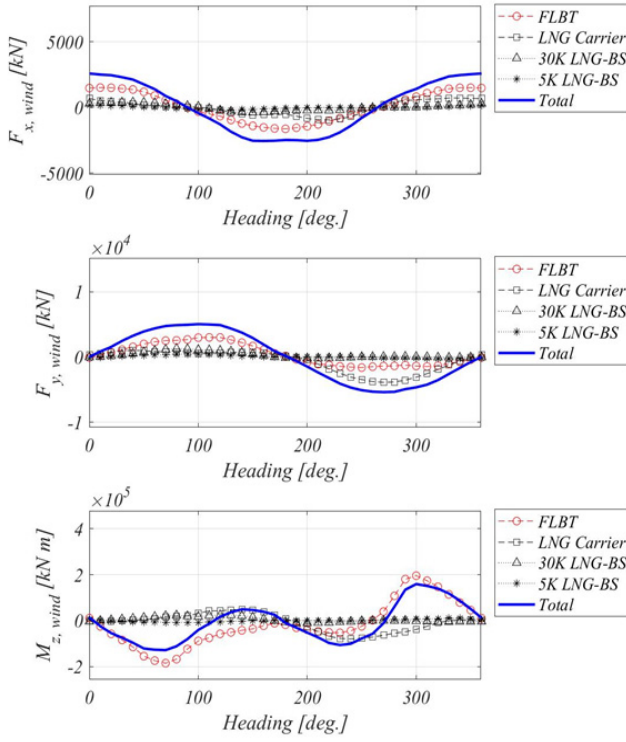
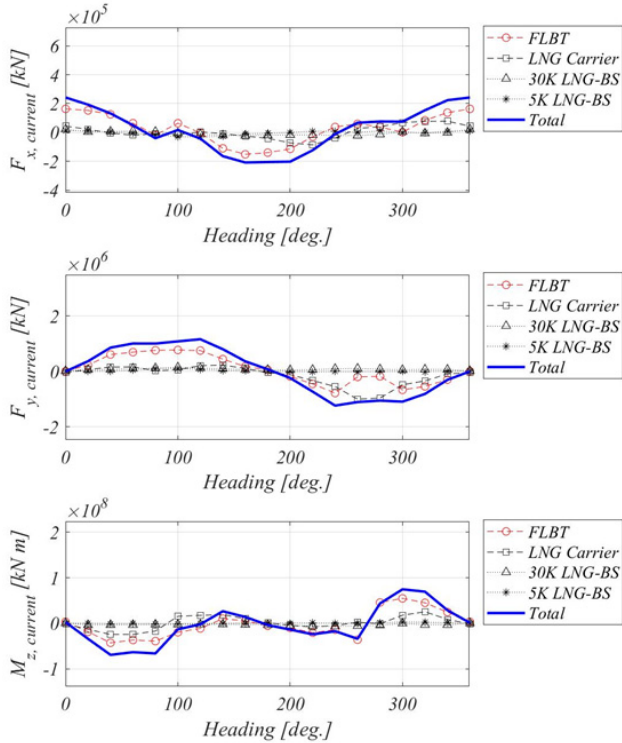**Fig. 9** Wind loads in-unit velocity (V_{wind} = 1 m/s)

Fig. 10 Current loads in-unit velocity ($V_{current}$ = 1 m/s)

Fig. 11 Wave drift loads RAO

allow to simulate the heading angle control.

$$(M+a_{11})\ddot{x}_1 - (M+a_{22})\dot{x}_2\dot{x}_6 \qquad (9)$$
$$= F_x^{wind} + F_x^{current} + F_x^{wave} + F_x^{mooring} + F_x^{thrust}$$

$$(M+a_{22})\ddot{x}_2 + a_{26}\ddot{x}_6 + (M+a_{11})\dot{x}_1\dot{x}_6 \qquad (10)$$
$$= F_y^{wind} + F_y^{current} + F_y^{wave} + F_y^{mooring} + F_y^{thrust}$$

$$a_{62}\ddot{x}_2 + (I_{66} + a_{66})\ddot{x}_6 \qquad (11)$$
$$= M_z^{wind} + M_z^{current} + M_z^{wave} + M_z^{mooring} + M_z^{thrust}$$

In the derived motion equation, M and I_{ii} represent the mass and moment of mass inertia of the floating body, respectively. a_{ij}, $\ddot{x}_i$ and $\dot{x}_i$ represent the added mass, acceleration, and velocity in each direction of motion, respectively, where the values of 1, 2, and 6 for i and j represent the surging, swaying, and yawing directions, respectively. Moreover, F_x^m, F_y^m, and M_z^m represent the forces in the surging, swaying, and yawing directions, respectively, where the superscript m indicates the type of load, including the loads due to wind, current, wave, mooring, and thrust.

The heading angle of the FLBT is controlled by using the stern thruster, and accordingly, it is necessary to produce and distribute the thruster outputs. In this study, a PD controller was used to control the output of the thruster, and a Lagrange multiplier was used as the thrust allocation algorithm.

Based on the inertia, added mass, and environmental loads substituted by the load of a single floating body, two-dimensional planar low-frequency motion equations, i.e., Eqs. (9)-(11), which consist of turret mooring and tunnel thruster, can be derived, which
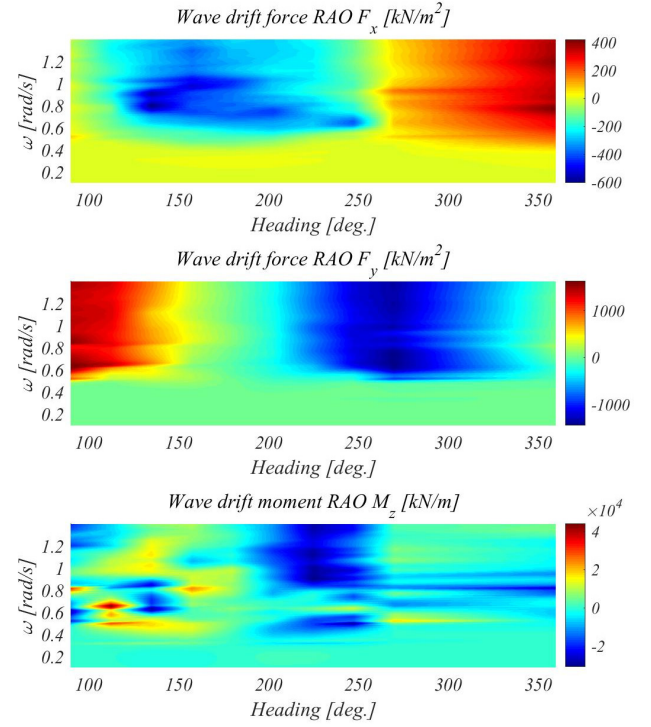
3. FLBT Heading Angle Simulation with Multiple Moored Vessels

Numerical analysis was performed to understand the heading angle characteristics and control performance of the FLBT with multiple moored vessels. In the numerical analysis, a simplified model, in which the relative motion between floating bodies was omitted, was used, as mentioned in Section 2. This is reasonable considering the operating conditions and the objective of the study. To validate the simplified model, the result was compared with the dynamic positioning (DP) model test, which was performed at the ocean engineering basin (Kim et al., 2019). Through the comparatively validated model, the heading angle control for the operating conditions was simulated to study the heading angle characteristics and control performance.

3.1 Simplified Model Verification through Model Test

The model test was conducted at the ocean engineering basin in KRISO. The specifications of the floating body used in the model test are shown in Table 2, and the accumulation ratio was 1:65. The models of the 170K LNG carrier, 30K LNG-BS, and 5K LNG-BS in addition to the FLBT were constructed and arranged according to the loading and off-loading scenarios as described previously and shown in Fig. 12.

The FLBT was moored through the turret mooring system inside the structure and was designed to rotate freely in the hull heading. Pneumatic fenders and parallel mooring lines were modeled for the mooring between floating bodies in the same manner as in the study
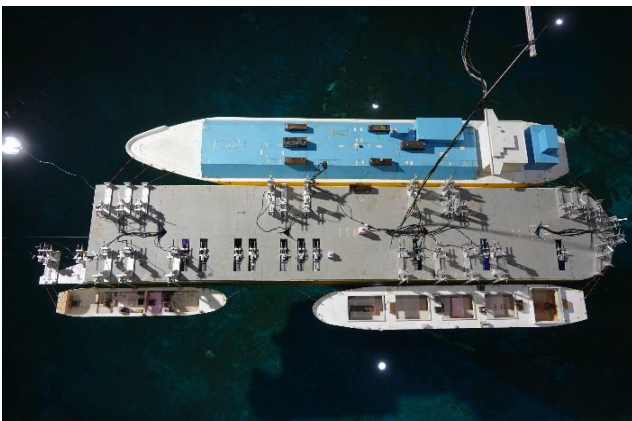

Fig. 12 Model test set-up for 4-body operation

Table 5 Environmental condition of model test

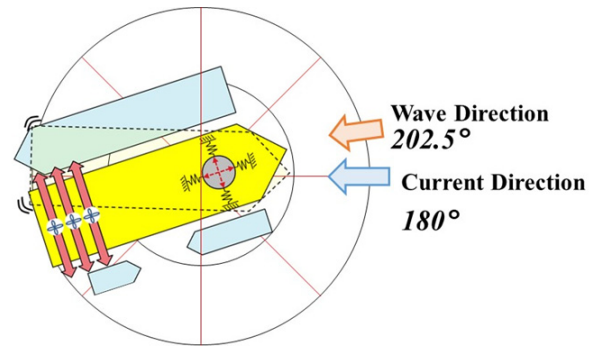|		Test condition
Current	Vc (m/s)	1.23
	Direction	180°
Wave	Hs (m)	1.54
	Tp (s)	10.0
	Direction	202.5°

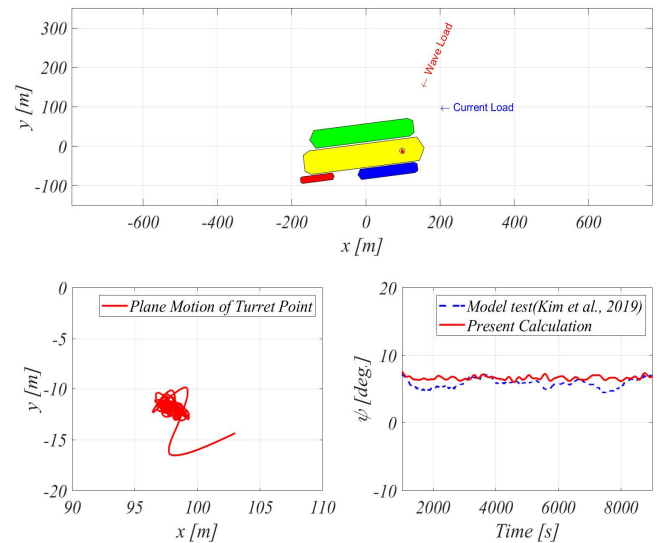**Fig. 13** Directions of environmental loads

Fig. 14 Simulation of FLBT without DP Control

conducted by Jung et al. (2018). The environmental conditions of the model test are shown in Table 5 and Fig. 13, with a total of five cases including the cases where the heading angle was not controlled and where the heading angle was maintained and controlled at 10°, -10°, -20°, and -30°. The model test results were used for verification.

The simulation was performed for the case where there was no heading angle control and the result was compared with the model test result, as shown in Fig. 14. As a result of the numerical analysis, the heading angle reached a static equilibrium point at an average of 6.6°, which shows a similar result to the average heading angle of 5.8° in the model test. Through the model tests and numerical analysis, it was confirmed that there is no slewing motion phenomenon.

The simulation was performed for the case where the heading angle was controlled and the result was compared with the model test result, as shown in Fig. 15.

It can be confirmed from the time series results that the heading angle of the numerical analysis was controlled by the reference heading angle, as in the model test. The required thrust time series, which was calculated from the numerical analysis, also has a sectional difference from the result in the model test, but the similarity was observed in the time series results. The average heading angle and the average required thrust calculated using the numerical analysis were
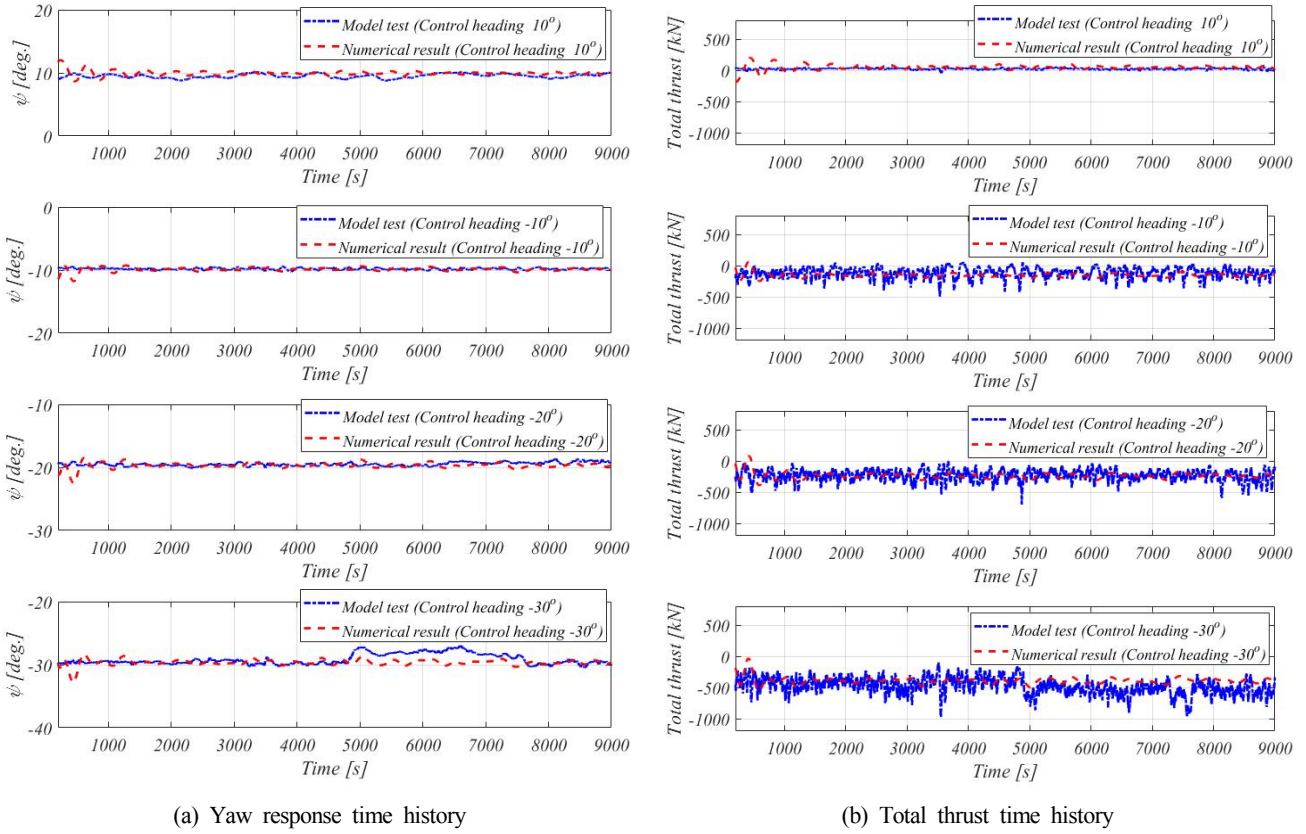
(a) Yaw response time history

(b) Total thrust time history

Fig. 15 Time histories of simulation results (FLBT with DP Control)

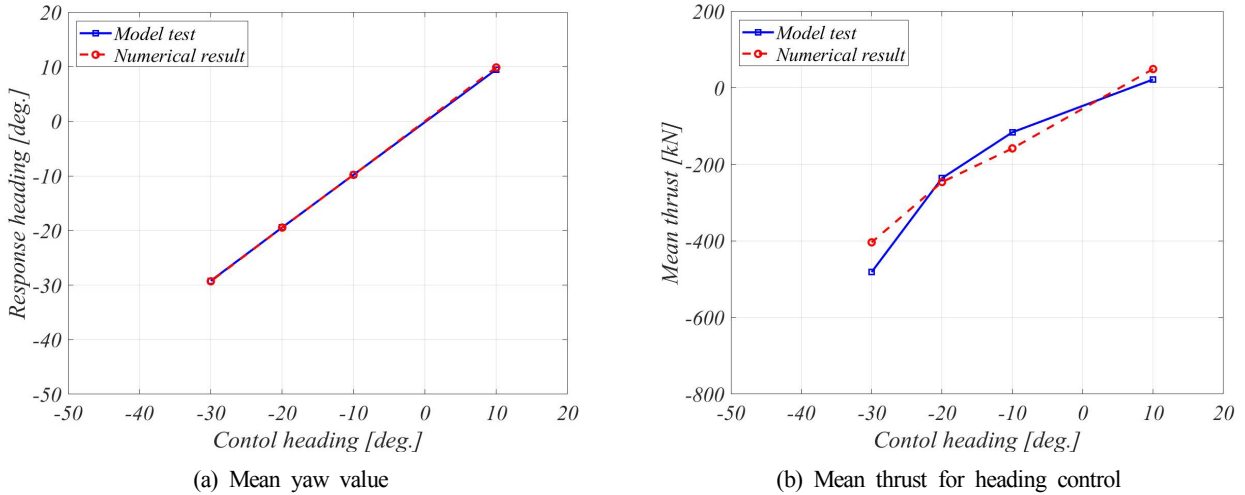(a) Mean yaw value

(b) Mean thrust for heading control

Fig. 16 Mean values of simulation results (FLBT with DP Control)

compared with the results of the model test and the comparisons are shown in Fig. 16. As shown in Fig. 15, it can be confirmed that the heading angle matches the reference heading angle and the angle is well controlled. It can be verified that the average required thrust also shows a similar trend to the model test result. Through comparative studies, it was determined that the heading angle characteristics and the required thrust calculated through the numerical analysis using a simplified model were similar to the results of the model test. Therefore, the effectiveness of the simplified model was verified.

3.2 Heading Angle Characteristics of FLBT with Moored Loading and Off-loading Vessels

A simulation was performed for the case with no heading angle control to understand the heading angle characteristics of the FLBT with moored loading and off-loading vessels. As the heading angle characteristics are governed by the environmental load acting on the marine structure, the static environmental load for the environmental conditions shown in Table 1 was calculated for the incident direction and the result is shown in Fig. 17. As shown in Fig. 17, the main
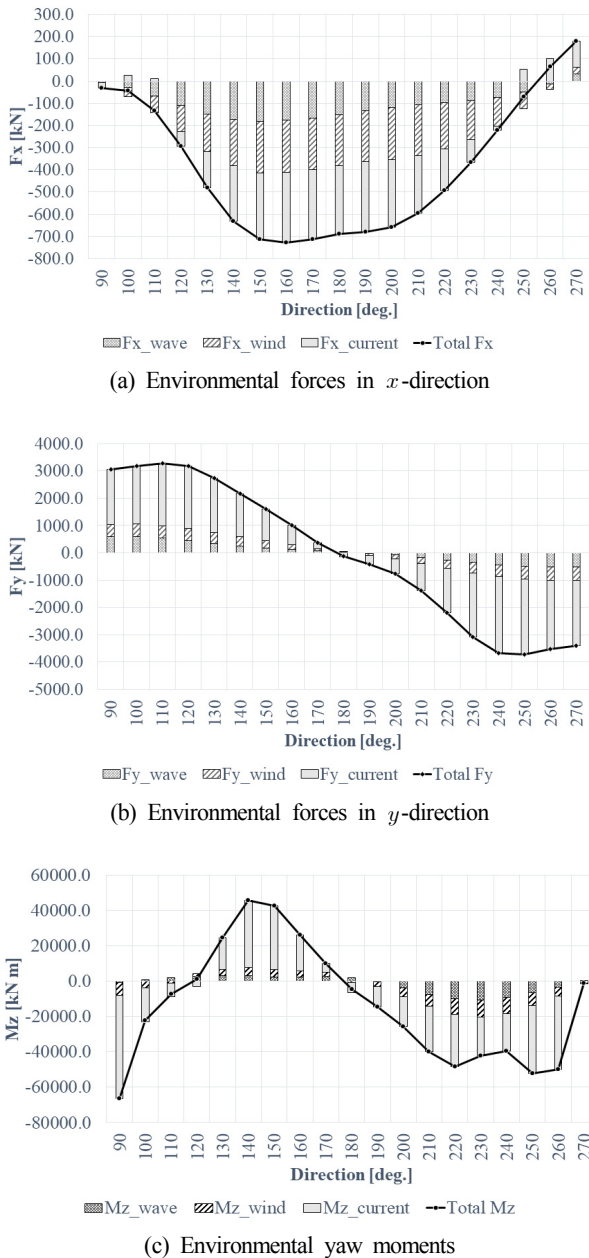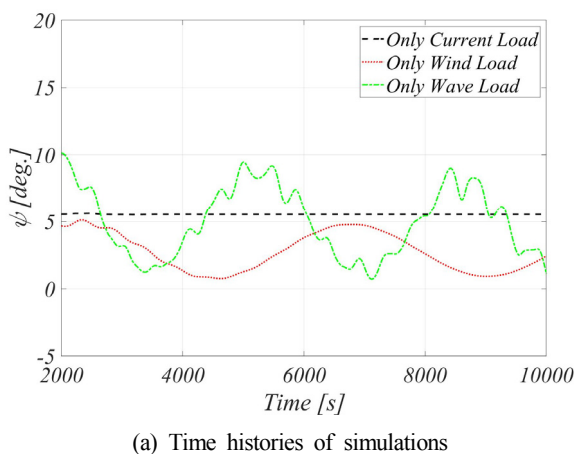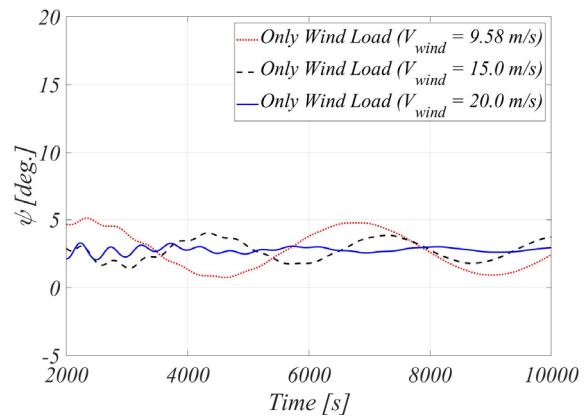
(a) Environmental forces in x-direction

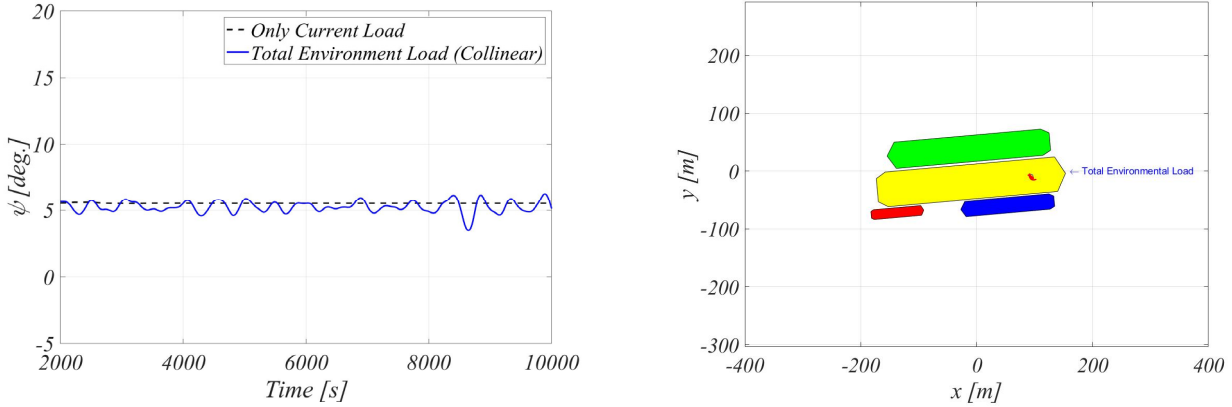(b) Environmental forces in y-direction

(c) Environmental yaw moments

Fig. 17 Static environmental loads

components of the environmental load in the y-direction and the moment of the horizontal plane are attributed to the current, and it can be easily predicted that the direction of the current will have the most significant effect on the change in the heading angle.

Fig. 18 shows the heading angle simulation for each environmental load and all the linear disturbance loads (collinear environmental load; hereafter denoted as the unidirectional composite environmental load). In Fig. 18(a), when only the wind and wave drift loads are included in the simulation, a long period slewing motion is observed. This is mainly due to the yawing instability that occurs in the vessel, and it is known that the yawing stability is improved when the surging resistance increases (Nam et al., 2013). Such characteristics can be confirmed by simply conducting a simulation with increased wind speed as shown in Fig. 18(b). When only the current load is included in the analysis, the heading angle is maintained to a static value. In Fig. 19 (a), it can be confirmed that the heading angle for the unidirectional composite environmental load in the simulation is almost similar to the heading angle when only the current load acts. As shown in Fig. 17, the current load has the greatest effect on the composite environmental load. In the case of the unidirectional composite environmental load, the slewing motion, which occurred in the wind and wave drift loads, did not occur, and this indicates that the current suppresses the slewing motion. Through the results of the heading angle simulation for various loads, when there is no DP control, the slewing motion occurs with an average heading angle of approximately 5° as shown in Fig. 19(b). This is because the 5K LNG-BS and 30K LNG-BS, which are vulnerable to relative motion due to the wave load, are exposed to the wave load, and thus, it is not possible to have the shielding effect against the ocean waves of the FLBT and LNG carriers. Such a heading angle characteristic indicates that the heading angle control of the FLBT is essential to improve the loading and off-loading performances.

3.3 Control Performance of Heading Angle of FLBT with Moored Loading and Off-loading Vessels

The heading angle control was simulated to understand the heading angle control performance of the FLBT on which the loading and

(a) Time histories of simulations

(b) Comparison with various wind speeds

Fig. 18 Simulations without DP control

(a) Time histories of simulations

(b) Total environmental load case

Fig. 19 Simulations in combined environmental conditions without DP control

Table 6 Simulation cases for check of controllability

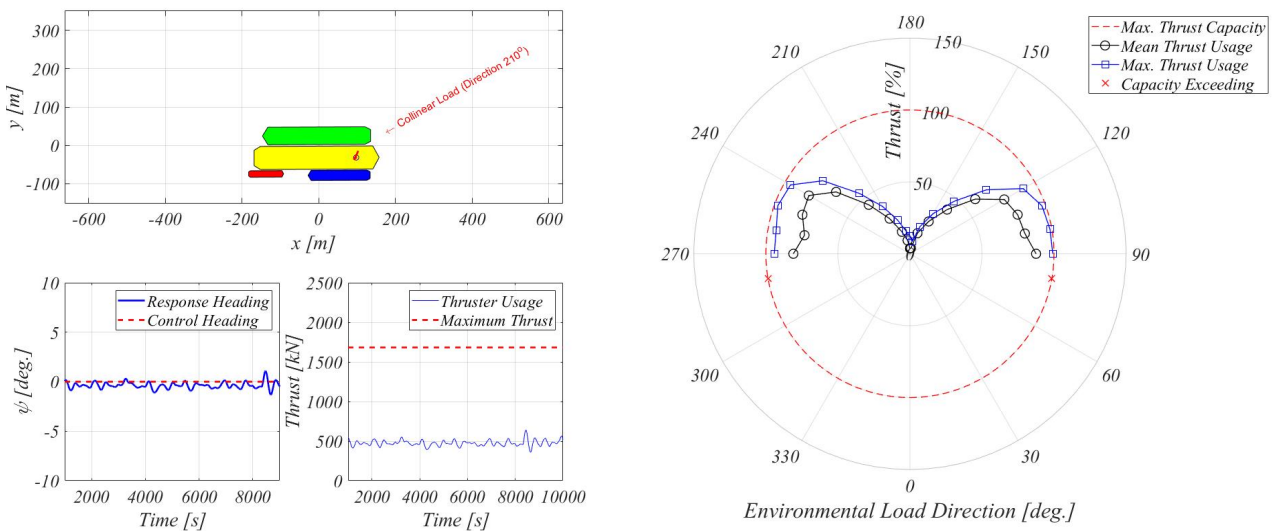|	Collinear environmental load condition			Pseudo-operating condition		
	Wave	Wind	Current	Wave	Wind	Current
Environmental load direction	80°–280° (10° spacing)			202.5°	0°–360° (30° spacing)	
Control direction	0°			0°		

off-loading vessels are moored, as shown in Table 6, for the fixed collinear environmental load condition, fixed wave direction, and changing wind and current loads (hereafter denoted as pseudo-operating conditions). For the heading angle control, the PD control using three stern thrusters was performed. The P gain was calculated based on the yawing and it was set to approximately 300 s, which is the natural period. The D gain was set to 35% of the critical damping.

As shown in Fig. 20(a), the heading angle control was simulated for the collinear environmental load condition. Fig. 20(b) shows the amount of thrust used for environmental disturbances based on the dynamic simulation of the heading angle. It was confirmed that heading angle control is possible for the directions of the

environmental load ranging from 90° to 270°.

According to a previous study (Jung, 2019), if the heading angle is maintained at 202.5° or higher based on the incident direction of the 180° wave, the loading and off-loading performances can be improved by the shielding effect of the ocean wave. The simulation for the collinear environmental load condition shows that it is possible to maintain a heading angle at 202.5° or higher against environmental disturbances.

Furthermore, simulations for the pseudo-operating condition were performed. As shown in the heading angle characteristics, the static heading angle is mainly affected by the direction of the current. However, the loading and off-loading performances are considerably

(a) Simulation case (Environmental load direction 210°)

(b) Maximum thrust usage

Fig. 20 Simulations under combined environmental conditions with DP control (Collinear condition)

(a) Maximum thrust usage

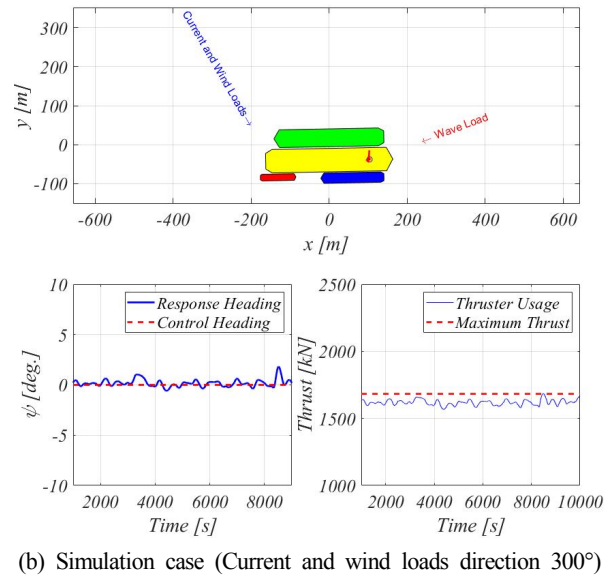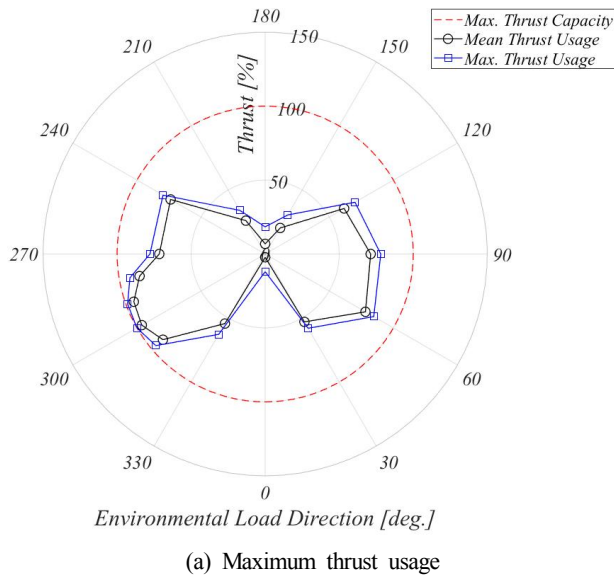(b) Simulation case (Current and wind loads direction 300°)

Fig. 21 Simulations under combined environmental conditions with DP control (Pseudo-operating condition)

affected by the wave-induced relative motion of the vessel. Through these characteristics, by fixing the wave direction to have the shielding effect against the ocean wave and understanding the heading angle control performance against environmental disturbances except for the wave, the range of environmental conditions that ensure the improvement of the loading and off-loading work performances can be estimated. A simulation was performed at 30° intervals under the pseudo-operating condition as shown in Table 6, and an additional simulation was performed at 10° intervals in the range of 280° to 310° to confirm the maximum thrust around 300°, where the maximum required thrust is expected. The simulation result of the heading angle control is shown in Fig. 21(a), where the results are specified in terms of the thrust usage. The section where the maximum thrust occurred is a scenario in which the current and wind loads act at 300° as shown in Fig. 21(b). Therefore, as shown in Fig. 21(a), the heading angle for having the shielding effect against the ocean waves is maintained for all the current and wind load directions. This indicates that the heading angle control secures an additional work operation period and improves work performance in operating condition with a one-year return period. The capacity of the designed stern thruster was also confirmed through numerical analysis results.

4. Conclusion

In this study, the heading angle characteristics and control performance were confirmed to improve the loading and off-loading performances of an FLBT. For the purpose of the study and efficiency of the analysis, a simplified model was used assuming that there was no relative motion of the moored vessel in the FLBT. The simulation result was compared with a model test result to confirm the effectiveness of the simplified model in which the environmental load and inertia of several floating bodies, including the FLBT, were replaced with the loads and inertia of a single vessel. The low-frequency planar motion of the heading angle of the FLBT, in which several vessels were moored, was simulated using a simplified model. Through the simulation, the heading angle characteristics and control performance were analyzed by reflecting the environmental conditions calculated based on the estimated installation area, and the following conclusions were drawn.

(1) The validity of the simplified model was confirmed through a comparison with a model test result. Although this model is only applicable to the same operating conditions under low maritime conditions, this study will be useful to determine the operational range.

(2) Through the heading angle characteristic under the operating conditions defined in this study, it was confirmed that the current load, which is the largest component, has the most significant effect on the static heading angle and this suppresses the long period slewing motion that occurs when the wind and wave drift loads act individually. Long period slewing motion against the wind and wave drift loads is due to the yawing instability, and it was observed from the numerical analysis that the stability could be improved by increasing the surging resistance.

(3) The static heading angle due to the operating conditions was the angle at which 5K and 30K LNG-BSs were exposed to environmental loads, and it was confirmed that the ocean wave shielding effect of the FLBT and LNG carriers cannot be obtained, which indicates that the loading and off-loading performances are degraded. This heading angle characteristic suggests that heading angle control using a stern thruster is necessary to improve the loading and off-loading work performances.

(4) A numerical analysis was performed under the collinear environmental load conditions to verify the general heading angle control performance. Through the results of numerical analysis, it was confirmed that heading angle control is possible for the environmental loads ranging from 90° to 270°.

(5) To estimate the environmental conditions under which the

loading and off-loading work performances can be improved, the direction of the wave drift load that can have a shielding effect was fixed, and the heading angle control performance was examined while changing the remaining environmental disturbances. Consequently, it was possible to control the wind and current loads in all the directions. This indicates that it is possible to have the shielding effect against the ocean wave for the operating conditions defined in this study with the capacity of the currently designed stern thruster.

The operating range of the FLBT was confirmed through these heading angle characteristics and control performance. As the reviewed results reflect various assumptions, some limitations need to be corrected through actual sailing data. However, the analysis and results using the simplified model and model tests can be used as a guide for establishing an operating procedure before construction.

Acknowledgment

References

Choi, Y.R., & Hong, S.Y. (2002). An Analysis of Hydrodynamic Interaction of Floating Multi-Body Using Higher-Order Boundary Element Method. Proceedings of the 12th International Offshore and Polar Engineers, Kitakyushu Japan, 303-308.

Jung, J.H., Jung, H.W., Cho, S.K., Hwang, S.C., Park, B., Jung, D.H., & Sung, H.G. (2017). Current Load Estimation of FLBT in Numerical Wind Tunnel. Proceedings of the Annual Fall Conference of the Korea Society of Ocean Engineers, Geoje, Korea.

Jung, D.W., Kim, Y.H., Cho, S.K., Jung, D.H., Sung, H.G., & Kwon, S.H. (2018). Experimental Study on Floating LNG Bunkering Terminal for Assessment of Loading and Offloading Performance. Journal of Ocean Engineering and Technology, 32(1), 51-61. https://doi.org/10.26748/KSOE.2018.2.32.1.051

Jung, D.W. (2019) A Study On Hydrodynamic Characteristics In Waves Of Multi-Body Floaters (Ph.D Dissertation). Pusan National University.

Kim, Y.H., Jung, D.W., Jung, H.W., Park, I.B., Won, Y.Y., Jung, J.S., ... Sung, H.G. (2017). Experimental Study On Shielding Effect Of 5K LNG Bunkering Shuttle By FLBT Or 30K LNG Bunkering Shuttle. Proceedings of the Annual Fall Conference of the Korea Society of Ocean Engineers, Geoje, Korea.

Kim, Y.H., Jung, D.W., Cho, S.K., & Sung, H.G. (2018). Experimental Study on Hydrodynamic Characteristics and Operational Feasibility of Floating LNG Bunkering Terminal Moored Side-by-side with LNG Carrier and Two LNG Bunkering Shuttles. Ship and Offshore Structure, 13(5), 504-518. https://doi.org/10.1080/17445302.2018.1430099

Kim, Y.H., Song, H., Jung, D.W., Won, Y.Y., Oh, Y.J., Nam, H.S., ... Sung, H.G. (2019). An Experimental Study on Heading Control Effectiveness for Floating LNG Bunkering Terminal Side-by-Side Moored with LNGC and two LNG Bunkering Shuttles. Proceedings of the Annual Fall Conference of the Korea Society of Ocean Engineers, Gimhae, Korea.

Nam, B.W., Park, J.Y., Hong, S.Y., Sung, H.G., & Kim, J.W. (2013). Numerical Simulation of Towing Stability of Barges in Calm Water. Journal of Ocean Engineering and Technology, 27(1), 67-73. https://doi.org/10.5574/KSOE.2013.27.1.067

Oh, S.H., Jung, J.H., Jung, S.J., Park, B.W., Jung, D.W., Kim, ... Sung, H.G. (2019). Numerical Study on Characteristics and Control of Heading Angle of Floating LNG Bunkering Terminal under Environmental Loads. Proceedings of the Joint Conference of the Korean Association of Ocean Science and Technology Societies (KAOSTS), Jeju, Korea.

Park, B., Jung, D.W., Kim, Y., Won, Y., Cho, S.K., & Sung, H.G. (2019). An Experimental Study on Heading Control of Turret Moored FLBT Using Stern Tunnel Thrusters. Proceedings of the Proceedings of the Joint Conference of the Korean Association of Ocean Science and Technology Societies (KAOSTS), Jeju, Korea.

Park, B., Jung, J.H., Hwang, S.C., Cho, S.K., Jung, D.H., & Sung, H.G. (2017). Wind Tunnel Test of Wind Loads and Current Loads Acting on FLBT and LNG Bunkering Shuttles in Side-by-Side Configuration and Comparison with Empirical Formula. Journal of Ocean Engineering and Technology, 31(4), 266-273. https://doi.org/10.26748/KSOE.2017.08.31.4.266

Author ORCIDs and Contributions

Author name	ORCID	Contributions
Oh, Seunghoon	0000-0002-7249-2353	①②③④⑤
Jung, Dong-Woo	0000-0002-9154-8500	②
Kim, Yun-Ho	0000-0003-1465-5844	②
Kwak, Hyun-Uk	0000-0003-1042-7780	③
Jung, Jae-Hwan	0000-0001-9384-5720	③
Jung, Sung-Jun	0000-0001-5938-2988	③
Park, Byeongwon	0000-0001-8294-1696	③
Cho, Seok-Kyu	0000-0002-7821-4848	⑤
Jung, Dongho	0000-0002-7265-8034	⑤
Sung, Hong Gun	0000-0001-8029-523X	⑤

① Conceived of the presented idea or developed the theory
② Carried out the experiment or collected the data
③ Performed the analytic calculations or numerical simulations
④ Wrote the manuscript
⑤ Supervised the findings of this study

Original Research Article

Analysis of Steady Vortex Rings Using Contour Dynamics Method for the Stream Function

Yoon-Rak Choi[iD]

Professor, School of Naval Architecture and Ocean Engineering, University of Ulsan, Ulsan, Korea

ABSTRACT: *In this study, the Norbury-Fraenkel family of vortex rings is analyzed using a contour dynamics method for the stream function, which significantly reduces the numerical burden in the calculation. The stream function is formulated as the integral along the contour of the vorticity core. The integration over the logarithmic-singular segment is evaluated analytically, and the positions of the nodal points of the contour are calculated directly. The shapes of the cores and the dividing stream surfaces are found based on the mean core radius. Compared with other studies, the proposed method is verified and found to be more efficient.*

1. Introduction

Various types of vortex flows occur in nature and engineering applications (Van Dyke, 1982; Lugt, 1983; Samimy et al., 2003). Helmholtz (1858) first investigated such vortex flows, and research on vortex rings, such as smoke rings, attracted attention from the beginning. In general, vortex rings are generated through the impulsive ejection of fluids. For example, vortex rings can be observed in jet flows for the propulsion of cephalopods (Krueger and Gharib, 2005).

Sir W. Thomson presented the translational velocity of the vortex ring of a small circular cross-section in the appendix of the paper written by Helmholtz (1867). Lamb (1932) verified the results obtained by Sir W. Thomson using the kinetic energy of the vortex ring. Fraenkel (1970) and Fraenkel (1972) analytically identified various physical occurrences of the small cross-sectional vortex rings through Fourier analysis. Spherical vortices were analyzed by Hill (1894).

Norbury (1973) investigated the general cases of the vortex rings including small cross-sections and the spherical vortex rings mentioned above, which are known as Norbury-Fraenkel family of vortex rings. Durst et al. (1981) determined the shape of a vortex ring by numerically solving partial differential equations for the stream function.

In this study, the Norbury-Fraenkel family of vortex rings is analyzed using a contour dynamics method (Shariff et al., 1989; Shariff et al., 2008). Stokes' stream function was expressed as a contour integral using the Green's function, and the integration of the logarithmic-singular segment, which occurs when the core shape is to be determined, was expressed analytically. The core shapes and the characteristic values of the vortex rings were compared with the results of previous studies to verify the validity of the proposed method.

2. Problem Formulation

The fluid is assumed to be an ideal fluid. The flow is analyzed when the core of a vortex ring, in which the flow is rotational, exists in an irrotational infinite flow field, as shown in Fig. 1. The flow is axisymmetric with respect to the x-axis. If cylindrical polar coordinates are introduced in the analysis of the axisymmetric flow, as shown in the figure, the vorticity vector $\vec{\omega}$ is expressed as follows:

$$\vec{\omega} = \nabla \times \vec{u} = \omega_\phi \hat{e}_\phi \tag{1}$$

where $\vec{u}$ is the flow velocity vector. The velocity vector of the axisymmetric flow is expressed as Stokes' stream function ψ, as follows:

$$\vec{u} = u_x \hat{e}_x + u_\sigma \hat{e}_\sigma = \frac{1}{\sigma}\frac{\partial \psi}{\partial \sigma}\hat{e}_x - \frac{1}{\sigma}\frac{\partial \psi}{\partial x}\hat{e} \tag{2}$$

Fig. 1 Core of vortex ring and cylindrical polar coordinates

Fig. 2 Meridional cross-section of the core of vortex ring

For an axisymmetric flow, the Helmholtz vorticity equation for a non-viscous incompressible fluid is expressed as follows (Batchelor, 1967):

$$\frac{D}{Dt}\left(\frac{\omega_\phi}{\sigma}\right)=0 \tag{3}$$

From Eq. (3), the vorticity ω_ϕ is proportional to σ inside the core and is zero outside the core.

$$\omega_\phi = \begin{cases} \Omega\sigma & \text{inside} \quad \partial D, \\ 0 & \text{outside} \quad \partial D \end{cases} \tag{4}$$

where ∂D is the boundary of D, which is the inner core region, and Ω is a constant.

In considering the rotational flow of the incompressible fluid, the velocity vector is obtained by introducing the vector potential $\vec{A}$, as follows:

$$\vec{u}=\nabla\times\vec{A} \tag{5}$$

$$\nabla\cdot\vec{A}=0 \tag{6}$$

Eq. (6) is a gauge condition introduced to ensure the uniqueness of the solution. $\vec{A}$ is expressed using cylindrical polar coordinate components, as follows:

$$\vec{A}=A_x\hat{e}_x + A_\sigma\hat{e}_\sigma + A_\phi\hat{e}_\phi \tag{7}$$

Based on Eq. (2) and Eqs. (5)-(7), the stream function ψ is expressed as follows:

$$\psi=\sigma A_\phi \tag{8}$$

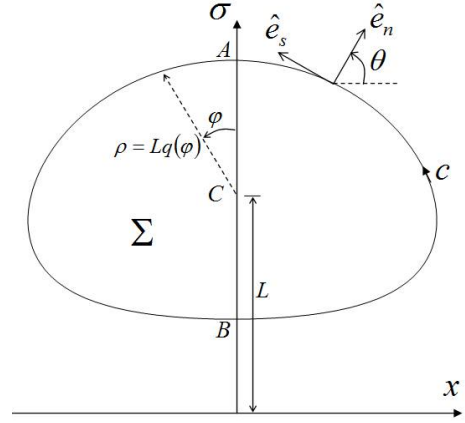In addition, substituting Eqs. (5) and (6) into Eq. (1) yields the Poisson equation for $\vec{A}$, as follows:

$$\nabla^2\vec{A}=-\omega_\phi\hat{e}_\phi \tag{9}$$

After A_ϕ is obtained by applying Green's second identity to this equation, ψ is expressed, as shown in Eq. (10) using Eq. (8) (Fraenkel, 1970; Norbury, 1973).

$$\psi(x,\sigma)=\frac{1}{2\pi}\Omega\sqrt{\sigma}\iint_\Sigma \sigma'\sqrt{\sigma'}\left\{\left(\frac{2}{k}-k\right)K(k)-\frac{2}{k}E(k)\right\}dx'd\sigma' \tag{10}$$

where Σ is the inner region of the core cross-section (Fig. 2). Additionally, $K(k)$ and $E(k)$ are the complete elliptic integrals of the first and second kinds (Gradshteyn and Ryzhik, 2000), and modulus k is defined as follows:

$$k=\frac{2\sqrt{\sigma\sigma'}}{\sqrt{(x-x')^2+(\sigma+\sigma')^2}} \tag{11}$$

Shariff et al. (1989) and Shariff et al. (2008) obtained ψ as a contour integral using the vorticity jump (Eq. (4)) across ∂D. The results can be expressed as the following equations.

$$\psi(x,\sigma)=\frac{1}{2}\Omega\sigma\oint_c M(s')ds' \tag{12}$$

$$M(s')=-(x-x')\sigma'H(s')\cos\theta' + \sigma'\{\sigma'H(s')-\sigma G(s')-2\sigma J(s')\}\sin\theta' \tag{13}$$

$$G(s')=\frac{\sigma'}{4\pi}\int_0^{2\pi}\frac{1}{\Delta}d\phi'=\frac{1}{2\pi}\sqrt{\frac{\sigma'}{\sigma}}\,kK(k) \tag{14}$$

$$H(s')=\frac{\sigma'}{4\pi}\int_0^{2\pi}\frac{\cos\phi'}{\Delta}d\phi'=\frac{1}{2\pi}\sqrt{\frac{\sigma'}{\sigma}}\left\{\left(\frac{2}{k}-k\right)K(k)-\frac{2}{k}E(k)\right\} \tag{15}$$

$$J(s')=\frac{1}{4\pi\sigma}\int_0^{2\pi}\Delta\cos\phi'd\phi'=\frac{2}{3\pi}\sqrt{\frac{\sigma'}{\sigma}}\frac{1}{k}\left\{2\left(\frac{1}{k^2}-1\right)K(k)-\left(\frac{2}{k^2}-1\right)E(k)\right\} \tag{16}$$

$$\Delta\equiv\sqrt{(x-x')^2+\sigma^2+\sigma'^2-2\sigma\sigma'\cos\phi'} \tag{17}$$

where s, θ, and path c are defined in Fig. 2. The application of the contour dynamics method is beneficial in numerical calculations because it requires the one-dimensional integration on the contour instead of the two-dimensional integration of Eq. (10). In Eqs. (14) and (15), $k \rightarrow 1$ holds in the case of $(x',\sigma') \rightarrow (x,\sigma)$, and thus, $G(s')$ and $H(s')$ exhibit logarithmic singularity.

In this study, the Norbury-Fraenkel family of vortex rings, which are steady-state vortex rings, were the aim of the analysis. In this case, the vortex rings move forward at a steady-state velocity U in the positive x-direction. The free stream $-U\hat{e}_x$ superposition used to express the flow velocity relative to the vortex rings leads to the expression of the stream function, as follows:

$$\Psi(x,\sigma) = \psi(x,\sigma) - \frac{1}{2} U\sigma^2 = \frac{1}{2} \Omega\sigma \oint_c M(s')ds' - \frac{1}{2} U\sigma^2 \tag{18}$$

where Ψ is the stream function in the coordinate system fixed to the vortex rings. As the flow cannot penetrate contour c, the stream function value must be a constant if the field point (x,σ) of Eq. (18) exists on contour c:

$$\kappa = \psi(x,\sigma) - \frac{1}{2} U\sigma^2 = \frac{1}{2} \Omega\sigma \oint_c M(s')ds' - \frac{1}{2} U\sigma^2 \quad \text{for } (x,\sigma) \text{ on } c \tag{19}$$

where κ is a constant. Therefore, the contour shape can be determined if the field point (x,σ) that satisfies Eq. (19) is obtained.

The circulation (Γ), vortical impulse (P), and kinetic energy (T) were evaluated as the physical properties of the vortex rings, as follows, to compare their values with those of previous studies.

$$\Gamma = \iint_\Sigma \omega_\phi dxd\sigma = \Omega \iint_\Sigma \sigma dxd\sigma \tag{20}$$

$$P = \pi\rho_f \iint_\Sigma \omega_\phi \sigma^2 dxd\sigma = \pi\rho_f \Omega \iint_\Sigma \sigma^3 dxd\sigma \tag{21}$$

$$T = \pi\rho_f \iint_\Sigma \psi\omega_\phi dxd\sigma = \pi\rho_f \Omega \iint_\Sigma \psi\sigma dxd\sigma \tag{22}$$

where ρ_f is the density of the fluid. Eqs. (21) and (22) are shown in Lamb (1932).

Norbury (1973) standardized the contour shape in non-dimensional form. In Fig. 2, the midpoint between Points A and B are defined as Point C, and the distance between the x-axis and Point C is defined as the ring radius L. Furthermore, the dimensionless mean core radius α defined by the following equation is introduced:

$$A_\Sigma = \pi L^2 \alpha^2 \tag{23}$$

where A_Σ is the area of the core cross-section. L is used to non-dimensionalize the geometrical quantities, as follows:

$$(x,\sigma,s,A_\Sigma,V_\Sigma) = \left(L\tilde{x}, L\tilde{\sigma}, L\tilde{s}, L^2\tilde{A}_\Sigma, L^3\tilde{V}_\Sigma\right) \tag{24}$$

where V_Σ is the volume of the core, and the symbol (~) represents the non-dimensionalized physical quantity. Additionally, U, Ψ, κ, Γ, P, and T are non-dimensionalized, as follows:

$$(U,\Psi,\kappa) = \left(\Omega L^2\alpha^2\tilde{U}, \Omega L^4\alpha^2\tilde{\psi}, \Omega L^4\alpha^2\tilde{\kappa}\right) \tag{25}$$

$$(\Gamma, P, T) = \left(\Omega L^3\alpha^2\tilde{\Gamma}, \rho_f\Omega L^5\alpha^2\tilde{P}, \rho_f\Omega^2 L^7\alpha^4\tilde{T}\right) \tag{26}$$

In the following descriptions, the symbol (~) is omitted in the expression of the non-dimensional quantities for convenience. Eqs. (12), (18), and (19) can be non-dimensionalized, as follows:

$$\psi(x,\sigma) = \frac{1}{2\alpha^2}\sigma \oint_c M(s')ds' \tag{27}$$

$$\Psi(x,\sigma) = \psi(x,\sigma) - \frac{1}{2} U\sigma^2 = \frac{1}{2\alpha^2}\sigma \oint_c M(s')ds' - \frac{1}{2} U\sigma^2 \tag{28}$$

$$\kappa = \psi(x,\sigma) - \frac{1}{2} U\sigma^2 = \frac{1}{2\alpha^2}\sigma \oint_c M(s')ds' - \frac{1}{2} U\sigma^2 \text{ for } (x,\sigma) \text{ on } c \tag{29}$$

The parametric angle φ and the radial distance $q(\varphi)$ from Point C are introduced to express the contour shape, as shown in Fig. 2.

$$x(\varphi) = -q(\varphi)\sin\varphi, \quad \sigma(\varphi) = 1 + q(\varphi)\cos\varphi \quad \text{for } (x,\sigma) \text{ on } c \tag{30}$$

The non-dimensionalized cross-sectional area and the characteristic values of the vortex rings are expressed as follows:

$$A_\Sigma = \pi\alpha^2 = \frac{1}{2} \int_0^{2\pi} q^2 d\varphi \tag{31}$$

$$\Gamma = \frac{1}{\alpha^2} \iint_\Sigma \sigma dxd\sigma = \frac{1}{\alpha^2} \int_0^{2\pi} \left(\frac{1}{2} q^2 + \frac{1}{3} q^3\cos\varphi\right)d\varphi \tag{32}$$

$$P = \frac{\pi}{\alpha^2} \iint_\Sigma \sigma^3 dsd\sigma \tag{33}$$
$$= \frac{\pi}{\alpha^2} \int_0^{2\pi} \left(\frac{1}{2} q^2 + q^3\cos\varphi + \frac{3}{4} q^4\cos^2\varphi + \frac{1}{5} q^5\cos^3\varphi\right)d\varphi$$

$$T = \frac{\pi}{\alpha^2} \iint_\Sigma \psi\sigma dxd\sigma \tag{34}$$

In Eq. (31), the range of the mean core radius α is $0 < \alpha \leq \sqrt{2}$; in the case of $\alpha = \sqrt{2}$, it represents Hill's spherical vortex (Batchelor, 1967). A contour integral was used in Eqs. (31)-(33), but a two-dimensional integration must be performed to obtain the kinetic energy of Eq. (34).

Fraenkel (1970) and Norbury (1973) determined the contour shape using the following two-dimensional integral equation that was used in Eq. (10).

$$\kappa = \frac{1}{2\pi\alpha^2}\sqrt{\sigma}\iint_{\Sigma}\sigma'\sqrt{\sigma'}\left\{\left(\frac{2}{k}-k\right)K(k)-\frac{2}{k}E(k)\right\}dx'd\sigma' - \frac{1}{2}U\sigma^2 \quad (35)$$

$$\text{for } (x,\sigma) \text{ on } c$$

3. Numerical Scheme

The contour shape is discretized as shown in Fig. 3, to numerically obtain the shape using Eq. (29). In this case, the number of nodal points and segments was set to $2N$, considering the symmetry of the geometry.

The following relationships hold based on the definition of Point C (Fig. 2) and symmetry.

$$\varphi_1 = 0, \ \varphi_{N+1} = \pi, \ q_{N+1} = q_1, \ x_1 = x_{N+1} = 0,$$
$$\sigma_1 = 1 + q_1, \ \sigma_{N+1} = 1 - q_1 \quad (36)$$

$$\varphi_{2N-n+2} = 2\pi - \varphi_n, \ q_{2N-n+2} = q_n, \ x_{2N-n+2} = -x_n = q_n\sin\varphi_n,$$
$$\sigma_{2N-n+2} = \sigma_n = 1 + q_n\cos\varphi_n \quad \text{for } n = 2 \sim N \quad (37)$$

The discretized contour shape can be determined by obtaining $q_1 \sim q_N$ that satisfies Eq. (29) for the given α. In Eq. (29), κ and U are also the unknowns to be determined. Therefore, the total number of unknowns is $N+2$, and $N+2$ equations are, therefore, required to obtain the unknowns. $N+1$ equations are obtained by substituting $N+1$ field points (x_n,σ_n) corresponding to $q_1 \sim q_N$ into Eq. (29). If the condition of Eq. (31) is additionally assigned, $N+2$ nonlinear simultaneous equations are constructed. Broyden's method, an iterative calculation scheme, is used to obtain the solutions of these equations (Press et al., 1992). In addition, the angle φ is divided into equal intervals.

In the iterative calculations, the numerical burden when the contour integral of Eq. (29) is used can be significantly reduced compared to the two-dimensional integration of Eq. (35), which was used by Norbury (1973).
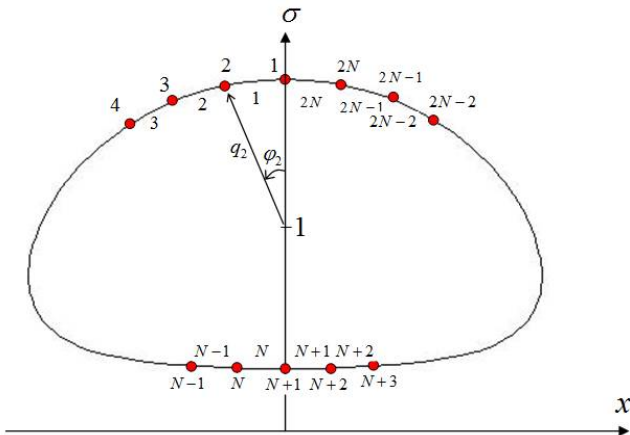

Fig. 3 Discretization of contour

The contour integral of Eq. (29) is obtained as the sum of segmental integrals, as follows:

$$\psi(x_n,\sigma_n) = \sum_{i=1}^{2N}\delta\psi_i(x_n,\sigma_n) \quad (38)$$

$$\delta\psi_i(x_n,\sigma_n) = \frac{1}{2\alpha^2}\sigma_n\int_{c_i}\begin{bmatrix}-(x_n-x')\sigma'H(s')\cos\theta' \\ +\sigma'\{\sigma'H(s')-\sigma_nG(s')-2\sigma_nJ(s')\}\sin\theta'\end{bmatrix}ds'$$
$$= \frac{1}{2\alpha^2}\sigma_n\int_{c_i}\begin{bmatrix}-(x_n-x')\sigma'H(s')d\sigma' \\ -\sigma'\{\sigma'H(s')-\sigma_nG(s')-2\sigma_nJ(s')\}dx'\end{bmatrix} \quad (39)$$

where (x_n,σ_n) is the field point, and c_i is the i-th segment. In this study, integration is performed by simplifying the segments into linear segments (Shariff et al., 1989; Shariff et al., 2008).

$$x' = x_i + \xi l_x, \quad \sigma' = \sigma_i + \xi l_\sigma, \quad (40)$$
$$where \ l_x = x_{i+1} - x_i, \ l_\sigma = \sigma_{i+1} - \sigma_i, \quad 0 \le \xi \le 1$$

Substituting Eq. (40) into Eq. (39) yields the following expression.

$$\delta\psi_i(x_n,\sigma_n) = \frac{1}{2\alpha^2}\sigma_n\begin{bmatrix}l_\sigma\int_0^1 -(x_n-x_i-\xi l_x)(\sigma_i+\xi l_\sigma)Hd\xi \\ -l_x\int_0^1(\sigma_i+\xi l_\sigma)\{(\sigma_i+\xi l_\sigma)H-\sigma_nG-2\sigma_nJ\}d\xi\end{bmatrix} \quad (41)$$

When $n \ne i$ and $n \ne (i+1)$, conventional numerical integration can be performed because the integrands of Eq. (41) exhibit non-singular behavior. In this study, numerical integration is performed using three-point Gauss-Legendre quadrature.

However, when $n = i$ or $n = (i+1)$, the integration must be performed considering the logarithmic singularity that occurs at $\xi = 0$ or $\xi = 1$ respectively. For the case of $n = i$, Eq. (41) is expressed as follows:

$$\delta\psi_n(x_n,\sigma_n) = -\frac{1}{2\alpha^2}\sigma_n^2 l_x\begin{bmatrix}\sigma_n\int_0^1(H-G-2J)d\xi \\ +l_\sigma\int_0^1\xi(H-G-2J)d\xi\end{bmatrix} \quad (42)$$

In this study, $H-G-2J$ is asymptotically expanded in series form at $\xi = 0$ and analytically integrated based on the methods proposed by Shariff et al. (1989) and Shariff et al. (2008).

$$H-G-2J = \ln\left(\frac{8\sigma_n}{l\xi}\right)\sum_{j=0}^{JM}a_j\xi^j + \sum_{j=0}^{JM}b_j\xi^j + O(\xi^{JM+1}\ln\xi), \quad (43)$$

$$\text{where } l = \sqrt{l_x^2 + l_\sigma^2}$$

The integral values calculated by setting $JM = 5$ in Eq. (43) are presented in Appendix.

When $\delta\psi_n(x_{n+1},\sigma_{n+1})$, it is possible that the signs of l_x and l_σ are reversed in Eq. (42), as well as in Eqs. (A1) and (A2) in Appendix. Then, the sign of the integral value is reversed after using σ_{n+1} instead of σ_n.

4. Numerical Results

The appropriate selection of the initial guess is required to achieve the stable performance of the iterative calculation method. A circle with a radius of α was set as the initial guess contour for $\alpha \leq 0.95$, and a circle with a radius of 0.95 was used as the initial guess contour for $0.95 < \alpha \leq 1.1$. In this case, 0.5 was used as the initial guess of κ and U. In the case of $\alpha > 1.1$, the solutions for $\alpha = 1.1, 1.2, 1.3,$ and 1.39 were sequentially obtained and set as the initial guesses.

The convergence of the numerical solutions based on the number of segments was analyzed at $\alpha = 0.8$. Fig. 4 shows the results of κ and the translational velocity U. As shown in Fig. 4, the solution is considered to have sufficiently converged if the number of segments, $2N$, is approximately equal to 120. Therefore, for all the α values, calculations were performed using $2N = 120$.

Fig. 5 shows the shapes of the cores for several α values. In Fig. 5, the results of Norbury (1973) are also displayed using dotted lines. Norbury (1973) used the two-dimensional integration of Eq. (35) and an indirect method to construct the core shape using Fourier coefficients that expressed the contour shape. The Fourier coefficients were obtained as the solutions of simultaneous equations. Although the technique applied by Norbury (1973) could be used to analyze the problem up to $\alpha = 1.35$, in this study, it is possible up to $\alpha = 1.40$, which is very closer to $\alpha_{max} = \sqrt{2} \simeq 1.414$ (Hill's spherical vortex). In addition, the numerical burden is significantly reduced by performing the contour integral instead of extensive calculations owing to the two-dimensional integration. In Fig. 5, the values between nodal points were interpolated through Fourier analysis of the decretized shape. The two results are almost identical when the value of α is small, but when the value is large,
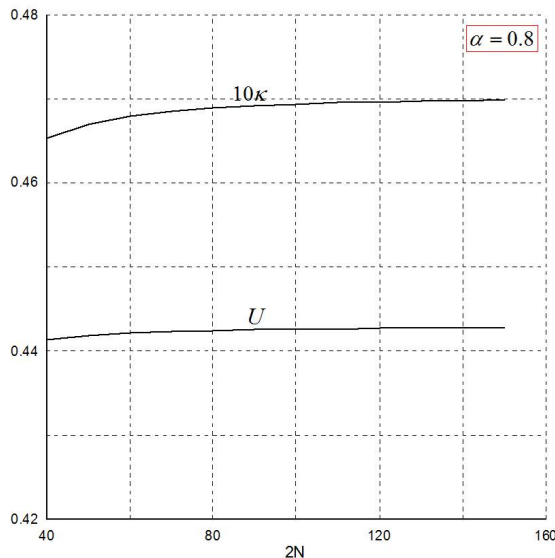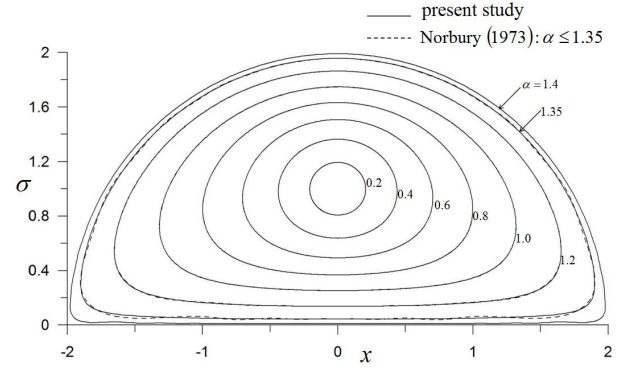
Fig. 5 Contour shapes for various values of α

slight irregularities are observed in the results of Norbury (1973). This trend is due to the limited number of Fourier coefficients. In this study, however, this phenomenon was hardly observed because the positions of the nodal points were directly obtained.

In a steady-state vortex ring, an irrotational flow region that moves forward at the same velocity with the ring exists. This region is known as the vortex atmosphere (Akhmetov, 2009). The shape of the vortex atmosphere is expressed by the dividing stream surface (Fig. 6) and can be obtained using the following equation.

$$0 = \psi(x,\sigma) - \frac{1}{2}U\sigma^2 = \frac{1}{2\alpha^2}\sigma\oint_c M(s')ds' - \frac{1}{2}U\sigma^2 \qquad (44)$$
$$\text{for } (x,\sigma) \text{ on } \partial\Sigma_d$$

The dividing stream surface was obtained for several α values, as shown in Fig. 7. As can be seen from Fig. 7, the results are in good agreement with those of Norbury (1973).
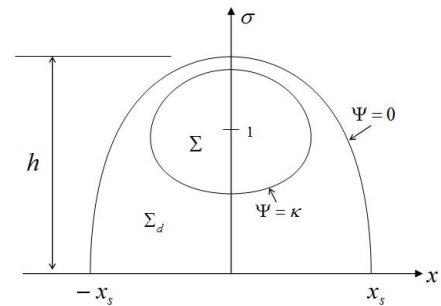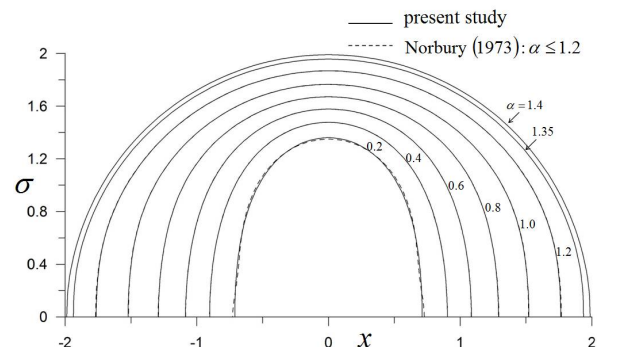
Fig. 6 Vortex atmosphere

Fig. 4 Convergence test of the numerical scheme

Fig. 7 Shapes of dividing stream surface for various values of α

Fig. 8 shows the results for U, κ, and V_Σ. Those for small α values are as follows (Fraenkel, 1972):

$$U = \frac{1}{4}\left(\ln\frac{8}{\alpha} - \frac{1}{4}\right) - \frac{3}{32}\alpha^2\left(\ln\frac{8}{\alpha} - \frac{5}{4}\right) + O(\epsilon^4) \tag{45}$$

$$V_\Sigma = 2\pi^2\alpha^2\{1 + O(\epsilon^2)\}, \quad \text{where } \epsilon = \alpha\ln\frac{8}{\alpha}, \ \alpha \ll 1 \tag{46}$$

Furthermore, asymptotic solutions for $\alpha \to \sqrt{2}$ are as follows (Norbury, 1973):

$$U = \frac{4}{15}\left(1 + \frac{\bar{\alpha}}{\sqrt{2}} + \cdots\right) \tag{47}$$

$$\kappa = \frac{\bar{\alpha}^2}{10} + \cdots \tag{48}$$

$$V_\Sigma = \frac{2}{3}\pi\alpha^2 a^3\left(1 + \bar{\alpha}\sqrt{2} - \frac{3}{16}\bar{\alpha}^2\ln\frac{8\sqrt{2}}{\bar{\alpha}} + \tau\bar{\alpha}^2 + \cdots\right),$$
$$\text{where } \bar{\alpha} = (\sqrt{2} - \alpha) \ll 1, \ a = 2\left\{1 - \frac{\bar{\alpha}}{2\sqrt{2}} + O(\bar{\alpha}^2\ln\bar{\alpha})\right\}, \tau \simeq 1.69 \tag{49}$$

As can be seen from Fig. 8, the results of this study are in good agreement with those of Norbury (1973). The results of this study are also in good agreement with the asymptotic solutions for $\alpha \to 0$ and $\alpha \to \sqrt{2}$, thereby validating the results of the proposed method.

Fig. 9 shows the characteristic values of the dividing stream surface. The definitions of x_s and h are shown in Fig. 6, and V_{Σ_d} is the volume of Σ_d, which is an irrotational flow field in the vortex atmosphere. In
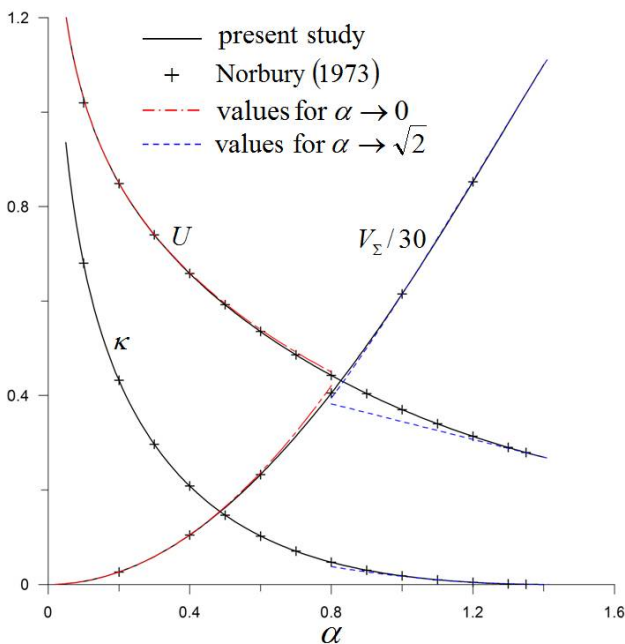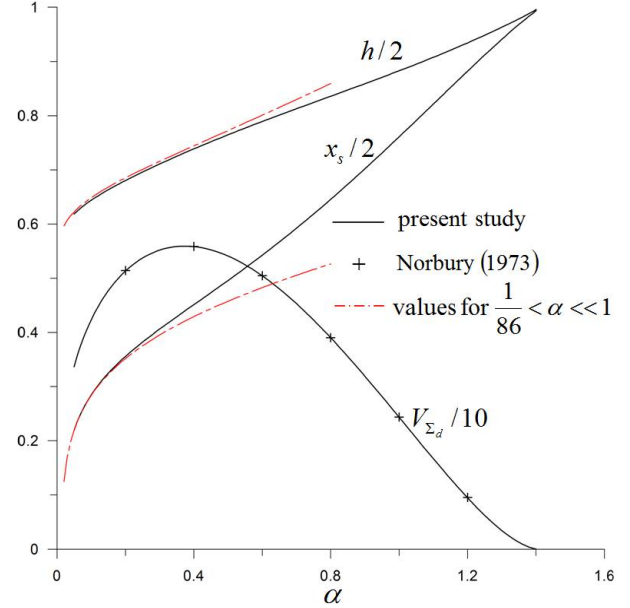

Fig. 9 Characteristic values of the dividing stream surface

the case of $\alpha > 1/86$, the stagnation points exist on the x-axis ($x = \pm x_s$), and the asymptotic solution of x_s for a small α value is expressed in Eq. (50) (Akhmetov, 2009). In addition, based on the model of Lamb (1932) for a small α value, h is expressed as the solution of Eq. (51).

$$x_s = \sqrt{\left(\frac{2\pi}{A(\alpha)}\right)^{2/3} - 1} \tag{50}$$

$$\ln\frac{8}{h-1} - \frac{1}{4}\ln\frac{8}{\alpha} - \frac{31}{16} + \frac{1}{2}(h-1)\left\{\ln\frac{\alpha}{h-1} - \frac{3}{4}\left(1 - \frac{\alpha^2}{(h-1)^2}\right)\right\} = 0,$$
$$\text{where } A(\alpha) = \ln\frac{8}{\alpha} - \frac{1}{4}, \quad \frac{1}{86} < \alpha \ll 1 \tag{51}$$

The results of the dividing stream surface are also in good agreement with those of previous studies.

Fig. 10 shows the results of the circulation (Γ), vortical impulse (P), and kinetic energy (T). Based on the core volume (V_Σ), Γ can be obtained as follows:

$$\Gamma = V_\Sigma / (2\pi\alpha^2) \tag{52}$$

The asymptotic solutions for $\alpha \to 0$ and $\alpha \to \sqrt{2}$ are as follows (Fraenkel, 1972; Norbury, 1973):

$$P = \pi^2\left\{1 + \frac{3}{4}\alpha^2 + O(\epsilon^4)\right\} \tag{53}$$

$$T = \pi^2\left\{\frac{1}{2}\left(\ln\frac{8}{\alpha} - \frac{7}{4}\right) + \frac{3}{16}\alpha^2\ln\frac{8}{\alpha} + O(\epsilon^4)\right\},$$
$$\text{where } \epsilon = \alpha\ln\frac{8}{\alpha}, \ \alpha \ll 1 \tag{54}$$

Fig. 8 Translational velocity(U), κ, and ring volume(V_Σ)

$$P = \frac{2\pi a^5}{15}\left(1 + \bar{\alpha}\sqrt{2} + \frac{141}{64}\bar{\alpha}^2 + \cdots\right),$$

$$T = \frac{2\pi a^7}{315}\left(1 + 2\bar{\alpha}\sqrt{2} + \frac{383}{64}\bar{\alpha}^2 + \cdots\right) \tag{55}$$

$$\text{where } \bar{\alpha} = (\sqrt{2} - \alpha) \ll 1, \quad a = 2\left\{1 - \frac{\bar{\alpha}}{2\sqrt{2}} + O(\bar{\alpha}^2 \ln\bar{\alpha})\right\}$$

As can be seen from Fig. 10, the results for the circulation and vortical impulse are consistent with the findings of previous studies. The results for the kinetic energy are slightly higher than those of Norbury (1973), but they are in good agreement.
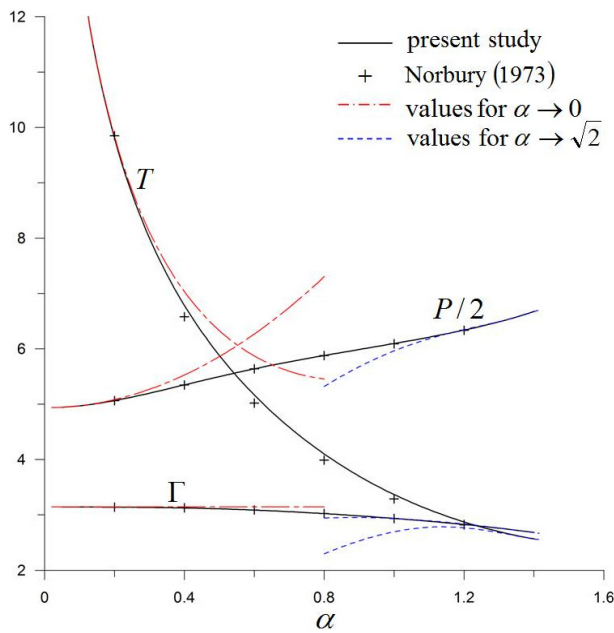

Fig. 10 Circulation (Γ), vortical impulse (P), and kinetic energy (T)

5. Conclusions

The Norbury-Fraenkel family of vortex rings was analyzed using a contour dynamics method for the Stokes' stream function. The calculation results for the core shape, dividing stream surface, and physical properties of the rings were compared with the findings of previous studies and asymptotic solutions to verify the validity of the proposed method.

The numerical burden was significantly reduced by performing the contour integral instead of a two-dimensional integration over the core cross-section. In addition, the difficulty of numerical integration was solved by analytically integrating over the logarithmic-singular segment. By directly determining the nodal point positions of the core shape, the results were better than those of the existing Fourier coefficients analysis method.

It is expected that the proposed method can also be applied to unsteady vortex ring problems if combined with the contour dynamics method for velocity.

References

Akhmetov, D.G. (2009). Vortex Rings. New York, USA: Springer.

Batchelor, G.K. (1967). An Introduction to Fluid Dynamics. Cambridge, UK: Cambridge University Press.

Durst, F., Schönung, B., & Simons, M. (1981). Steady Ellipsoidal Vortex Rings with Finite Cores. Journal of Applied Mathematics and Physics, 32(2), 156-169. https://doi.org/10.1007/BF00946745

Fraenkel, L.E. (1970). On Steady Vortex Rings of Small Cross-Section in an Ideal Fluid. Proceedings of the Royal Society A, 316(1524), 29-62. https://doi.org/10.1098/rspa.1970.0065

Fraenkel, L.E. (1972). Examples of Steady Vortex Rings of Small Cross-Section in an Ideal Fluid. Journal of Fluid Mechanics, 51(1), 119-135. https://doi.org/10.1017/S0022112072001107

Gradshteyn, I.S., & Ryzhik, I.M. (2000). Table of Integrals, Series, and Products (6th ed.). San Diego, USA: Academic Press.

Helmholtz, H. (1858). Über Integrale der Hydrodynamischen Bleichungen, Welche den Wirbelbewegungen Entsprechen. Journal Für die Reine und Angewandte Mathematik, 55, 25-55. https://doi.org/10.1515/crll.1858.55.25

Helmholtz, H. (1867). On Integrals of the Hydrodynamical Equations, Which Express Vortex-Motion. Philosophical Magazine and Journal of Science (4th series), 33, 485-512. https://doi.org/10.1080/14786446708639824

Hill, M.J.M. (1894). On a Spherical Vortex. Philosophical Transactions of the Royal Society A, 185, 213-245. https://doi.org/10.1098/rsta.1894.0006

Krueger, P.S. & Gharib, M. (2005). Thrust Augmentation and Vortex Ring Evolution in a Fully Pulsed Jet. AIAA Journal, 43(4), 792-801. https://doi.org/10.2514/1.9978

Lamb, H. (1932). Hydrodynamics (6th ed.). Cambridge, UK: Cambridge University Press.

Lugt, H.J. (1983). Vortex Flow in Nature and Technology. New York, USA: John Wiley & Sons.

Norbury, J. (1973). A Family of Steady Vortex Rings. Journal of Fluid Mechanics, 57(3), 417-431. https://doi.org/10.1017/S0022112073001266

Press, W.H., Teukolsky, S.A., Vetterling, W.T., & Flannery, B.P. (1992). Numerical Recipes in Fortran 77 (2nd ed.). Cambridge, UK: Cambridge University Press.

Samimy, M., Breuer, K.S., Leal, L.G., & Steen, P.H. (2003). A Gallery of Fluid Motion. New York, USA: Cambridge University Press.

Shariff, K., Leonard, A., & Ferziger, J.H. (1989). Dynamics of a Class of Vortex Rings (NASA Technical Memorandum 102257). Moffett Field, USA: NASA.

Shariff, K., Leonard, A., & Ferziger, J.H. (2008). A Contour Dynamics Algorithm for Axisymmetric Flow. Journal of Computational Physics, 227(10), 9044-9062. https://doi.org/10.1016/j.jcp.2007.10.005

Van Dyke, M. (1982). An Album of Fluid Motion. Stanford, USA: Parabolic Press.

Appendix

The integral values at the logarithmic-singular segment based on the asymptotic expansion of Eq.(43) are expressed as follows.

$$
\begin{aligned}
\int_0^1 (H - G - 2J)\, d\xi \simeq{} & \frac{l^2}{5120\pi\sigma_n^5}\left(75l^2 l_\sigma - 60l^2\sigma_n + 100l_\sigma^3 - 144l_\sigma^2\sigma_n + 240l_\sigma\sigma_n^2 - 640\sigma_n^3\right)\ln\!\left(\frac{8\sigma_n}{l}\right) \\
& - \frac{1}{921600\pi\sigma_n^5}\binom{6075l^4 l_\sigma - 900l^4\sigma_n + 57600l^2 l_\sigma^3 - 76896l^2 l_\sigma^2\sigma_n + 111600l^2 l_\sigma\sigma_n^2 - 172800l^2\sigma_n^3}{-1400l_\sigma^5 + 2400l_\sigma^4\sigma_n - 4800l_\sigma^3\sigma_n^2 + 12800l_\sigma^2\sigma_n^3 - 76800l_\sigma\sigma_n^4 - 307200\sigma_n^5}
\end{aligned}
$$
(A1)

$$
\begin{aligned}
\int_0^1 \xi(H - G - 2J)\, d\xi \simeq{} & \frac{l^2}{17920\pi\sigma_n^5}\left(225l^2 l_\sigma - 175l^2\sigma_n + 300l_\sigma^3 - 420l_\sigma^2\sigma_n + 672l_\sigma\sigma_n^2 - 1680\sigma_n^3\right)\ln\!\left(\frac{8\sigma_n}{l}\right) \\
& - \frac{1}{22579200\pi\sigma_n^5}\binom{134325l^4 l_\sigma - 25725l^4\sigma_n + 1218600l^2 l_\sigma^3 - 1587600l^2 l_\sigma^2\sigma_n + 2229696l^2 l_\sigma\sigma_n^2 - 3351600l^2\sigma_n^3}{-29400l_\sigma^5 + 49000l_\sigma^4\sigma_n - 94080l_\sigma^3\sigma_n^2 + 235200l_\sigma^2\sigma_n^3 - 1254400l_\sigma\sigma_n^4 - 3763200\sigma_n^5}
\end{aligned}
$$
(A2)

Author ORCIDs and Contributions

Author name	ORCID	Contributions
Choi, Yoon-Rak	0000-0002-3865-6721	①②③④⑤

① Conceived of the presented idea or developed the theory
② Carried out the experiment or collected the data
③ Performed the analytic calculations or numerical simulations
④ Wrote the manuscript
⑤ Supervised the findings of this study

Original Research Article

Study on Applicability of Ultimate Strength Design Formula for Sandwich Panels - Application Cases of Double Hull Tanker Bottom Structures

Bong Ju Kim[iD]

Associate Professor, The Korea Ship and Offshore Research Institute, Pusan National University, Busan, Korea

ABSTRACT: *In this study, ultimate strength characteristics of clamped sandwich panels with metal faces and an elastic isotropic core under combined in-plane compression and lateral pressure loads are investigated to verify the applicability of the ultimate strength design formula for ship structures. Alternative elastomer-cored steel sandwich panels are selected instead of the conventional bottom stiffened panels for a Suezmax-class tanker and then the ultimate strength characteristics of the selected sandwich panels are examined by using nonlinear finite element analysis.*
The change in the ultimate strength characteristics due to the change in the thickness of the face plate and core as well as the amplitude of lateral pressure are summarized and compared with the results obtained by using the ultimate strength design formula and nonlinear finite element analysis. The insights and conclusions developed in the present study will be useful for the design and development of applications for sandwich panels in double hull tanker structures

1. Introduction

Sandwich panels are widely used at various industrial sites owing to their excellent mechanical strength and lightweight structure. In ships, sandwich panels are beneficial during construction and maintenance because they can greatly reduce the number of longitudinal stiffeners as compared to the stiffened plate structures. They have further design advantages owing to the reduced stress concentration and fatigue problems by avoiding stiffeners. Over the last two decades, the applications of sandwich panels in ships and offshore installations have gradually increased and several related studies have been conducted. Brooking and Kennedy (2004) showed the advantages of sandwich panel structures in oil tankers with a dead weight tonnage (DWT) of 14K through a case study. They derived that the sandwich panel structure can reduce the weight by approximately 2% and weld volume by approximately 50% as compared to the conventional stiffened plate structure using the finite element analysis (FEA) technique. They emphasized that sandwich panels have great advantages in structural stability and environmental production owing to their energy absorption capacity and fire stability. Momcilovic and Motok (2009) showed that a sandwich structure for a 77-m-long barge can reduce the hull weight by approximately 5~8% compared to the

stiffened plate structure. Ramakrishna and Sunil Kumar (2016) specified that using sandwich panels is advantageous in reducing construction costs because the number of stiffeners is reduced, which in turn decreases the surface area and weight along with the number of structural members, junctions, and welding lines. Using sandwich panels can further reduce operating costs including maintenance owing to structural discontinuities in which stress concentration and fatigue cracking occur. Despite these advantages, case studies in the shipbuilding field are insufficient due to lack of design tools and techniques for sandwich panel construction. The International Classification Society is also attempting to develop design guidelines for sandwich panel construction, but additional research is required on various loading conditions and sandwich panel structures including research on design validation methods using FEA techniques (DNV-GL, 2016; LR, 2019). Furthermore, efficient methods, such as the strength evaluation automation systems introduced in the case study by Kim and Jang (2017), are required for shipyards and related business sites to design and apply sandwich panel structures more extensively.

The present study is a case study to apply sandwich panel structures to the bottom structure of a Suezmax-class oil tanker. The ultimate strength characteristics of sandwich panels under lateral pressure and

longitudinal axial compression loads are examined by using a nonlinear FEA technique, and the results are compared with the ultimate strength design formula that has been derived in the author's previous study (Kim, 2019).

2. Bottom Structure Characteristics of Suezmax-class Tanker and Selection of Sandwich Panels

2.1 Principal Dimensions and Load Characteristics

Tables 1 and 2 show the principal dimensions and the details of bottom stiffened plates of a Suezmax-class tanker (Kim et al., 2014). The inner and outer bottom structures are stiffened plates with 19

Table 1 Principal dimensions of the target structure

L_s (m)	B_s (m)	D (m)	C_b
261.0	48.0	23.2	0.843

Note: L_s, Ship legnth; B_s, Ship breadth; D, Ship depth; C_b, Block coefficient

longitudinal stiffeners as shown in Fig. 1, which have a length of 4,800 mm and a width of 17,100 mm.

In Fig. 2, lateral pressure distributions of the Suezmax-class tanker in full load condition and ballast condition are shown. The inner bottom plate has a lateral pressure of approximately 0.3 MPa, and the outer bottom plate has a lateral pressure of approximately 0.2 MPa.

Table 2 Properties of the stiffened panels of Suezmax-class tanker with net scantlings

Suezmax class tanker	a (mm)	b (mm)	B (mm)	t (mm)	Stiff. type	No. of stiff.	h_w (mm)	t_w (mm)	b_f (mm)	t_f (mm)	σ_Y (MPa) Plate	σ_Y (MPa) Stiff.
Inner bottom (I.B.)	4,800	855	17,100	14.84	Tee	19	504	8.0	146.5	20.5	315	355
Outer bottom (O.B.)	4,800	855	17,100	19.49	Tee	19	503	8.5	147.0	21.0	315	355

Note: a, Length of stiffened panel; b, Breadth between longitudinal stiffeners; B, Breadth of stiffened panel; t, Plate thickness; σ_Y, Yield strength
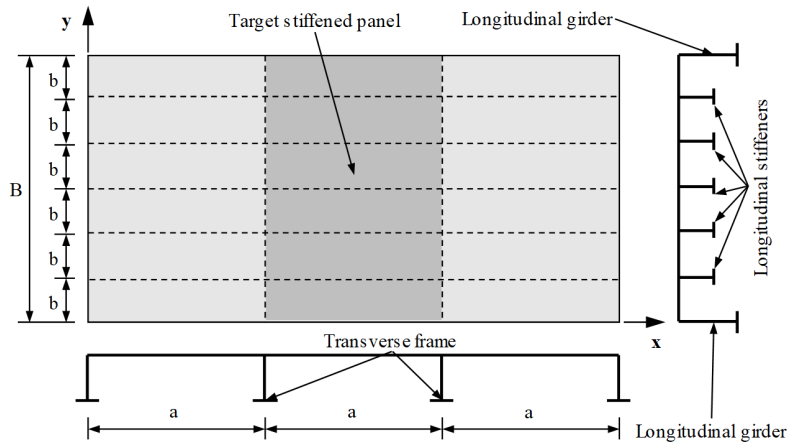
Fig. 1 Schematic diagram of general stiffened panel structures

(a) Ballast condition
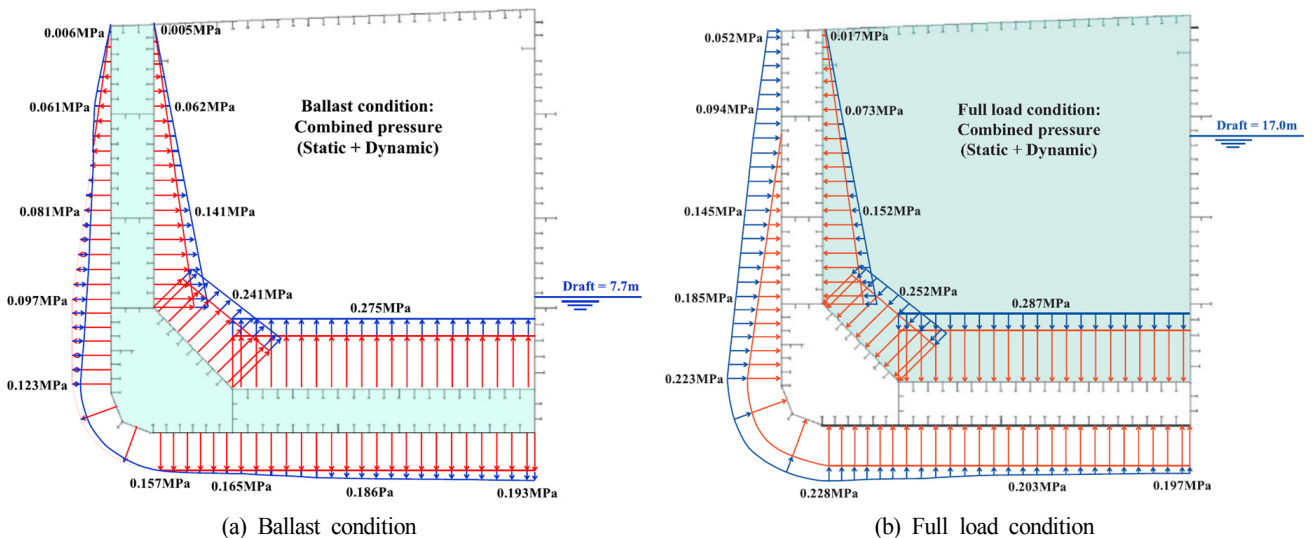
(b) Full load condition

Fig. 2 Lateral pressure distribution of the Suexmax-class tanker in ballast and full load condition (Kim et al., 2013)

In this study, the stiffened plate of the inner bottom was selected as the subject of research. The inner bottom plate has a thickness (t) of 14.84 mm and 19 T-type longitudinal stiffeners. The web height (h_w), web thickness (t_w), breadth of flange (b_f), and flange thickness (t_f) of the longitudinal stiffeners are $h_w \times t_w + b_f \times t_f = 504 \times 8.0 + 146.5 \times 20.5$ mm.

2.2 Selection of Sandwich Panels

In this study, The structure of the stiffened plate of the inner bottom, which is the target stiffened plate, was changed to the target sandwich
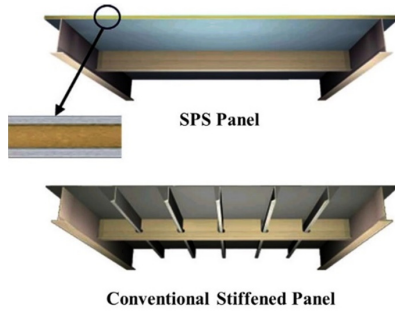

Fig. 3 A general structure arrangement of sandwich panels and conventional stiffened panels (SPS Technology, 2020)
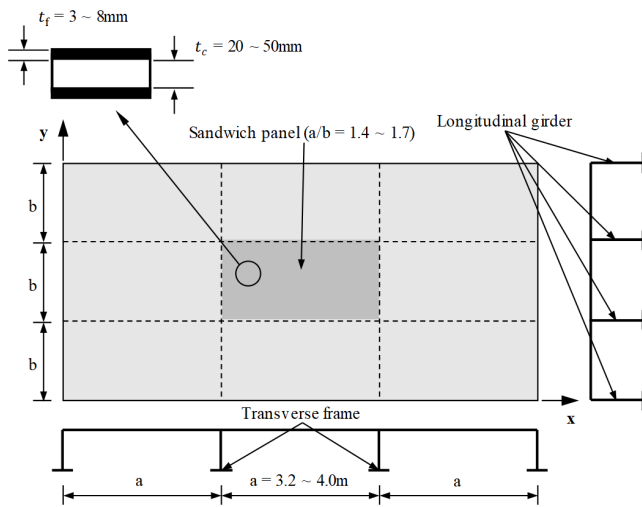

Fig. 4 A schematic diagram of the sandwich panel arrangement (Ramakrishnan and Sunil Kumar, 2016)

panel, as shown in Fig. 3. According to a previous study, as shown in Fig. 4, the thickness (t_f) of the sandwich panel's face plate was 3−8 mm, the thickness (t_c) of the core was 20−50mm, the transverse frame spacing was 3.2−4.0 m, and the aspect ratio (a/b) was 1.4−1.7 (Ramakrishnan and Sunil Kumar, 2016). The classification rules suggest a face plate thickness of 3−30 mm, core thickness of 15−100 mm, core elastic coefficient (E_c) of 748 MPa, and Poisson's ratio (ν_c) of 0.26 (DNV-GL, 2016).

In this study, we selected different breadths of sandwich panels (b) while maintaining the same spacing (4,800 mm) of the existing transverse frames. Furthermore, we selected sandwich panels with breadths of 3,240 mm in the aspect ratio range of 1.4−1.7 and sandwich panels with breadths of 4,275 mm in the aspect ratio range of $1.0 < a/b < 1.4$. The difference in the breadths of the selected panels is approximately equal to one longitudinal stiffener spacing (855 mm) in the existing stiffened plate structure. Face plate thicknesses of 4, 5.5, 7, and 8 mm were chosen. For the core thickness, we selected sandwich panels having weights equal to the weight of the target stiffened plate. The core thickness was selected according to the face plate thickness, which was selected such that the weight per unit area of the target stiffened plate structure having a length of 4,800 mm and width of 17,100 mm would be equal to the weight per unit area of the selected sandwich panel. Table 3 shows the dimensions of the selected sandwich panels. Only the aspect ratio (a/b) of the sandwich panels and the thicknesses of the face plate and core were changed while maintaining the same yield strength (σ_Y), elastic coefficient (E), Poisson's ratio (ν), and density (ρ_p) of the face plate and the same elastic coefficient (E_c), Poisson's ratio (ν_c), and density (ρ_c) of the core.

3. Nonlinear Finite Element Analysis

3.1 Finite Element Modeling and Boundary Conditions

In Fig. 5, the finite element modeling and boundary conditions used in this study are shown. Based on the experience obtained from previous studies and the mesh convergence study, a sandwich panel with a size of 4,800 × 4,275 mm (aspect ratio is approximately 1.1) was modeled using 48 × 44 four-node layered shell elements and a

Table 3 Selected sandwich panels in the present study

Panel no.	a (mm)	b (mm)	a/b	Face plate					Core			
				t_f (mm)	E (GPa)	ν	σ_Y (MPa)	ρ_p (kg/m³)	t_c (mm)	E_c (MPa)	ν_c	ρ_c (kg/m³)
I-a				4.0					100.0			
I-b	4,800	3,420	1.4	5.5					79.6			
I-c				7.0					59.1			
I-d				8.0	206	0.3	315	7,850	45.4	748	0.26	1,150
II-a				4.0					100.0			
II-b	4,800	4,275	1.1	5.5					79.6			
II-c				7.0					59.1			
II-d				8.0					45.4			

(a) Detailed boundary conditions   (b) Isometric view of the finite element model with boundary conditions

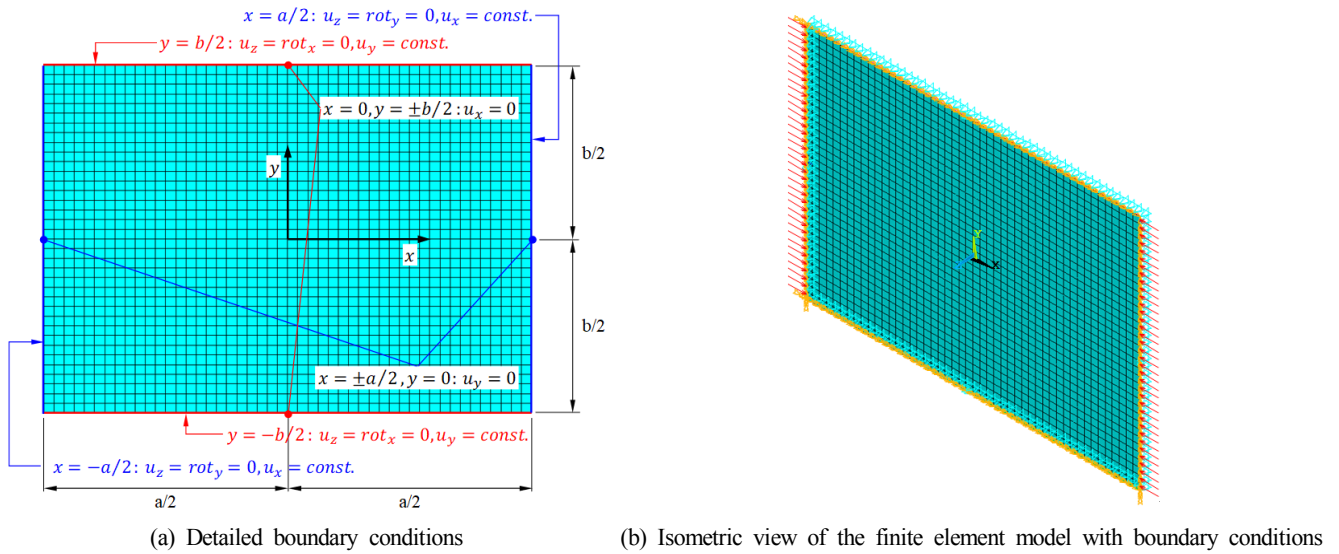**Fig. 5** Finite element modeling for rectangular sandwich panels with clamped boundary edges

(a) BC#1   (b) BC#2
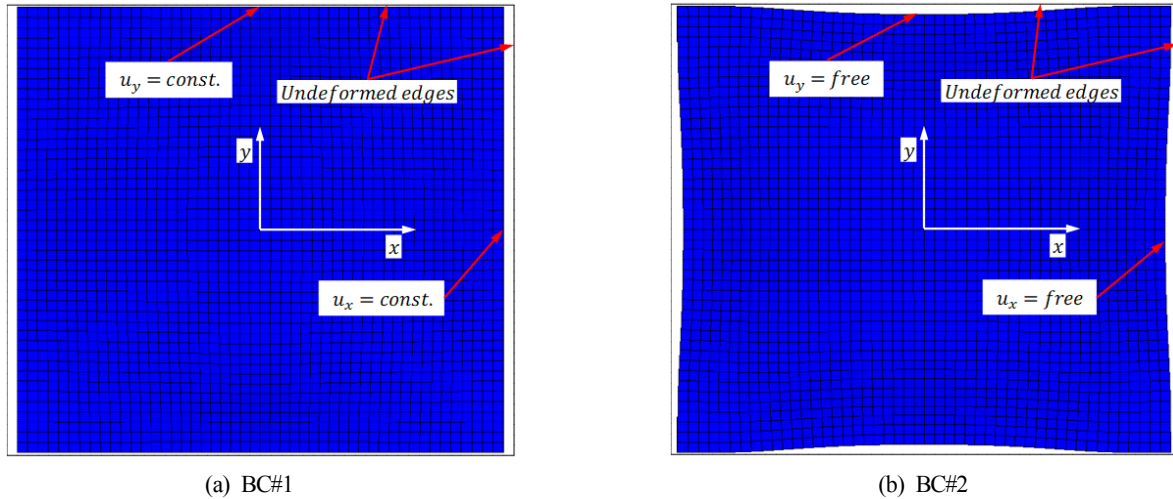
Fig. 6 Schematic patterns of edge deformation according to the boundary conditions (BC)

panel with a size of 4,800 × 3,420 mm (aspect ratio is approximately 1.4) was modeled using 48 × 36 four-node layered shell elements. The elements comprise of three layers, i.e., the face plate, core, and face plate having 100 mm or smaller sizes and square shapes. Both the face plate and core were modeled as isotropic materials. In addition, the core was modeled as a perfectly elastic material and the face plate as an elastic-perfectly plastic material. The material constants of the face plate and core are outlined in Table 3.

The boundary conditions of the four edges of the panels were assumed to be clamped. The previous study used the boundary condition (BC#1) where the four edges of the panel boundary always maintain a straight line in the plane even if the panel is deflected as shown in Fig. 6. In this study, however, we considered an additional boundary condition (BC#2) where a free in-plane displacement may occur. The support members around the panel were not included in the model. The details of these two boundary conditions are outlined in Table 4.

Table 4 Details of clamped edge boundary conditions in the present study

BC number	Node location	Boundary conditions
BC#1	$y = \pm\, b/2$	$u_z = rot_x = 0,\ u_y = const.$
	$y = \pm\, a/2$	$u_z = rot_y = 0,\ u_x = const.$
	$x = 0,\ y = \pm\, b/2$	$u_x = 0$
	$x = \pm\, a/2,\ y = 0$	$u_y = 0$
BC#2	$y = \pm\, b/2$	$u_z = rot_x = 0,\ u_y = free$
	$y = \pm\, a/2$	$u_z = rot_y = 0,\ u_x = free$
	$x = 0,\ y = \pm\, b/2$	$u_x = 0$
	$x = \pm\, a/2,\ y = 0$	$u_y = 0$

For load application to the panel, lateral pressure was first applied before applying the in-plane compression load. In this study, to observe the ultimate strength behavior according to different lateral

pressures, 0.15 MPa and 0.3 MPa were applied as uniform pressure vertically to the element plane of the finite element model, and the in-plane compression load was applied as uniform pressure to the edges of the element. The lateral pressure reached the operating load through load increments of 30 or more steps. Then, the ultimate strength was obtained by incrementing the in-plane compression load using the arc-length method. To prevent the rigid body motion, the displacements of the x and y directions were fixed to the four nodes at the center of the panel edges as shown in Fig. 5. The elasto-plastic large deformation analysis was performed using the ANSYS software (ANSYS, 1999).

3.2 Analysis of Ultimate Strength Behavior Characteristics

In Figs. 7-8, the nonlinear FEA results for the selected sandwich panels are shown. The maximum deflection (w) at the center of the panel is normalized with the total thickness of the sandwich panels ($T = 2t_f + t_c$) and the in-plane compression load (σ_{xa}) along the length (x direction) is normalized with the yield strength (σ_Y) of the face plate. First, to examine the behavior characteristics at the lateral pressure of 0.15 MPa, we can observe a relatively clear threshold where the strength is degraded after the in-plane compression load increases and reaches the ultimate strength, as shown in Fig. 7. However, as shown in the graph for panel I-a, when the thickness of the sandwich panel is large, the threshold is not clear and a deflection behavior obtains for loads exceeding the yield strength. This analysis result is similar to the behavior of a thick plate with a low slenderness ratio and small initial deflection amount and appears more conspicuously in narrow thick panels. Furthermore, the deflection behavior for the boundary condition where the four edges of the sandwich panel always maintain an in-plane straight line (BC#1) and

(a) $b = 3{,}420$ mm

(b) $b = 4{,}275$ mm

Fig. 7 Load-deflection curves of sandwich panels under in-plane edge compression and lateral pressure with clamped edges ($p = 0.15$ MPa)
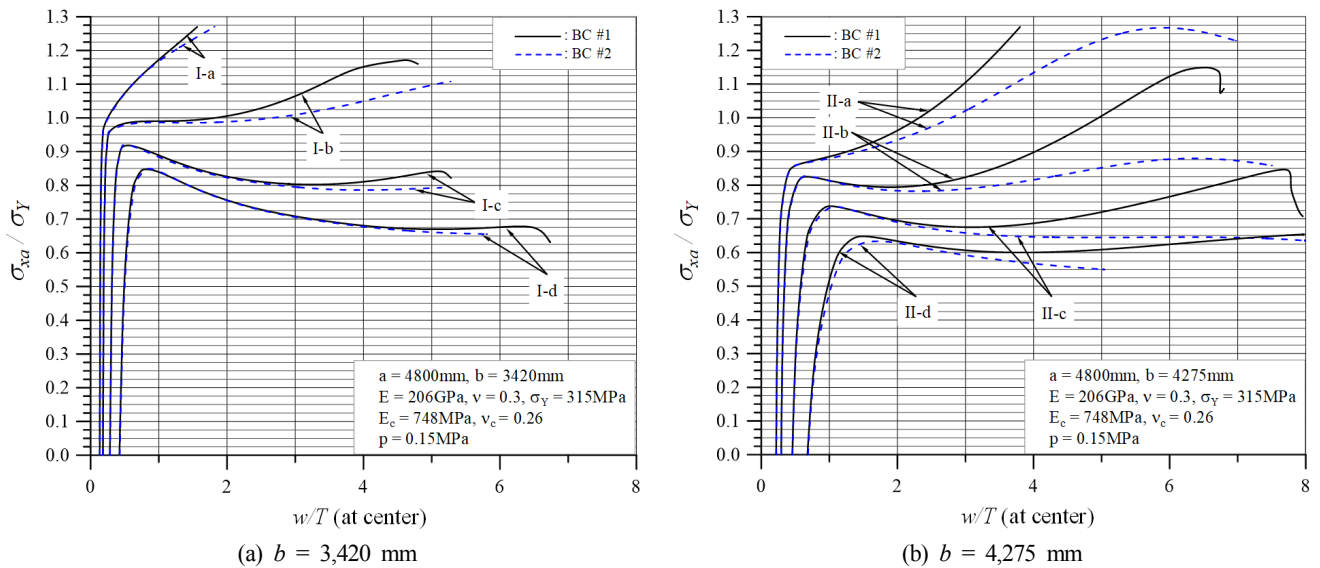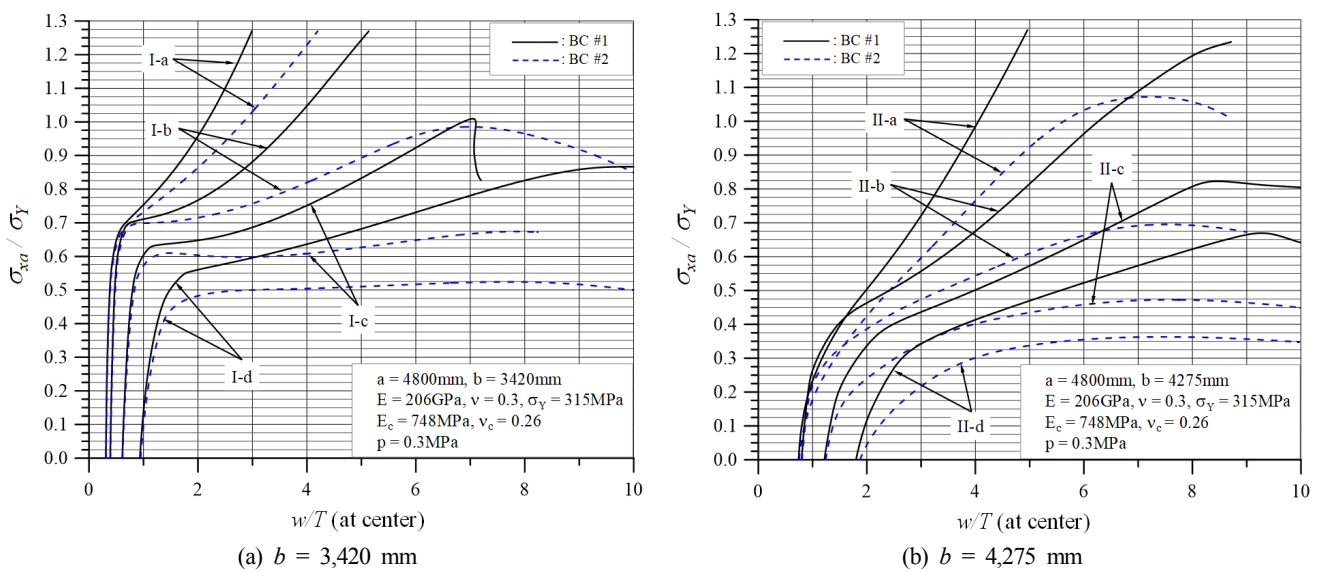

(a) $b = 3{,}420$ mm

(b) $b = 4{,}275$ mm

Fig. 8 Load-deflection curves of sandwich panels under in-plane edge compression and lateral pressure with clamped edges ($p = 0.3$ MPa)

the boundary condition where the in-plane displacements are free (BC#2) remain almost constant up to the threshold and then begin to vary beyond the threshold. The strength degradation of BC#2 is larger than that of BC#1. The greater the thickness and breadth of the sandwich panel, the greater the difference. In the case when lateral pressure is 0.3 MPa as shown in Fig. 8, the threshold is often unclear, and the difference in deflection behavior between BC#1 and BC#2 is larger than the case when the lateral pressure is 0.15 MPa. The difference was large in a low in-plane compression load as well when the panel breadth was 4,275 mm.

The maximum deflection at the center of each sandwich panel under a lateral pressure of 0.15 MPa is shown in Fig. 9. When a lateral pressure of 0.15 MPa was applied, the maximum deflection increased almost linearly with the increase in lateral load. In the case of panels I-a and II-a with the largest bending rigidity, the deflection in lateral pressure was smaller. As a result, strength degradation did not occur after the ultimate strength in Fig. 7 and deflection behavior appeared for loads exceeding the yield strength. In the case of I-b, a deflection smaller than that of II-a occurred by lateral pressure, and it is presumed that strength degradation did not appear clearly for the same reason because the bending rigidity was 92% that of II-a.

To define the ultimate strength for panels I-a, II-a, and I-b, we examined the progressive yielding pattern of the face plate. According to a previous study, in sandwich panels that were subjected to lateral pressure and in-plane compression load, yielding occurred continuously along the y-axis from the center to the edges of the panel in the face plate (Concave; face plate I) where compression stress occurred along the length owing to lateral pressure. In addition, the ultimate strength was reached on the opposite face plate (Convex; face plate II) as well if yielding occurred continuously from the center to the edges of the panel along the direction of the y-axis (Kim, 2019).

The progressive yielding pattern for panel I-d with clear strength degradation after the ultimate strength is shown in Fig. 10. With the

increasing in-plane compression load, yielding occurs continuously on the face plate I along the y-axis from the center to the edges. On the face plate II as well, the ultimate strength is reached as the yielding of the edges and center are combined right before the ultimate strength is reached. This progressive yielding pattern is consistent with the previous study. In Fig. 7, the same strength degradation was observed in the panels after reaching the ultimate strength. The same progressive yielding patterns could be also found for panels I-a, II-a, and I-b. The yielding pattern for panel I-a is shown in Fig. 11 while the yielding pattern for panel II-a is shown in Fig. 12. Only the yielding pattern of face plate II is shown because it is the same for face plate I. The yielding pattern of panel I-b is equal to that of panel I-a. Thus, the same yielding shown in Fig. 10 occurred in all the panels. The deflection curves with locations of the yielding patterns in Figs. 10−12 (a), (b), and (c) are shown in Fig. 13. Once point (c) was passed, the deflection for the increased in-plane compression load increased sharply. In the case of panels I-a, II-a, and I-b, it will be reasonable to find point (c) and evaluate the threshold using the ultimate strength.

The maximum deflection at the center of each sandwich panel under a lateral pressure of 0.3 MPa is shown in Fig. 14. When a lateral pressure of 0.15 MPa was applied to the panel, the maximum deflection increased almost linearly. However, when the lateral pressure of 0.3 MPa was applied, the deflection did no increase linearly. Particularly for panels with a breadth of 4,275 mm, the deflection increased sharply when the lateral pressure was close to 0.3 MPa. The deflections under lateral pressure showed a very large difference between the widths of 3,420 mm and 4,275 mm even though the difference was roughly equal to a single space of longitudinal stiffeners in the stiffened plate structure. It can be seen that after applying a lateral pressure of 0.3 MPa, high stress due to lateral pressure occurred at the edges and center of every panel. Excluding panels I-b and I-c, yielding occurred at the center of face plate II (Convex). In Fig. 15, the von Mises stress distributions of panel I-a,
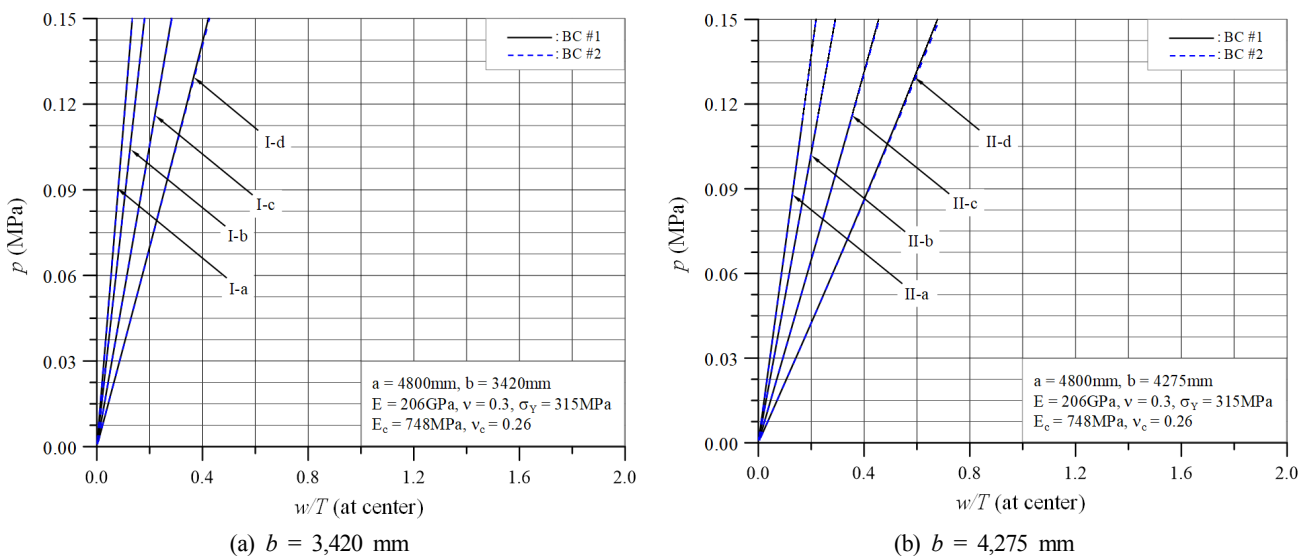
(a) b = 3,420 mm

(b) b = 4,275 mm

Fig. 9 Load-deflection curves of sandwich panels under only lateral pressure with clamped edges (p = 0.15 MPa)

(a) $\sigma_{xa}/\sigma_Y = 0.838$

(b) $\sigma_{xa}/\sigma_Y = 0.846$

(c) $\sigma_{xa}/\sigma_Y = 0.848$ (Ultimate strength)
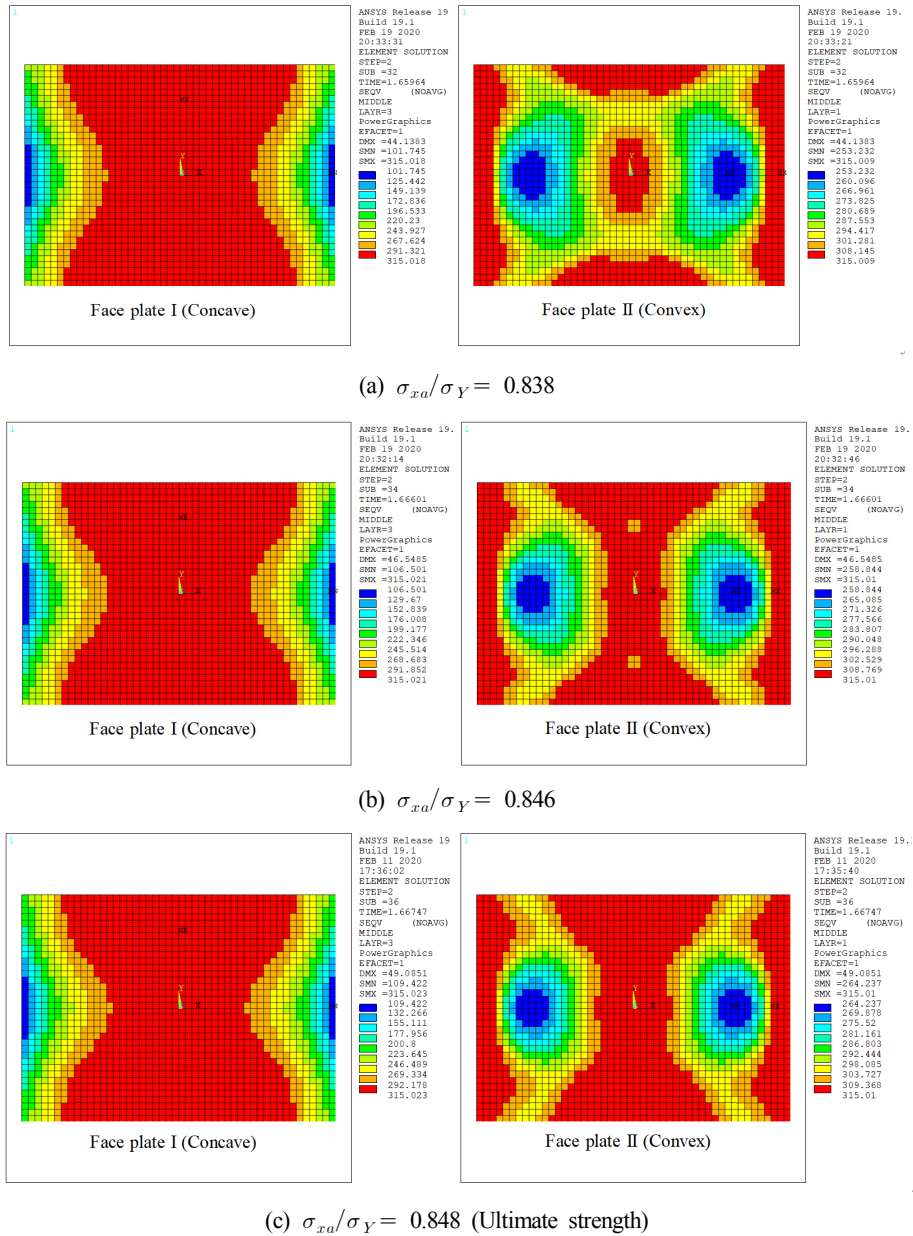
Fig. 10 Progressive yielding of the face plates of sandwich panel I-d under in-plane edge compression and lateral pressure with clamped edges (BC#1, $p = 0.15$ MPa)

(a) $\sigma_{xa}/\sigma_Y = 0.939$

(b) $\sigma_{xa}/\sigma_Y = 0.962$

(c) $\sigma_{xa}/\sigma_Y = 0.974$

Fig. 11 Progressive yielding of the face plate II (Convex) of sandwich panel I-a under in-plane edge compression and lateral pressure with clamped edges (BC#1, $p = 0.15$ MPa)

(a) $\sigma_{xa}/\sigma_Y = 0.833$ (b) $\sigma_{xa}/\sigma_Y = 0.839$ (c) $\sigma_{xa}/\sigma_Y = 0.884$

Fig. 12 Progressive yielding of the face plate II (Convex) of sandwich panel II-a under in-plane edge compression and lateral pressure with clamped edges (BC#1, $p = 0.15$ MPa)

Fig. 13 Progressive yielding of the face plates of sandwich panels (I-a, I-b and I-d) under in-plane edge compression and lateral pressure with clamped edges (BC#1)
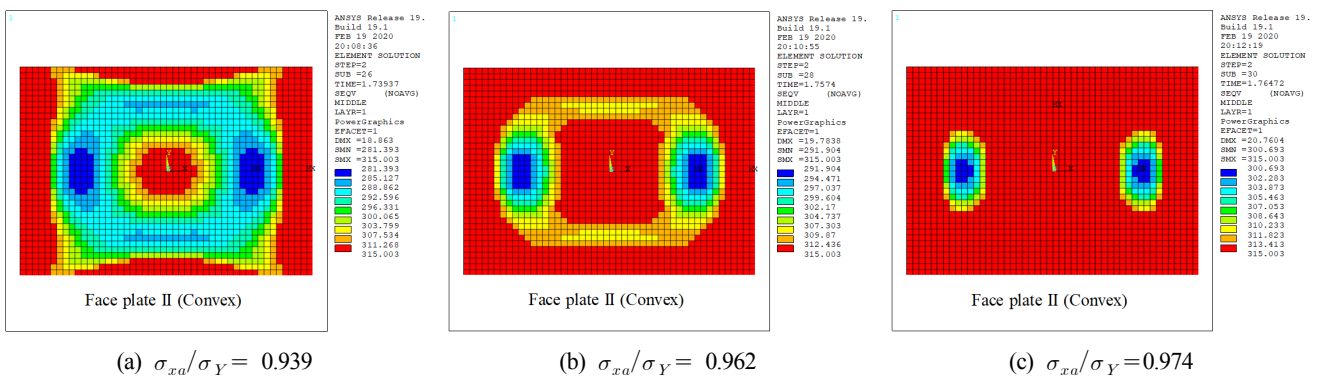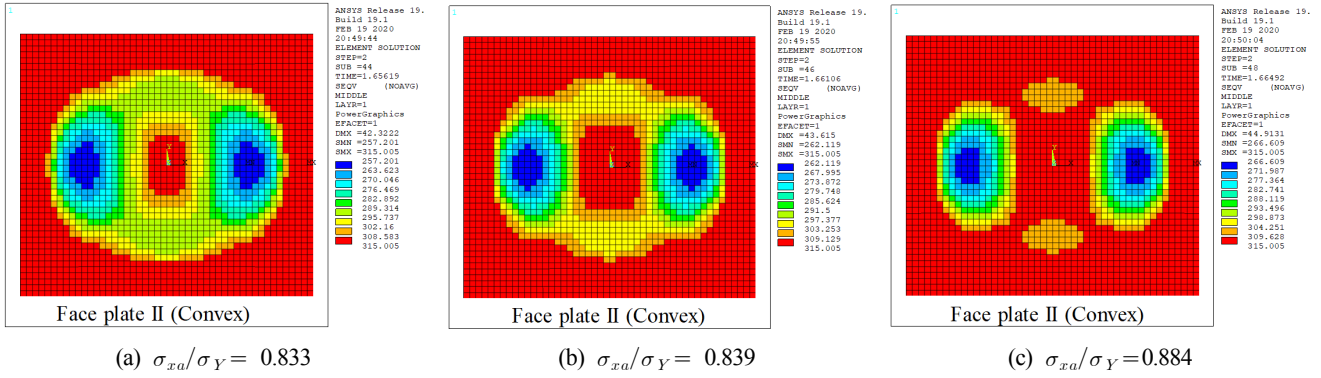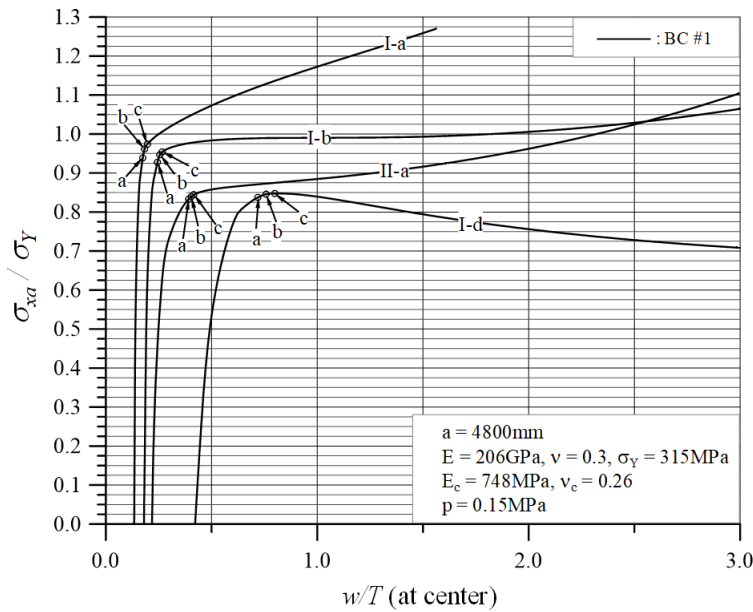

(a) $b = 3,420$ mm   (b) $b = 4,275$ mm
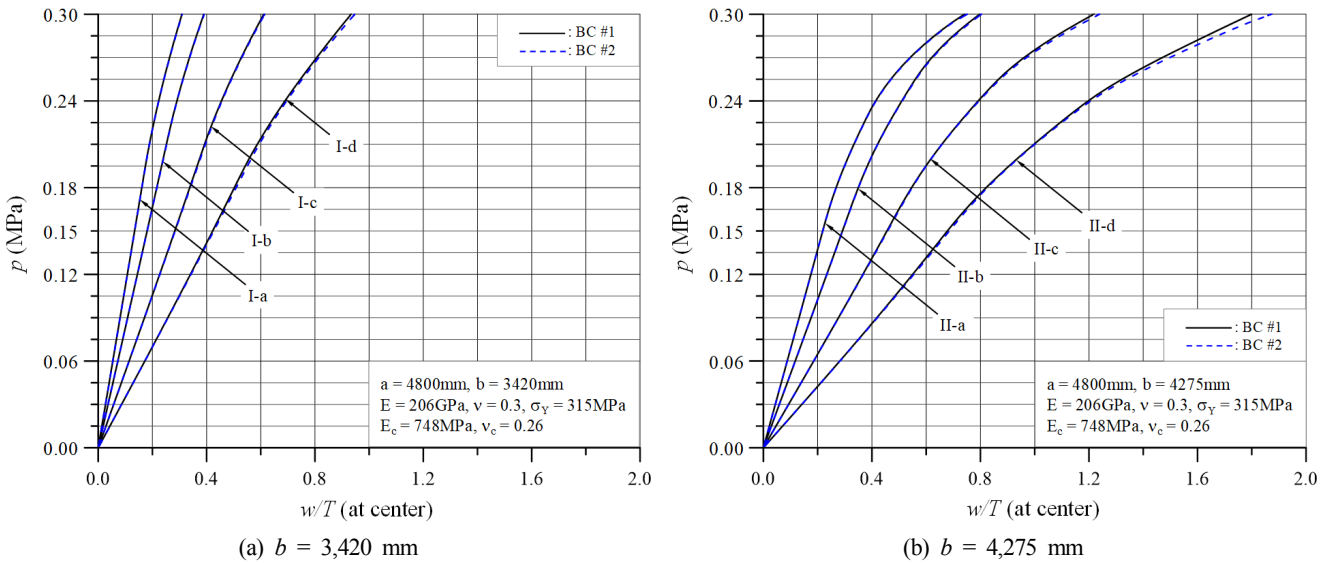
Fig. 14 Load-deflection curves of sandwich panels under only lateral pressure with clamped edges ($p = 0.3$ MPa)

I-d, II-a, and II-d are shown. Only the case of BC#1 is shown in Fig. 15, but a similar stress distribution was observed in BC#2 as well. Similar stress distributions were observed in panels I-b, I-c, II-b, and II-c, but there were fewer yielded areas, and yielding did not progress to the center of the face plate II in the case of panels I-b and I-c. The reason for this is that panels I-a and II-a have the largest bending rigidity, but they have the smallest thickness of the face plate, whereas panels I-d and II-d have large thickness face plates, but has the smallest bending rigidity, resulting in high stress. The panel with a breadth of 4,275 mm is considered to show a greater effect of the lateral pressure. This is

(a) Panel I-a

(b) Panel I-d

(c) Panel II-a

(d) Panel II-d
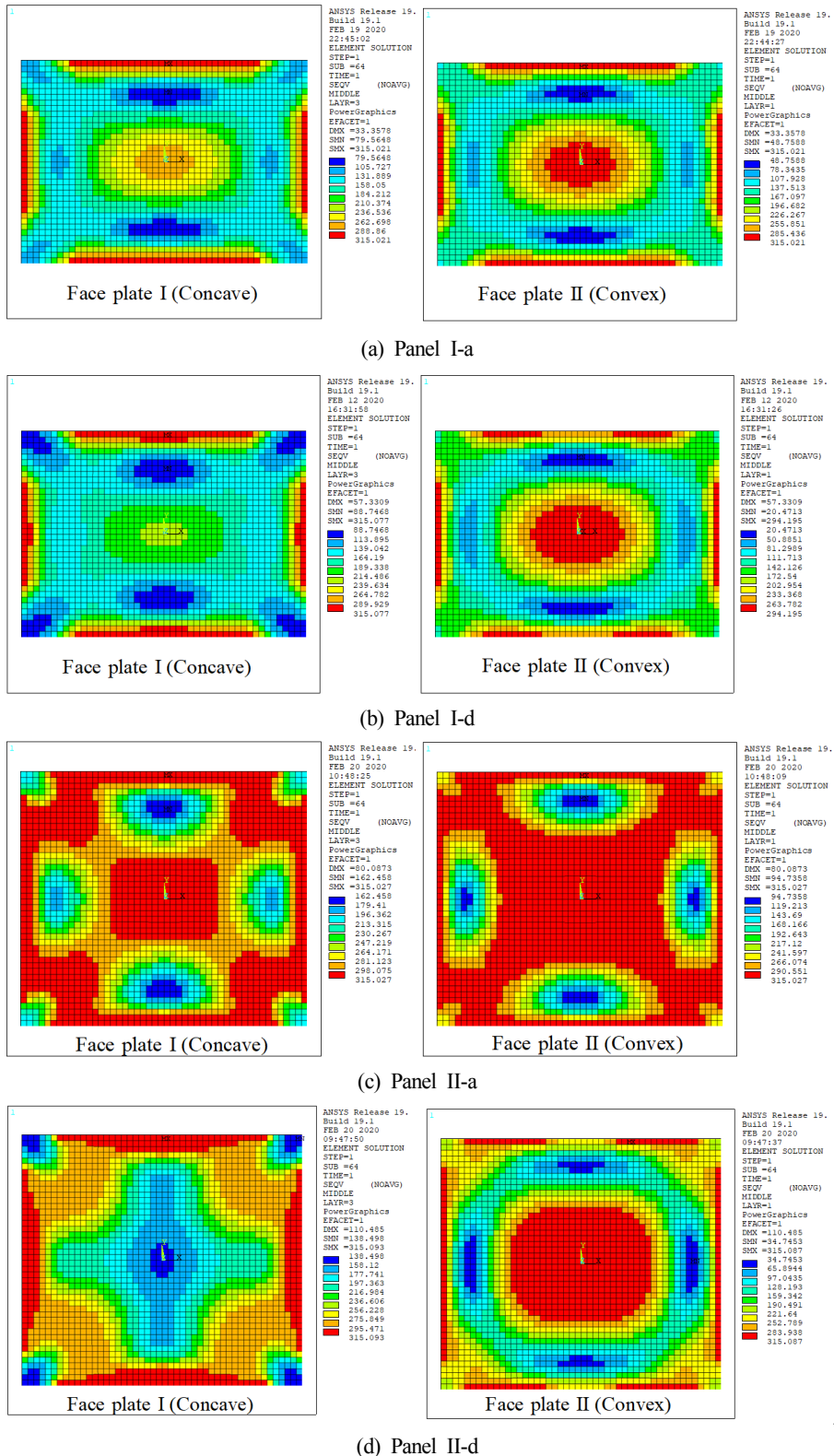
Fig. 15 The von Mises stress distribution of sandwich panels with clamped edges under lateral pressure (BC#1, $p = 0.3$ MPa)

thought to be the reason that the deflection of the panel increases sharply as shown in Fig. 14.

To define the ultimate strength of the panel under a lateral pressure of 0.3 MPa and an in-plane compression load, the progressive yielding patterns of face plates were investigated again. First, in the case of panel I-c, which is BC#2 in Fig. 8, strength degradation occurred when

the normalized deflection was less than 2. The yielding pattern of the face plate at the threshold was as shown in Fig. 16. The yielding pattern in Fig. 16 was as follows. With the increasing in-plane compression load, which has the same yielding pattern as the one in Figs. 10–12, yielding in face plate I occurred continuously along the y-axis from the center to the edges of the panel. Subsequently, the ultimate strength

Face plate I (Concave)   Face plate II (Convex)

(a) $\sigma_{xa}/\sigma_Y = 0.609$

Face plate I (Concave)   Face plate II (Convex)

(b) $\sigma_{xa}/\sigma_Y = 0.610$ (Ultimate strength)

Fig. 16 Progressive yielding of the face plates of sandwich panel I-c under in-plane edge compression and lateral pressure with clamped edges (BC#2, $p = 0.3$ MPa)
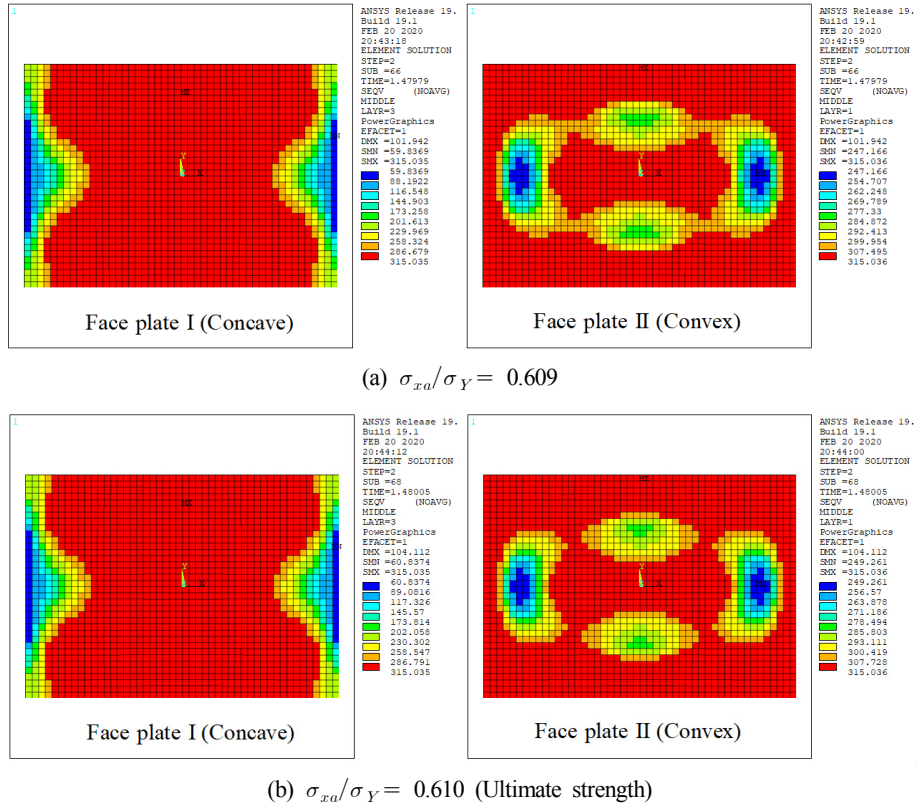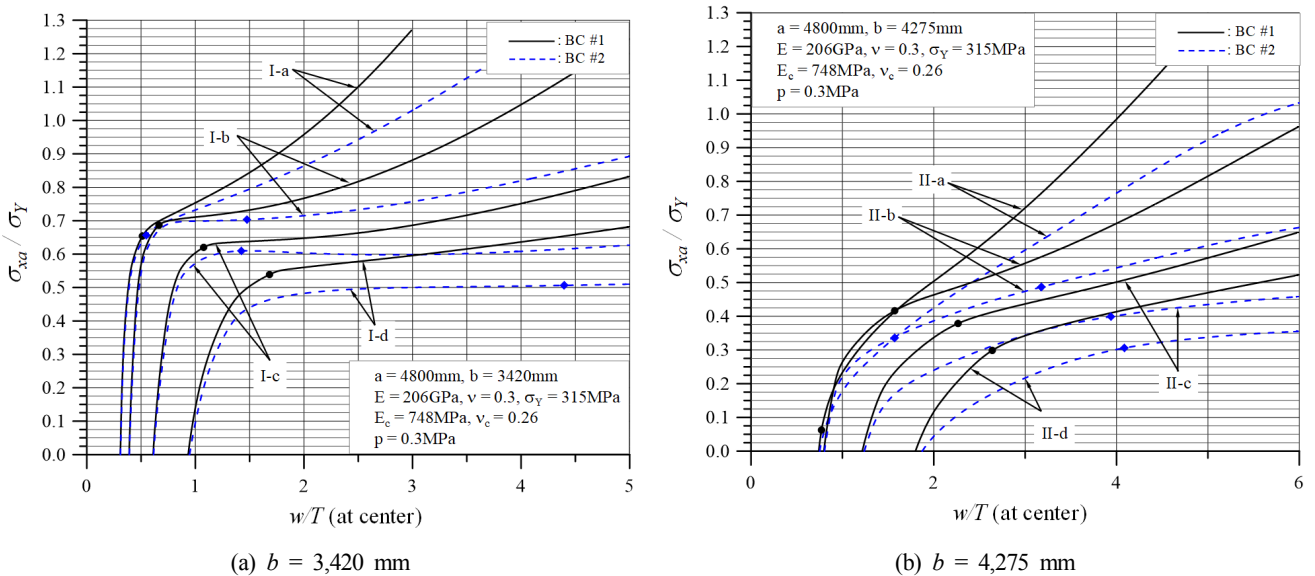

(a) $b = 3,420$ mm

(b) $b = 4,275$ mm

Fig. 17 Ultimate strength of sandwich panels under in-plane edge compression and lateral pressure with clamped edges defined by progressive yielding ($p = 0.3$ MPa)

was reached again as the yielding of the center and edges of the panel were interlinked in face plate II. Thus, the ultimate strength of each panel can be defined in the same way as shown in Fig. 17. As confirmed in Fig. 15, the ultimate strength was relatively lower in the case of panels I-a, I-d, II-a, and II-d in which yielding at the center of the panel progressed to some extent due to a lateral load, as shown in Fig. 15. The ultimate strength was particularly low for panel II-a due to the reason that yielding progressed considerably on both sides of the face plate due to the lateral load.

4. Applicability of the Ultimate Strength Design Formula

The ultimate strength (σ_{xu}) of sandwich panels calculated using the nonlinear FEA method was compared with the ultimate strength design formula derived in a previous study (Kim, 2019). Table 5 outlines the results of the ultimate strength design formula and the FEA results. Since the ultimate strength design formula corresponds to the boundary condition of BC#1, only the FEA results for BC#1 are shown in this table. In the case of panels II-a and II-d with widths of 4,275 mm each, yielding occurred widely at the center of the face plate due to lateral pressure, 0.0 was written for the ultimate strength design formula because the ultimate strength criterion was already met before the in-plane compression load was applied.

Fig. 18 shows the ultimate strength according to the thickness variations of the face plate of sandwich panels. The nonlinear FEA results matched relatively well with the results of the ultimate strength design formula. However, when the panel width was 4,275 mm and the lateral pressure was 0.3 MPa, the ultimate strength design formula underestimated the ultimate strength compared to the FEA. This indicates that when a large deflection behavior is governing, the ultimate strength design formula that was derived using the primary shear deformation plate theory and small deflection theory evaluates the ultimate strength very conservatively. When we review the above-mentioned FEA results, in the case of panels II-a and II-d, the lateral deflection of the panel increased sharply due to the lateral pressure, as shown in Fig. 14. Furthermore, as shown in Fig. 15, considerable yielding occurred at the edge and center of the panel, but the ultimate strength was reached by receiving an additional in-plane compression load. However, the ultimate strength design formula determines that the ultimate strength was reached only using lateral pressure. For this reason, when the panel width is 4,275 mm and the lateral pressure is 0.3 MPa, the result of the ultimate strength design formula is undervalued compared to the FEA result. In the case of panels II-b and II-c as well, the ultimate strengths predicted by the formula are approximately 51% and 36% of the FEA results, respectively. By the same token, the ultimate strength design formula also evaluates the ultimate strength conservatively for the panels that have large bending rigidity and small thickness face plates (I-a and II-a) and the panels that have a large thickness face plates and low bending rigidity (I-d and II-d). However, excluding the panel with a width of 4,275 mm and lateral pressure of 0.3 MPa, the formula predicts the ultimate strength at approximately 95.3% compared to the FEA result (standard deviation 6.5%). Therefore, the formula is considered to have excellent applicability.

Table 5 Ultimate strength of sandwich panels obtained by nolinera FEA and design formula

a (mm)	b (mm)	t_f (mm)	t_c (mm)	p (MPa)	σ_{xu}/σ_Y		Formula/FEA	Panel no.
					FEA (ANSYS)	Formula		
4,800	3,420	4.0	100.0	0.15	0.971	0.906	0.933	I-a
		5.5	79.6		0.952	0.919	0.965	I-b
		7.0	59.1		0.918	0.899	0.979	I-c
		8.0	45.4		0.848	0.846	0.998	I-d
		4.0	100.0	0.30	0.654	0.562	0.859	I-a
		5.5	79.6		0.687	0.645	0.939	I-b
		7.0	59.1		0.620	0.583	0.940	I-c
		8.0	45.4		0.539	0.438	0.813	I-d
	4,275	4.0	100.0	0.15	0.854	0.825	0.966	II-a
		5.5	79.6		0.825	0.839	1.017	II-b
		7.0	59.1		0.738	0.774	1.049	II-c
		8.0	45.4		0.648	0.636	0.981	II-d
		4.0	100.0	0.3	0.063	0.000	0.000	II-a
		5.5	79.6		0.416	0.213	0.512	II-b
		7.0	59.1		0.379	0.135	0.356	II-c
		8.0	45.4		0.299	0.000	0.000	II-d

Note: $E = 206$ GPa, $\nu = 0.3$, $\sigma_Y = 315$ MPa, $E_c = 748$ MPa, $\nu_c = 0.26$

(a) *b* = 3,420 mm   (b) *b* = 4,275 mm
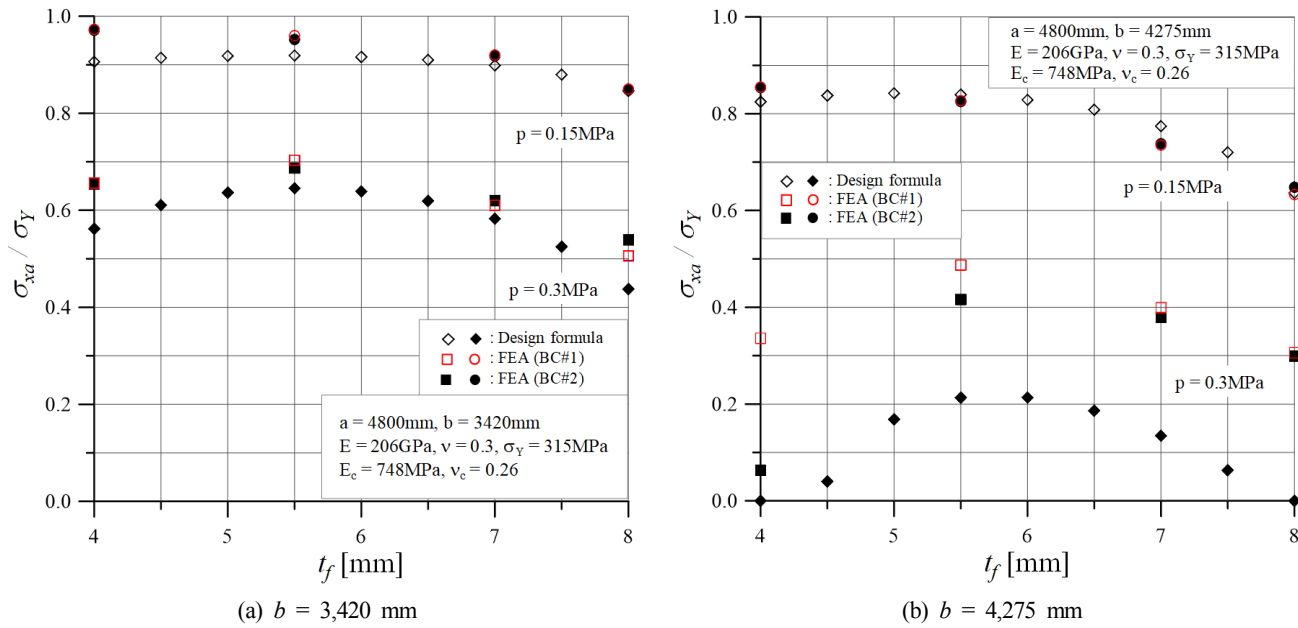
Fig. 18 The ultimate strength comparisons of the design formula with FEA results for sandwich panels under in-plane edge compression and lateral pressure with clamped edges

5. Conclusions

To improve the design technique for sandwich panel structures that are increasingly applied to ship and offshore installations, we selected sandwich panels that have the same weights as those of the existing stiffened plate structures for the inner bottom of a Suezmax-class tanker. Then the ultimate strength behavior characteristics were analyzed using nonlinear FEA and verified by comparing them with the results of the ultimate strength design formula. Hence, we obtained the following insights and conclusions.

(1) For sandwich panels under in-plane edge compression and lateral pressure with clamped edges, it was sometimes difficult to define the ultimate strength by using nonlinear FEA technique with four-node layered shell elements because the threshold and strength degradation were not clear.

(2) The threshold and strength degradation were not clear when the bending rigidity was large and the lateral deflection was small as well as when the lateral load and lateral deflection were large. In this case, the ultimate strength could be defined by analyzing the progressive yielding pattern of the face plate.

(3) (The analysis result of the progressive yielding pattern showed that the ultimate strength was reached when yielding occurred continuously along the y-axis from the center to the edges on the face plates of both sides due to lateral pressure and in-plane compression loads.

(4) When the boundary condition for the four edges of the sandwich panels was set to maintain a straight line (BC#1) and to allow free in-plane displacement (BC#2), the deflection behaviors and ultimate strength characteristics of the panels were almost the same if the lateral deflection was not large (approximately $w/T < 1.0$).

(5) The ultimate strength of sandwich panels with breadth of 3,420 mm and 4,275 mm as an alternative to stiffened plates of the inner bottom structure of Suezmax-class tanker with a transverse web frame spacing of 4,800 mm was obtained by nonlinear FEA technique and ultimate strength design formula, and then it was found that the ultimate strength was higher when the breadth of the sandwich panel was 3,420 mm ($a/b \approx 1.4$) than when it was 4,275 mm ($a/b \approx 1.1$).

(6) It was found it was necessary to select an appropriate face plate thickness and core thickness considering lateral pressure rather than maximizing the bending rigidity using a thick core and thin face plate.

(7) The ultimate strength design formula developed in a previous study evaluated the ultimate strength relatively conservatively, governed by a large deflection behavior. Additional research is required to verify the appropriate application scope in this regard.

(8) Detailed FEA procedures to evaluate the ultimate strength of the sandwich panels need to be developed which requires additional research.

(9) The sandwich panels with high lateral pressures and large deflections are likely to generate delamination of the core and face plate, and cause damage to the core; this requires additional research.

(10) The findings of this study are expected to be applicable to various studies required to design and build ships and offshore plant facilities by applying sandwich panels.

Acknowledgments

References

ANSYS. (1999). Theory Reference (Release 5.6). Canonsburg, PA: ANSYS Inc.

Brooking, M.A., & Kennedy, S.J. (2004). The Performance, Safety and Production Benefits of SPS Structures for Double Hull Tankers. International Coference on Design & Operation of Double Hull Tankers, Royal Institution of Naval Architects, London, UK.

DNV-GL. (2016). Steel Sandwich Panel Construction (DNVGL-CG-0154). Retrieved September 2019 from: https://rules.dnvgl.com/docs/pdf/DNVGL/CG/2016-04/DNVGL-CG-0154.pdf

Lloyd's Register (LR). (2019). Rules for the Application of Sandwich Panel Construction to Ship Structure. Boca Raton, FL.

Kim, B.J. (2019). Analytical Solution for the Ultimate Strength of Sandwich Panels under In-plane Compression and Lateral Pressure. Journal of Ocean Engineering and Technology, 33(6), 535-546. https://doi.org/10.26748/KSOE.2019.087

Kim, D.K., Park, D.H., Kim, H.B., Kim, B.J., Seo, J.K., & Paik, J.K. (2013). Lateral Pressure Effects on the Progressive Hull Collapse Behaviour of a Suezmax-class Tanker under Vertical Bending Moments. Ocean Engineering, 63, 112-121. https://doi.org/10.1016/j.oceaneng.2012.12.040

Kim, D.K., Kim, H.B., Zhang, X., Li, C.G., & Paik, J.K. (2014). Ultimate Strength Performance of Tankers associated with Industry Corrosion Addition Ppractices. International Journal of Naval Architecture and Ocean Engineering, 6(3), 507-528. https://doi.org/10.2478/IJNAOE-2013-0196

Kim, U.N., & Jang, J.T. (2017). A Study on the Strength Evaluation Method of Plate Structures with Penetration-holes. Journal of the Society of Naval Architects of Korea, 54(6), 476-484. https://doi.org/10.3744/SNAK.2017.54.6.476

Momcilovic, N., & Motok, M. (2009). Estimation of Ship Lightweight Reduction by Means of Application of Sandwich Plate System. FME Transactions, 37(3), 123-128. Retrieved February 2020 from https://www.mas.bg.ac.rs/_media/istrazivanje/fme/vol37/3/03_mmotok.pdf

Ramakrishna, K.V., & Sunil Kumar, P.G. (2016). Applications of Sandwich Plate System for Ship Structures. IOSR Journal of Mechanical and Civil Engineering, International Conference on Emerging Trends in Engineering & Management, 83-90. Retrieved February 2020 from http://www.iosrjournals.org/iosr-jmce/papers/ICETEM/Vol.%201%20Issue%204/60-83-90.pdf

SPS Technology. (2020). What is SPS. Retrieved February 2020 from https://www.spstechnology.com/what-is-sps

Author ORCIDs and Contributions

Author name	ORCID	Contributions
Kim, Bong Ju	0000-0002-8234-1030	①②③④⑤

① Conceived of the presented idea or developed the theory
② Carried out the experiment or collected the data
③ Performed the analytic calculations or numerical simulations
④ Wrote the manuscript
⑤ Supervised the findings of this study

Original Research Article

Dynamic Response of Drill Floor to Fire Subsequent to Blowout

Teak-Keon Kim[1], Seul-Kee Kim[2] and Jae-Myung Lee[3]

[1]*Senior Engineer, Department of Structure Basic Design, Samsung Heavy Industries, Geoje, Korea*
[2]*Research Professor, Hydrogen Ship Technology Center, Pusan National University, Busan, Korea*
[3]*Professor, Department of Naval Architecture and Ocean Engineering, Pusan National University, Busan, Korea*

ABSTRACT: *Explosions and fires on offshore drilling units and process plants, which cause loss of life and environmental damage, have been studied extensively. However, research on drilling units increased only after the 2010 Deepwater Horizon accident in the Gulf of Mexico. A major reason for explosions and fires on a drilling unit is blowout, which is caused by a failure to control the high temperatures and pressures upstream of the offshore underwater well. The area susceptible to explosion and fire due to blowout is the drill floor, which supports the main drilling system. Structural instability and collapse of the drill floor can threaten the structural integrity of the entire unit. This study simulates the behavior of fire subsequent to blowout and assesses the thermal load. A heat transfer structure analysis of the drill floor was carried out using the assessed thermal load, and the risk was noted. In order to maintain the structural integrity of the drill floor, passive fire protection of certain areas was recommended.*

1. Introduction

With oil prices rising and terrestrial development of oil & gas being constrained, offshore oil fields are being extensively explored and developed. Safety is extremely important in the development and operation of offshore oil fields, which are generally situated in remote marine locations. This is because the platforms are in direct contact with local environments, and accidents can result in loss of human life and ecological damage. This was seen in the aftermath of the Piper Alpha platform accident (Fiona and Stephen, 2018) and the Deepwater Horizon rig accident (Lazarus, 2016). There is an ever-present risk of fire and explosion due to oil & gas spills in offshore plants, and many studies have been conducted to protect people and the environment from these risks (Bai and Jin, 2016; Jin and Jang, 2015; Suardin et. al., 2009). However, there have been relatively few studies on fires and explosions caused by blowouts on drillships than on oil & gas refining and storage facilities such as floating production storage and off-loading (FPSO) (Dadashzadeh et al., 2013). A drillship fire caused by blowout is initiated by the ejection of a large amount of oil & gas from the oil well, implying that the size of the fire and heat flux is significantly greater than fires caused by other reasons (Skogdalen and Vinnem, 2012). For this reason, more in-depth research is needed. This study aims to address the fire subsequent to blowout, which refers to

the sudden ejection of oil & gas that may occur due to the failure of pressure and heat control in underwater wells during drilling operations. The drill floor is directly exposed to oil and gas spills and is most directly affected by blowout fires, because the main drilling rigs stand on it. With this in mind, the aim of this study is to consider the behavior characteristics of the drill floor due to fires when a blowout occurs in the drillship. First, the blowout and fire scenarios are described, and heat flux of the drill floor and the surrounding area due to fire are predicted through fire analysis, then the behavior of the drill floor structure are investigated. The problem of structural stability in the drill floor under fire subsequent to blowout was investigated, and as a result, we have proposed that passive fire protection (PFP) is required for structural stability of the drillship, and a PFP method befitting the drill floor structure was presented with reference to prior optimization studies considering the economic cost of PFP application.

2. Fire Analysis
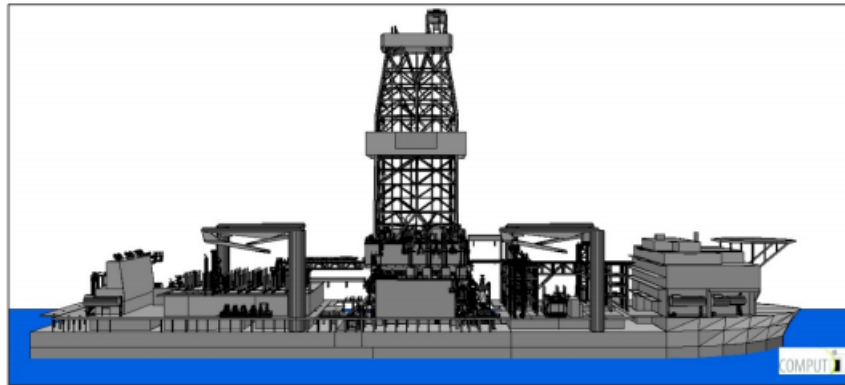
2.1 Analysis procedure

The Kameleon FireEx (KFX) fire analysis program solves partial differential equations of three-dimensional turbulent flows over time using finite volume techniques. The development and extinction process of fire over time are simulated in complex 3D spaces such as

(a) Overview 3D geometry model of the drillship from starboard
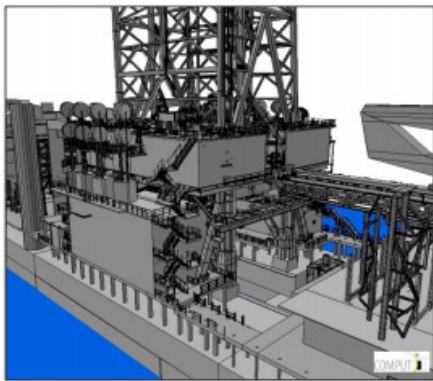
(b) 3D view on drill floor
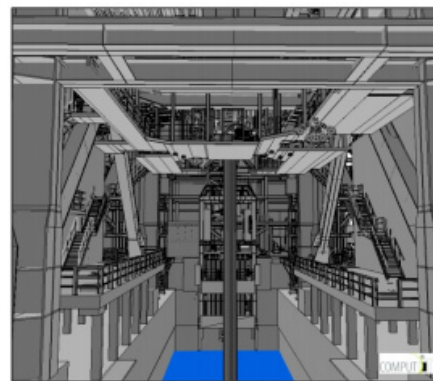
(c) 3D view under drill floor

Fig. 1 Fire analysis model in KFX

offshore structures or open space with consideration of the dispersion of flames and gas, and the results are illustrated (Vembe et al., 2014). For fire analysis following blowout, a blowout scenario is firstly established, and the entire drillship model including the drill floor is imported from the 3D CAD model using the KFX program. As shown in Fig. 1, it is converted to a 3D geometry model to be used in KFX, and in case of blowout, dispersion analysis of gas and fire subsequent to ignition is performed using CFD (Jin et al., 2016). From this, the heat flux distribution of the drill floor and the surrounding area is obtained for each fire scenario. The above procedure can be applied to fire analysis of offshore structures (Bai and Jin, 2016). The specifications of the drillship used for the analysis were 230 m in length, 42 m in width, and drill floor elevation 38 m.

2.2 Main assumptions

Blowout flow rates of 10–35 kg/s for normal blowout and 50–200 kg/s for high pressure high temperature (HPHT) blowout are generally presented (Health and Safety Executive, 2017). In a study on deepwater drilling (ABS Consulting, 2015), a restricted flow rate of 35 kg/s and a full flow rate of 150 kg/s were presented. In this study, 35 kg/s and 150 kg/s were adopted. The gas flow composition was 80% methane and 20% pentane, and the environmental conditions were based on Meta ocean data (Santos Basin, 2008) of the Santos waters in Brazil, where the drillship is in operation. The ambient temperature used was the annual mean of 23 °C, wind speed was the annual mean

5.4 m/s, and 9 m/s, which is the upper value of the annual 10%, representing a rougher environmental condition than may occur during drilling. The wind is in the direction of the bow and the stern, because the direction of the wind is equal to the direction of the wave. Accordingly, the wind direction and the bow-stern direction are matched to reduce the roll motion of the ship during drilling operations.

2.3 Fire scenarios

Fire analysis was performed using typical drilling scenarios. The results are shown in Table 1. As explained in 2.2 Main Assumptions, the annual mean values of a specific area of the sea from a previous

Table 1 Fire analysis scenario considering blowout flow rate

No.	Release location	Flow rate (kg/s)	Wind speed (m/s)	Wind direction
1		35	5.4	From forward
2	On drill floor	150	5.4	From forward
3		35	5.4	To forward
4		150	5.4	To forward
5		35	5.4	From forward
6	Under drill floor	35	5.4	To forward
7		35	9	From forward
8		150	5.4	From forward

study were used for the ambient temperature and wind speed, and the wind direction was selected in consideration of drilling operations. With the construction of the scenarios, the results of fires that may occur in a general drilling environment were obtained, and these were applied to the analysis of the drill floor structure to investigate the behavior, enabling the practical application of the results.
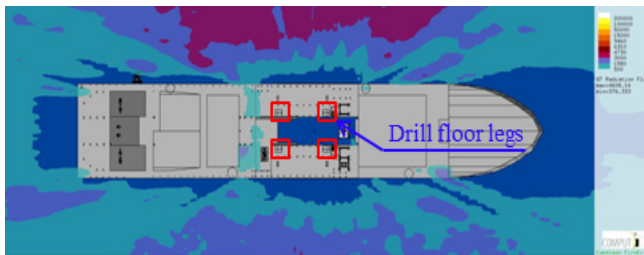
2.4 Analysis results

The results of fire analysis in various scenarios are presented in Figs. 2−9. White represents values over 200 kW/m^2 and bright yellow
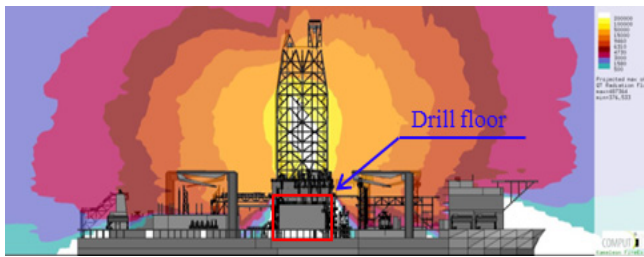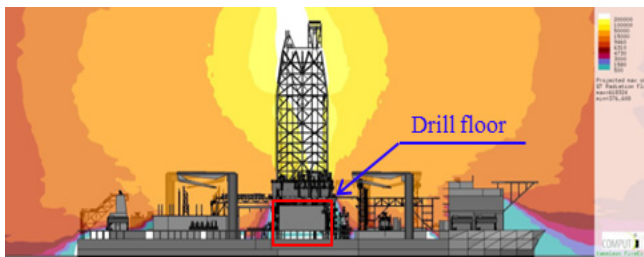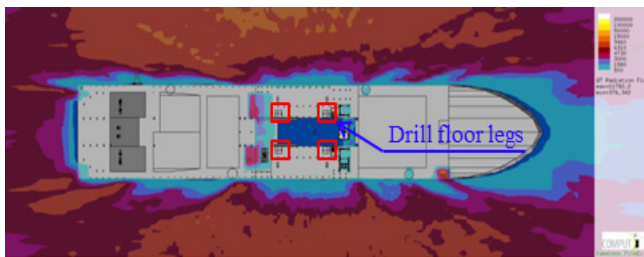

(a) Elevation view of heat radiation

(b) Plan view of heat radiation

Fig. 2 Fire analysis results : 35 kg/s release on the drill floor is ignited and 5.4 m/s wind blows from forward (scenario no.1)

(a) Elevation view of heat radiation

(b) Plan view of heat radiation

Fig. 3 Fire analysis results : 150 kg/s release on the drill floor is ignited and 5.4 m/s wind blows from forward (scenario no. 2)

(a) Elevation view of heat radiation

(b) Plan view of heat radiation

Fig. 4 Fire analysis results : 35 kg/s release on the drill floor is ignited and 5.4 m/s wind blows from aft (scenario no. 3)
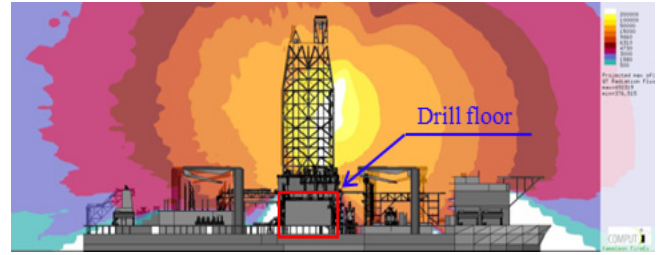

(a) Elevation view of heat radiation

(b) Plan view of heat radiation

Fig. 5 Fire analysis results : 150 kg/s release on the drill floor is ignited and 5.4 m/s wind blows from aft (scenario no. 4)

represents 100−200 kW/m^2. With a blowout flow rate of 35 kg/s, the heat flux around the drill floor is approximately 100 kW/m^2, and at 150 kg/s, it is 200 kW/m^2. In case of a drill floor fire, the heat flux values under the drill floor are small as shown in Figs. 2−5. When Fig. 6 and Fig. 8 of scenario No. 5 and 7 were compared, the cases of wind speed 5 m/s and 9 m/s do not show significant difference in terms of the values and range of heat flux. Therefore, in the on drill floor case, the wind speed 9 m/s was not added. Since similar results are expected in the under drill floor case, the values of scenario No. 8 were used for the heat transfer analysis and the subsequent structural behavior analysis.

(a) Elevation view of heat radiation

(b) Plan view of heat radiation

(c) Section view of heat radiation

Fig. 6 Fire analysis results : 35 kg/s release under the drill floor is ignited and 5.4 m/s wind blows from forward (scenario no. 5)
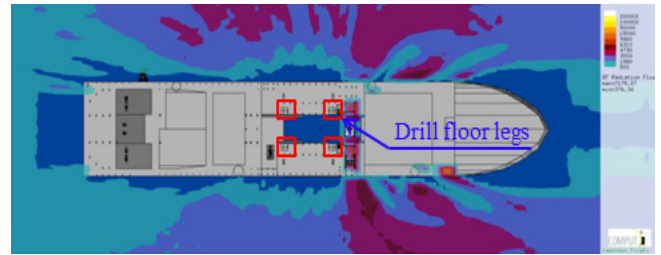

(a) Elevation view of heat radiation

(b) Plan view of heat radiation

(c) Section view of heat radiation

Fig. 7 Fire analysis results : 35 kg/s release under the drill floor is ignited and 5.4 m/s wind blows from aft (scenario no. 6)
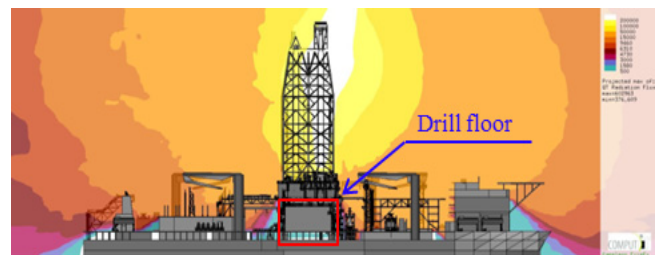

(a) Elevation view of heat radiation
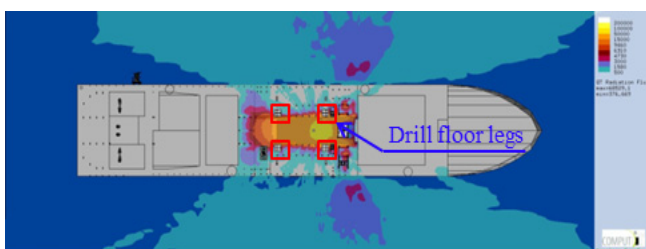
(b) Plan view of heat radiation
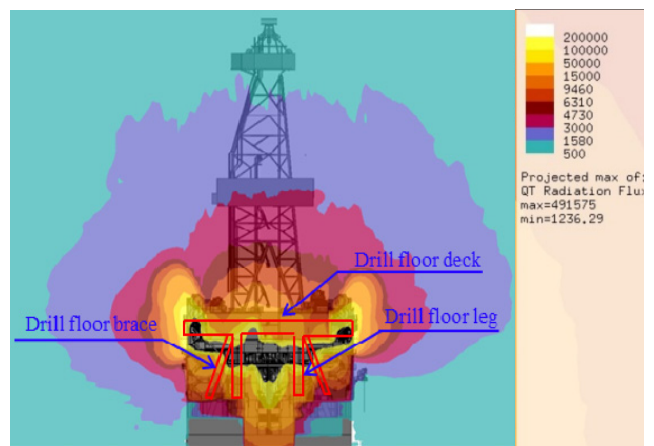
(c) Section view of heat radiation

Fig. 8 Fire analysis results : 35 kg/s release under the drill floor is ignited and 9 m/s wind blows from forward (scenario no. 7)
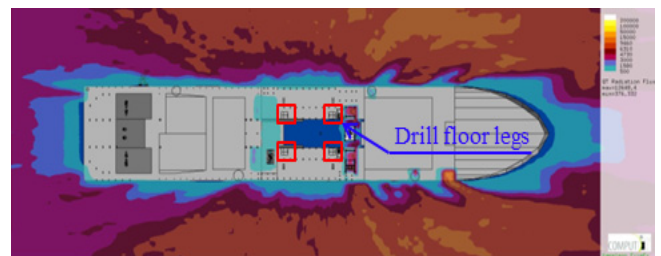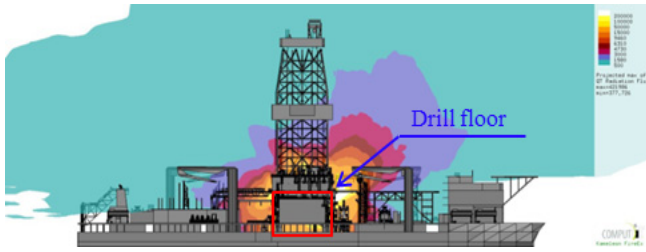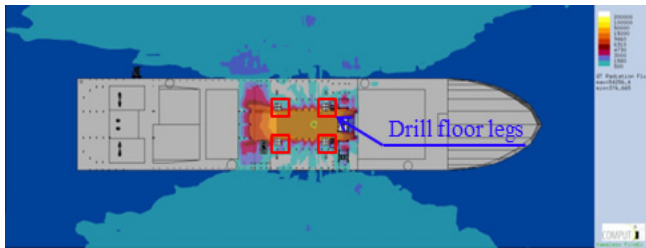
(a) Elevation view of heat radiation

(b) Plan view of heat radiation

(c) Section view of heat radiation
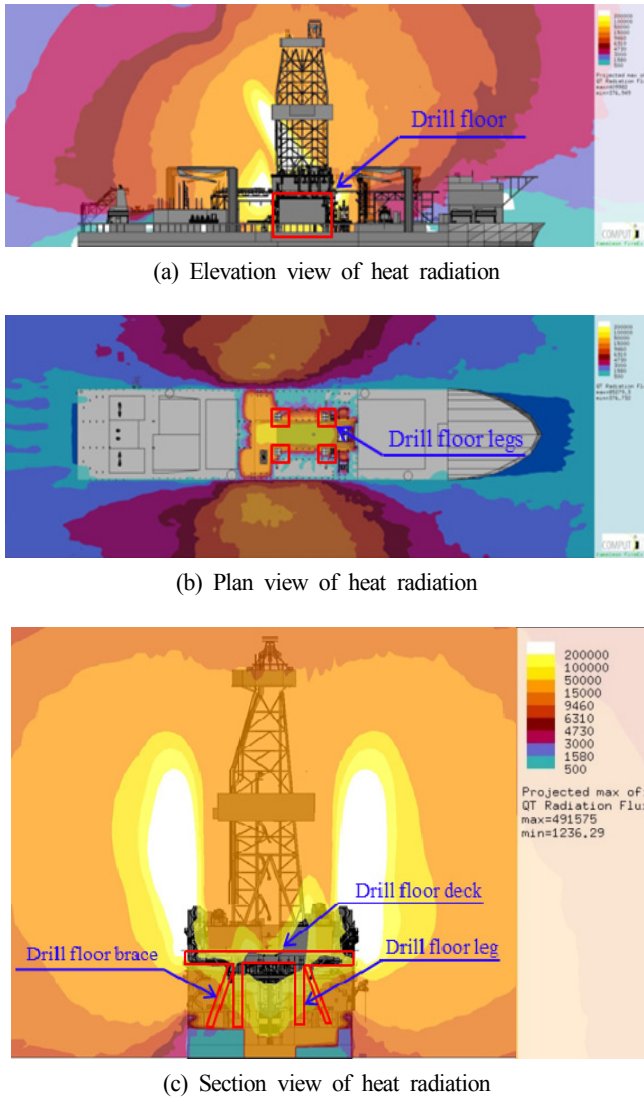
Fig. 9 Fire analysis results : 150 kg/s release under the drill floor is ignited and 5.4 m/s wind blows from forward (scenario no. 8)
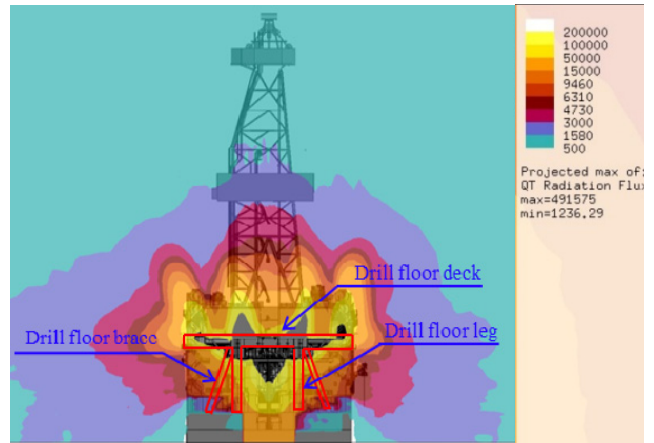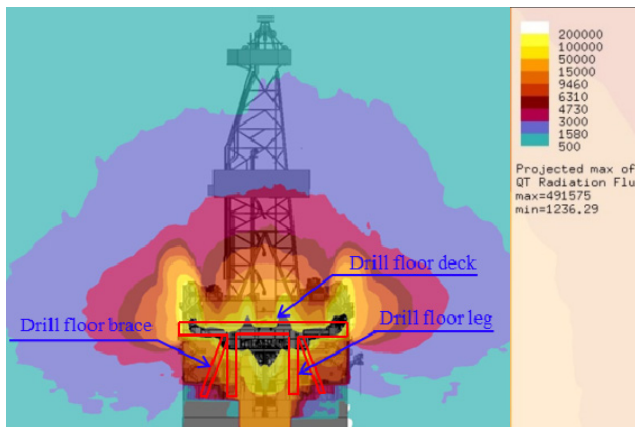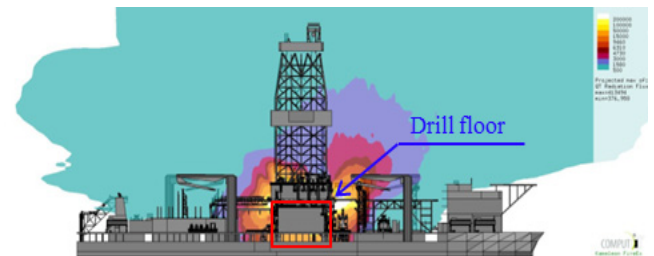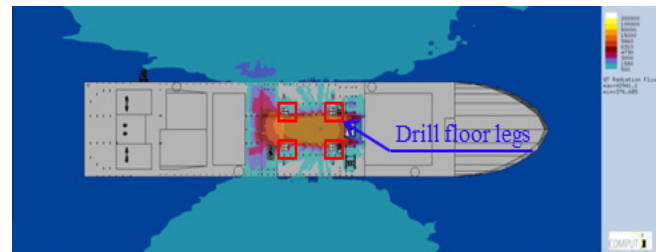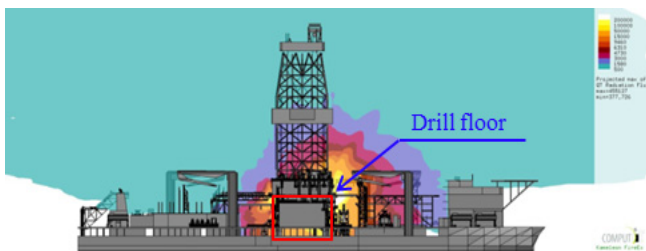
3. Heat Transfer Analysis

3.1 Analysis procedure

Using the heat flux result, the temperature around the drill floor is obtained using Eq. (1), and the FAHTS program (USFOS A/S, 2013a) is used to predict the temperature change over time of the drill floor structure. In Figs. 2–9, the heat flux on the drill floor area was estimated at 200 kW/m^2, and applied in the analysis.

$$Q = \varepsilon \cdot \sigma (T_g^4 - T_s^4) \tag{1}$$

Where, Q is the radiative heat flux, ε is the emissivity, σ is Stefan-Boltzmann constant, T_g is gas temperature, and T_s is the surface temperature of the structure.

3.2 Thermal properties of the model

The nominal thermal properties are given in Table 2 (API, 2006)

Table 2 Thermal property of carbon steel

Steel type	Specific heat capacity (J/kg K)	Thermal conductivity (W/m K)	Surface emissivity
ASTM A36	520	50	0.8
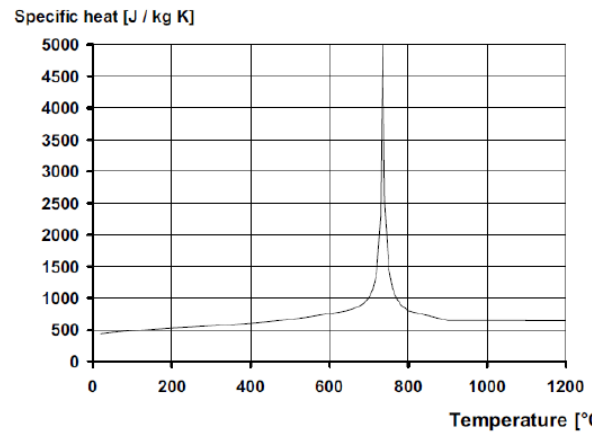
Fig. 10 Specific heat of carbon steel as a function of temperature, Eurocode 3 (BSI, 2005)
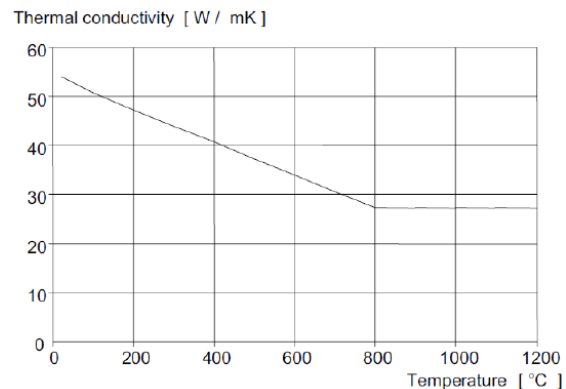
Fig. 11 Thermal conductivity of carbon steel as a function of temperature, Eurocode 3 (BSI, 2005)

The thermal properties of steel vary with temperature. Figs. 10 and 11 show the specific heat and conductivity of carbon steel as a function of temperature, as presented in Eurocode 3 (BSI, 2005). These values were used in this study to reflect the temperature-specific characteristics of the steel.

3.3 Analysis results

The fire of the drill floor by blowout was simulated for 1,800 s and the results presented. Figs. 12 and 13 are the temperature distribution results of the drill floor structure after 900 and 1,800 s, respectively. Fig. 14 shows the temperature distribution over time at each point of the drill floor structure.

As shown in Fig. 14, the thinner the drill floor structure, the faster the temperature rises. The reason that the temperature rise is slower in the brace than in the beam structure member is that the brace is in a box structure and there is no heat transfer on one side.
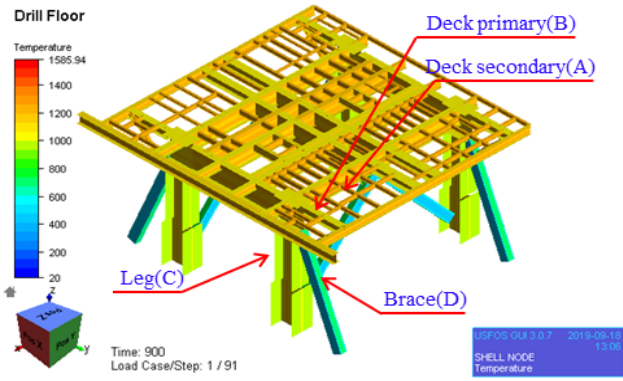
Fig. 12 Temperature (℃) distribution of drill floor during fire (900 s)

Fig. 13 Temperature (℃) distribution of drill floor during fire (1,800 s)

Fig. 14 Temperature curve of various locations on drill floor

4. Nonlinear structural response analysis

4.1 Analysis procedure

Structural response analysis following blowout comprises performing thermal stress analysis of the heat flux distribution using the USFOS program (USFOS A/S, 2013b) based on the temperature distribution over time of the drill floor by Eq. (1). At this time, a reduction factor is applied for the yield stress and elastic modulus of the carbon steel with the temperature elevation. The critical strain at

Table 3 Reduction factor for stress-strain relationship of carbon steel at elevated temperatures

Steel Temperature θ_a	Reduction factors at temperature θ_a relative to value of f_y or E_a at 20 ℃		
	Reduction factor (relative to f_y) for effective yield strength $k_{y,\theta} = f_{y,\theta}/f_y$	Reduction factor (relative to f_y) for proportional limit $k_{p,\theta} = f_{p,\theta}/f_y$	Reduction factor (relative to E_a) for the slope of the linear elastic range $k_{E,\theta} = E_{a,\theta}/E_a$
20 ℃	1.000	1.000	1.000
100 ℃	1.000	1.000	1.000
200 ℃	1.000	0.807	0.900
300 ℃	1.000	0.613	0.800
400 ℃	1.000	0.420	0.700
500 ℃	0.780	0.360	0.600
600 ℃	0.470	0.180	0.310
700 ℃	0.230	0.075	0.130
800 ℃	0.100	0.050	0.090
900 ℃	0.060	0.0375	0.0675
1000 ℃	0.040	0.0250	0.0450
1100 ℃	0.020	0.0125	0.0225
1200 ℃	0.000	0.0000	0.0000

Note: For intermediate values of steel temperature, linear interpolation may be used.

f_y: the yield strength at 20 ℃

E_a: the modulus of elasticity of steel for normal temperature design

$k_{y,\theta}$: effective yield strength, relative to yield strength at 20 ℃

$k_{p,\theta}$: proportional limit, relative to yield strength at 20 ℃

$k_{E,\theta}$: slope of linear elastic range, relative to slope at 20 ℃

$f_{y,\theta}$: the effective yield strength of steel

$f_{p,\theta}$: the proportional limit of strength of steel

$E_{a,\theta}$: the modulus of elasticity of steel for the slope of the linear elastic range

which the design limit occurs is determined, and the change in the strain is examined over time.

4.2 Model Properties

The yield stress and elastic modulus of the carbon steel reduce as temperature changes, and the reduction factors presented by Eurocode 3 are shown in Table 3 and Fig. 15. These values were applied to the analysis in this study.
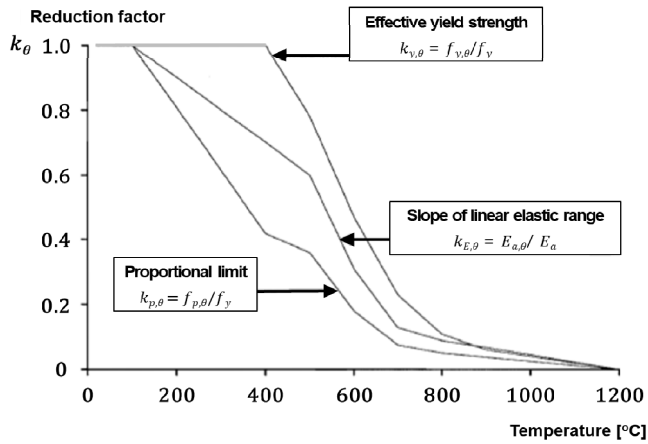
Fig. 15 Reduction factor for stress-strain relationship of carbon steel at elevated temperatures, Eurocode 3 (BSI, 2005)

4.3 Design Criteria

In the structural analysis, the critical strain of carbon steel at which fracture develops is in accordance with DNV-RP-C208 (DNV, 2013), and is shown in Table 4. Since most recent drillships use high tensile carbon steel, S355 was used as the standard.

Table 4 Critical local maximum principal plastic strain for uniaxial stress states

Steel grade	S235	S355	S460
Critical local yield strain	0.15	0.12	0.09

4.4 Structural analysis results

Following heat transfer analysis of the drill floor structure over time,
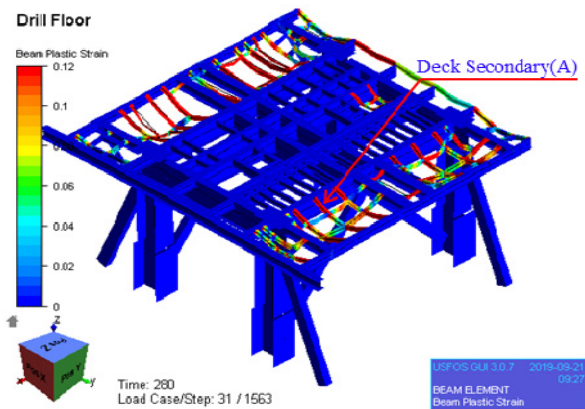
Fig. 16 Strain of drill floor 280 s after ignition
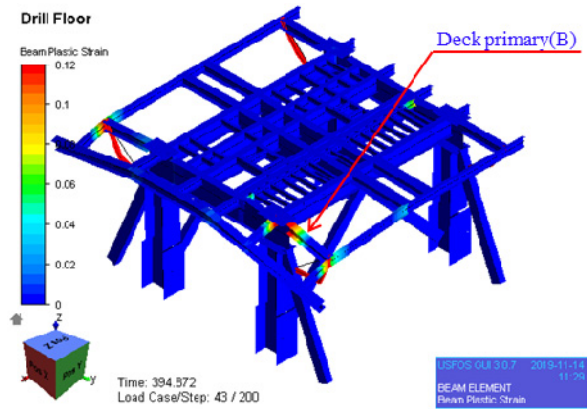
Fig. 17 Strain of drill floor 395 s after ignition
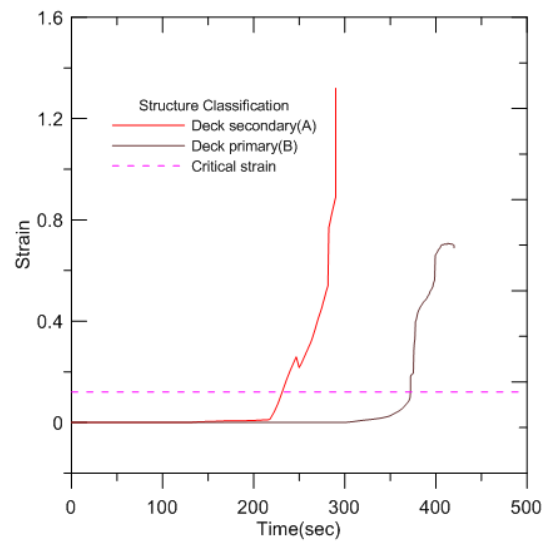
Fig. 18 Strain of deck secondary and primary of drill floor

the strain representing the structural integrity is shown in Figs. 16–18. Secondary beams supporting the path taken by the crew or small equipment reach critical strain before 300 s (5 min) elapse, and deck primary members supporting the main equipment and drill floor structure reach critical strain soon after secondary members. As in the Deepwater Horizon accident, the drill floor collapses shortly after the fire subsequent to the blowout.

5. Application of passive fire protection

The result of the structural analysis of heat transfer during blowout of the drill floor shows that the drill floor was exposed to structural risk for a short duration, which is a threat to the structural integrity of the drillship. Therefore, measures to maintain the structure against fire are required. Epoxy-based paint applied to the surface of the structure is a general measure of passive fire protection (PFP), and research on the effect of the application has been conducted (Ahmad, et al., 2013; Friebe et al., 2014; Kim et al., 2013). However, since PFP application should take time and cost efficiency into account, this study examined the structural stability and efficiency from the PFP application.

5.1 Analysis procedure

In the heat transfer analysis, the structural members that PFP is applied to, exhibited PFP characteristics. In the Amdahl model, the effective heat transfer coefficient is presented at below 5 W/m^{2}K (Amdahl et al., 2003), and 3 W/m^{2}K was used in this study. Since PFP cannot be applied to the upper part of the drill floor deck, as it is a work space, PFP characteristics are applied to the side and lower parts of the member.

5.2 Result of structural analysis

To satisfy the structural stability of the drill floor and reduce the cost of the PFP application, the results of the structural analysis with minimal PFP application are shown.

5.2.1 Application of PFP on Deck

The results of the heat transfer analysis of the deck area are shown in Figs. 19–21. The temperature of the upper deck, leg, and brace without PFP application increased to 800 °C over 30 min. As seen in the structural thermal stress analysis, critical strain was reached in the leg and the brace after 20 min. From the results, it can be seen that it is necessary to apply PFP not only to the deck but also to the legs and braces for the structural stability of the drill floor.
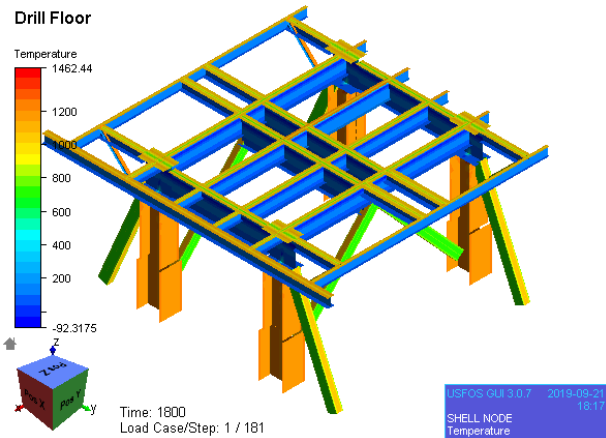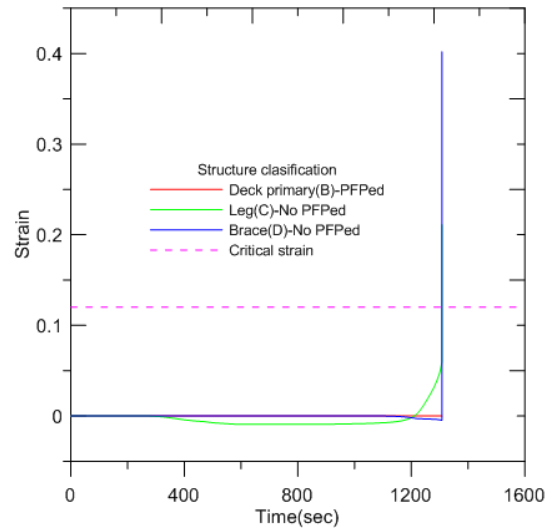
Fig. 21 Strain of PFP of deck after ignition

5.2.2 Application of PFP on Deck, Leg, and Brace

Heat transfer analysis of PFP applied to the deck, legs, and braces show that the temperature is maintained below 400 °C except for the upper part of deck, as shown in Figs. 22–24. Structural thermal stress analysis results show structurally stable strain values after 30 min.

Fig. 19 Temperature (℃) of PFP of deck
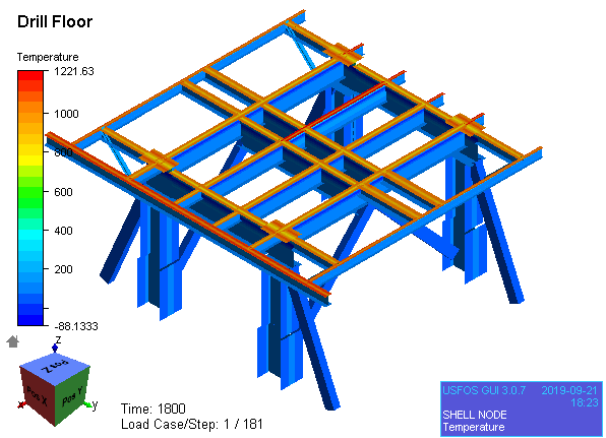
Fig. 22 Temperature (℃) of PFP of deck, leg and brace
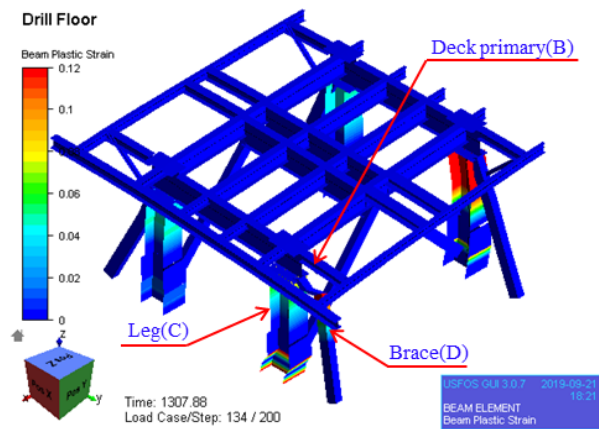
Fig. 20 Strain of PFP of deck 1307 seconds after ignition
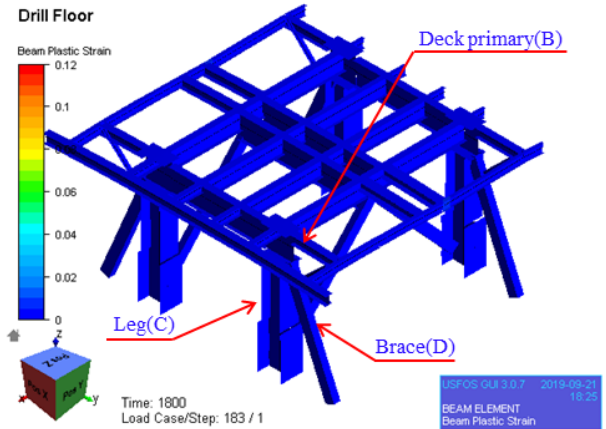
Fig. 23 Strain of PFP of deck, leg and brace
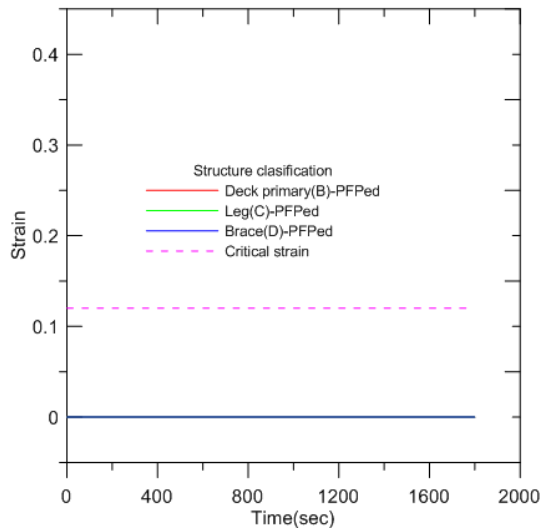
Fig. 24 Strain of PFP of deck, leg and brace after ignition

6. Conclusion

This study describes the temperature distribution and behavior of the drill floor structure due to heat transfer from a fire subsequent to general blowout in a drillship. An appropriate PFP application area was proposed to achieve structural stability.

(1) The behavior of the drill floor structure in a fire following blowout during drillship operations was estimated by calculating the heat flux through fire analysis. Heat transfer analysis, and structural analysis as a function of temperature, were performed.

(2) Fire analysis was performed based on blowout scenarios of two types of leakage⎯restricted leakage (35 kg/s) and full leakage (150 kg/s). Based on the larger heat flux of the results, heat transfer analysis and structural analysis as a function of temperature were performed.

(3) In general, fire protection is not provided on the drill floor of the drillship. However, in the event of fire, the area is vulnerable to collapse and is a risk factor for the structural stability of the drillship. Therefore, in this study, we propose the application of PFP so that the drill floor structure does not collapse for the 30-minute fire duration, which is required for safe evacuation of crew.

(4) This study found that application of PFP on the primary deck, leg, and brace is the optimum method ensuring both structural stability and economic efficiency.

Acknowledgements

References

ABS Consulting. (2015). Case Study 2: Deepwater Drilling with Surface BOP from a Floating Facility. The Bureau of Safety and Environmental Enforcement (BSEE). Retrieved from https://www.bsee.gov/sites/bsee.gov/files/752ac.pdf

Ahmad, A., Hassan, S.A., Ripin, A., Ali, M.W., & Haron, S. (2013). A Risk-based Method for Determining Passive Fire Protection Adequacy. Fire Safety Journal, 58, 160-169. https://doi.org/10.1016/j.firesaf.2013.01.020

Amdahl, J., Holmås, T., & Skallerud, B. (2003). Ultimate Strength of Structural Members with Attachments during Accidental Fires. Proceedings of International Conference of Response of Structures to Extreme Loading, Tronto, Canada.

American Petroleum Institute (API). (2006). Recommended Practice for the Design of Offshore Facilities Against Fire and Blast Loading. API Publishing Services, Washington.

Bai, Y., & Jin, W.L. (2016). Marine Structural Design (2nd ed). Elsevier Butterworth Heinemann, UK.

British Standards Institution (BSI). (2005). EN 1993-1-2: Eurocode 3: Design of Steel Structures, Part 1-2: General Rules⎯Structural Fire Design. London: British Standards Institution,.

Dadashzadeh, M., Abbassi, R., Khan, F., & Hawboldt, K. (2013). Explosion Modeling and Analysis of BP Deepwater Horizon accident. Safety Science, 57, 150-160. https://doi.org/10.1016/j.ssci.2013.01.024

Det Norske Veritas (DNV). (2013). Determination of Structural Capacity by Non-linear FE Analysis Methods (DNV-RP-C208). Det Norske Veritas.

Fiona M., & Stephen R. (2018). Piper Alpha - What Have We Learned?. Loss Prevention Bulletin, 261, 3-9. Retrieved from https://www.icheme.org/media/1982/lpb261_pg03.pdf

Friebe, M., Jang, B.-S., & Jim, Y. (2014). A Parametric Study on the Use of Passive Fire Protection in FPSO Topside Module. International Journal of Naval Architecture and Ocean Engineering, 6(4), 826-839. https://doi.org/10.2478/ijnaoe-2013-0216

Health and Safety Executive. (2017). The Deepwater Horizon Incident: Fire and Explosion Issues. Retrieved from https://www.hse.gov.uk/research/rrhtm/rr1122.htm

Jin, Y., & Jang, B.S. (2015). Probabilistic Fire Risk Analysis and Structural Safety Assessment of FPSO Topside Module. Ocean Engineering, 104, 725-737. https://doi.org/10.1016/j.oceaneng.2015.04.019

Jin, Y., Jang, B.-S., & Kim, J. (2016). Fire Risk Analysis Procedure Based on Temperature Approximation for Determination of Failed Area of Offshore Structure: Living Quarters on Semi-drilling Rig. Ocean Engineering, 126, 29-46. https://doi.org/10.1016/j.oceaneng.2016.07.010

Kim, J.H., Kim, D.C., Kim, C.K., Islam, M.S., Park, S.I., & Paik, J.K. (2013). A Study on Methods for Fire Load Application with Passive Fire Protection Effects. Ocean Engineering, 70, 177-187. https://doi.org/10.1016/j.oceaneng.2013.05.017

Lazarus, N.W. (2016). A County-Level Risk Assessment of the Deep Water Horizon Oil Spill in the Gulf of Mexico. Geographical Review, 106(3), 360-380. https://doi.org/10.1111/j.1931-0846. 2016.12178.x

Santosa Basin BM-S Cluster Region, 2008. MetOcean Data. Petrobras.

Skogdalen, J.E., & Vinnem, J.E. (2012). Quantitative Tisk Snalysis of Oil and Gas Drilling, using Deepwater Horizon as Case Study. Reliability Engineering & System Safety, 100, 58-66. https://doi.org/10.1016/j.ress.2011.12.002

Suardin, J.A., McPhate, A.J., Sipkema, A., Childs, M., & Mannan, M.S. (2009). Fire and Explosion Assessment on Oil and Ggas Floating Production Storage Offloading (FPSO): An Effective Screening and Comparison Tool. Process Safety and Environmental Protection, 87(3), 147-160. https://doi.org/10.1016/j.psep.2008. 12.002

USFOS A/S. (2013a). User's Manual for FAHTS (Version 637). USFOS A/S, Sandsli.

USFOS A/S. (2013b). User's Manual for USFOS (Version 86a). USFOS A/S, Sandsli.

Vembe, B.E., Kleiveland, R.N., Grimsmo, B., Lilleheie, N.I., Rian, K.E., Olsen, R., ···, Evanger, T. (2014). User's Manual for Kameleon FireEx. Tronheim, Norway: Computational Industry Technologies AS.

Author ORCIDs and Contributions

Author name	ORCID	Contributions
Kim, Teak-Keon	0000-0002-1877-4667	①③
Kim, Seul-Kee	0000-0002-1293-675X	④
Lee, Jae-Myung	0000-0001-8655-2591	⑤

① Conceived of the presented idea or developed the theory
② Carried out the experiment or collected the data
③ Performed the analytic calculations or numerical simulations
④ Wrote the manuscript
⑤ Supervised the findings of this study

Fatigue Assessment of Very Large Container Ships Considering Springing Effect Based on Stochastic Approach

Byoung-Hoon Jung[1], In-Gyu Ahn[2], Sun-Kee Seo[3] and Beom-Il Kim[4]

[1]Senior Researcher, Maritime Research Institute, Hyundai Heavy Industry, Ulsan, Korea
[2]Deputy Senior Researcher, Maritime Research Institute, Hyundai Heavy Industry, Ulsan, Korea
[3]Senior Researcher, Hull Rule Development Team, Korean Register of Shipping, Busan, Korea
[4]Senior Researcher, Ship and Offshore Technology Center, Korean Register of Shipping, Busan, Korea

ABSTRACT: Evaluation of fatigue strength considering the springing effect of very large container ships is crucial in the design stage. In this study, we established a fatigue strength evaluation method considering a linear springing component in the frequency domain. Based on a three-dimensional global model, a fluid–structure interaction analysis was performed and the modal superposition method was applied to determine the hot spot stress at the hatch corner of very large container ships. Fatigue damage was directly estimated using the stress transfer function with a linear springing response. Furthermore, we proposed a new methodology to apply the springing effect to fatigue damage using hull girder loads. Subsequently, we estimated the fatigue damage contribution due to linear springing components along the ship length. Finally, we discussed the practical application of the proposed methods.

1. Introduction

Hull hydroelastic response, which is represented by springing, has been reported to first occur in low-speed blunt ships constructed with larger hulls, such as ore carriers. Furthermore, owing to the wide openings of high-speed slender ships such as container ships, torsional natural frequency is generated in the low-frequency domain; furthermore, a recent increase in the size and speed of ships causes the natural vibration period of the hull and the wavelength of an incident wave to overlap, thereby increasing the likelihood of resonance between the ship and wave.

Hydroelastic responses, such as springing, which are referred to as vibration-induced waves, have been predicted to cause fatigue failure by increasing the cumulative fatigue damage in structurally discontinuous areas. As such, unexpected fatigue failure may occur if the structural vibration response is not considered in the design stage of very large container ships, which have been constructed recently. Ship owners are demonstrating a steady, increasing demand for the prediction of fatigue damage due to springing response when ordering large ships. However, an efficient numerical methodology applicable to the design stage is still being developed. Research on the springing

phenomenon in ships primarily began with numerical approaches. Applying the beam theory of Euler and Timoshenko, Bishop et al. (1985) conducted a dynamic calculation of a cross-section beam and demonstrated that the beam theory produced better results than experimental results. Kim et al. (2009) developed a response analysis method that directly connected a three-dimensional (3D) Rankine panel method with the Vlasov beam model, which considered warping deformation, analyzed the linear and nonlinear responses, and proposed a new method for numerical problems.

In addition to numerical attempts to solve the hydroelasticity problems as described above, studies using the model test and real ship measurement are continuously being conducted. Storhaug et al. (2011) calculated the ultimate load and fatigue damage due to the hydroelastic response of large container ships through model tests. Kim et al. (2018a) and Kim et al. (2018b) analyzed the strain data based on actual ship data measured in a very large container ship, analyzed the vibration mode generated in the ship, and predicted the long-term fatigue damage.

Moreover, Kim et al. (2018c) evaluated the ultimate load considering an increasing vertical bending moment due to slamming–whipping at the center of large container ships. Kim and Song (2019)

conducted a study on structural strength using the vertical bending moment in large ore carriers to estimate long-term fatigue damage, while considering nonlinear hydroelastic responses.

This study seeks to establish an efficient methodology based on a statistical fatigue analysis method for springing responses caused by wave loading on a representative weak member of a large container ship. Hence, spectral fatigue analysis based on linear statistical analysis was applied, which is the most widely used technique for evaluating fatigue strength. The stress transfer function including the springing response must be calculated to obtain the fatigue damage by applying a wideband fatigue model. In this context, the stress transfer function considers only the linear component of the unit wave height. To consider the geometric nonlinearity and nonlinearity in a rough sea state with high waves, the nonlinear springing response in each sea state in the time domain must be directly obtained. Although this technique results in a response that is similar to the actual phenomenon, it poses severe time limitations when used in the design stage. Therefore, the spectral fatigue analysis method, which can estimate fatigue damage relatively quickly and accurately, is primarily used in the design stage. In addition, to obtain the springing response, an effective method is presented herein for combining the existing rigid body-based results when estimating fatigue damage in a flexible body-based structural model rather than a rigid-based structural model, which is regarded as the final fatigue design life in ship design evaluations. Finally, the method proposed for 15,000TEU-class very large container ships is applied in this study to analyze its effect on design evaluation.

2. Fatigue analysis procedure

Currently, one of the most extensively used methods in classification and shipyards is a statistical fatigue analysis technique based on the dynamic loading approach, known as spectral fatigue analysis. In this method, fatigue damage is predicted based on an irregular wave sea state, and the cumulative fatigue damage is estimated by applying a probability statistical function to the stress range of a structural member generated by wave loading. As the fatigue damage is subject to the stress range and number of cycles, the statistical fatigue analysis method mentioned above for classification and shipyards utilizes a stress range that follows a narrowband-based Rayleigh distribution calculated by assuming a rigid-body ship (Choung et al. 2013). In the existing fatigue analysis guidelines and hull motion analysis for ship classification, hull motion analysis is conducted based on a rigid body to analyze the fatigue of offshore structures caused by ocean waves. A fatigue analysis program has been developed assuming that the stress range is a Rayleigh distribution. This fatigue analysis methodology calculated from a stress response that assumes a rigid-body-based Rayleigh distribution has been developed and corrected over the decades, in which the results of each ship classification are similar or identical.

Spectral fatigue analysis based on existing stochastic approach can

be also applied to calculation of fatigue damage considering springing responses. To directly estimate the fatigue damage of weak areas, a 3D-model-based analysis of ship motion was conducted to estimate the hydroelastic response, and a structural analysis was performed to calculate the stress transfer function for the unit wave height comprising the springing component. Subsequently, a method for estimating the short-term fatigue damage in each sea state was applied assuming a wideband-based response rather than a narrowband-based response. The wideband model proposed by Benasciutti and Tovo (2005) was applied as it was the most similar to the narrowband-based calculation process. In this method, the fatigue damage based on the narrowband response is first calculated, as in the existing technique. Next, the presented wideband correction coefficient is applied to estimate the fatigue damage considering the springing response (Choung et al., 2012; Park and Jeong, 2014). By considering the expression probability for fatigue damage in each short-term sea state, the long-term fatigue damage ($D_{SPR,LIN}$) considering the linear springing component can be estimated, as shown in the left of Fig. 1. This method is applicable to design as the fatigue damage is calculated directly considering the springing effect. However, the tendency of results with the fatigue damage estimated in the existing rigid body-based narrowband method, which is regarded as the final fatigue damage in ship design evaluations, may be degraded. Hence, different structural response values can be calculated by applying different theories for structural response calculation and motion analysis to the existing rigid body and flexible body-based structural model theories. Because the fatigue damage is proportional to the inverse slope of the S−N curve, this difference in structural stress responses can result in a substantially greater difference in fatigue damage.

Accordingly, a method is proposed herein that considers the effect of springing response on the fatigue damage estimated from the existing verified rigid-body-based method, as shown in the procedure
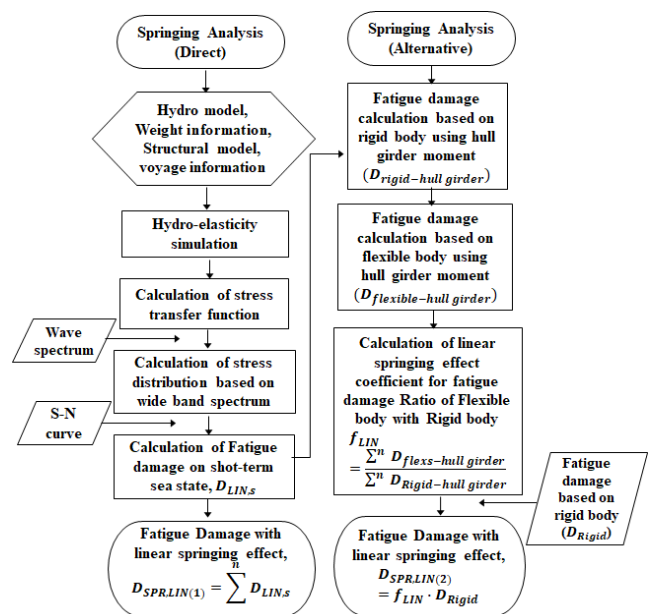

Fig. 1 Flowchart of fatigue analysis considering springing effect

in the right of Fig. 1. This method can estimate the fatigue damage ($D_{SPR.LIN}$) by considering the springing effect (f_{Lin}) calculated by other motion and structural analysis theory-based programs, based on the fatigue damage (D_{Rigid}) estimated in a fully tested rigid body-based program. In this study, the springing effect was calculated by obtaining the stress transfer function from a hull girder load, which has been studied by Jung (2013) and Li et al. (2018). Because the existing rigid-body-based fatigue damage is still regarded as the final fatigue damage in the design evaluation of most ships, the method proposed herein may be an efficient alternative for applying the springing effect, which is estimated in programs that use numerous hydroelasticity theories from academia and the industry, to design evaluation.

3. Numerical theories

3.1 Spectral fatigue analysis

According to the Palmgren–Miner linear cumulative damage rule, the cumulative fatigue damage (D) can be defined as shown in Eq. (1) using the S-N curve

$$D = \frac{n}{a} \int_0^\infty f(\triangle\sigma) \circ \triangle\sigma^m \circ d\triangle\sigma \tag{1}$$

D : Cumulative damage
N : Fatigue life
n : Cycle counting of stress range
a & m : Material factor of S-N curve

where n is the number of cycles of the stress range that causes fatigue damage. It can be calculated through the product of the peak frequency (f_P) and life time period (T_d). When the hull is assumed to be a rigid body, the frequency of the stress range due to wave loading becomes relatively narrow; as it narrows, the peak frequency and zero-crossing frequency (f_Z) become equal. Hence, when the response frequency is a narrowband, Eq. (1) can be expressed as in Eq. (2).

$$D_{narrow} = \frac{f_z T_d}{a} \int_0^\infty f(\triangle\sigma) \circ \triangle\sigma^m \circ d\triangle\sigma \tag{2}$$

When applying the linear wave theory, the height of the wavefront exhibits a normal distribution, whereas the peak of the wave height exhibits a Rayleigh distribution. In this case, as the stress range affecting the fatigue damage is equal to the peak of the wave height, a Rayleigh distribution is applied in the spectral fatigue analysis method, as shown in Eq. (3).

$$f(\triangle\sigma) = \frac{\triangle\sigma}{4m_0} exp(-\frac{\triangle\sigma^2}{8m_0}) \tag{3}$$

The zero-crossing frequency and peak frequency can be derived using the zero-order moment (m_0) and second-order moment (m_2) of the response spectrum, as shown in Equations (4) and (5). Furthermore, as shown in Equation (6), if the ratio of the zero-crossing frequency and peak frequency (α) is approximately 1, it can be considered a narrowband; if it is approximately 0, it can be considered a wideband.

$$f_z = \frac{1}{2\pi} \sqrt{\frac{m_2}{m_0}} \tag{4}$$

$$f_p = \frac{1}{2\pi} \sqrt{\frac{m_4}{m_2}} \tag{5}$$

$$\alpha = \frac{f_z}{f_p} \tag{6}$$

3.2 Motion equations for hydroelastic analysis

For hydroelastic analysis, the program WISH-FLEX developed by Kim and Kim (2014) was used, in which 3D global models can be applied. The solution for the fluid domain was obtained by applying the boundary element method, and the 3D finite element method was applied to analyze the rigid body and elastic motion of the hull and directly calculate the stress transfer function at hot spot locations. When using a 3D finite element model to obtain a solution in the time domain, the equation of motion has a large degree of freedom. As such, the method of obtaining the solution at each time interval is not suitable. Hence, a method that divides the solutions of low-order and high-order modes was used. The high-order mode of a flexible body motion possesses strong structural resilience, and therefore exhibits a quasi-static behavior with small displacements and an extremely high natural frequency. As this motion does not disturb the fluid field significantly, the assumption shown in Eq. (7) holds.

$$\xi^j(t) \gg \xi^k(t) \quad (1 \le j \le 6+n \le k \le m) \tag{7}$$

where ξ is the displacement vector in the generalized coordinate system, j the number of low-order modes, and k the number of high-order modes. Numbers 1 to 6 correspond to rigid body motions, whereas numbers 7 and above correspond to flexible body modes in the low natural frequency mode. m is the number of unconstrained degrees of freedom, and n is the number of low-order flexible body modes satisfying Eq. (7), which does not exceed 10 in a typical ship. A negligible level of flexible body motion ($n = 0$) corresponds to a rigid body assumption. Therefore, the approximate value of the displacement vector in the Cartesian coordinate system is as follows:

$$\tag{8}$$
$$\vec{u}(t) = \sum_{i=1}^m \vec{a}^i \, \xi^{i(t)} \approx \sum_{i=1}^{6+n} \vec{a}^i \, \xi^{i(t)} =$$

$$\begin{bmatrix} \vec{a}^1 & \cdots & \vec{a}^{6+n} \end{bmatrix} \begin{Bmatrix} \xi^{i(t)} \\ \vdots \\ \xi^{6+n(t)} \end{Bmatrix} = \vec{u}^{'}(t)$$

$\vec{a}$ is an eigenvector, and Eq. (8) can be substituted into the equation

of motion to obtain equations of low-order and high-order modes as follows:

$$\begin{bmatrix} M_L & 0 \\ 0 & M_H \end{bmatrix} \begin{Bmatrix} \ddot{\xi}^j(t) \\ \ddot{\xi}^k(t) \end{Bmatrix} + \begin{bmatrix} C_L & 0 \\ 0 & C_H \end{bmatrix} \begin{Bmatrix} \dot{\xi}^j(t) \\ \dot{\xi}^k(t) \end{Bmatrix} + \begin{bmatrix} K_L & 0 \\ 0 & K_H \end{bmatrix} \begin{Bmatrix} \xi^j(t) \\ \xi^k(t) \end{Bmatrix} \tag{9}$$

$$= \begin{Bmatrix} f_A^j(\overrightarrow{\ddot{u}}(t), \overrightarrow{\dot{u}}(t), \overrightarrow{u}(t), t) \\ f_A^k(\overrightarrow{\ddot{u}}(t), \overrightarrow{\dot{u}}(t), \overrightarrow{u}(t), t) \end{Bmatrix}$$

In Equation (9), the subscript L indicates the low-order mode and H the high-order mode. $\vec{u}$ is the velocity vector; superscripts j and k are the numbers for the low-order and high-order modes indicated in Eq. (7), respectively. Eq. (9) can be separated into two equations, i.e., motion equations for low-order and high-order modes, as follows:

$$M_L\left\{\ddot{\xi}^j(t)\right\} + C_L\left\{\dot{\xi}^j(t)\right\} + K_L\left\{\xi^j(t)\right\}$$
$$= \left\{f^j(\overrightarrow{\ddot{u}}(t), \overrightarrow{\dot{u}}(t), \overrightarrow{u}(t), t)\right\} \tag{10}$$

$$H_H\left\{\xi^k(t)\right\} = \left\{f^k(\overrightarrow{\ddot{u}}(t), \overrightarrow{\dot{u}}(t), \overrightarrow{u}(t), t)\right\} \tag{11}$$

In the motion equation of the low-order mode, all terms on the left hand side are considered, and the solutions on the left hand side are included in the external force term on the right. Hence, the motion of the low-order mode is a dynamic coupled response. Conversely, because the motion equation of the high-order mode assumes a quasi-static decoupled response, both the speed and acceleration components on the left hand side are ignored, and the external force term on the right hand side does not include the motion of the high-order mode. Hence, the motion of the high-order mode is a quasi-static decoupled response. The rigid body motion and low-order mode springing and whipping responses can be obtained from Eq. (10). However, as the local deformation corresponds to the high-order mode, the stress must be calculated from Eq. (11) to the solution of the high-order mode. The motion response of the high-order mode can be calculated from the motion response of the low-order mode.

3.3 Extraction of stress response using hull girder load

In this study, a method using only hull girder loads was used to estimate the ratio of fatigue damage due to springing, as shown in the procedure on the right side of Fig. 1. The hull girder loads include longitudinal bending, transverse bending, and torsional moment due to wave loading; the acceleration component of the hull generated by an external force is considered in these values and can be expressed by superimposing the hull girder mode. The corner parts of the upper deck and hatch top, i.e., the main fatigue strength evaluation locations of the very large container ship used in this study, were barely affected by changes in the local loads, such as the internal and external pressures. Accordingly, a method can be applied to estimate the stress response history of the hot spot locations including the springing response using only the hull girder load. The load distribution in a specific strip can be

defined as the load distributed in the longitudinal direction divided into several strips in the longitudinal direction. For longitudinal and transverse bending, the load distribution in the longitudinal direction (x) can be easily calculated using the existing beam theory. The longitudinal distribution (M_T) acting on each cross section of the torsional load component can be derived as follows:

$$M_T(x) = -\int_0^x m(x)dx \tag{12}$$

It is assumed that the torsional moment of the ship acts at the shear center (SC) of the transverse section, and because the horizontal shear force does not act at the SC, the horizontal bending moment is always coupled with the torsional moment. The adhesion point where the horizontal shear force acts is assumed to be 65% of the draft (T) used to calculate the strength; based on this assumption, another constraint is created by the horizontal shear force acting at $0.65\,T$ of the ship baseline T. Fig. 2 shows the basic shape of the load distribution acting at the points inside each strip, which can be defined as follows. (1) The point load in the horizontal direction acts uniformly on each point (point load $N_y = const. = 1$); (2) The point load in the horizontal direction is linear in the height direction (point load $N_y = const. = r_2z$); (3) The point load in the vertical direction acts uniformly (point load $N_z = const. = r_3$); (4) The point load in the vertical direction changes linearly in the width direction (point load $N_z = const. = r_4y$). If the number of points in the strip section is n, then the sum of point forces (f_H) in the horizontal direction can be expressed as Eq. (13). The moment generated by the horizontal force at the SC satisfies Eq. (14).

$$f_H = \sum_n (\Upsilon_1 + \Upsilon_2 z) \tag{13}$$

$$f_H(0.65T + SC) = \sum_n (\Upsilon_1 + \Upsilon_2 z)(z + SC) \tag{14}$$

Similarly, the sum of the point forces in the vertical direction (f_v) can be expressed as Eq. (15), and the torsional load at the SC generated by the sum of vertical direction point forces satisfies Eq. (16).
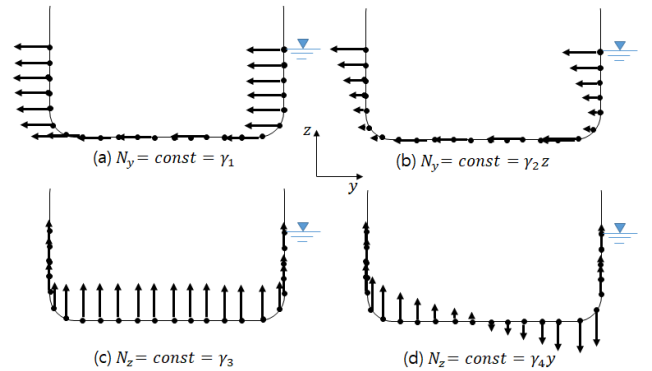
Fig. 2 Nodal force distributions

$$f_v = \sum_n (\Upsilon_3 + \Upsilon_4 y) \tag{15}$$

$$m_T + f_H(0.65T + SC) = \sum_n (\Upsilon_3 + \Upsilon_4 y)y \tag{16}$$

m_T indicates the torsional load generated by the horizontal and vertical loads acting on the points in the strip section. Four equations for four unknowns Υ_1, Υ_2, Υ_3, and Υ_4 can be used to compute the determinant as in Eq. (17) below, and the point load coefficient can be obtained.

$$\begin{pmatrix} n & \sum_{i=1}^{n} z_i & 0 & 0 \\ \sum_{i=1}^{n} z_i & \sum_{i=1}^{n} z_i^2 + SC\sum_{i=1}^{n} z_i & 0 & 0 \\ 0 & 0 & n & \sum_{i=1}^{n} y_i \\ 0 & 0 & \sum_{i=1}^{n} y_i & \sum_{i=1}^{n} y_i^2 \end{pmatrix} \begin{pmatrix} \gamma_1 \\ \gamma_2 \\ \gamma_3 \\ \gamma_4 \end{pmatrix} = \begin{pmatrix} f_H \\ f_H(0.65T+SC) \\ f_V \\ m_T + f_H(0.65T+SC) \end{pmatrix} \tag{17}$$

The following task is required to analyze the correlation between the load distribution calculated from the equation above and the hot spot stress. In the 3D finite element model, the three hull girder load components were assembled for three cases: (i) uniform in the positive direction (+); (ii) uniform in the negative direction (-); and not applied at all. Subsequently, the correlation between load distribution and stress was determined by conducting a structural analysis to examine the stress acting on a specific location. The stress acting on a specific location of the hull (σ) can be obtained using Eq. (18), of which a more detailed theoretical explanation has been provided by Jung (2013).

$$\sigma = \sigma_{VBM} + \sigma_{HBM} + \sigma_{TM} \tag{18}$$

σ_{VBM} : Stress due to vertical bending moment component

σ_{HBM} : Stress due to horizontal bending moment component

σ_{TM} : Stress due to torsional moment component

4. Fatigue analysis

4.1 Fatigue evaluation model

The model used in the analysis was a 15,000 TEU-class very large
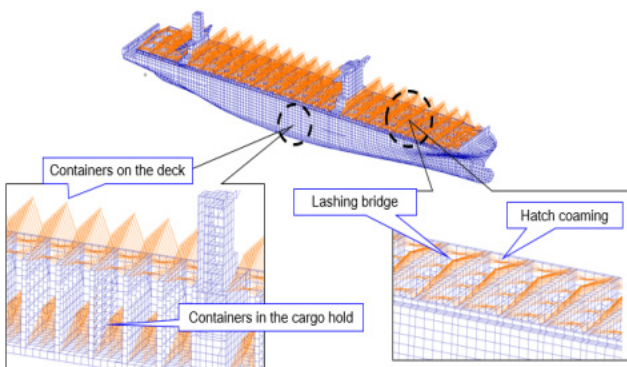
Fig. 3 Mass realization to 3D global model
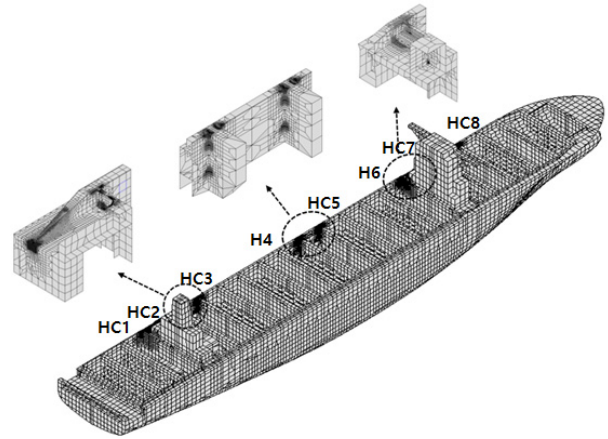
Fig. 4 Very fine mesh for fatigue strength evaluation

container ship. Fig. 3 shows the 3D global model considering the mass distribution used in this study. The point mass and rigid body element were used to idealize the mass of the hatch cover, lashing bridge, container, and light weight distribution. Fig. 4 shows the fatigue damage evaluation location. To evaluate the hatch corner in the longitudinal direction, i.e., a representative area weak to fatigue in the container ships, the area was divided into eight sections around the crossing point of the longitudinal and transverse bulkheads.

4.2 Mode analysis

In this study, the stress transfer function was obtained to calculate the fatigue damage through modal superposition. WISH-FLEX, the hydroelastic analysis program introduced in Section 3.2, was used to calculate the modal response to the unit wave height at a specific frequency. By multiplying the stresses corresponding to each mode in the elements of the fatigue strength evaluation locations previously

$\omega_1 = 0.387$ Hz $\omega_2 = 0.491$ Hz

$\omega_3 = 0.604$ Hz $\omega_4 = 0.846$ Hz

$\omega_5 = 1.161$ Hz $\omega_6 = 1.224$ Hz
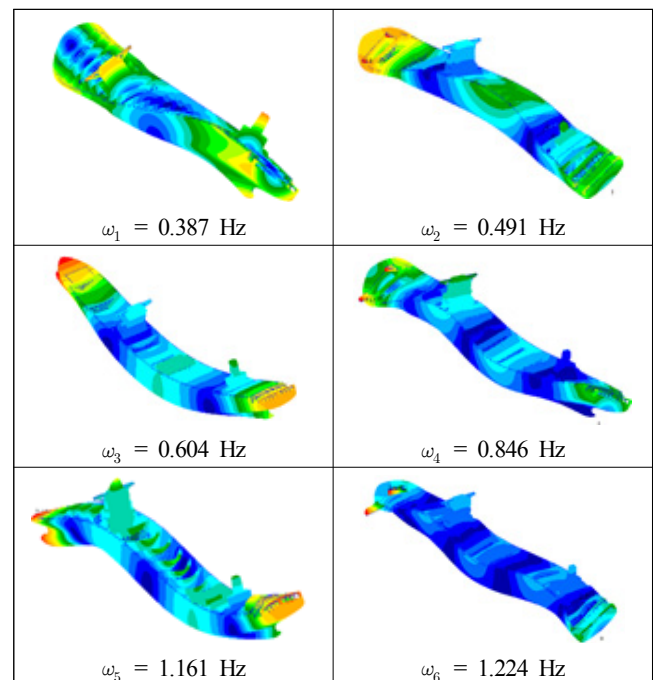
Fig. 5 Results of eigenmode analysis on dry condition

calculated in finite element analysis, the stress corresponding to each modal response can be obtained. Next, by superimposing the stresses corresponding to each modal response and using them for each frequency, the stress transfer function at that location can be obtained. The procedure for evaluating the fatigue strength after calculating the stress transfer function is detailed in Section 3.1. Fig. 5 shows the results of the eigenmode analysis for calculating the structural response. While applying as many eigenmodes as possible to the calculation enables more accurate stress response calculations, when using an entire ship structural model that includes mass, many local modes occur owing to problems arising from the boundary conditions of the structural members and concentrated mass. As shown in Fig. 5, the stress response was obtained using six global modes. For the target ship, after first identifying two low-order torsion modes, a first-order vertical mode occurred; subsequently, four torsion modes and two vertical modes were applied to the analysis.

4.3 Fatigue damage calculation

When a ship encounters a wave in the heading direction at a constant speed and advances forward, the resonance frequency generated from the springing vibration response is shortened owing to the effect of the encounter frequency. This creates a cross section involving the wave spectrum with energy in the fatigue analysis calculation based on statistical analysis, which increases the contribution of the springing component in the response spectrum for fatigue damage calculation. By contrast, when the ship encounters a following sea or beam sea and then advances forward, the resonance frequency of the springing vibration response does not lengthen or change. Figs. 6–9 show representative structurally discontinuous areas of container ships for the fatigue evaluation areas shown in Fig. 4. The figures show the stress transfer functions for a bow quartering sea and a head sea in order at HC3 and HC6, which correspond to points $0.25L$ and $0.75L$ with weak fatigue strength, respectively, where L is the ship length. Four stress transfer functions were included in the figure, defined as follows:

(a) Stress transfer function considering the springing response obtained by conducting a flexible body analysis using WISH FLEX and applying modal superposition (a coupled analysis was conducted to obtain the modal response, and modal superposition was applied to directly calculate the stress at the hot spot position)

(b) Stress transfer function considering the springing response obtained using only the hull girder load in the flexible body-based structural model (a coupled analysis was conducted to obtain the hull girder moment, and the technique in Section 3.3 was applied to calculate the stress at the hot spot position)

(c) Stress transfer function not considering the springing response obtained using only the hull girder load in the rigid body-based structural model (a decoupled analysis was conducted to obtain the hull girder moment, and the technique in Section 3.3 was applied to calculate the stress at the hot spot position)

(d) Stress transfer function not considering the springing response

obtained from the rigid-body-based structural model applying a program (KR 3D) using potential theory, which is currently used in the design evaluation stage (This is the rigid-body-based stress transfer function applied in the existing design stage presented in this study. It is calculated using KR 3D based on potential theory).

First, the figures show that in the head sea, the springing response occurs in a lower frequency domain compared with the following sea, which is attributed to the effect of the encounter frequency described
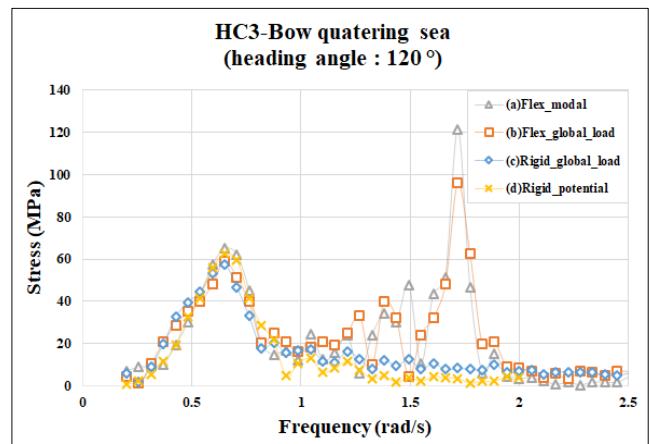

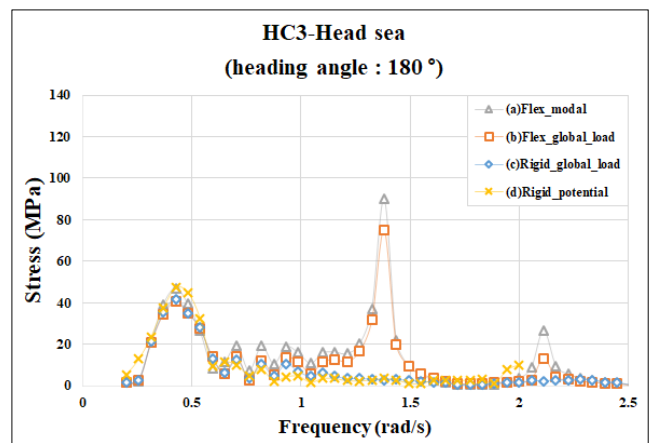**Fig. 6** Stress transfer function of at HC3 (Bow sea)

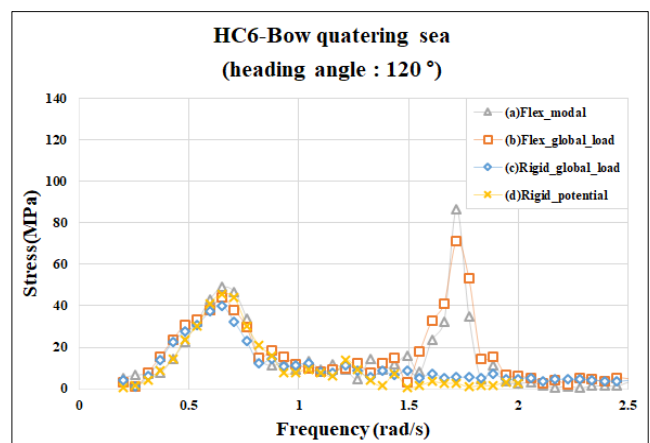**Fig. 7** Stress transfer function at HC3 (Head sea)

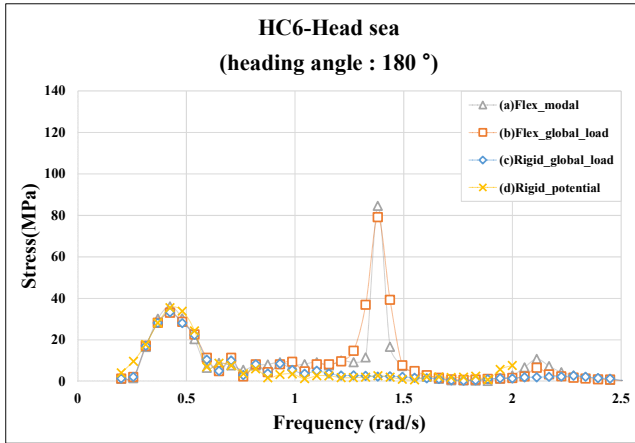**Fig. 8** Stress transfer function at HC6 (Bow sea)

Fig. 9 Stress transfer function at HC6 (Head sea)

Fig. 10 Comparison of fatigue damage

above. In terms of the overall response sizes, the responses of (a) and (b) comprising the hydroelastic response tended to be slightly larger or similar to those of (c) and (d), which comprised only rigid-body responses. As the stress response in the bow quartering sea and head sea occurred at similar levels, it is confirmed that the method introduced in Section 3.2 for estimating the stress response using the hull girder load can efficiently estimate the stress transfer function at any location.

When calculating the response spectrum to estimate fatigue damage, the frequency band with high energy in the wave spectrum is the stress response in the low-frequency domain due to wave loading, instead of a high-frequency response such as springing. As such, a small difference in response due to wave loading compared with the difference in the springing response can result in larger differences in fatigue damage that are proportional to the inverse slope of the S−N curve. Therefore, the difference between the response calculated based on the rigid body-based potential (d) and the response of the low-frequency band caused by wave loading calculated using flexible body-based modal superposition (a) can result in large differences in the final fatigue damage, as well as differences in the trend of the results. Hence, an alternative method is proposed that considers the effect of springing on the existing rigid-body-based value, as shown in the procedure on the right of Fig. 1 in Section 2.

To implement this alternative method, the existing rigid-body-based fatigue damage was calculated from (d), and using the hull girder load, the ratio of fatigue damage calculated from the stress responses containing the springing response (b) and not containing the springing response (c) was calculated as the springing effect. Fig. 10 shows the calculated fatigue damage from HC-1 to HC-8. A worldwide scatter table (DNVGL RP-C205) with a design life of 25 years was applied; for the S−N curves, British Standard "c" curves applicable to welds were applied to all locations. Three fatigue damage levels are shown for each location, and each fatigue damage was calculated as follows:

(1) As the fatigue damage (D_{rigid}) was rigid-body based, it was calculated from the stress transfer function in Fig. 6(d), which is the most widely applied method in actual design stages.

(2) Fatigue damage ($D_{sprlin.1}$) was the value at the hot spot location
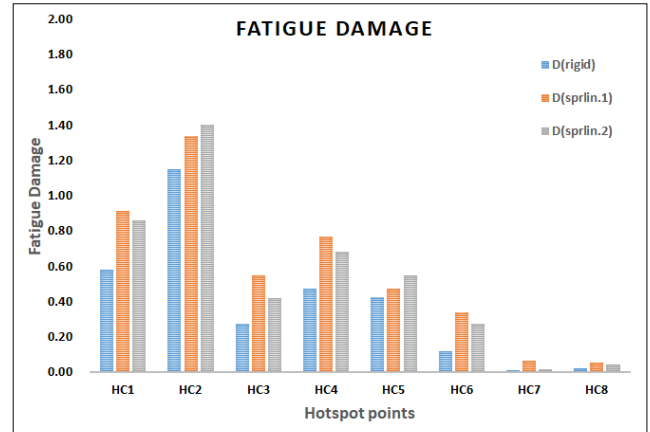
and was calculated directly using modal superposition, as shown in the analysis procedure on the left of Fig. 1. Hence, as shown in Fig. 6(a), the fatigue damage was calculated directly from the stress transfer function containing the springing response.

(3) Fatigue damage ($D_{sprlin.2}$) was calculated by applying a method that incorporated the springing effect on the existing rigid-body-based fatigue damage, as shown in the procedure on the right of Fig. 1. Hence, fatigue damages with and without the springing response were calculated using only the hull girder loads calculated based on Figs. 6(b) and 6(c); furthermore, the ratio of the two fatigue damage values was defined as the effect of springing on fatigue damage. This ratio was multiplied by the rigid-body-based damage (D_{rigid}) to obtain $D_{sprlin.2}$.

The rigid-body-based fatigue damage showed the smallest value. A comparison between the value calculated directly using modal superposition and the rigid-body-based value calculated considering the springing effect indicated that the fatigue damage estimated in either method was not biased. Moreover, because the fatigue damage was proportional to the inverse slope of the S−N curve as described above, the fatigue damage calculated from the stress transfer function including the springing responses estimated from different methods can be assumed to be similar. This demonstrates that the feasibility of this method for the final design evaluation, even when applying a theory other than the existing rigid body-based theory to estimate the ratio of fatigue damage due to springing.

5. Conclusions

This study aimed to establish a procedure to evaluate fatigue strength based on a linear statistical analysis technique that is widely used in fatigue strength evaluation. Therefore, the springing response of very large container ships was considered, the abovementioned procedure was applied to an actual ship, and its applicability was evaluated. First, a methodology was established for directly calculating the fatigue damage at hot spot locations using a 3D global model. Subsequently, a method was proposed for estimating the final fatigue damage, considering the fatigue damage calculated from the

rigid body-based spectral fatigue analysis method, which is currently used as the final fatigue damage in design evaluation, while applying the ratio between the fatigue damage estimated from the theory applied to the design evaluation stage in actual shipbuilding and that due to springing estimated from a different theory. In addition, the proposed method was used to estimate the fatigue damage of a hatch corner along the longitudinal direction of the container ship. To evaluate the applicability of the proposed method, the results and characteristics of the fatigue damage calculated from each method were analyzed.

Some limitations were encountered when evaluating the proposed method's applicability and efficiency in the design evaluation of actual ships. In the future, the stress transfer functions and stress responses applied to fatigue damage calculation need to be investigated by analyzing the proposed structural theories and analysis procedures. Additionally, studies pertaining to the nonlinear components mentioned in the introduction need to be conducted.

References

Benasciutti, D., & Tovo, R. (2005). Spectral Methods for Lifetime Prediction under Wide-band Stationary Random Processes. International Journal of Fatigue, 27(8), 867-877. https://doi.org/10.1016/j.ijfatigue.2004.10.007

Bishop, R.E.D., Price, W.G., & Zhang, X.C. (1985). A Note on the Dynamical Behavior of Uniform Beams Having Open Channel Section, Journal of Sound and Vibration, 99(2), 155-167.

Choung, J.M., Kim, K.S., Nam, J.M., Koo, J.B., Kim, M.S., Shim, Y.L, & Um, H.S. (2012). Study on Applicability of Frequency Domain-Based Fatigue Analysis for Wide Band Gaussian Process I : Rayleigh PDF, Journal of the Society of Naval Architects of Korea, 49(4), 350-358.

Jung, B.H. (2013). A Study Strength Evaluation Considering Hydroelasticy Effect for Very Large Container Ship (Ph.D. Thesis). Busan National University, Busan, Korea.

Kim, B.H., Choi, B.K., Park, J.S., Park, S.K., Ki, H.K., Kim Y.I. (2018a). Full Scale Measurement Data Analysis of Large Container Carrier with Hydroelastic Response, Part I-identification of Modal Parameters. Journal of Society of Naval Architects of Korea, 55(1), 37-44. https://doi.org/10.3744/SNAK.2018.55.1.37

Kim, B.H., Choi, B.K., Park, J.S., Park, S.K., Ki, H.K., & Kim Y.I. (2018b). Full Scale Measurement Data Analysis of Large Container Carrier with Hydroelastic Response, Part II, Fatigue damage estimation. Journal of Society of Naval Architects of Korea, 55(1), 45-55. https://doi.org/10.3744/SNAK.2018.55.1.45

Kim, B.I., Kim, M.S., Seo, S.K., & Park, J.H. (2018c). A Study on the Whipping Phenomena Effect on the Structural Response of Large Container Ships. Journal of Society of Naval Architects of Korea, 55(4), 341-349. https://doi.org/10.3744/SNAK.2018.55.4.341

Kim, B.I., & Song, K.H. (2019). Study of the Prediction of Fatigue Damage Considering the Hydro-elastic Response of a Very Large Ore Carrier(VLOC). Journal of Ocean Engineering and Technology, 33(1), 33-41. https://doi.org/10.26748/KSOE.2018.085

Kim, J.H., & Kim, Y.H., (2014). Numerical Analysis on Springing and Whipping Using Fully-coupled FSI Models. Ocean Engineering, 91, 28-50.

Kim, Y.I., Kim, K.H., & Kim, Y.H. (2009). Analysis of Hydroelasticity of Floating Ship-like Structure in Time Domain Using a Fully Coupled Hybrid BEM-FEM. Journal of Ship Research, 53(1), 31-47.

Li, H., Xu, H., Ren, H., Shen, X., & Wang, Y. (2018). The Effect on Large Container Ships' Fatigue Due to Springing Loads Coupling Horizontal and Torsional Vibrations. Proceedings of the ASME 2018 37th International Conference on Ocean, Offshore and Arctic Engineering. American Society of Mechanical Engineers Digital Collection, Mardrid, Spain. https://doi.org/10.1115/OMAE2018-77982

Park, J.B., & Jeong, S.M. (2014). Fatigue Damage Model with Tri-modal Spectrum under Stationary Gaussian Random Process. Journal of Ocean Engineering and Technology, 28(3), 185-192. https://doi.org/10.5574/KSOE.2014.28.3.185

Storhaug, G., Derbanne. Q., Choi, B.K., Moan, T., & Hermundstad, O.A. (2011). Effect of Whipping on Fatigue and Extreme Loading of a 13000TEU Container Vessel in Bow Quatering Seas Based on Mode Tests. Proceedings of the ASME 2011 30th international Conference on Ocean, Offshore and Artic Engineering, Rotterdam, The Netherlands, 293-302. https://doi.org/10.1115/OMAE2011-49370

Author ORCIDs and Contributions

Author name	ORCID	Contributions
Jung, Byoung-Hoon	0000-0003-0939-2023	①③
Ahn, In-Gyu	0000-0003-2954-9526	②
Seo, Sun-Kee,	0000-0001-5723-9264	②
Kim, Beom-Il	0000-0002-8981-4777	④⑤

① Conceived of the presented idea or developed the theory
② Carried out the experiment or collected the data
③ Performed the analytic calculations or numerical simulations
④ Wrote the manuscript
⑤ Supervised the findings of this study

Original Research Article

Development of Wave Overtopping–Overflow Transition Model Based on Full-scale Experiments

Hajime Mase [1], Sooyoul Kim [2], Makoto Hasegawa [3], Jae-Hoon Jeong [4] and Jong-Sung Yoon [5]

[1]*Professor, Disaster Prevention Research Institute, Kyoto University, Kyoto, Japan*
[2]*Associate Professor, Graduate School of Engineering, Tottori University, Tottori, Japan*
[3]*CEO, Hydro Technology Institute Korea Co., Ltd., Busan, South Korea*
[4]*Managing Director, Hydro Technology Institute Korea Co., Ltd., Busan, South Korea*
[5]*Professor, Department of Civil and Urban Engineering, Inje University, Kimhae, Gyeongsangnam-do, South Korea*

ABSTRACT: *When high waves and storm surge strike simultaneously, the characteristics of the fluid field change drastically from overtopping according to the wave runup height to overflow through a transition state that combines overtopping and overflows. However, an estimation model or evaluation method has not yet been established because there is not enough engineering data. This study developed a wave overtopping-overflow transition model based on a full-scale experiment involving wave overtopping and overflow transition, which appropriately reproduced the effect of waves or the temporal change in inundation flow. Using this model to perform a calculation for the wave overtopping and overflow transition process under typical circumstances, this study determined the wave runup height and features of the inundation flow under time series changes as an example.*

1. Introduction

Coastal areas are more vulnerable to storm surge disasters because of the concentration of important facilities, high utilization of underground spaces, reduction in crisis awareness of the residents, and changes in typhoon characteristics caused by global warming. In recent years, New York City was hit by Hurricane Sandy in 2012 (Matsuzaki et al., 2013) and the Philippines suffered massive storm surges in 2013 due to typhoon Haiyan (Kawai et al., 2014). Although the magnitudes of the storm surges in Japan in recent years have not reached those in other countries, the storm surge caused by Typhoon 21 in 2018 recorded the highest tidal level of 3.29 m in Osaka and updated the highest peak level of 2.93 m observed in Typhoon Nancy (2nd Muroto Typhoon) in 1961 (Investigation Team of Coastal Damage from Typhoon Jebi in 2018, 2018). In addition, Typhoon No. 15 in 2019 caused a high wave and storm surge in Tokyo Bay and other areas, resulting in power outages and water shortages across Chiba prefecture. Therefore, because typhoons have become extreme as a result of global warming, the high wave and storm surge disaster risks in coastal areas are expected to increase in the near future.

As with the tsunami measures taken after the Great East Japan Earthquake, Japan's water control policy has also changed based on a disaster prevention/reduction viewpoint taking into account the worst case for the maximum storm surge scale beyond design conditions. The government is currently working to calculate and announce the expected flood area resulting from the largest predicted storm surge in order to reorganize the warning and evacuation system for the management of storm surge risk.

As technical support for preparing the storm surge flooding area map, the "Storm Surge Flooding Area Mapping Guide Ver 1.00" (Disaster Prevention and Restoration Division, Rural Infrastructure Department, Rural Development Bureau, 2015) (hereinafter referred to as the "guide") was compiled in 2015. This "guide" is designed to add the wave runup height or wave overtopping to the storm surge in a storm surge flooding simulation. This is used to assess the design conditions of coastal structures. In the actual phenomena, the inundation pattern is transferred in the order of (a) the wave runup height + wave overtopping, (b) combined overtopping and overflow (transition process), and (c) overflow due to the simultaneous occurrence of high waves and storm surges. However, the guide does not present the transition process when a high wave is accompanied by storm surge, regardless of whether there is mutual interference

between the high wave and storm surge. As described above, the previous studies did not cover the development of a model or identification of characteristics to express a series of processes for the wave runup height, wave overtopping, transition, and overflow.

This study was intended to develop the studies of Mase et al. (2018) and Kim et al. (2018) to improve the accuracy of the worst case storm surge and high wave simulation, in which the tide deviation is maximized at each coast based on the largest typhoon. Specifically, a wave overtopping-overflow model was constructed to continuously calculate the inundation in response to a series of inundation flow processes involving the simultaneous occurrence of high waves and storm surges (i.e., the change from the initial inundation flow due to the wave overtopping to the overlapped inundation flow in the wave overtopping-overflow transition process), and improve the understanding of the trend of the inundation flow type until reaching flooding as a result of the final overflow.

This study qualitatively and quantitatively reproduced the characteristics of the experimental results for the transitional state in which seawater was accompanied by high waves, based on the full-scale overtopping-overflow transition experiment. Next, an analysis was made of the characteristics of the time series changes in the wave overtopping-overflow transition process by applying this model under typical conditions.

2. Overtopping-overflow transition model

2.1 Existing studies

Fig. 1 shows a schematic diagram of the (a) inundation due to overflow, (b) inundation in the transition process where the overtopping and overflow are combined, and (c) inundation due to overflow. The inundation states depend on the relative positions of the sea level and top elevation and the wave state.

Reeve et al. (2008) interpreted the overtopping-overflow transition process of impervious slope structures with numerical calculations using the Reynolds-averaged Navier-Stokes equation. They compared the results of numerical calculations of the wave overtopping flow with those of empirical equations, verified their validity, and then calculated the overtopping-overflow transition process. After that, they compared the result obtained from the overflow formula at the dyke with the value calculated using the method reported by Schuttrumpf et al. (2001), which was the sum of the overflow at a top elevation of zero and the wave overtopping at the dyke. As a result, the value obtained from the numerical calculation of Reeve et al. (2008) was larger than that of Schuttrumpf et al. (2001). In addition, because the numerical results were considerably larger than the experimental results of Hughes and Nadal (2009), their precision was not good enough.

Hughes and Nadal (2009) measured the inundation flow and inundation flow in the overtopping-overflow transition state through a 1/25 scale numerical experiment. Based on the experimental results, they obtained experimental formulas for the average overtopping-

(a) Inundation caused by overtopping

(b) Inundation caused by overtopping and overflow

(c) Inundation caused by overflow
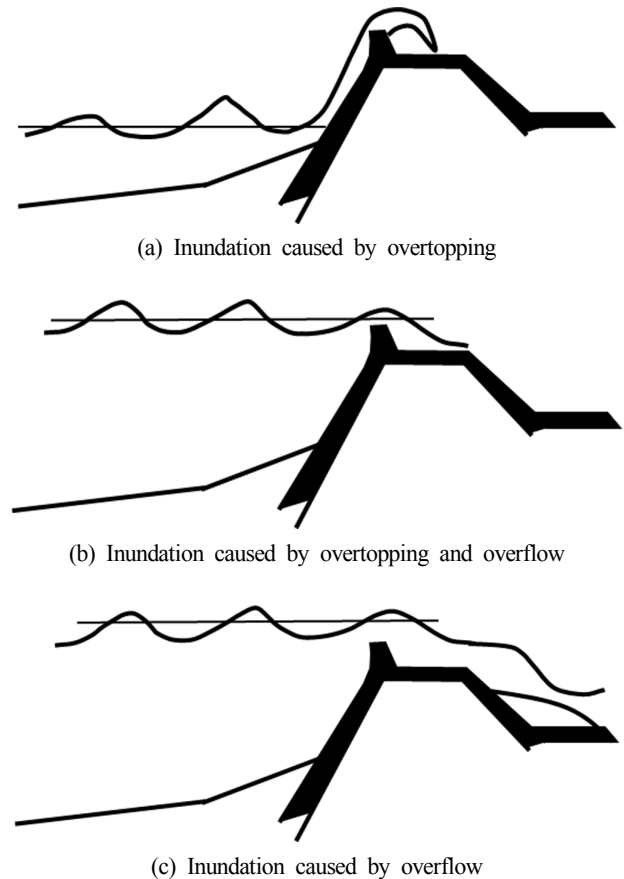
Fig. 1 Diagrams of inundation caused by overtopping, overtopping ・overflow, and overflow behind coastal dykes

overflow flow, instantaneous flow, and rate distribution of unit waves. The formula for the average inundation flow (combined flow of overtopping and overflow), q_{ws} is as follows:

$$\frac{q_{ws}}{\sqrt{gH_{m0}^3}} = 0.034 + 0.53\left(-\frac{R_c}{H_{m0}}\right)^{1.58} \tag{1}$$

where g is the acceleration of gravity, H_{m0} is the significant wave height obtained from the spectrum at water depth, and R_c is the relative top elevation and indicates the difference between the dyke top elevation and the water level. If the water level is higher than the dyke top elevation, R_c has a negative value.

Suzuki and Shibaki (2010) and Suzuyama et al. (2016) suggested a method to estimate the inundation flow in the overtopping-overflow transition process by adjusting coefficients of the expected overtopping flow formula and correcting the results of the overflow flow calculation of Takayama et al. (1982) to make it suitable for the flow calculation results. In this method, it is necessary to calculate the flow for each step by using an equivalent deep-water wave when calculating the inundation flow.

Tanaka et al. (2018) suggested a method to calculate the overflow using the front wave height obtained from a numerical calculation as a substitute for the equivalent deep-water wave. The overflow formula is

a complex formula involving six parameters. In addition, the wave and structure conditions used for setting the parameters are limited. In particular, the condition of the small top elevation before the overtopping-overflow transition state is not included.

Li et al. (2012) examined the inundation flow in the overtopping-overflow state with an experiment using a full-scale coastal seawall with a height of 3.25 m, top width of 2.57 m, front slope of 4.25, and rear slope of 3. The experimental results were compared to the results of the combined overtopping and overflow empirical formula of Hughes and Nadal (2009) and were a good match, except for the condition where the overtopping depth was small.

2.2 Overtopping-overflow transition model

2.2.1 Formalization of inundation flow representing entire process

This study established a formula to continuously obtain the inundation flow, q_{ws}, indicating a change from the inundation due to overflow (Fig. 1(a)) to inundation in the combined overtopping-overflow field (transition process) (Fig. 1(b)), to inundation due to overflow (Fig. 1(c)), considering the mutual interference of waves and storm surges. In modeling the inundation flow in the series of processes, q_{ws} is linearized with the overflow, q_w, due to waves and overtopping flow, q_s, in the revetment top. In addition, the influence ratio of the waves in the combined overtopping-overflow field is expressed as $Ratio$, which is defined on the basis of the ratio of the relative top elevation to front wave height, which is R_c/H_{m0}.

$$q_{ws} = q_w \times Ratio + q_s \tag{2}$$

The overtopping-overflow transition model shown in Eq. (2) is a combined model of the overtopping flow due to waves and the overflow flow due to the flow on the revetment top. Hughes and Nadal (2009) found that the effect of overflow on the inundation flow, q_{ws}, was negligible if the overflow depth increased, and the dimensionless overflow depth met the condition of $R_c/H_{m0} < -0.3$ (note that R_c is negative when the water level is higher than the revetment top) (Fig. 1(c)). This threshold value of 0.3 could be interpreted as follows. In nonlinear waves, the wave crest is pointed and the wave through is flattened. The wave through depth of a linear wave is 0.5 times the wave height, but the wave through depth of a nonlinear wave is 0.5 times smaller than 0.5 times the wave height. Therefore, it seems that the threshold value of 0.3 indicates a threshold value in which the wave through height of an average non-linear wave is equal to the revetment top, and the flow due to overflow indicates the threshold value setting forth the inundation flow. In this model, the influence ratio of the wave, $Ratio$, is represented by the following equation taking account the threshold value of 0.3.

$$Ratio = \begin{cases} 1.0 & \text{for} & (R_c/H_{m0}) \geq 0 \\ \cos\{(R_c/H_{m0}) \times (1/0.3) \times (\pi/2)\} & \\ & \text{for} -0.3 \leq (R_c/H_{m0}) < 0 \\ 0 & \text{for} & (R_c/H_{m0}) < -0.3 \end{cases} \tag{3}$$

According to Eq. (3), $Ratio = 1.0$ under the inundation condition (Fig. 1(a)) as a result of the wave overtopping, and all the impacts of the overtopping are reflected. On the other hand, $Ratio = 0$ under the inundation condition as a result of the wave overtopping (Fig. 1(c)), and the impact of the overtopping is ignored. In addition, the combined overtopping and overflow field shown in Fig 1(b) corresponding to the middle of these conditions has a $Ratio$ value that is larger than 0 and smaller than 1 considering the impact of the overtopping according to R_c/H_{m0}. There are a linear function, exponential function, etc. as functions representing the reduction characteristics from $Ratio = 1.0$ to $Ratio = 0$ of the combined overtopping and overflow, but the cos function is used here. The reason is later described in 3.2.

Moreover, the equations for the overtopping flow, q_w, due to the wave are classified based on a large front water depth ($h/H_D \geq 3$), small front water depth, or the target being a land structure ($h/H_D < 3$), as described later. The threshold value, 3, is used to distinguish a wave condition that has little effect on wave breaking and another wave condition where the wave breaking may be affected. H_D is used to make this distinction and as the design wave height of the corresponding coastal structure.

2.2.2 Calculation of overflow on revetment top

The overflow q_s on the revetment top due to the water rising as a result of storm surge is calculated by applying Henderson's equation (1966) shown in Eq. (4).

$$q_s = 0.5443 \sqrt{g} \ \left| -R_c \right| \tag{4}$$

The coefficient (i.e., 0.5443) of Eq. 4 is almost the same as that of Honma's overflow formula (1940), which is used in Japan. Moreover, Mase et al. (2018) used EurOtop's formula (Pullen et al., 2007) with a coefficient of 0.6. However, in the second edition, the coefficient of EurOtop's formula (Van der Meer at al., 2018) became smaller. Therefore, Henderson's equation was adopted in this study.

2.2.3 Calculation of overtopping caused by wave from water depth

The overtopping flow, q_w, caused by the wave when the front wave depth is large ($h/H_D \geq 3$) is calculated using the equation suggested by Reis et al. (2008), which is the basis of the Integrated Formula of Wave Overtopping and Runup Modeling (IFORM) that the authors have been developing.

$$q_w = \begin{cases} A\sqrt{gR_{\max}^3}\left(1 - \dfrac{R_c}{R_{\max}}\right)^B & \text{for } 0 \leq \dfrac{R_c}{R_{\max}} < 1 \\ 0 & \text{for } \dfrac{R_c}{R_{\max}} \geq 1 \end{cases} \tag{5}$$

$$(R_{\max})_{99\%,100} = 2.15 R_s \tag{6}$$

where $R_{\max}$ is the maximum wave runup height,. However, this study applied a wave runup height $(R_{\max})_{99\%,100}$ that did not exceed 99% of

the maximum runup height distribution among 100 waves, as shown in Eq. (6). In addition, the relationship between the 2% excess runup height ($R_{2\%}$) and the maximum runup height is as follows:

$$(R_{\max})_{99\%,100} = 1.54\,R_{2\%} \tag{7}$$

Coefficients A and B of Eq. (5) are found as follows:

$$A = \begin{cases} 0.0016 + 0.002\cot\alpha & \text{for } 1 \le \cot\alpha < 10 \\ 0.0216 & \text{for } 10 \le \cot\alpha \le 20 \end{cases} \tag{8}$$

$$B = \begin{cases} 5.34 + 1.15\cot\alpha & \text{for } 1 \le \cot\alpha < 7 \\ 16.61 - 0.46\cot\alpha & \text{for } 7 \le \cot\alpha \le 20 \end{cases} \tag{9}$$

where $\cot\alpha$ is the slope inclination. $(R_{\max})_{99\%,100}$ is obtained from the following:

$$\frac{(R_{\max})_{99\%,100}}{H_{m0}} = \begin{cases} 0.54 + 2.37\xi & \text{for } 0 < \xi \le 2.2 \\ 6.45 - 0.32\xi & \text{for } 2.2 < \xi \le 9.0 \\ 3.55 & \text{for } 9.0 < \xi \end{cases} \tag{10}$$

where ξ is the surf similarity parameter.

Eq. (5) has the characteristics that (1) no overflow occurs when the maximum runup height is lower than the top elevation, and (2) even when the top elevation is zero, the overflow has a specific value. It can also be applied to a sloping dyke as well as a vertical wall (Reis et al., 2013). In addition, IFORM is not used in the calculation of q_w because the large-scale experiments were conducted under the condition of $h/H_{m0} \ge 4.96$ and significantly deviated from the application conditions of IFORM.

2.2.4 Calculation of overflow due to waves in low front water depth or with land structure

For actual coastal seawalls or revetments, the installation depth may be shallow. In addition, the structures are placed on the ground, so the wave specifications may not be defined. In this case, IFORM, which is an overflow formula that is applicable to structures installed in terrestrial areas, is used for $h/H_D < 3$. This study applied the overflow formula (Yuhi et al., 2019), which improved the accuracy of the IFORM calculation, to obtain q_w.

$$\frac{q_w}{\sqrt{gH_0'^3}} = \begin{cases} C\left[\Gamma\left(\dfrac{R_{\max}}{H_0'}\right)^{\frac{3}{2}}\left\{1 - \left(\dfrac{R_c}{H_0'}\right)\Big/\left(\dfrac{R_{\max}}{H_0'}\right)\right\}^{\Omega}\right] \\ \qquad\qquad\qquad\qquad \text{for } 0 \le R_c < R_{\max} \\ 0 \qquad\qquad\qquad \text{for } R_{\max} \le R_c \end{cases} \tag{11}$$

$$C = \begin{cases} 0.25\cot\alpha + 0.5 & \text{for } 0 \le \cot\alpha < 2 \\ 1.0 & \text{for } \cot\alpha \ge 2 \end{cases} \tag{12}$$

$$\Gamma = \begin{cases} 0.018 & \text{for } -0.5 \le X \\ \exp(-3.27 - 2.91X^2) & \text{for } -1.4 < X < -0.5 \\ 0.00013 & \text{for } X \le -1.4 \end{cases} \tag{13}$$

$$\Omega = \begin{cases} 6.240 & \text{for } -0.5 \le X \\ 5.82X + 9.15 & \text{for } -1.4 < X < -0.5 \\ 1.000 & \text{for } X \le -1.4 \end{cases} \tag{14}$$

where H_0' is the equivalent deep-water wave height, and $X = \ln\{1 - (R)c/R_{\max}\}$.

The maximum runup height ($R_{\max}$) shown in Eq.(11) applies $(R_{\max})_{99\%,100}$ in the same way as Eq. (5).

$$(R_{\max})_{99\%,100} = 2.15\,R_s = 1.54\,R_{2\%} \tag{15}$$

$$R_{2\%}/H_0' = 2.99 - 2.73\exp\left(-0.57\tan\beta/\sqrt{H_0'/L_0}\right) \tag{16}$$

$$\tan\beta = (h_b + R_{2\%})^2/(2A_{real}) \tag{17}$$

$$\frac{h_b}{H_0'} = a_0 + a_1\exp\left[-\left\{\frac{\ln\{(H_0'/L_0)/a_2\}}{a_3}\right\}^2\right] \tag{18}$$

$$a_0 = 30.2470 - 27.3440\exp\left[-\left\{\frac{\ln(22.9130i)}{5.4509}\right\}^2\right] \tag{19}$$

$$a_1 = -9.9467 + 8.9213\exp\left[-\left\{\frac{\ln(29.3880i)}{3.1264}\right\}^2\right] \tag{20}$$

$$a_2 = 0.0302 - 0.0023\exp\left[-\left\{\frac{\ln(25.9160i)}{1.7065}\right\}^2\right] \tag{21}$$

$$a_3 = 6.1291 - 3.5001\exp\left[-\left\{\frac{\ln(36.3660i)}{1.3457}\right\}^2\right] \tag{22}$$

Here, L_0 is the wavelength of a deep water wave, $\tan\beta$ is the virtual grade obtained from the real cross-sectional area (A_{real}) between two points of the wave runup height ($R_{2\%}$) and the wave depth (h_b) of wave breaking, and i is the sea bottom slope ($=\tan\theta$). The application ranges of Eq. (11) are $h/H_{m0} < 2$, $0.002 < H_0/L_0 < 0.07$, and $1/100 < i < 1/10$.

In a case where the slope inclination ($\cot\alpha$) is more gradual than 2, the runup height in Eq. (15) and the overflow formula in Eq. (11) are the same as those suggested by Mase et al. (2013), and $C = 1$ is applied as in Eq. (12). Meanwhile, in the case of a steep slope with a slope inclination ($\cot\alpha$) of more than 2 (e.g., vertical revetment or slope revetment with a slope of 1), the section for calculation is uniformly designated as 2 for convenience (in the case of the actual section, vertical revetment or slope revetment with a slope of 1), and R2% is calculated for Eq. (16). After that, $(R_{\max})_{99\%,100}$ in Eq. (16) is estimated, and the overflow, q_w, is calculated with coefficient C corresponding to the slope inclination of the revetment subject to Eq. (11).

2.3 Comparison and review of full-scale experimental results

Li et al. (2012) conducted full-scale experiments for 11 cases, and the water level from the top (h_1), normal significant wave height (H_{m0}), peak period (T_p), average period ($T_{m-1,0}$), overflow flow (q_s), and observed inundation flow (q_{ws}) are listed in the table. The value of qw was obtained using Eq. (5) or Eq. (11), in which the specifications of a coastal seawall [the top position of 3.25 m and the slope inclination ($\cot\alpha$) of 4.25] and h_1, H_{m0}, T_p, and $T_{m-1,0}$ are given. After that, q_s was obtained from Eq. (4), and the inundation flow, q_w, was calculated using Eq. (2).

Fig. 2 is a comparison of the results of the calculation under this model with the full scale test results with respect to the dimensionless inundation flow rate at $\sqrt{gH_{m0}^3}$. This figure shows the difference between the inundation flows to which the periods T_p and $T_{m-1,0}$ are respectively applied, along with the effect of the wave influence $Ratio$ function (i.e., the difference between the inundation flows to which the linear function and cosine function are respectively applied). The
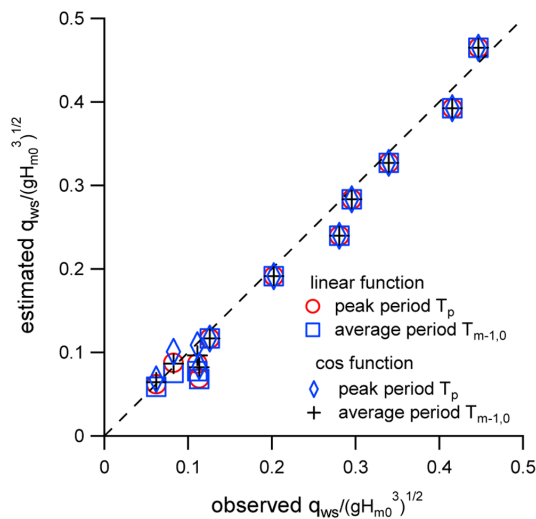

Fig. 2 Comparison of measured values and present estimation for dimensionless inundation flow
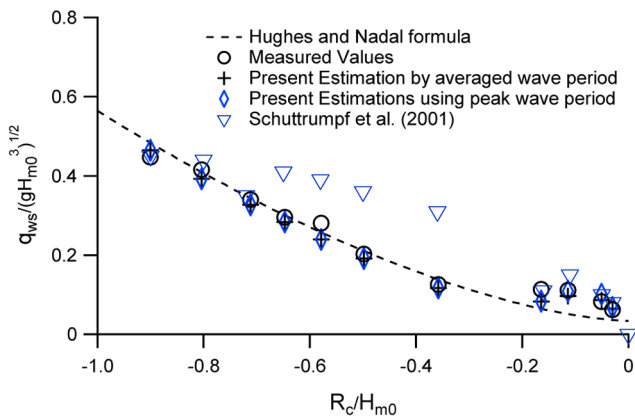

Fig. 3 Comparison of results of Huges and Nadal formula, measured values and present estimation for dimensionless inundation flow

experimental results, including the effects of the waves, were obtained within a range of 0.2 or less of the dimensionless inundation flow on the horizontal axis. As shown in Fig. 2, the choice of the period applied to the calculation had little effect on the estimation of the dimensionless inundation flow.

From the wave influence ($Ratio$) function, it can be seen that the estimated value becomes larger than or equal to the previous value when the cosine function is applied. In addition, a comparison of the experimental and estimated results shows that they are a good match quantitatively. In particular, when T_p was applied as the period and the cosine function was the influence function for waves (diamond symbol in the figure), the agreement with the experimental results was the best.

Fig. 3 shows a comparison of the full-scale experimental results, those of the formula of Hughes and Nadal (2009) shown in Eq. (1), and the estimated results based on the model shown in Eq. (2) as full-scale experimental results in relation to the dimension inundation flow. In the estimated results, the cosine function was applied as the influence function for the waves. The results of the experimental formula, experimental results, and estimated results were a good match, but the observed or estimated results were larger than the results of the experimental formula given by Hughes and Nadal (2009) in the range of $R_c/H_{m0} > -0.2$. Their experimental formula was obtained from experimental results on a 1/25 scale, and the scale effect for waves that could only be expressed in full-scale experiments was found to make a significant difference. The figure also shows the value according to the model of Schuttrumpf et al. (2001), which is the inundation flow calculated as the sum of the overtopping flow at the top elevation and the overflow at the dyke. His estimated results and these estimated results are also a good match in the range of $R_c/H_{m0} > -0.2$. However, under the condition of $R_c/H_{m0} < -0.2$, the estimated results according to Schuttrumpf et al. (2001) were fairly overestimated. This was because Schuttrumpf et al. (2001) did not consider the change in the wave influence according to the dimensionless overtopping depth, but, in such a case, the agreement of the experimental and estimated results at $R_c/H_{m0} < -0.8$ was not explained.

3. Analysis of overtopping-overflow transition according to model topography and marine conditions

3.1 Model topography conditions and marine conditions

Fig. 4 shows the marine conditions and model topographies used for modeling. Here, Fig. 4(a) shows the change in the tidal level with the wave height period. The significant wave height and significant wave period are respectively set to linear ranges of 1-4 m and 4-8 s and then return to their initial values. In addition, Fig. 4(b) shows the conditions of the revetment installed in a location where the front water depth is sufficient. The top elements are set to 6 m and 7 m. In either case, overflow occurs during a storm surge. Fig. 4(c) simulates a coastal sidewall when the normal line is on the shoreline. There are a steep
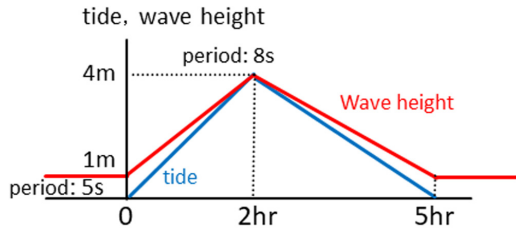
(a) Calculation conditions of wave and tide level
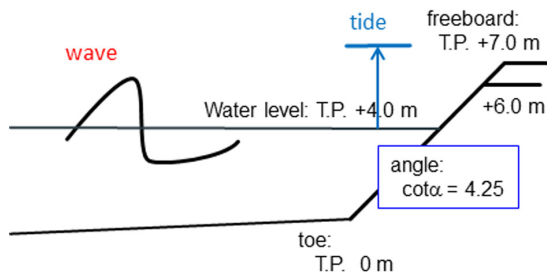
(b) Coastal seawall located under sea
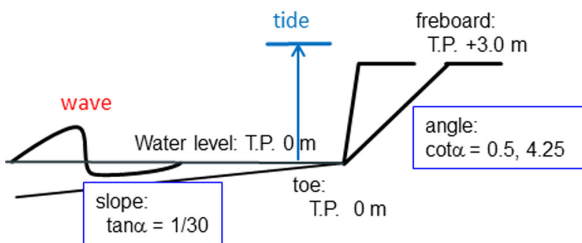
(c) Coastal seawall located on shoreline

Fig. 4 Calculation conditions of model

slope with a value of 0.5 and a gentle slope with a value of 4.25 for the slope inclinations ($\cot\alpha$). In this case, the specifications of the deep-water depth will be used as the specifications of waves at the shore-normal line. Therefore, Eq. (11) is used for the calculation of q_w.

3.2 Computational results and discussions

Fig. 5 shows the change over time of the wave runup height and inundation flow at the coastal shore with a gentle slope placed on the sea side. In relation to the wave runup height in the time zone when the sea level exceeds the top, the runup height (a certain value displaying the revetment top elevation) when the relative top elevation is zero is displayed. Given the inundation due to overtopping as shown in this model, it is possible to properly reproduce the start of flooding even before the start of overflow. When the top elevation is 7 m, the difference between the overflow effects in this model and the experimental formula of Hughes and Nadal (2009) is more clearly seen. In addition, when only the peak of the inundation flow is observed, the inundation flow calculated using the experimental formula of Hughes and Nadal (2009) in Eq. (1) is greater than the amount estimated by this model. This is because Eq. (1) calculates a larger value when only the overflow given in Fig. 1(c) is used in Eq. (1). In their thesis, the overflow flow (tj) is taken from the formula of Henderson (1966), but, the coefficient of the EurOtop (Pullen et al.
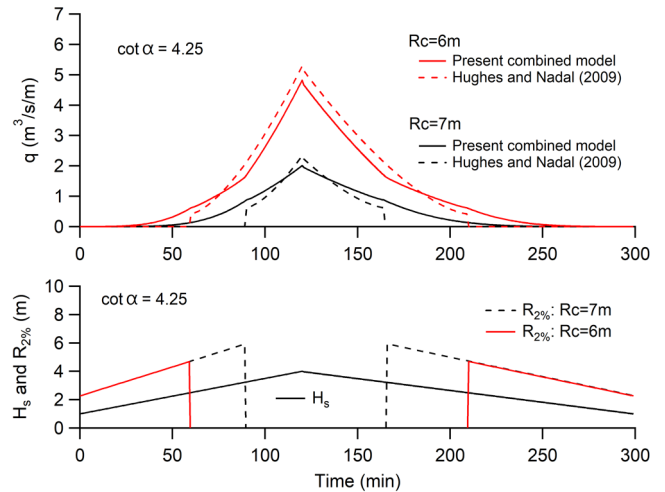
Fig. 5 Wave runup height and inundation flow toward coastal seawall located under sea
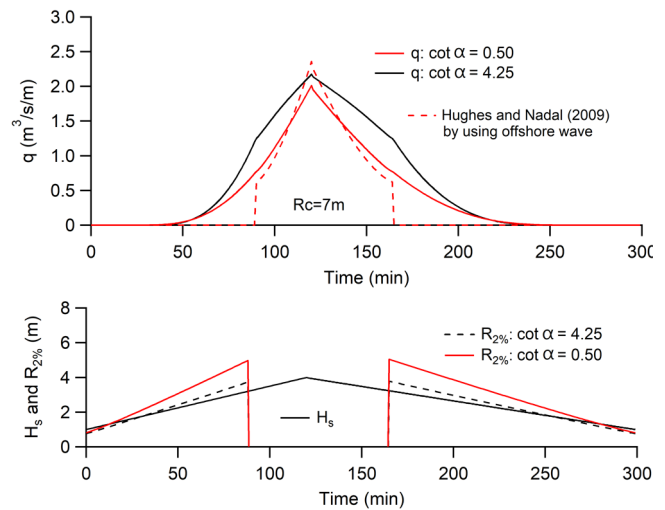
Fig. 6 Wave runup height and inundation flow toward coastal seawall located on shoreline

2007) formula in the first edition is used.

Fig. 6 shows the change over time of the wave runup height and inundation flow at the coastal shore with a gentle slope. The runup height is increased in the shore with a steep slope, but the inundation flow is reduced. These situations exactly reflect the characteristics when the runup height increases for a steep slope, but the overtopping flow decreases along the slope inclination ($\cot\alpha$) as the boundary. The figure maps out the experimental formula of Hughes and Nadal (2009). In this formula, however, the front wave height defined in front of the shore (normal line) is used, but the deep water height is substituted in this figure for convenience. Therefore, it should be noted that it cannot be compared strictly with the IFORM calculation results. However, the estimated result of IFORM is consistent with the experimental formula of Hughes and Nadal (2009) from the stage where the water level exceeds the shore top in the case of a shore with a gentle slope of 0.5. For the peak of the inundation flow, the experimental formula of Hughes and Nadal (2009) provides a slightly

larger value, as shown in Fig. 5.

The cosine function is used for the *Ratio* indicating the wave influence in Eq. (3) for the following reason. When the wave influence (*Ratio*) in Eq. (2) is approximately reduced for R_c/H_{m0} using the exponential or linear function, the contribution from the overtopping flow is rapidly reduced just after the sea level begins to cross the shore top. Meanwhile, the increase in the overflow is small during this time. As a result, the combined flow explained as the sum of both flows becomes smaller than that when the water level is consistent with the shore top and does not match the actual situation. In this case, if a cosine function is used for the expression of *Ratio*, it is possible to express whether the reduction of the overtopping flow proceeds gradually after the water level has crossed the shore top, and the previously indicated physical inconsistency can be avoided.

4. Conclusion

This study approximately evaluated the wave influence in the transitional state when the overtopping and overflow were combined on the basis of the full-scale overtopping-overflow transitional experiments and established an overtopping-overflow model that could accurately reproduce the experimental results in order to improve the accuracy of the storm surge inundation simulation, By applying this model, the wave runup height and inundation flow were calculated with the deviation of the storm surge and change in the wave over time, and the effect of the combined overtopping and overflow fields was examined.

The overtopping-overflow transition model constructed in this study was a combined model that estimated the overtopping flow at a top height of zero and the overflow at a dyke. As a special advantage of this model, the effect of the overtopping flow is properly expressed when the overflow water depth is small, and the characteristics of reducing and eliminating the influence of waves with an increase in the overflow water depth were well reproduced. If the front water depth of a coastal structure is large, the condition of the wave at the front water depth is used. In addition, when it is difficult to calculate the condition of the wave at the normal line installed on an extremely shallow sea or land, it is possible to calculate using the wave depth of the deep sea. Therefore, it is possible to apply under a wide range of installation conditions.

Acknowledgment

References

De Rouck, J., Verhaeghe, H., & Geeraets, J. (2009). Crest Level Assessment of Coastal Structures - General Overview. Coastal Engineering, 56(2), 99-107. https://doi.org/10.1016/j.coastalemg.2008.03.014

Disaster Prevention and Restoration Division, Rural Infrastructure Department, Rural Development Bureau (2015). Guidance for Creating a Storm Surge Inundation Estimation Area Map, 1, 29. Tokyo, Japan: Ministry of Agriculture, Forestry and Fisheries.

Henderson, F.M. (1966). Open Channel Flow. New York: MacMillian.

Honma, H. (1940). The Discharge Coefficient of Low Overflow Weir (Part 2). Journal of Japan Society of Civil Engineers, 26(9), 849-862. http://library.jsce.or.jp/Image_DB/mag/m_jsce/26-09/26-9-12910.pdf

Hughes, S.A. & Nadal, N.C. (2009). Laboratory Study of Combined Wave Overtopping and Storm Surge Overflow of a Levee. Coastal Engineering, 56(3), 244-259. https://doi.org/10.1016/j.coastaleng.2008.09.005

Li, L., Pan, Y., Amini, F. & Kuang, C. (2012). Full Scale Study of Combined Wave and Surge Overtopping of a Levee with RCC Strengthening System. Ocean Engineering, 54, 70-86. https://doi.org/10/1016/j.oceaneng.2012.07.021

Kawai, H., Arikawa, T., Honda, K., Asai, T., Fujiki, T., & Kuwajima, R. (2014). Field Survey on Typhoon 1330 Wind, Wave, Storm Surge Effects on Philippine Ports. Jounal of Japan Society of Civil Engineers, Ser. B2(Coastal Engineering), 70(2), I_1436-I_1440. https://doi.org/10.2208/kaigan.70.I_1436

Mase, H., Tamada, T., Yasuda, T., Hedges, T.S., & Reis, M.T. (2013). Wave Runup and Overtopping at Seawalls Built on Land and in Very Shallow Water. Journal of Waterway, Port, Coastal, and Ocean engineering, 139(5), 346-357. https://ascelibrary.org/doi/10.1061/%28ASCE%29WW.1943-5460.0000199

Mase, H., Yuhi, M., Kim, S., Kawasaki, K., Mixutani, H., & Hiraishi, T. (2018). Transient Wave Runup, Overtopping and Overflow Modelling for Inundation Simulation Due to Storm Surge. Jounal of Japan Society of Civil Engineers, Ser. B2(Coastal Engineering), 74(2), I_553-I_558. https://doi.org/10.2208/kaigan.74.I_553

Matsuzaki, Y., Takahashi, S., Banno, M., Takayama, T., & Goda, K. (2013). Characteristics of Storm Surge Disaster on the U.S. East Coast by Hurricane Sandy. Jounal of Japan Society of Civil Engineers, Ser. B3(Ocean Engineering), 69(2), I_976-I_981. https://doi.org/10.2208/jscejoe.69.I_976

Pullen, T., Allsop, N.W.H., Bruce, T., Kortenhaus, A., Schuttrumpf, H., & Van der Meer, J.W. (2007). EurOtop: European Manual for the Assessment of Wave Overtopping. Wallingford, United Kingdom: HR Wallingford.

Reeve, D.E., Soliman, A., & Lin, P.Z. (2008). Numerical Study of Combined Overflow and Wave Overtopping over a Smooth Impermeable Seawall. Coastal Engineering, 55(2), 155-166. https://doi.org/10.1016/j.coastaleng.2007.09.008

Reis, M.T., Hedges, T.S., Neves, S., Neves, M.G. & Mase, H. (2013). Extending the H&R Wave Overtopping Model to Vertical Structures. Proceedings of International Short Course and Conference on Applied Coastal Reserch, Lisbon, Portugal, 1-10.

Reis, M.T., Hu, K., Hedges, T.S., & Mase, H. (2008). A Comparison of Empirical, Semiempirical, and Numerical Wave Overtopping Models. Journal of Coastal Research, 24(2A), 250-262. https://doi.org/10.2112/05-0592.1

Investigation Team of Coastal Damage from Typhoon Jebi in 2018 (2018). Survey Report on Coastal Damage from Typhoon Jebi in 2018, 5. Japan: Coastal Engineering Committee in Japan Society of Civil Engineers.

Kim, S., Mase, H., Kawasaki, K., Tuhi, M., Mizutani, H., & Hiraishi, T. (2018). Surge-Wave-Tide Prediction Model Including Transient Wave Runup, Overtopping and Overflow Modelling. Jounal of Japan Society of Civil Engineers, Ser. B2(Coastal Engineering), 74(2), I_547-I_552. https://doi.org/10.2208/kaigan.74.I_547

Schuttrumpf, H., Moller, J., Oumeraci, H., Grune, J., & Weissmann, R. (2001). Effects of Natural Sea States on Wave Overtopping of Seadikes. Proceedings of 4th International Symposium on Ocean Wave Measurement and Analysis, 1565-1574. https://doi.org/10.1061/40604(273)158

Suzuki, T., & Shibaki, H. (2010). Numerical Simulation Model for Storm Surge Inundation Incorporating Accurate Estimation of Transition Process from Overtopping to Overflow. Jounal of Japan Society of Civil Engineers, Ser. B2(Coastal Engineering), 66(1), 1301-1305. https://doi.org/10.2208/kaigan.66.1301

Suzuyama, K., Higuvhi, N., & Shibaki, H. (2016). The Numerical Analysis of Overtopping, Overflowing and Transition Process in the Storm Condition. Jounal of Japan Society of Civil Engineers, Ser. B2(Coastal Engineering), 72(2), I_241-I_246. https://doi.org/10.2208/kaigan.72.I_241

Tamada, T., Mase, H., & Yasuda, T. (2015). Integrated Fomula of Wave Overtopping and Runup Modeling for Vertical Seawalls Based on CLASH Datasets. Jounal of Japan Society of Civil Engineers, Ser. B2(Coastal Engineering), 71(2), I_847-I_852. https://doi.org/10.2208/kaigan.71.I_847

Tanaka, Y., Suzuyama, K., Higuchi, N., & Shibaki, H. (2018). Proposal of Wave Overtopping Fomula Using Significant Wave Hright at Toe of Struc-ture for Vertical Seawalls and Unified Fomula for Wave Overtopping and Overflow. Jounal of Japan Society of Civil Engineers, Ser. B2(Coastal Engineering), 74(2), I_1015-I_1020. https://doi.org/10.2208/kaigan.74.I_1015

Takayama, T., Nagai, T., & Nnshida, K. (1982). Decrease of Wave Overtopping Amount due to Seawalls of Low Crest Types. Report of the Port and Harbour Research Institute, 21(2), 151-205.

Van der Meer, J.W., Allsop, N.W.H., Bruce, T., De Rouck, J., Kortenhaus, A., Pullen, T., ... Zanuttigh, B. (2018). EurOtop: Manual on Wave Overtopping of Sea Defences and Related Structures: An Overtopping Manual Largely Based on European Research, but for Worldwide Application (2nd ed.). Retrieved December 2018 from www.overtopping-manual.com

Yuhi, M., Ohtani, N., Mase, H., KIM, S., Umeda, S., & Altomare, C. (2019). Applicability Enhancement of Integrated Fomula of Wave Overtopping and Runup Modeling. Jounal of Japan Society of Civil Engineers, Ser. B2(Coastal Engineering), 75(2), I_739-I_744. https://doi.org/10.2208/kaigan.75.I_739

Author ORCIDs and Contributions

Author name	ORCID	Contributions
Hajime Mase	0000-0002-1232-0795	①②③④⑤
Sooyoul Kim	0000-0002-6727-866X	②③
Makoto Hasegawa	0000-0002-1266-6112	②③
Jae-Hoon Jeong	0000-0003-3134-2102	②③
Jong-Sung Yoon	0000-0002-2382-530X	④⑤

① Conceived of the presented idea or developed the theory
② Carried out the experiment or collected the data
③ Performed the analytic calculations or numerical simulations
④ Wrote the manuscript
⑤ Supervised the findings of this study

Original Research Article

Analysis of Effect on Seawater Flow Change and Circulation Inside Port Due to the Construction of South Breakwater and Weir at Gamcheon Port

Namseeg Hong

Professor, Department of Civil Engineering, Donga University, Busan, Korea

ABSTRACT: *In this study, numerical simulations are used to analyze the effect of the south breakwater and weir on seawater flow change and circulation within the Gamcheon port. Flow patterns in the eastern direction are particularly affected by the breakwater during the ebb tide and current velocity is slightly reduced by construction of the weir. Additionally, seawater circulation is reduced by both features. In order to increase seawater circulation, a seawater flux structure is needed on the west breakwater. A weir-type structure will be more efficient than a seawater flux culvert.*

1. Introduction

Gamcheon Port is located on the eastern side of the southern coast of Korea. Although it is a harbor that supports the Busan Northern Port, it opens to the south, which is its main wave direction. Normally, there is a high appearance ratio of waves with heights exceeding 0.5 m, which is the critical depth for loading medium and large ships. During typhoons, there are many regions in the port where the wave height exceeds 3.0 m. The outer parts of the port open directly to the deep sea, without any natural sheltering topography such as islands. Because the water around Gamcheon Port is deep and the sea bed is mild slope, deep-water waves enter the port entrance without being reduced. In recent years, the cargo volume of the port has increased, as has the number and size of ships that use the port. As such, plans have been examined for rearranging or remodeling the port's existing outer facilities, in order to increase ship navigation safety. Remodeling the port's facilities could also increase harbor tranquility along the outer side of the Gamcheon Port fish market and improve the usage efficiency of the harbor's facilities. Currently, the Gamcheon Port is not sufficiently protected from waves travelling from the south, and specially, Busan Metropolitan city is promoting the construction of a public fish market behind the east breakwater which affects harbor tranquility. The Ministry of Planning and Budget has conducted a feasibility study on maintenance projects for Busan's Gamcheon Port. It was found that the construction of another breakwater was not economically feasible (B/C(Benefit/Cost): 0.46), but it is necessary to

look for alternatives through numerical analysis, hydraulic model experiments, ship handling simulations, etc. Outer facilities, such as the southern breakwater, were constructed to improve the tranquility of Gamcheon Port, in order to revitalize it and boost its level of usage. However, the tidal currents between Dudo Island and Danggangmal are strong, and ship navigation can be hazardous in this area. Accidents have occurred in which ships entering Gamcheon Port have struck the west breakwater (Fig. 1). Because the construction of a south breakwater was expected to exacerbate this phenomenon, a current-reduction facility (weir) was installed between Dudo Island and Danggangmal to mitigate the current.
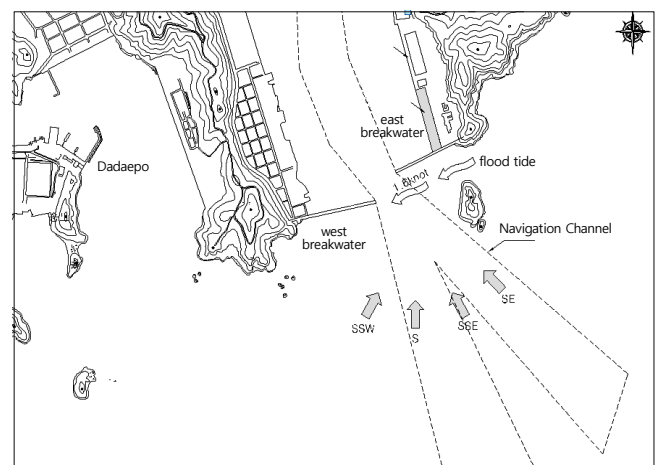

Fig. 1 Area for this study

Before the construction of the south breakwater, seawater circulation in Gamcheon Port was facilitated by inflow between the east and west breakwaters, from the combined action of open-sea waves and tidal currents between Dudo Island and Danggangmal (Fig. 1). However, the construction of the south breakwater weakened the open-sea waves entering the port and the current between Dudo Island and Danggangmal was reduced by the installation of the weir. This unavoidably changed the seawater flow in the port and affected circulation. The installation of a seawater flux structure such as culvert was planned on the existing west breakwater. However, due to concern regarding reduced seawater circulation in the port, it is necessary to review the planned location of this structure. An example of a seawater flux structure installation is the seawater exchange breakwater that was installed in Jumunjin Port, on the east coast of Korea, to improve seawater circulation in the port. Simulations (Oh et al., 2002) were performed to confirm its effectiveness, and it was completed in 2004. It successfully alleviated pollution in Jumoonjin Port by promoting seawater circulation within the port. In addition, studies have examined the effects of seawater flux structures on the circulation of seawater in ports (Kim et al., 2003; Kim and Kim, 2003; Jang et al., 2010). Recently, Hong (2016) examined how seawater circulation is affected by loading and unloading at the pier bridge of the New Busan Port.

The goal of this study is to use a numerical simulation to analyze changes in the port's flow field due to the construction of the south breakwater and weir and to evaluate the efficiency of the seawater circulation flux structure. In the flow model, the weir is seen as a porous plate and depicted using a quadratic loss term. The loss coefficient was applied according to the penetration rate, by calculating the amount of flow penetrating the weir. In addition, the seawater flux structure was regarded as a culvert and various positions along the breakwater were analyzed. Due to the difference in water levels before and after the culvert, 6 different types of flow regimes were classified, and the amount of flow penetrating the submerged culvert was then calculated.

2. Mathematical and Numerical Models

To analyze the port seawater flow, this study used the seawater flow model developed by Hong (2009) and Hong (2012). This model was partially modified for the seawater circulation analysis in order to examine the effects of the weir and the seawater flux structure on the flow field.

2.1 Outline of Mathematical and Numerical Seawater Flow Model

This study used a 3D model that was developed by Hong (2012). The model was verified by comparing its simulation results with field observations (Hong, 2012). The mathematical model uses a σ coordinate system, and its depth-averaged continuous equation in the σ coordinate system is Eq. (1), while the equations for the amount of flow in the horizontal direction ξ and the η direction are Eqs. (2) and (3), respectively.

$$\frac{\partial \zeta}{\partial t} + \frac{1}{\sqrt{J_{\xi\xi}}\sqrt{J_{\eta\eta}}} \frac{\partial \left[(d+\zeta)U\sqrt{J_{\eta\eta}} \right]}{\partial \xi}$$
$$+ \frac{1}{\sqrt{J_{\xi\xi}}\sqrt{J_{\eta\eta}}} \frac{\partial \left[(d+\zeta)V\sqrt{J_{\xi\xi}} \right]}{\partial \eta} = Q \tag{1}$$

Here, $J_{\xi\xi}$ and $J_{\eta\eta}$ are the Jacobian values in the horizontal coordinate system (ξ, η). U and V are the depth-averaged flow rates in the horizontal direction. Q is the inflow and water yield per unit area.

$$\frac{\partial u}{\partial t} + \frac{u}{\sqrt{J_{\xi\xi}}}\frac{\partial u}{\partial \xi} + \frac{v}{\sqrt{J_{\eta\eta}}}\frac{\partial u}{\partial \eta} + \frac{\overline{w}}{d+\zeta}\frac{\partial u}{\partial \sigma} - \frac{v^2}{\sqrt{J_{\xi\xi}}\sqrt{J_{\eta\eta}}}\frac{\partial \sqrt{J_{\eta\eta}}}{\partial \xi}$$
$$+ \frac{uv}{\sqrt{J_{\xi\xi}}\sqrt{J_{\eta\eta}}}\frac{\partial \sqrt{J_{\xi\xi}}}{\partial \eta} - fv = \frac{1}{(d+\zeta)^2}\frac{\partial}{\partial \sigma}\left(\nu \frac{\partial u}{\partial \sigma} \right) + S_{\xi} \tag{2}$$

$$\frac{\partial v}{\partial t} + \frac{u}{\sqrt{J_{\xi\xi}}}\frac{\partial v}{\partial \xi} + \frac{v}{\sqrt{J_{\eta\eta}}}\frac{\partial v}{\partial \eta} + \frac{\overline{w}}{d+\zeta}\frac{\partial v}{\partial \sigma} + \frac{uv}{\sqrt{J_{\xi\xi}}\sqrt{J_{\eta\eta}}}\frac{\sqrt{J_{\eta\eta}}}{\partial \xi}$$
$$- \frac{u^2}{\sqrt{J_{\xi\xi}}\sqrt{J_{\eta\eta}}}\frac{\sqrt{J_{\eta\eta}}}{\partial \eta} + fu = \frac{1}{(d+\zeta)^2}\frac{\partial}{\partial \sigma}\left(\nu \frac{\partial v}{\partial \sigma} \right) + S_{\eta} \tag{3}$$

Here, f is the Coriolis constant. S_{ξ} and S_{η} are the flow source and sink in the ξ and η directions, respectively. u and v are the flow in the horizontal ξ, direction and the η direction, respectively. $\overline{w}$ is the the relative flow in regards to the vertical ζ direction's movement σ plane. It is calculated from the continuous Eq. (1).

The numerical model uses a staggered grid system and the 3D governing equation is finite-difference discretized, in relation to time and space. In the vertical direction, it used a σ coordinate grid with the same number of layers for all areas in the horizontal direction, irrespective of changes in water depth.

The ADI (alternating direction integration) scheme (Leendertse and Gritton, 1971; Leendertse et al., 1973) was used as a basic method for integrating time historical data. A method that improves upon the ADI scheme (Stelling and Leendertse, 1991) was used to perform spatial discretization of the horizontal nonlinear term. The horizontal flows between the vertical layers were coupled with each other due to the vertical nonlinear term and the viscosity term, and fully implicit time integration was performed on the mutually connected vertical terms to remove the instability of solution. Spatial separation was performed by using second-order central differencing on the nonlinear term and first-order central differencing on the viscosity term.

2.2 Weir Modeling

If there are obstacles such as weirs in a flow field, a difference in water levels occurs upstream and downstream from the obstacle. Because of this, a pressure gradient occurs at the location where the weir is installed. However, in flow models, there may be problems

with the solution accuracy, even if the grid intervals are minimized to depict presure gradient on the grid numerically. Therefore, this study considered the weir to be a porous plate and performed parameterization to depict the energy loss caused by the structure at the grid boundaries. That is, energy loss was depicted by adding the quadratic loss term in Eqs. (4) and (5) to the source term in the momentum equations, Eqs. (2) and (3) (Hong et al., 2008).

$$S_\xi = -\frac{c_{loss-u}}{\Delta x} u \sqrt{u^2 + v^2} \tag{4}$$

$$S_\eta = -\frac{c_{loss-v}}{\Delta y} v \sqrt{u^2 + v^2} \tag{5}$$

Here, c_{loss-u} and c_{loss-v} are the energy loss coefficients. Eqs. (4) and (5) show the energy loss caused by the reduced cross section. The subcritical flow caused by the reduced cross section is related to the difference in water levels on either side of the hydraulic structure, and is shown in Eq. (6).

$$Q = \mu A \sqrt{2g|\zeta_u - \zeta_d|} \tag{6}$$

Here, $\mu(0 \leq \mu \leq 1)$ is the cross section reduction coefficient. A is the wet area. ζ_u and ζ_d are the water levels upstream and downstream of the weir, respectively. Both sides of Eq. (6) are squared and divided by $2\mu^2 A^2 \Delta x$ to create Eq. (7). Making the right side of Eq. (7) equal to Eq. (4) results in Eq. (8).

$$g\frac{\zeta_u - \zeta_d}{\Delta x} = \frac{Q^2}{2\mu^2 A^2 \Delta x} \tag{7}$$

$$g\frac{\zeta_u - \zeta_d}{\Delta x} = \frac{Q^2}{2\mu^2 A^2 \Delta x} = \frac{c_{loss-u}}{\Delta x} u|\vec{u}| \tag{8}$$

The relational equation in Eq. (9) can be found by comparing the second and third terms in Eq. (8). If the contraction coefficient is known from this relational equation, the energy loss coefficient can be determined.

$$c_{loss-u} = \frac{1}{2\mu^2} \tag{9}$$

However, it is not easy to calculate the contraction coefficient for a porous plate, unlike a regular plate that blocks the front of the flow. For this study we selected a method that calculates the contraction coefficient directly from the results of tank experiments, using the relationship between the first and third terms in Eq. (8).

2.3 Seawater Flux Structure Modeling

The seawater flux structure was regarded as a culvert, and the flow passing through it can be calculated using Eq. (10) due to the difference between the water levels upstream and downstream of the culvert.

$$Q = \mu A \sqrt{2gMAX(0, \zeta_{intake} - \zeta_{outlet})} \tag{10}$$

Here, μ is the culvert loss coefficient (dimensionless). A is the area of the culvert opening (in m2). ζ_{intake} and $\zeta_{culvert}$ are the water levels at the intake and outlet, respectively.

The flow can penetrate only part of the culvert's cross section due to its installation location, slope, etc., and several flow regimes can occur in the culvert. Eqs. (11) and (12) define the water levels upstream and downstream from the culvert. Eqs. (14) to (19) depict the classification of 6 types of flow regimes within the culvert according to the water level limit defined in Eq. (13) (Jagers and van Schijndel, 2000).

$$\zeta_{ups} = \max(0, \zeta_{intake} - \zeta_{culvert}) \tag{11}$$

$$\zeta_{downs} = \max(0, \zeta_{outlet} - \zeta_{culvert}) \tag{12}$$

$$H_c = \sqrt[3]{\frac{Q^2}{gW^2}} \tag{13}$$

Here, H_c is the critical depth and $\zeta_{culvert}$ is the culvert's vertical location. ζ_{ups} and ζ_{downs} are the culvert's upstream and downstream tide levels, while W is the culvert's width. In Eqs. (14) and (19), H^* is the modified depth, and L is the length of the culvert. n is Manning's coefficient (in m$^{1/3}$/s). c$_D$$^{1/2/33}$ is the discharge coefficient and α is the energy loss correction coefficient.

Type 1 (Supercritical flow with critical depth at intake; steep culvert slope)

$$Q = \mu(H^*) H_c W \sqrt{2g(\zeta_{ups} - H_c)} \ \ with \ \mu(H^*) = c_D^1 \tag{14}$$

Type 2 (Supercritical flow with critical depth at outfall; mild culvert slope)

$$Q = \mu(H^*) H_c W \sqrt{2g(\zeta_{ups} - H_c)} \ \ with \ H^* = 0.5H_c + 0.5\zeta_{ups}$$

$$\mu(H^*) = c_D^1 / \sqrt{\left(1 + \left\{\frac{2gLn^2}{(R^*)^{4/3}} + \alpha\right\}(c_D^1)^2 \left(\frac{H_c}{H^*}\right)^2\right)} \ and \ R^* = \frac{H^* W}{2H^* + W} \tag{15}$$

Type 3 (Tranquil flow)

$$Q = \mu(H^*) \zeta_{downs} W \sqrt{2g(\zeta_{intake} - \zeta_{outlet})} \ \ with \, H^* \ 0.5\zeta_{ups} + 0.5\zeta_{downs}$$

$$\mu(H^*) = c_D^1 / \sqrt{\left(1 + \left\{\frac{2gLn^2}{(R^*)^{4/3}} + \alpha\right\}(c_D^1)^2 \left(\frac{\zeta_{downs}}{H^*}\right)^2\right)} \ and \ R^* = \frac{H^* W}{2H^* + W} \tag{16}$$

Type 4 (Submerged flow)

$$Q = \mu(H^*) H W \sqrt{2g(\zeta_{intake} - \zeta_{outlet})} \ \ with \, H^* = H$$

$$\mu(H^*) = c_D^2 / \sqrt{\left(1 + \left\{\frac{2gLn^2}{(R^*)^{4/3}} + \alpha\right\}(c_D^2)^2\right)} \ and \ R^* = \frac{HW}{2H + 2W} \tag{17}$$

Table 1 Flow regime due to water level differences on either side of the culvert

Type	Flow regime	Conditions			
		ζ_{ups}	ζ_{downs}	ζ_{downs}	other
1	Supercritical flow with critical depth at intake	$< 1.5H$	$\leq H$	$\leq H_c$	$S_0 > S_c$
2	Supercritical flow with critical depth at outlet	$< 1.5H$	$\leq H$	$\leq H_c$	$S_0 \leq S_c$
3	Tranquil flow	$< 1.5H$	$\leq H$	$> H_c$	
4	Submerged flow	$> H$	$> H$		
5	Rapid flow at inlet	$\geq 1.5H$	$\leq H$	$\leq H_c$	
6	Full flow free at outlet	$\geq 1.5H$	$\leq H$	$\geq H_c$	

S_0: Slope of the culvert, S_c: Critical slope

Type 5 (Rapid flow at inlet)

$$Q = \mu(H^*)\, H\, W\, \sqrt{2g\zeta_{ups}} = with\; \mu(H^*) = c_D^3 \quad and\; H^* = H \qquad (18)$$

Type 6 (Full flow free at outlet)

$$Q = \mu(H^*)\, H\, W\, \sqrt{2g\,(\zeta_{ups} - H)} \;\; with\; H^* = H$$

$$\mu(H^*) = c_D^2 \Big/ \sqrt{\left\{1 + \left\{\frac{2gLn^2}{(R^*)^{4/3}} + \alpha\right\}(c_D^2)^2\right\}} \;\; and\; R^* = \frac{HW}{2H + 2W} \qquad (19)$$

The amount of flow is calculated according to the flow classification in Eqs. (14) to (19), and the flow regime classifications are shown in Table 1. As shown in Table 1, the flow regimes are classified according to the range of water levels upstream and downstream of the culvert.

3. Establishing the Numerical Model

3.1 Establishing the Seawater Flow Model

As shown in Fig. 2, a variable grid system was used as the wide area grid for the seawater flow numerical model experiments. The grid interval was variable, and had a default value of 250 m with a dx of 200–500 m and a dy of 300–600 m. For open boundary conditions of the target sea area, Matsumoto et al. (2005) created a simulation using TOPEX Poseidon satellite depth data and used the results to construct a partial tide table, from which 16 partial tide values (2N2, J1, K1, K2, L2, M1, M2, MU2, N2, NU2, OO1, O1, P1, Q1, S2, T2) were selected for this model. For the eddy viscosity, 10m2/s was used uniformly across the entire wide area. For the floor frictional force, 45m$^{1/2}$/s was used for the entire sea area, based on the Chezy equation. The wind data in this study was sourced from observational data recorded in Busan Port between 2016 and 2018, and was applied uniformly to the entire sea during whole time. The friction coefficient between the wind and sea surface was set as 0.0026. To verify and certify the established wide area model, the observed tide level and flow rate field, from points P1 to P4

in Fig. 3, were compared with the calculated values from the seawater flow numerical experiments performed in this study, as shown in Fig. 4.
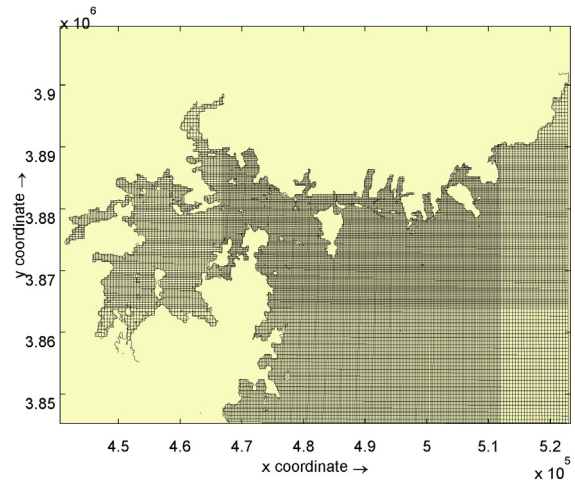
Fig. 2 Coarse grid system
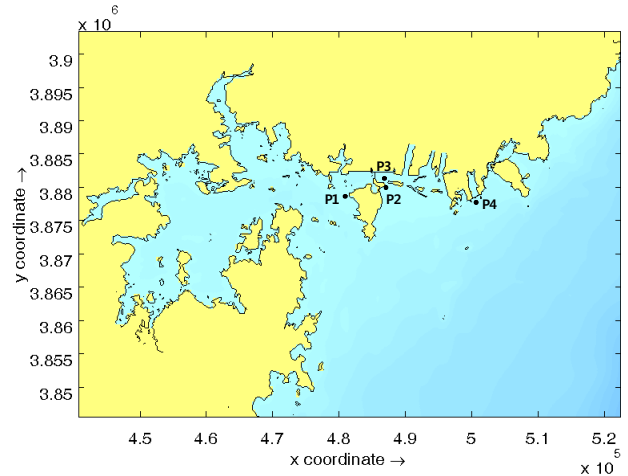
Fig. 3 Position for model verification
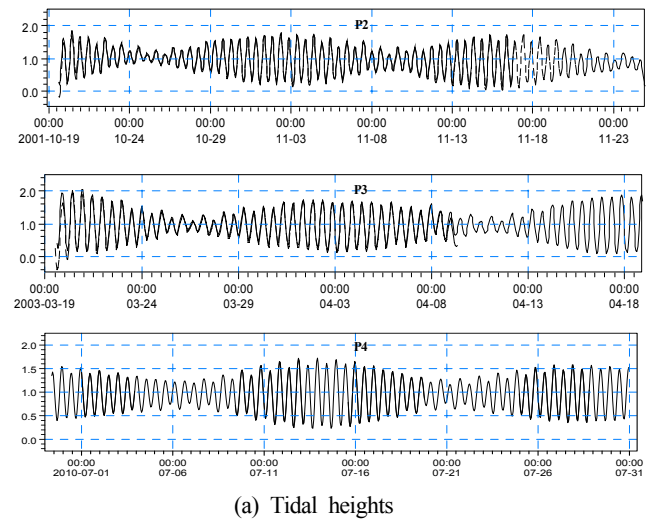
(a) Tidal heights

Fig. 4 Model calibration through comparisons between measured results (dotted line) and simulation results (solid line) (continuation)
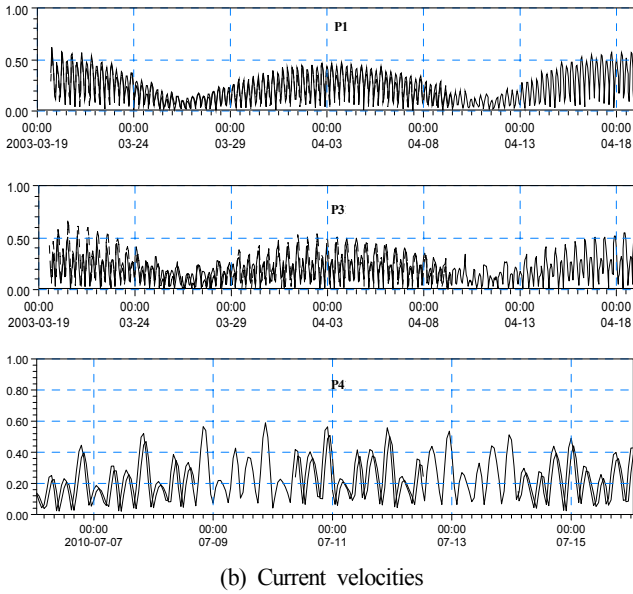
(b) Current velocities

Fig. 4 Model calibration through comparisons between measured results (dotted line) and simulation results (solid line)
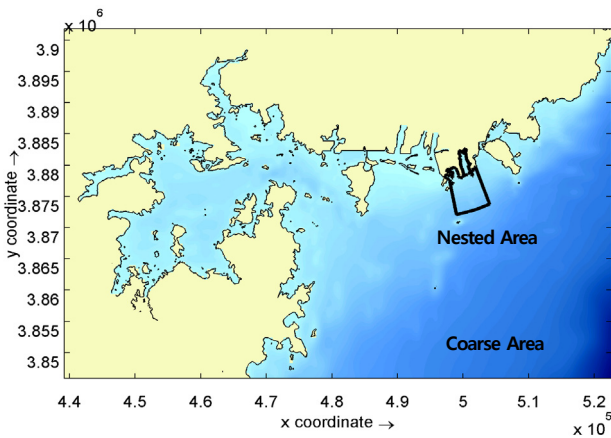
Fig. 5 Coarse and Nested grid
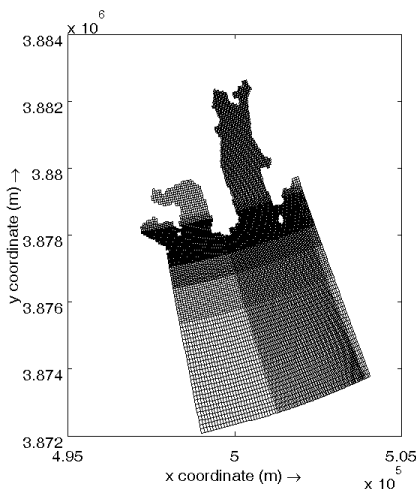
Fig. 6 Nested grid system

From the regional results, the boundary conditions of the specific areas were transferred as shown in Fig. 5, and seawater flow

simulations were performed on specific areas. The specific area grid system that was selected for the seawater flow numerical model experiments was a variable grid system with a dx grid interval of 20–100 m and a dy of 15–100 m, as shown in Fig. 6. The eddy viscosity of the entire area was set as 5 m^2/s. The floor frictional force was set as 30 $m^{1/2}$/s for the entire sea area, based on the Chezy equation. The same observational wind data, from 2016–2018 in Busan Port, was again applied uniformly to the entire sea area over time. The friction coefficient between the wind and the sea surface was set as 0.0026.

3.2 Calculating the Weir Loss Coefficient

When the quadratic loss term in Eqs. (4) and (5) is used to depict submerged structures in the flow model, the most important element is a rational calculation of the loss coefficient, c_{loss}. This study calculated the amount of flow that penetrated the weir (illustrated in Fig. 7) and applied the loss coefficient that resulted from the penetration ratio. For example, when the target penetration ratio was 50%, the numerical model experiments were performed by changing the loss coefficient until the amount of penetrating flow over the course of 14 days was 50% of the flow before and after the installation of the weir. Fig. 8 shows the change in flow before and after weir installation. The loss coefficients, calculated via the method above, were 2.1, 1.1, and 0.58 when the weir penetration ratios were 50%, 65%, and 80%, respectively.
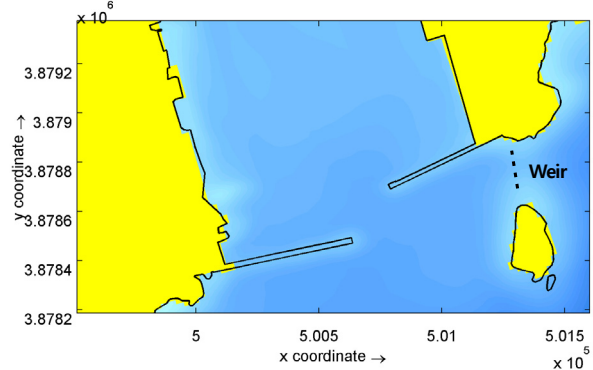
Fig. 7 Position of weir
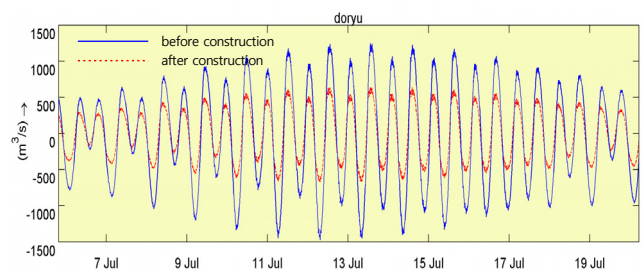
Fig. 8 Change of discharge according to construction of weir

3.3 Calculating the Seawater Flux Flow of culvert due to Waves and Applying It to the Flow Mode

When the culvert was added to the model to simulate the installation of a seawater flux structure at the east breakwater, the difference in

water level on either side of the culvert were mainly due to waves, rather than tides, and this created flow in the seawater flux structure. However, when a numerical model experiment is performed for a long period, as is the case with the seawater flow model, it is inefficient to use an integral time applied to short periods such as waves. Therefore, we calculated the 6 types of culvert flow regimes from the tide model, by using the mean wave height of the integral period for the sea-facing side of the breakwater, and the tide level height for the port-facing side. The amount of penetrating flow was then calculated, and these values were used as the source and sink in the seawater flow numerical model experiments (Fig. 8).

4. Results Analysis

4.1 Changes in Seawater Flow Around the Breakwater due to the South Breakwater and Weir

Numerical model experiments were conducted on the 5 scenarios shown in Table 2 in order to examine how the flow field of the surrounding ocean area was affected by the construction of the south breakwater and the weir between Dudo Island and the east breakwater. Figs. 9 to 13 show the flow fields for each experiment case, during ebb and flood tides. In Case 2, in which only the south breakwater had been built, it can be seen that during flood tide, the flow direction at sea area between main ground and Dudo was not very different to the tangential direction of the south breakwater, and the south breakwater did not have a large effect, compared to the scenario before its construction. However, during the ebb tide, the eastward flow was affected by the south breakwater. Also, in the cases where the weir was constructed (Case 3, Case 4, Case 5), the overall flow was not changed, but the weir reduced the flow rate on either side of it. The weir affected

Table 2 Numerical model scenarios for the investigation of the effects of south breakwater and weir on flow

Case	Condition
1	Without south breakwater and weir
2	South breakwater
3	South breakwater + Weir (penetration ration 0f 50%)
4	South breakwater + Weir (penetration ration 0f 65%)
5	South breakwater + Weir (penetration ration 0f 80%)

(a)   (b)
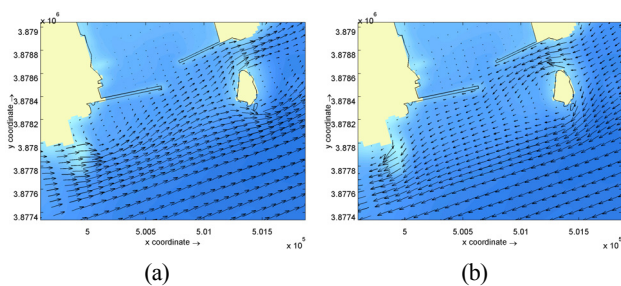
Fig. 9 Flow velocity field for Case 1 during (a) ebb tide and (b) flood tide

(a)   (b)
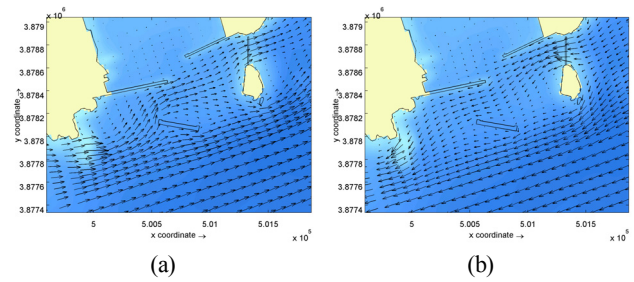
Fig. 10 Flow velocity field for Case 2 during (a) ebb tide and (b) flood tide

(a)   (b)
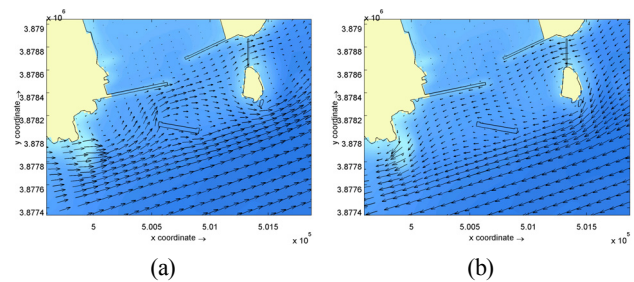
Fig. 11 Flow velocity field for Case 3 during (a) ebb tide and (b) flood tide

(a)   (b)
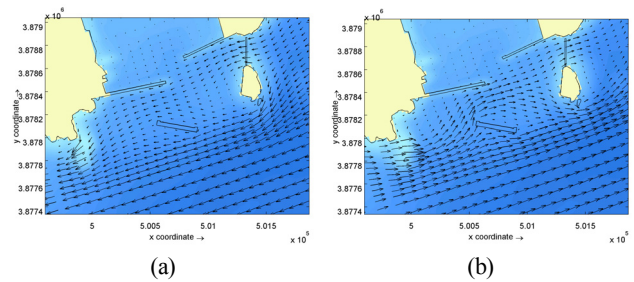
Fig. 12 Flow velocity field for Case 4 during (a) ebb tide and (b) flood tide

(a)   (b)
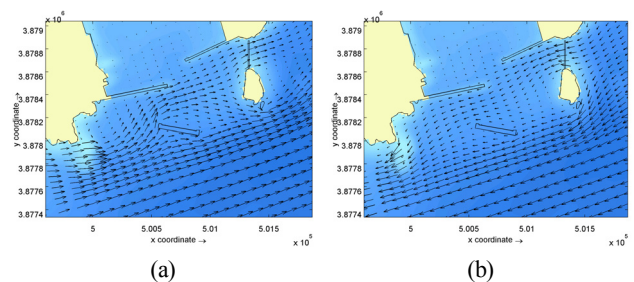
Fig. 13 Flow velocity field for Case 5 during (a) ebb tide and (b) flood tide

the port entrance area slightly. This effect increased marginally when the penetration ratio was increased from 50% to 65%, and to 80%.

As mentioned before, the flow rate at the Gamcheon Port entrance waterway increased as a result of the construction of the south breakwater, and this affected ships entering and exiting the harbor. Therefore, in order to control the flow rate around the port entrance, a weir was installed at the north end of Dudo Island, and its construction

is linked to a change in flow rate around the port entrance. The flow rate around the south breakwater was quantified and examined at the locations in Fig. 14. The strongest flow rates at each point are shown in Table 3. At PC1 (the front of the west breakwater) the flow was greater in Case 2 than in Case 1, due to the construction of the south breakwater. However, as seen in Cases 3, 4, and 5, the flow rate decreased after the weir was installed. In the case with a low penetration ratio (Case 3), it decreased further. At point PC2 (port entrance), a phase difference occurred due to the combined effect of the south breakwater and the weir, and no clear increase or decrease occurred. The flow rate was less than 0.3 m/s. However, at point PC3 (the front of the east breakwater), the strongest flow rate increased to 0.49 m/sec due to the effect of the south breakwater. At points PC4 (between Dudo Island and the south breakwater) and PC5 (the front of the south breakwater), the flow decreased in comparison to Case 1, due to the shadow effect of the south breakwater. The amount of decrease was determined by the south breakwater rather than the effect of the weir.
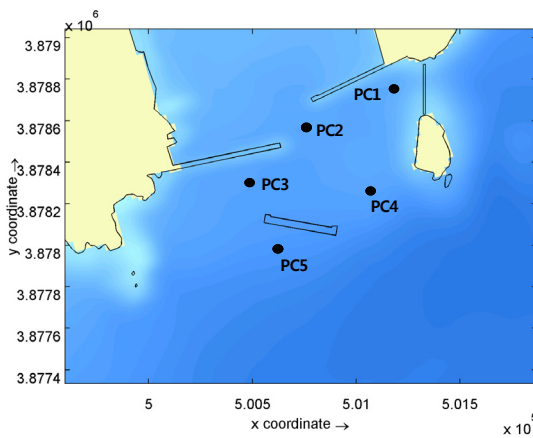
Fig. 14 Designated positions of calculating current velocity

Table 3 Magnitude of maximum current velocity at a designated position in Fig. 13 (unit: m/s)

Case	Condition	Tide	Maximum current velocity				
			PC-1	PC-2	PC-3	PC-4	PC-5
1	Without south breakwater and weir	Flood	0.60	0.31	0.23	0.10	0.32
		Ebb	0.53	0.21	0.24	0.36	0.57
2	South breakwater	Flood	0.66	0.30	0.34	0.08	0.22
		Ebb	0.55	0.26	0.49	0.17	0.40
3	South breakwater + Weir (penetration ration of 50%)	Flood	0.24	0.19	0.22	0.07	0.25
		Ebb	0.19	0.15	0.41	0.20	0.39
4	South breakwater + Weir (penetration ration of 65%)	Flood	0.36	0.22	0.27	0.08	0.26
		Ebb	0.28	0.14	0.45	0.22	0.38
5	South breakwater + Weir (penetration ration of 80%)	Flood	0.47	0.23	0.29	0.08	0.25
		Ebb	0.36	0.20	0.47	0.20	0.39

(a) Case 1   (b) Case 2

(c) Case 3   (d) Case 4

(e) Case 5
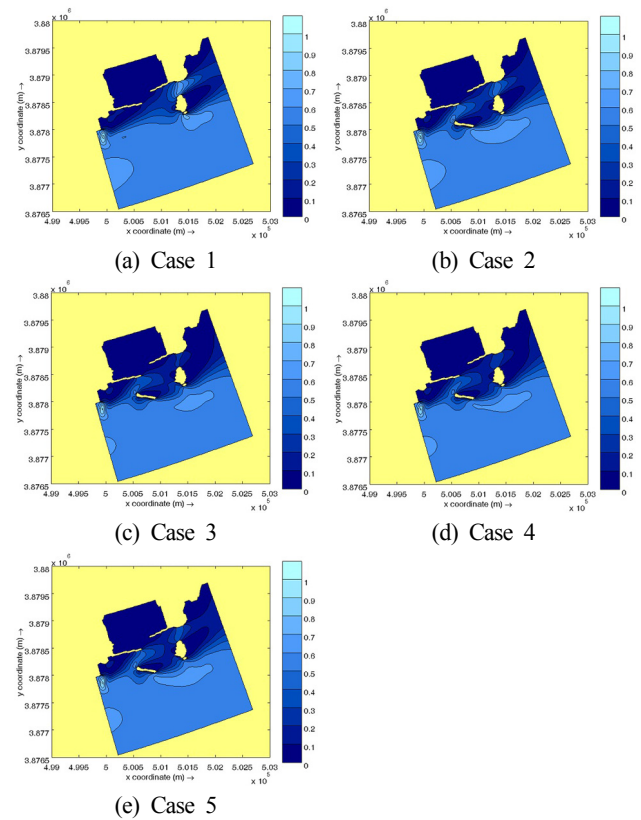
Fig. 15 Maximum ebb current velocity

The flow rate distribution during the strongest ebb tide is shown in Fig. 15. Compared to Case 1, Case 2 showed flow rate changes around the south breakwater, and Cases 3, 4 and 5 show changes in the flow field around the weir. Also, it was found that the trends were very similar to those of the flood tides. That is, during flood tide, the flow direction at northern sea area of Dudo was not very different from the tangential direction of the south breakwater, and the effect of the south breakwater was not large. However, during ebb tide, the eastward flow was affected by the south breakwater. In addition, when the weir was constructed, the overall flow was not changed, but the weir reduced the flow rate on either side of it. The weir affected the port entrance area slightly. This phenomenon tended to occur slightly more when the penetration ratio was increased from 50% to 65% and 80%.

4.2 Effect of Construction of the South Breakwater and Weir Construction on Port Seawater Circulation

This study examined the changes in flow rate at the port entrance due to the construction of the south breakwater and weir, and the resulting effects on port seawater circulation. The effects of culvert to be installed at the west breakwater were also examined. To examine seawater circulation, this study performed a drogue drop experiment (Fig. 16(a)), which is a particle tracking method. 128 drogues were dropped into the port and one month later their positions and the number of drogues remaining in the port were noted, to estimate the transport patterns of materials that are dropped in the port. In order to conduct detailed quantitative port seawater exchange experiments

while considering the circulation patterns obtained from the drogue drop experiment, we used a COD (Chemical oxygen demand) diffusion simulation, which only considers the physical dispersal process. To calculate the seawater exchange rate, the initial COD concentration in the Gamcheon Port was set at 100 ppm, and the changes in concentration after one month were measured at 27 major points in the port, as shown in Fig. 16(b). The model developed by Hong (2010a) and Hong (2010b) was used in the COD concentration diffusion simulation.

Fig. 17 shows the simulated drogue locations after 1 month for the cases shown in Table 4. Due to the construction of the breakwater, the amount of inflow into the port was reduced. In Case 2, a larger number of drogues remained in the port, and they were distributed over a larger area, while the seawater circulation was lower than in Case 1. When seawater flux structures were installed at the center part of the west breakwater (Case 3) and the head of the breakwater (Case 4) to improve seawater circulation, the number of drogues was the same as in Case 2, but the distribution area was slightly different.

This shows that seawater flux structures are somewhat effective in improving seawater circulation. As such, there is a need to quantitatively examine these seawater circulation improvements. To do this, COD concentration changes were examined, as mentioned previously.

(a)   (b)
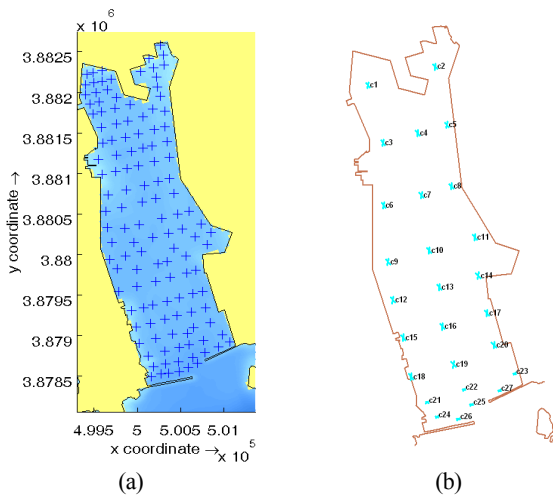
Fig. 16 Numerical experiment for the investigation of seawater circulation in port (a) Drogue drop experiment (+: initial drogue position), (b) position for the investigation of COD concentration

Table 4 Numerical experimental cases for the investigation of seawater change

Case	Condition
1	Without south breakwater and weir
2	South breakwater + Weir (penetration ration 0f 50%)
3	Case1 + Center of west breakwater for seawater change zone
4	Case1 + Head of west breakwater for seawater change zone

(a)   (b)   (c)   (d)
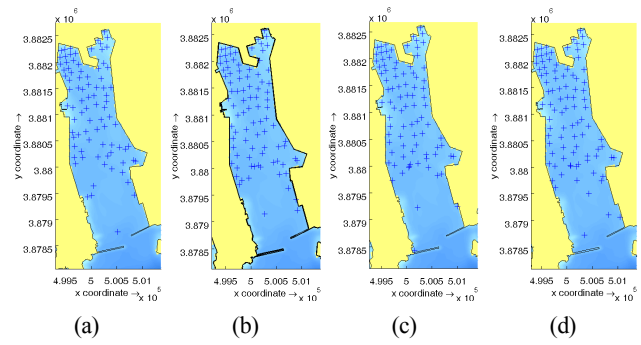
Fig. 17 Drogue positions 1 month into simulation

The initial COD concentration in Gamcheon Port was set at 100 ppm, and the concentration changes at major points in the port were examined after 1 month simulation, to examine how seawater circulation is affected by factors such as the south breakwater, the location of the seawater flux structure, the scale of the seawater flux structure, the weir penetration ratio, and the weir overflow amount. Fig. 18 shows the concentration distribution after one month in the scenario with the south breakwater and weir (penetration ratio of 50%), before and after construction. It was found that the overall COD concentration in the port increased due to the construction of the south breakwater and the weir.

To provide a quantitative examination, Table 5 shows the concentration changes at the examination points in Fig. 16(b) after one month, with and without the breakwater and weir construction. The final column of Table 5 depicts the change in concentration between these scenarios as a percentage [= 100 × (concentration after installation − concentration before installation) / concentration before installation]. The concentration increase ratios show that closer to the west breakwater, the increases in concentration tend to be larger. This means that the construction of the south breakwater and weir caused

(a)   (b)
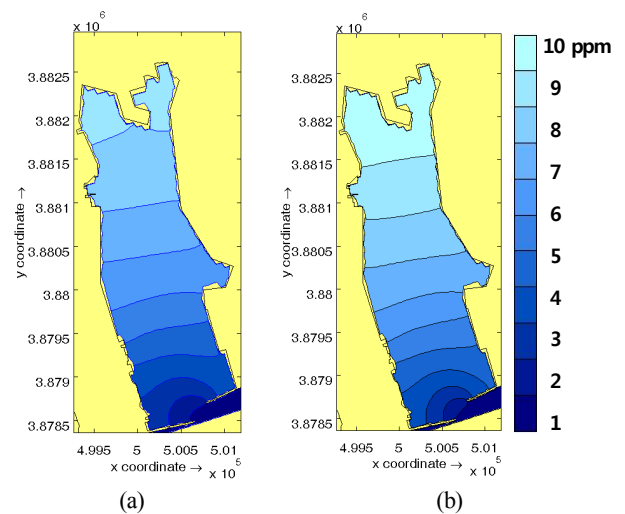
Fig. 18 Change in COD concentration after 1 month of COD simulation (a) before construction of south breakwater and weir, and (b) after construction of south breakwater and weir, with 50% penetration ratio

the overall seawater circulation pattern at the port entrance to flow in a clockwise direction.

As mentioned above, the seawater circulation pattern in the port changed to a clockwise direction due to the construction of the south breakwater. The seawater flux structure should therefore be installed on the west breakwater. It is necessary to examine how the change in COD concentration, before and after construction, varies according to the different locations and scales of the seawater flux structure. Fig. 19 shows the different positions of the seawater flux structure (west, east, center). The scale was increased to 130% and 150% when the structure was located in the center of the west breakwater. Fig. 20 shows the concentration increase ratios obtained from major points in the simulation, with the seawater flux structure at different locations. In terms of seawater circulation in the port, it is most advantageous to

Table 5 Change of COD concentration after 1 month of COD simulation

Position	Before construction of south breakwater and weir (ppm)	After construction of south breakwater and weir of 50% penetration ratio (ppm)	Percentage change from column 1 to column 2 (%)
c1	9.14	10.43	14.11
c2	9.31	10.62	14.07
c3	8.70	9.96	14.48
c4	8.73	9.99	14.43
c5	8.77	10.04	14.48
c6	7.69	8.87	15.34
c7	7.81	9.00	15.24
c8	7.86	9.05	15.14
c9	6.71	7.81	16.39
c10	6.76	7.87	16.42
c11	6.91	8.01	15.92
c12	5.94	7.00	17.85
c13	5.90	6.92	17.29
c14	6.17	7.19	16.53
c15	4.88	5.88	20.49
c16	4.78	5.72	19.67
c17	4.88	5.85	19.88
c18	3.54	4.48	26.55
c19	3.41	4.21	23.46
c20	4.14	4.88	17.87
c21	2.71	3.61	33.21
c22	2.23	2.83	26.91
c23	3.55	4.19	18.03
c24	2.34	3.19	36.32
c25	1.35	1.80	33.33
c26	1.55	2.28	47.10
c27	2.99	3.49	16.72
Average	5.51	6.49	17.76

Fig. 19 Position of seawater flux structure (p1: West, p2: Center, p3: East)
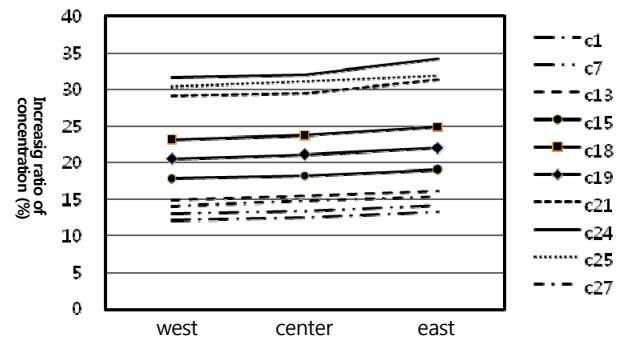
Fig. 20 Variation of concentration increase ratio with position of seawater flux structure
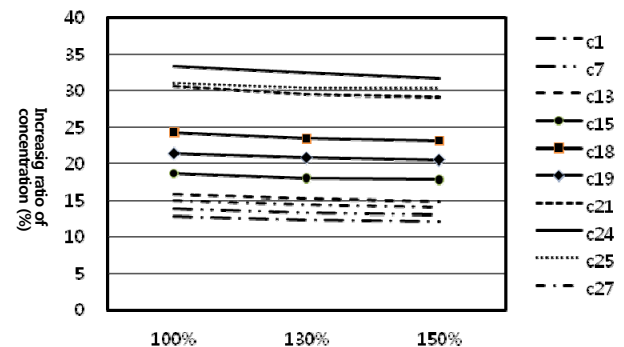
Fig. 21 Variation of concentration increase ratio with size of seawater flux structure

install the seawater flux structure on the western end of the west breakwater. Fig. 21 shows the variation in concentration increase ratios, obtained from major points in the simulation, according to increases in the cross-sectional area of the seawater flux structure. As the area increased, the change in COD concentration decreased, and the seawater circulation in the port improved. However, with the exception of some points, the decrease was slight, and the degree of improvement was not large.

Fig. 22 shows the variation in the concentration increase ratio due to changes in the weir penetration ratio. As the penetration ratio increased, the concentration increase ratio rapidly decreased, and the
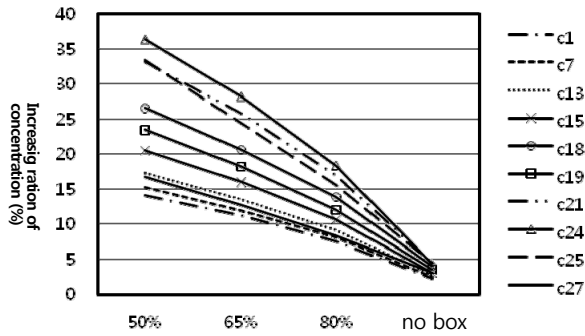
Fig. 22 Variation in concentration increase ratio due to changes in penetration ratio of seawater flux structure
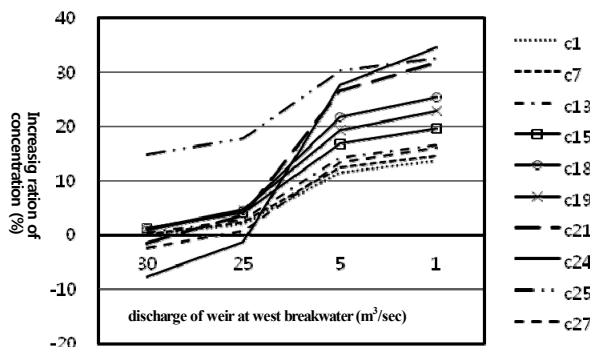
Fig. 23 Variation in concentration increase ratio due to increasing discharge of at west breakwater

seawater circulation in the port was effectively improved. It is believed that this occurred because the westward flow rate increased during the flood tide, and inflow through the port entrance increased as the weir's penetration ratio increased.

The seawater flux structure that was installed to improve seawater circulation in the port depends on open sea waves because it operates based on the upstream/downstream difference in water levels that is mainly caused by waves. In contrast, a weir can continuously provide flow to the port because the flow that is accumulated within the structure due to waves is released into the port. Therefore, this study calculated the percentage change in COD concentration within the port after construction of the south breakwater and weir, while altering the amount of flow provided by the weir to the port. The flow that was supplied to the port was treated as the flow source. The weir was located on the western end of the west breakwater, based on the improvement created by the seawater flux structure being placed there. Fig. 23 shows the variation in concentration increase ratio due to the amount of flow provided by the weir. As the flow provided by the weir increased, there was a greater improvement in the seawater circulation in the port.

The results above show that the most efficient method for improving circulation of the Gamcheon port seawater is to increase the weir's penetration ratio as much as possible. Increasing the cross-sectional area of the seawater flux structure did not cause a large improvement in seawater circulation. However, when the amount of flow provided by the weir was increased, there was a clear improvement in seawater

circulation. Therefore, it is beneficial to use an weir at the west side of the west breakwater, while properly controlling the amount of provided flow, rather than using a seawater flux structure. Increasing the weir's penetration ratio as much as possible, in limited circumstances, is beneficial for improving seawater circulation in the port.

5. Conclusions

This study analyzed the nearby sea flow changes caused by the construction of the south breakwater and weir at Gamcheon Port. The results showed that when the south breakwater was constructed, the flow direction from Dudo Saigol during a flood tide was not very different from the tangential direction of the south breakwater, and the effect of the south breakwater was not large. However, during ebb tide, the eastward flow was affected by the south breakwater. In addition, when the weir was constructed, the overall flow was not changed, but the flow rate on either side of the weir was reduced. The weir affected the port entrance area only slightly, but the effect was slightly greater when the penetration ratio was increased from 50%, to 65%, and to 80%.

In addition, this study examined the effects of the south breakwater and weir construction on port seawater circulation caused by changes in the flow rate at the port entrance. The results show that there is a need to install a seawater flux structure to prevent pollution problems occurring due to reduced seawater circulation in the port. The most efficient method for improving seawater circulation in the port is to increase the penetration ratio of the weir. Increasing the cross-sectional area of the seawater flux structure did not cause a large improvement in seawater circulation. However, when the amount of flow that was provided by the weir was increased, there was a clear improvement in seawater circulation. Therefore, it is beneficial to use an weir at the west side of the west breakwater while properly controlling the amount of provided flow, rather than using a seawater flux structure. Increasing the weir's penetration ratio as much as possible, in limited circumstances, is beneficial for improving seawater circulation in the port.

References

Hong, N.S., Kim, G.Y., & Kang, Y.G. (2008). Three Dimensional Numerical Model for Flow with Silt Protector. Journal of Ocean Engineering and Technology, 22(3), 1-7.

Hong, N.S. (2009). Three Dimensional Numerical Model for Flow with Floating Structures Using Rigid Lid Boundary Condition. Proceedings of KOASTS, Changwon, Korea.

Hong, N.S. (2010a). The 4th Project Report of Research and Development for Ocean Environmental Hyraulics of Busan New Port - Spreading of Suspended Sediment and Morphological Change. Busan Port Construction Office, Miinistry of Ocean and Fisheries.

Hong, N.S. (2010b). Investigation of Reducing Characteristics for the

Spreading of Dredging Soil and the Diffusion of Contaminant by Silt Protector Curtain through Three Dimensional Numerical Model Experiment. Journal of Ocean Engineering and Technology, 24(4), 78-85.

Hong, N.S. (2012). The Application of Rigid Lid Boundary Condition for Three Dimensional Flow Analysis beneath the Floating Structure. Journal of Ocean Engineering and Technology, 26(5), 55-62.

Hong, N.S. (2016). Effect of Consecutive Ship Docking and Undocking on Seawater Circulation in Harbor. Journal of Ocean Engineering and Technology, 30(3), 177-185. https://doi.org/10.5574/KSOE.2016.30.3.177

Jagers, H.R.A., & van Schijndel, S.A.H. (2000). 3D Computations around Structures (Technical Report Q2487). WL | Delft Hydraulics, Delft, The Netherlands, In Dutch (3D Rekenen Rondom Constructies), 543.

Jang, C.H., Kim, S.T., Kim, H,S. Kim, K,H. & Song, M.S. (2010). Efficiency Tests of Seawater Exchange System for Enhancement of Seawater Quality. Journal of Korean Society for Marine Environmental and Energy, 13(3), 206-215.

Kim, K.M., Kang, S.H., Ryu, H.S., & Kim, S.H. (2003). A Study on Environmentally Friend Counter Facilities for Improvement of Harbor Water Quality. Journal of Korean Navigation and Port Research, 27(2), 233-238. https://doi.org/10.5394/KINPR.2003.27.2.233

Kim, H.M and Kim, K.H. (2003). Hydraulic Character of the Breakwaters with a Function of Water Exchange Using Hydraulic Model Eests. Proceedings of the Korean Society of Coastal and Ocean Engineers Conference, August, 124-129.

Leendertse, J.J., & Gritton, E.C. (1971). A Water-Quality Simulation Model for Well Mixed Estuaries and Coastal Seas: II - Computation Procedures (Report R-708-NYC). Santa Monica: The Rand Corporation.

Leendertse, J.J., Alexander, R.C., & Liu, S.K., 1973. A Three-Dimensional Model for Estuaries and Coastal Seas: I - Principles of Computation (Report R-1417-OWRT). Santa Monica: The Rand Corporation.

Matsumoto, K., Sato, T., & Takanezawa, T. (2005). Tidal Analysis Table Using TOPEX/ POSEIDON Satelite Tophograhy. Proceedings of 6th JSCE Conference on Ocean and Coastal Modelling, Tokyo.

Oh, B.C., Chun, I.S., Chung, T.S., & Lee, D.S. (2002). A Study on the Water Circulation Enhancement inside Harbor Utilizing Wave Energy. Journal of Korean Society of Coastal and Ocean Engineering, 14(3), 209-221.

Stelling, G.S., & Leendertse, J.J. (1991). Approximation of Convective Processes by Cyclic ACI Methods. Proceedings of 2nd ASCE Conference on Estuarine and Coastal Modelling, Tampa.

Author ORCIDs and Contributions

Author name	ORCID	Contributions
Hong, Namseeg	0000-0002-1589-2617	①②③④⑤

① Conceived of the presented idea or developed the theory
② Carried out the experiment or collected the data
③ Performed the analytic calculations or numerical simulations
④ Wrote the manuscript
⑤ Supervised the findings of this study

Underwater Acoustic Research Trends with Machine Learning: General Background

Haesang Yang[1], Keunhwa Lee[2], Youngmin Choo[3] and Kookhyun Kim[4]

[1]Research Professor, Department of Naval Architecture & Ocean Engineering, Seoul National University, Seoul, Korea
[2]Associate Professor, Department of Defense System Engineering, Sejong University, Seoul, Korea
[3]Assistant Professor, Department of Defense System Engineering, Sejong University, Seoul, Korea
[4]Associate Professor, School of Naval Architecture & Ocean Engineering, Tongmyong University, Busan, Korea

ABSTRACT: Underwater acoustics that is the study of the phenomenon of underwater wave propagation and its interaction with boundaries, has mainly been applied to the fields of underwater communication, target detection, marine resources, marine environment, and underwater sound sources. Based on the scientific and engineering understanding of acoustic signals/data, recent studies combining traditional and data-driven machine learning methods have shown continuous progress. Machine learning, represented by deep learning, has shown unprecedented success in a variety of fields, owing to big data, graphical processor unit computing, and advances in algorithms. Although machine learning has not yet been implemented in every single field of underwater acoustics, it will be used more actively in the future in line with the ongoing development and overwhelming achievements of this method. To understand the research trends of machine learning applications in underwater acoustics, the general theoretical background of several related machine learning techniques is introduced in this paper.

1. Introduction

Underwater acoustics is the study of all phenomena related to the occurrence, propagation, and reception of sound waves in the water medium. Because electromagnetic waves undergo a significant attenuation in water, sound waves, which have relatively low propagation loss and high propagation speed, are used for underwater communication and detection. In the field of underwater acoustics, studies are mainly conducted on underwater communications, underwater target detection, marine resources, and measurement and analysis of underwater sound sources.

Most applications for underwater acoustics can be described as remote sensing. Remote sensing is employed when an object, condition, or phenomenon of interest cannot be directly observed and information about the target of interest is acquired indirectly using data. In underwater acoustics, this can be described simply as a sound navigation and ranging (sonar) system. Sonar systems can be broadly classified into passive and active systems. Passive sonar systems acquire information by using sensors to measure the acoustic energy (signal) emitted by the target of interest. In active sonar systems, the

observer obtains information by directly emitting an acoustic pulse and gathering the returning signals that are reflected by the target.

Machine learning, which is widely known today, was initially used in academia for developing artificial intelligence. Recently, the use of machine learning has become widespread owing to the introduction of high-speed parallel computing that uses graphics processing units (GPUs) and can perform reliable learning based on big data, as well as develop various machine learning techniques that can find optimal solutions. Machine learning has contributed to the evolution of acoustic signal processing and voice recognition, and it is also utilized in various ways in the field of underwater acoustics. It is used for traditional remote sensing, such as in detection/classification of underwater sound sources and targets and localization. In addition, it is being used in the field of acoustic signal processing for seabed classification and marine environment information extraction and is producing an abundance of scientific results.

Data-driven machine learning divides the data into a training set and test set. The training set is used to create a model that is suitable for machine learning, and the model's accuracy is increased through a repetitive model update process in which the model is validated via the

test set (Bishop, 2006; Murphy, 2012). Here, it is necessary to have a process for extracting features from the training set. Some existing machine learning algorithms require these features to be found through human intervention. However, if deep learning is used, this feature extraction process can be performed automatically, and the model's accuracy can be improved markedly at the same time (Goodfellow et al., 2016). To use deep learning, big data is required, and the existing machine learning methods may be more appropriate than deep learning when a small number of computations are required in situations where there is insufficient data. Therefore, it can be said that there is a complementary relationship between deep learning and machine learning.

Many recent attempts have been made to apply various machine learning techniques, such as deep learning, to each aspect of underwater acoustics. However, due to the nature of the underwater environments, the use of these aggressive and open techniques is challenging because the data acquisition/processing procedure is more constrained than that on land (in the air). Therefore, in the field of underwater acoustics, there is a movement towards combining traditional underwater acoustic research techniques with machine learning and developing them in concert with each other.

This paper aims to understand how machine learning is applied to each aspect of underwater acoustics. The next section discusses the theories regarding the definitions, types, and basic concepts of machine learning.

2. Machine Learning Theory

2.1 Definitions, Types, and Basic Concepts of Machine Learning

Machine learning is a technology in which a machine (computer) uses data to automatically detect and even predict hidden characteristics or patterns (Bishop, 2006; Murphy, 2012). Therefore, machine learning can be regarded as data-driven, and the system performance is determined by the quality of the data. As such, it is very important to build databases that are quantitatively and qualitatively excellent. Machine learning methods can be generally classified into supervised and unsupervised learning. Supervised learning refers to learning the following mapping from N number of training data input/output pairs $\{(x_i, y_i)\}_{i=1}^{N}$ (Murphy, 2012).

$$y = f(x) + \epsilon \tag{1}$$

Here, x is the training data input and is referred to as a feature. It can have a complex structure such as an image or a time-series signal. In principle, the output y can be anything, but generally in the case of categorical variables, the problem in Eq. (1) becomes a problem of classification or pattern recognition. When y is a real value, it results in a regression problem (Bishop, 2006; Murphy, 2012). The most basic data set for creating such a system is called a sample. Normally, the collected samples are divided into two sets: a training set that is used to

create the system and a test set that is used to evaluate the system's performance after it has been created. The difference between $f(x)$ which is predicted from the input x, and y which is actually obtained, is expressed as ϵ. In acoustics, this normally corresponds to noise.

In the second type of machine learning that is unsupervised learning, only the input x is provided without any sample class information, and the goal is to find new patterns in this input data. As such, it is a much less clear problem than supervised learning, and there is no clear error metric. In underwater acoustics, a considerable number of previous sonar application studies have used machine learning for classification purposes, such as target type/state classification (Choi et al., 2019; Fischell and Schmidt, 2015; Ke et al., 2018; Wang et al., 2019) and target and clutter signal classification (Allen et al., 2011; Murphy and Hines, 2014; Young and Hines, 2007). In many of these studies, the properties of the data that were used for learning were recognized beforehand owing to the goals of the studies. As such, supervised learning was mainly used rather than unsupervised learning. Besides, studies on underwater source localization (Das, 2017; Das and Sejnowski, 2017; Gemba et al., 2019; Gerstoft et al., 2016; Nannuru et al., 2019) or seabed classification (Buscombe and Grams, 2018; Diesing et al., 2014) have used various machine learning algorithms that include unsupervised learning.

In the aforementioned studies, the system input was also referred to as features. When performing learning, such as pattern recognition or classification, it is necessary to extract the features that will be used to classify samples. Features are more useful for classification when N number of classes have different values from each other; therefore, these can be considered good features. Observed samples are generally expressed in the form of feature vectors. However, because using many features is not necessarily favorable, it is important to select only the part of the feature set that is highly useful. In addition, the amount of computation may increase exponentially as the dimensions of the feature vectors increase. This is called the curse of dimensionality (Hastie et al., 2009; Murphy, 2012). As a result, feature extraction methods may vary according to the field where pattern recognition is used, and researchers often use methods that reduce dimensionality by converting the extracted feature values into different values or employing techniques such as principal component analysis (PCA) (Murphy, 2012).

There may be a vast variety of models in which a certain entered input is classified into one out of N number of classes. Sometimes, when there are models with various degrees of complexity, each model's misclassification rate for the training set is calculated and compared to the others in order to select the most appropriate model (Hastie et al., 2009). However, machine learning systems are created to build models that recognize and classify new samples. Therefore, a true performance evaluation can only be accomplished by measuring the performance of the system using a sample set other than the training set, i.e., a test set. The performance that the system shows in regard to the test set is called generalization ability (Hastie et al., 2009). The standard for selecting machine learning models is to select

models with excellent generalization ability. However, it may not be possible to use a test set depending on the circumstances. In such cases, the training set may be split in two, with one part used for training and other part used for measuring the model's performance, assuming that the training set is very large. The latter sample set is called the validation set. In this case, the learning and validation process are repeated for several models, and the best model is selected (Hastie et al., 2009). In reality, there are many cases where there is insufficient data to split the training set in two. In such cases, researchers use resampling techniques that use the same sample several times. Typical methods include cross-validation and bootstrapping (Kohavi, 1995).

When we "recognize" events or objects, we usually calculate a "possibility" and recognize things as being "most likely." This is a universal decision-making method, and machine learning systems also follow this principle. Samples that are observed from input patterns are expressed in the form of feature vector x, and this must be classified as the most likely class. Here, the qualitative standard of "most likely" is defined as the quantitative standard of the posterior probability $p(y|x)$. That is, in classification problems, success is achieved by finding the class with the greatest posterior probability and classifying the target as that class. If it is based on Bayesian statistics, $p(y|x)$ can be estimated by using the Bayes rule shown below (Bishop, 2006).

$$p(y|x) = \frac{p(x|y)p(y)}{p(x)} \tag{2}$$

That is, it can be replaced by the product of prior probability $p(y)$ and likelihood $p(x|y)$. The probability distributions of each of these is estimated through learning or training, and the estimation methods can be broadly divided into parametric and nonparametric methods (Murphy, 2012). Parametric methods can only be applied to certain types of probability distributions that can be expressed as parameters. Typical methods include the maximum likelihood method and the maximum posterior method. The nonparametric method is suitable for cases that do not actually follow a certain probability distribution, and a well-known typical method is the k-nearest neighbor method.

In many cases, the process of estimating probability distributions is ultimately an optimization problem. The most important part of formulating a given problem as an optimization problem is defining the cost function. The cost function includes parameters, and the parameters that minimize or maximize the cost function are found. The process of finding the optimal solution depends greatly on differentiation and gradient-based algorithms, but other optimization algorithms can also be used (Goodfellow et al., 2016).

2.2 Supervised Learning

As mentioned previously, supervised learning can be divided into classification and regression. Classification can be categorized according to the number of output classes, from the simplest binary classification to multiclass classification. Regression is about estimating a certain continuous variable as the output.

2.2.1 Support vector machine (SVM)

An SVM is basically an algorithm that learns rules for data classification and regression. SVM is a method of creating a non-stochastic linear classification model that determines which class the data belongs to (for example, determining which group the data belongs to, out of two groups), assuming that the given data is in an n-dimensional vector space. A model that is created in this way can determine which class the newly entered data belongs to. Classification is generally directed toward maximizing the margin, which is defined as the minimum distance between the decision boundary and data of each class (Murphy, 2012).

The most basic goal of an SVM is to create the most complete linear classification model that classifies data into two groups (Fig. 1(a)). Such a classification model can generally be found by solving quadratic optimization problems. SVMs can be used even in cases where it is difficult to classify data with a linear model (Fig. 1(b)). To do this, the kernel trick is often used, as it transforms the dimensions of the training data and uses an SVM in a new space (Bishop, 2006).

2.2.2 Neural network: multi-layer perceptron

Deep neural networks are modeled after biological neural networks, and they have become widely known owing to deep learning. The neural networks that are described in this section are the initial form of the basic algorithm that was the precursor of deep neural networks. Neural networks are computation models in which there are many connections between numerous operators that perform simple calculations. The information processing procedure can be represented simply by $y = f(x)$. The perceptron theory is an algorithm that can mathematically solve neural networks. The simplest perceptron model is a single-layer perceptron that consists of an input layer and output layer, as shown in Fig. 2(a) (Goodfellow et al., 2016).

In Fig. 2(a), the x_i value is the input value, and w_i is the weight for that value. The circle between the input layer and output layer is the activation function. The activation function makes the learning calculations easy by imitating a biological neuron that only allows signals to pass through if they are above a fixed level (Goodfellow et
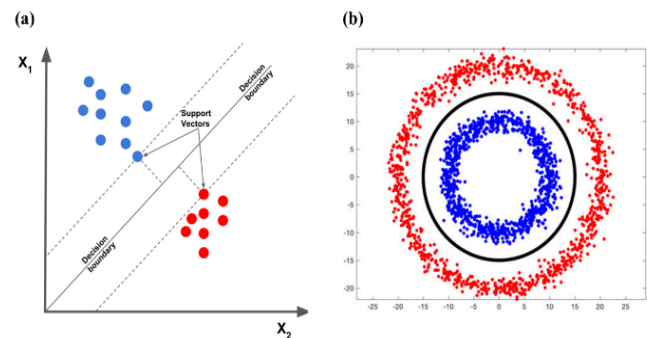

Fig. 1 Support vector machine. (a) Margin of support vector machine and (b) kernel trick (Learn OpenCV, 2018).
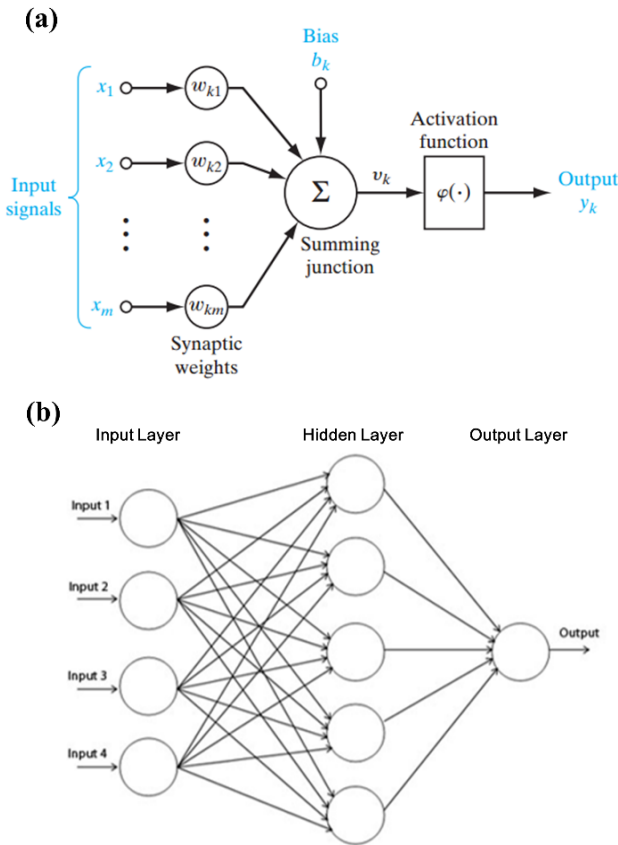
(a)

(b)

Fig. 2 (a) Single-layer perceptron and (b) multi-layer perceptron (Guest Blog, 2016).

al., 2016). Single-layer perceptron can only be applied to problems that can be expressed linearly, and it is difficult to apply them to problems that have a nonlinear structure. This is resolved by adding new layers between the input layer and output layer. A neural network structure that includes a new layer between the input layer and output layer, i.e., a hidden layer, as shown in Fig. 2(b), is called a multi-layer perceptron. A neural network that has several hidden layers is called a deep neural network (Goodfellow et al., 2016). Deep neural networks are discussed again in the deep learning part of Section 2.4.

Each layer linearly combines the data inputted from the previous layer while considering the weights. The activation function is applied to these values, and they are sent to the next hidden layer. During this process, the activation function that is used for the hidden layer employs a threshold value to filter out insignificant values. Functions that allow for easy first-order differentiation (e.g., a sigmoid function) are often used to facilitate calculations. The number of hidden layers is solely determined by the intuition and experience of the designer (Goodfellow et al., 2016). However, it is necessary to consider the possibility of overfitting and the problem of computational complexity unavoidably increasing as the number of hidden layers increases. However, to properly design a neural network, it is also necessary to consider the problem of reduced calculation accuracy that can occur when there are too few hidden layers. The process of finding the optimal value for the weights in each layer is called learning.

2.3 Unsupervised Learning

The goal of unsupervised learning is to find an interesting structure that can properly describe new patterns or data from input data x without the sample's class information. In sonar application research, various techniques that employ unsupervised learning have been attempted in studies on underwater source localization and seabed classification.

2.3.1 K-means clustering

K-means clustering is a simple unsupervised learning algorithm that performs clustering without the sample's class information (MacQueen, 1967). K-means clustering assumes that the sample can be divided into k number of clusters and classifies the training data into the most appropriate clusters. This process is generally performed by considering the distance-based similarity between groups or minimizing the cost. Each data item is classified into the most appropriate cluster as the total cost or the sum of the total distance between the data and clusters is steadily reduced.

2.3.2 Principle component analysis

In PCA, the training set is used to estimate the parameters that are needed for data transformation, and these results are used to transform the feature space. That is, PCA transforms the raw signal into a lower-dimension feature vector. To perform the transformation, the high-dimension data's variance is preserved as much as possible while finding a new low-dimension basis that is orthogonal and not linearly related (Murphy, 2012). The feature's principal component can be obtained from the eigenvector of the covariance matrix Σ of the data.

$$X^T X = A \Sigma^2 A^T, \tag{3}$$

Here, $A = [a_1, \cdots, a_N] \in R^{N \times N}$ is the principal component vector, and $\Sigma^2 = diag([\sigma_1^2, \cdots, \sigma_N^2]) \in R^{N \times N}$ is the variance resulting from the principal component direction defined by the principal component a_N. They can be found even when using singular value decomposition (Murphy, 2012). Generally, the direction of the axis that is selected by the first principle component shows the largest variance in the data, and the amount of variance becomes progressively smaller. Therefore, PCA can be used to reduce the dimensions of feature vectors while minimizing information loss. Because of this, it is widely used in fields such as data visualization and compression (Murphy, 2012).

2.3.3 Gaussian mixture model

As stated in the name, a Gaussian mixture model (GMM) is a clustering model that combines several Gaussian distributions. Complex forms of probability distributions that actually exist are depicted by combining the K number of Gaussian distributions (McLachlan et al., 2019). In a GMM, for a given data item x, the probability that x will occur is expressed as the sum of several Gaussian probability density functions, as shown below.
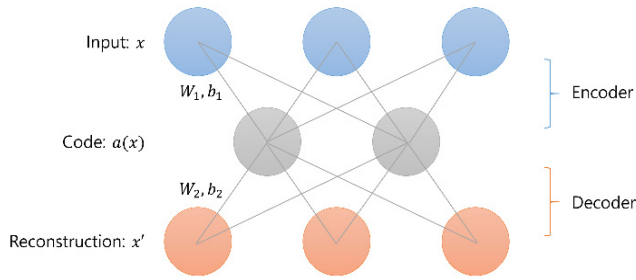
Fig. 3 A single-layer autoencoder

$$p(x) = \sum_{k=1}^{K} \pi_k N(x|\mu_k, \Sigma_k), \qquad (4)$$

Here, the mixture coefficient π_k shows the probability of selecting the k-th Gaussian distribution. It is set so that $0 \langle \pi_k \leq 1$ and $\sum_{k=1}^{K} \pi_k = 1$, and the appropriate π_k, μ_k, and Σ_k are estimated for the given data. The expectation-maximization (EM) method is generally employed as the estimation method (Dempster et al., 1977).

2.3.4 Autoencoder

An autoencoder is a type of unsupervised neural network, and it is often used to reduce dimensions or search feature spaces. In simple terms, an autoencoder is a neural network that copies the input values to the output values, but it has evolved in various ways via methods that apply several types of regularization to the neural network according to its purpose (Goodfellow et al., 2016). For example, as shown in Fig. 3, various autoencoders can be created, such as autoencoders that compress data by making the number of hidden layer neurons smaller than the input layer or autoencoders that train neural networks so that they can restore the original input after noise is added to the input data. This regularization prevents the unsupervised neural network from simply copying the input directly to the output, and it is adjusted to learn methods of efficiently representing data.

2.3.5 Sparse dictionary learning

Researchers have developed and applied various types of methods for introducing sparse coding to reduce the dimensions of the data that is to be processed (Elad, 2010). One of these, sparse dictionary learning, has the goal of finding sparse representations of input data in the form of the input data's basic elements or linear combinations of basic elements (Elad, 2010; Tosic and Frossard, 2011). For example, in $x = D\alpha$, x is the input data, and D is defined as the dictionary matrix. Here, the elements of D are defined as atoms. That is, x can be expressed as a linear combination of the column vector atoms that make up the dictionary. The solution that has the most coefficients that are 0 is found from among α. This is expressed mathematically, as shown below.

$$\alpha^* = \arg\min_{\alpha \in R^N} \|\alpha\|_0, \qquad s.t. \quad x = D\alpha \qquad (5)$$

α^* is the sparse representation coefficient. The constraint condition $\|\cdot\|_0$ represents the l_0-norm. This is a method of finding the total number of elements that are not 0 in the vector. However, the l_0-norm is a non-convex function, and thus, it has difficulty finding an accurate solution. As an alternative, it is sometimes changed to the l_1-norm constraint condition, and a fast approximate solution method such as orthogonal matching pursuit (Elad, 2010) or sparse Bayesian learning (Wipf and Rao, 2004) is used.

2.4 Deep learning

As implied by the name, today's deep learning methods are learning techniques that employ deep neural networks (Goodfellow et al., 2016). Previously, it was mentioned that a deep neural network is a complex neural network structure that includes several hidden layers and is based on a multi-layer perceptron structure. As such, it can be considered a machine learning model with a high level of complexity, and this is a structure that is similar to the series of neural layers that gradually extract complex information in the human brain. That is, relatively simple information processing is performed in the lower layers, and more complex information is extracted at the higher layers.

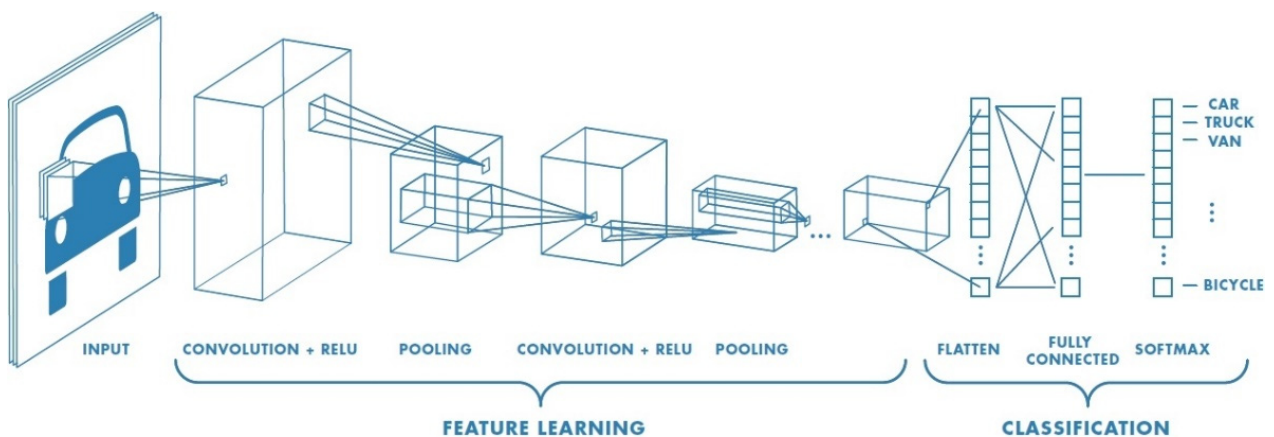In deep neural networks, learning is performed by optimizing the

Fig. 4 Basic architecture of convolutional neural network (Saha, 2018).

weights in each layer. The main method for deep neural network learning is the backpropagation algorithm (Rumelhart et al., 1986). This approach mainly uses the gradient descent method to continually propagate the error in the back direction to obtain the optimal weights. The backpropagation method shows very good performance for simple problems, but as the neural network's structure becomes more complex, several serious weaknesses become apparent. First, as the neural network's structure becomes more complex, the number of weights increases, and a large amount of learning data is required. In addition, the number of hidden layers increases, and the strength of the error weakens as it is backpropagated from the output layer to the input layer, making it difficult to perform learning. Because of these limitations, research on deep neural networks was stagnant for some time. Later, a considerable number of the aforementioned problems were resolved by using methods such as preprocessing each layer of the neural network using an unsupervised learning technique such as a restricted Boltzmann machine (RBM), using a rectified linear unit (ReLU) function as a new activation function, and preventing overfitting by including a regularization step in the learning process (Goodfellow et al., 2016). In addition to these technological advances, the construction of systems that can easily acquire large amounts of data, as well as huge advances in the computing capacity of GPUs, have allowed current learning techniques that use deep neural networks to provide performance that is vastly superior to the conventional machine learning techniques.

Currently, most deep learning models are based on convolutional neural networks (CNN). A CNN (Fukushima, 1980; LeCun et al., 1998) is a deep neural network that imitates the human visual recognition process, and it can be considered a neural network that is optimized for the field of image recognition. CNNs support convolution, and because of this characteristic, they are more useful than normal neural networks for receiving and learning input data of two dimensions or more. They have the advantage of being able to learn high-dimension data with relatively few parameters. Normally, CNNs consist of convolutional layers and pooling layers that extract the features of high-dimension data, as well as a fully connected layer that ultimately classifies the data. The order and number of the convolutional and pooling layers can be adjusted as needed according to the problem that the user is solving.

Convolution is used to separate and extract the features of input data, such as images. Specialized filters are used to extract features that consist of certain colors or tones in an image, and these filters and the input data can be convoluted to extract emphasized image features according to the characteristics of each filter. If this is repeated several times, ultimately the CNN can recognize the image. Due to these structural features, for higher-dimension analysis problems using images, CNNs show unrivaled performance compared to other algorithms. In the field of underwater acoustics, CNNs are actively being used to solve recognition and classification problems by transforming the input data into a frequency-time domain image using a short-time Fourier transform or a wavelet

transform, depicting the input data in the range-azimuth domain, or using array signal processing.

3. Conclusions

In this paper, a brief discussion of the theory of machine learning, including deep learning is provided from a general perspective before examining the research trends in underwater acoustics using machine learning. This paper outlines the definitions, types, and basic concepts of machine learning and introduces the main techniques that are used in underwater acoustics and sonar applications, which will be discussed in earnest in a follow-up paper. The follow-up paper will provide a more detailed discussion of how machine learning is used in the main fields of interest in underwater acoustics, including underwater sound source and target detection/classification, localization, and ocean information extraction.

The process of data-driven machine learning includes establishing a model that is suitable for its purpose, performing training and validation via datasets, and improving accuracy by performing repeated model updates. Considering that the measurement environment and measurement data quality in each research field are completely different, it would be best to use machine learning in concert with conventional methods in accordance with the goals of the research. Owing to the nature of underwater environments, there are some challenges in using more aggressive and open techniques because the data acquisition/processing procedure is more constrained than that used on land (in the air). Therefore, there is a movement towards combining traditional research techniques and machine learning techniques and developing them in concert with each other. The follow-up to this paper will provide a detailed examination of the research flow for underwater acoustics and sonar signal processing that directly employs machine learning.

References

Allen, N., Hines, P.C., & Young, V.W. (2011). Performances of Human Listeners and an Automatic Aural Classifier in Discriminating between Sonar Target Echoes and Clutter. The Journal of the Acoustical Society of America, 130(3), 1287-1298. https://doi.org/10.1121/1.3614549

Guest Blog. (2016). The Evolution and Core Concepts of Deep Learning & Neural Networks. Analytics Vidhya. Retrieved 06 February 2020 from https://www.analyticsvidhya.com/blog/2016/08/evolution-core-concepts-deep-learning-neural-networks

Bishop, C.M. (2006). Pattern Recognition and Machine Learning. Springer.

Buscombe, D., & Grams, P.E. (2018). Probabilistic Substrate Classification with Multispectral Acoustic Backscatter: A Comparison of Discriminative and Generative Models. Geoscience, 8(11), 395. https://doi.org/10.3390/geosciences8110395

Choi, J., Choo, Y., & Lee, K. (2019). Acoustic Classification of Surface and Underwater Vessels in the Ocean Using Supervised Machine Learning. Sensors, 19(16), 3492. https://doi.org/10.3390/s19163492

Das, A. (2017). Theoretical and Experimental Comparison of Off-grid Sparse Bayesian Direction-of-arrival Estimation Algorithms. IEEE Access, 5, 18075-18087. https://doi.org/10.1109/ACCESS.2017.2747153

Das, A., & Sejnowski, T.J. (2017). Narrowband and Wideband Off-grid Direction-of-arrival Estimation via Sparse Bayesian Learning. IEEE Journal of Oceanic Engineering, 43(1), 108-118. https://doi.org/10.1109/JOE.2017.2660278

Dempster, A.P., Laird, N.M., & Rubin, D.B. (1977). Maximum Likelihood from Incomplete Data via the EM Algorithm. Journal of the Royal Statistical Society, B, 1-38. https://doi.org/10.1111/j.2517-6161.1977.tb01600.x

Diesing, M., Green, S.L., Stephens, D., Lark, R.M., Stewart, H.A., & Dove, D. (2014). Mapping Seabed Sediment: Comparison of Manual, Geostatistical, Object-based Image Analysis and Machine Learning Approaches. Continental Shelf Research, 84, 107-119. https://doi.org/10.1016/j.csr.2014.05.004

Elad, M. (2010). Sparse and Redundant Representations. New York: Springer.

Fischell, E.M., & Schmidt, H. (2015). Classification of Underwater Targets from Autonomous Underwater Vehicle Sampled Bistatic Acoustic Scattered Fields. The Journal of the Acoustical Society of America, 138(6), 3773-3784. https://doi.org/10.1121/1.4938017

Fukushima, K. (1980). Neocognition: A Self-organizing Neural Network Model for a Mechanism of Pattern Recognition Unaffected by Shift in Position. Biological Cybernetics, 36(4), 193-202. https://doi.org/10.1007/BF00344251

Gemba, K.L., Nannuru, S., & Gerstoft, P. (2019). Robust Ocean Acoustic Localization with Sparse Bayesian Learning. IEEE Journal of Selected Topics in Signal Processing, 13(1), 49-60. https://doi.org/10.1109/JSTSP.2019.2900912

Gerstoft, P., Mecklenbräuker, C.F., Xenaki, A., & Nannuru, S. (2016). Multisnapshot Sparse Bayesian Learning for DOA. IEEE Signal Processing Letters, 23(10), 1469-1473. https://doi.org/10.1109/LSP.2016.2598550

Goodfellow, I., Bengio, Y., Courville, A., & Bengio, Y. (2016). Deep Learning. Cambridge, MA, USA: MIT Press.

Hastie, T., Tibshirani, R., & Friedman, J. (2009). The Elements of Statistical Learning: Data Mining, Inference and Prediction (2nd ed). Springer.

Ke, X., Yuan, F., & Cheng, E. (2018). Underwater Acoustic Target Recognition Based on Supervised Feature-Separation Algorithm. Sensors, 18(12), 4318. https://doi.org/10.3390/s18124318

Kohavi, R. (1995). A Study of Cross-validation and Bootstrap for Accuracy Estimation and Model-selection. Proceedings of the International Joint Conference on Artificial Intelligence, 14(2), 1137-1145.

Learn OpenCV. (2018). Support Vector Machines (SVM). Retrieved 06 February 2020 from https://www.learnopencv.com/support-vector-machines-svm

LeCun, Y., Bottou, L., Bengio, Y., & Haffner, P. (1998). Gradient-Based Learning Applied to Document Recognition. Proceedings of the IEEE, 86(11), 2278-2324. https://doi.org/10.1109/5.726791

MacQueen, J. (1967). Some methods for classification and analysis of multivariate observations. Proceedings of the 5th Berkeley Symposium on Mathematical Statistics and Probability. 1(14), 281-297.

McLachlan, G.J., Lee, S.X., & Rathnayake, S.I. (2019). Finite Mixture Models. Annual Review of Statistics and Its Application, 6, 355-378. https://doi.org/10.1146/annurev-statistics-031017-100325

Murphy, K. (2012). Machine Learning: a Probabilistic Perspective (1st ed). Cambridge, MA, USA, MIT Press.

Murphy, S.M., & Hines, P.C. (2014). Examining the Robustness of Automated Aural Classification of Active Sonar Echoes. The Journal of the Acoustical Society of America, 135(2), 626-636. https://doi.org/10.1121/1.4861922

Nannuru, S., Gemba, K.L., Gerstoft, P., Hodgkiss, W.S., & Mecklenbräuker, C.F. (2019). Sparse Bayesian Learning with Multiple Dictionaries. Signal Processing, 159, 159-170. https://doi.org/10.1016/j.sigpro.2019.02.003

Rumelhart, D.E., Hinton, G.E., & Williams, R.J. (1986). Learning Representations by Back-propagating Errors. Nature, 323, 533-536. https://doi.org/10.1038/323533a0

Tosic, I., & Frossard, P. (2011). Dictionary Learning. IEEE Signal Process. Magazine, 28(2), 27-38. https://doi.org/10.1109/MSP.2010.939537

Saha, S. (2018). A Comprehensive Guide to Convolutional Neural Networks - the ELI5 Way. Towards Data Science. Retrieved 06 February 2020 from https://towardsdatascience.com/a-comprehensive-guide-to-convolutional-neural-networks-the-eli5-way-3bd2b1164a53

Wang, X., Liu, A., Zhang, Y., & Xue, F. (2019). Underwater Acoustic Target Recognition: A Combination of Multi-Dimensional Fusion Features and Modified Deep Neural Network. Remote Sensing, 11(16), 1888. https://doi.org/10.3390/rs11161888

Wipf, D.P., & Rao, B.D. (2004). Sparse Bayesian Learning for Basis Selection. IEEE Transactions on Signal Processing, 52(8), 2153-2164. https://doi.org/10.1109/TSP.2004.831016

Young, V.W., & Hines, P.C. (2007). Perception-based Automatic Classification of Impulsive-source Active Sonar Echoes. The Journal of the Acoustical Society of America, 122(3), 1502-1517. https://doi.org/10.1121/1.2767001

Author ORCIDs and Contributions

Author name	ORCID	Contributions
Yang, Haesang	0000-0001-7101-5195	②④
Lee, Keunhwa	0000-0003-4827-3983	②⑤
Choo, Youngmin	0000-0002-9100-9494	②④⑤
Kim, Kookhyun	0000-0002-4214-4673	②⑤

① Conceived of the presented idea or developed the theory

② Carried out the experiment or collected the data

③ Performed the analytic calculations or numerical simulations

④ Wrote the manuscript

⑤ Supervised the findings of this study

Original Research Article, Technical Article, Review Article, etc

Title of Article

Firstname Lastname[1], Firstname Lastname[2] and Firstname Lastname[3]

[1]*Professor, Department of OO, OO School, OO University, Busan, Korea*
[2]*Graduate Student, Department of OO, OO University, Seoul, Korea*
[3]*Senior Researcher, Department of OO, OO Engineering. Corp., Seoul, Korea*

ABSTRACT: *A concise and factual abstract is required. The abstract should state briefly the purpose of the research, the principal results and major conclusions. An abstract should be written in around 300 words and is often presented separately from the article, so it must be able to stand alone. For this reason, References should be avoided, but if essential, then cite the author(s) and year(s). Also, non-standard or uncommon abbreviations should be avoided, but if essential they must be defined at their first mention in the abstract itself.*

Nomenclature

ITOC	Increment of total operating cost ($/yr)
LHV	Lower heating value (kJ/kg)
Pw	Power (kW)
T	Temperature (K)
V	Volume (m^3)
ρ	Density (kg/m^3)

1. Introduction

The introduction should briefly place the study in a broad context and highlight why it is important. It should define the purpose of the work and its significance. The current state of the research field should be reviewed carefully and key publications cited. Please highlight controversial and diverging hypotheses when necessary. Finally, briefly mention the main aim of the work and highlight the principal conclusions. As far as possible, please keep the introduction comprehensible to scientists outside your particular field of research.

2. General Information for Authors

2.1 Requirement for Membership

One of the authors who submits a paper or papers should be member of The Korea Society of Ocean Engineers (KSOE), except a case that editorial board provides special admission of submission.

2.2 Publication type

Manuscript is made up of scholarly monographs, technical reports and data. The paper should have not been submitted to other academic journal. Conference papers, research reports, dissertations and review articles can be submitted to Journal Of Ocean Engineering and Technology (JOET). When part or whole of a paper was already published to conference papers, research reports, dissertations, and review articles, then corresponding author should note it clearly in the manuscript. After published to JOET, the copyright of manuscript belongs to KSOE.

(example) It is noted that this paper is revised edition based on proceedings of KAOST 2100 in Jeju.

2.3 Manuscript submission

Manuscript should be submitted through the on-line manuscript website (http://www.joet.org). The date that corresponding author submits a paper through on-line website is official date of submission. Other correspondences can be sent by an email to the Editor in Chief. The manuscript must be accompanied by a signed statement that it has been neither published nor currently submitted for publication elsewhere. The manuscript should be written in English or Korean and a

minimum standard of the proficiency in the English or Korean language should be met before submission to the editorial office.

Ensure that online submission or submission by e-mail text files are in a standard word processing format (Hangul or MS Word are preferred). Ensure that graphics are high-resolution. Be sure all necessary files have been uploaded/attached.

2.3.1 Authoer's checklist and Transfer of copyright

Authoer's checklist and Transfer of copyright can be found in submission hompage (http://www.joet.org).

2.4 Research and Publication Ethics

Authorship should be limited to those who have made a significant contribution to the conception, design, execution, or interpretation of the reported study. All those who have made significant contributions should be listed as co-authors. Where there are others who have participated in certain substantive aspects of the research project, they should be acknowledged or listed as contributors.

The corresponding author should ensure that all appropriate co-authors and no inappropriate co-authors are included on the paper, and that all co-authors have seen and approved the final version of the paper and have agreed to its submission for publication.

If the work involves chemicals, procedures or equipment that have any unusual hazards inherent in their use, the author must clearly identify these in the manuscript. If the work involves the use of animal or human subjects, the author should ensure that the manuscript contains a statement that all procedures were performed in compliance with relevant laws and institutional guidelines and that the appropriate institutional committee(s) has approved them. Authors should include a statement in the manuscript that informed consent was obtained for experimentation with human subjects. The privacy rights of human subjects must always be observed.

When an author discovers a significant error or inaccuracy in his/her own published work, it is the author's obligation to promptly notify the journal editor or publisher and cooperate with the editor to retract or correct the paper. If the editor or the publisher learns from a third party that a published work contains a significant error, it is the obligation of the author to promptly retract or correct the paper or provide evidence to the editor of the correctness of the original paper.

3. Manuscript

Manuscript must consist of as follow: (1) Title, (2) Author's information (include title), (3) Key word, (4) Abstract, (5) Nomenclature description, (6) Introduction, (7) Body (analysis, test, results and discussion, (8) Conclusion, (9) Acknowledgements, (10) Reference, (11) Appendix, etc.

3.1 Unit

Use the international system units(SI). If other units are mentioned, please give their equivalent in SI.

3.2 Equations

All mathematical equations should be clearly printed/typed using well accepted explanation. Superscripts and subscripts should be typed clearly above or below the base line. Equation numbers should be given in Arabic numerals enclosed in parentheses on the right-hand margin. They should be cited in the text as, for example, Eq. (1), or Eqs. (1)-(3).

$$G_{GEV}(x;\mu,\sigma,\xi) = \begin{cases} \exp[-(1+\xi(x-\mu)/\sigma)^{-1/\xi}] & \xi \neq 0 \\ \exp[-\exp(-(x-\mu)/\sigma)] & \xi = 0 \end{cases} \quad (1)$$

in which μ, σ, and ξ represent the location ("Shift" in figures), scale, and shape parameters, respectively.

3.3 Tables

Tables should be numbered consecutively with Arabic numerals. Each table should be typed on a separate sheet of paper and be fully titled. All tables should be referred to in the text.

Table 1 Tables should be placed in the main text near to the first time they are cited

Item	Buoyancy riser
Segment length[1] (m)	370
Outer diameter (m)	1.137
Inner diameter (m)	0.406
Dry weight (kg/m)	697
Bending rigidity (N·m^2)	1.66E8
Axial stiffness (N)	7.098E9
Inner flow density (kg·m^3)	881
Seabed stiffness (N/m/m^2)	6,000

[1]Tables may have a footer.

3.4 Figures

All the illustrations should be of high quality meeting with the publishing requirement with legible symbols and legends. In preparing the illustrations, authors should consider a size reduction during the
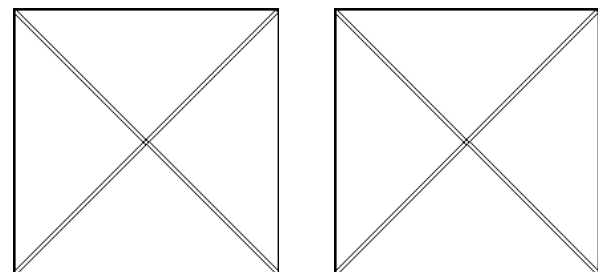
(a) Description of what is contained in the first panel

(b) Description of what is contained in the first panel

Fig. 1 Schemes follow the same formatting. If there are multiple panels, they should be listed as: (a) Description of what is contained in the first panel; (b) Description of what is contained in the second panel. Figures should be placed in the main text near to the first time they are cited

printing process to have acceptable line clarity and character sizes. All figures should have captions which should be supplied on a separate sheet. They should be referred to in the text as, for example, Fig. 1, or Figs. 1-3.

3.5 How to describe the references in main texts

All references should be listed at the end of the manuscripts, arranged in order of Alphabet. The exemplary form of listed references is as follows:

Single author: (Kim, 1998) or Kim (1998)

Two authors: (Kim and Lee, 2000) or Kim and Lee (2000)

Three or more authors: (Kim et al., 1997) or Kim et al. (1997)

Two or more papers: (Lee, 1995a; Lee, 1995b; Ryu et al., 1998)

Year unknown: (Kim, n.d.) or Kim (n.d.)

4. Conclusions

......

Acknowledgments

References

- Journal name should not be abbreviated.
- A private report with limited access or download availability can not be a reference.
- Include the digital object identifier DOI or URL for all references where available.

Referring to journal publications:

Author, A.A., Author, B.B., & Author, C.C. (Year). Title of Article. Journal Title, vol(no), pp-pp. https://doi.org/xx.xxxx/xxxxxx

Author, A.A., Author, B.B., Author, C.C. (accepted; in press). Title of Article. Title of Periodical. Retrieved from http://xx.xxx/x.pdf

Lee, T.K., Kim, T.W., Rim, C.W., & Kim, S.C. (2013). A Study on Calculation of Local Ice Pressures for ARAON Based on Data Measured at Arctic Sea. Journal of Ocean Engineering and Technology, 27(5), 88-92. https://doi.org/10.5574/KSOE.2013.27.5.088

Lee, T.K., Kim, T.W., Rim, C.W., & Kim, S.C. (accepted; in press). A Study on Calculation of Local Ice Pressures for ARAON Based on Data Measured at Arctic Sea. Journal of Ocean Engineering and Technology, Retrieved from http://xxx.xxx/xxx.pdf

Referring to conference proceedings:

Author, A.A., Author, B.B., & Author, C.C. (Year). Title of Article. Proceeding Title, City, Country, pp-pp. https://doi.org/xx.xxxx

Aoki, S., Liu, H., & Sawaragi, T. (1994). Wave Transformation and Wave Forces on Submerged Vertical Membrane. Proceedings of International Symposium Waves - Physical and Numerical Modeling, Vancouver, Canada, 1287-1296.

Tsukamoto, C.L., Lee, W., Yuh, J., Choi, S.K., & Lorentz, J. (1997). Comparison Study on Advanced Thruster Control of Underwater Robots. Proceedings of International Conference on Robotics and Automation, 1845-1850. https://doi.org/110.1109/ROBOT. 1997.619056

Referring to books:

Author, A.A. (Year). Title of Book (xx ed.). Location: Publisher.

Strunk, W., & White, E.B. (2000). The Elements of Style (4th ed.). NewYork, USA: Longman.

Schlichting, H. (1968). Boundary Layer Theory (6th ed.). New York, USA: McGraw-Hill.

Referring to theses or dissertations:

Author, A.A. (Year). Title of Doctoral Dissertation or Master's thesis (Doctoral Dissertation or Master's thesis). Name of Institution, City, Country.

Giovanni, I. (1998). Modelling and Identification of Underwater Robotic Systems (Ph.D. Thesis). University of Genova, Genova, Italy.

Referring to technical reports, rules, or guidelines:

Author, A.A. (Year). Title of report (Reprot No. xxx), Location: Publisher.

Likhomanov, V. (2010). Full-Scale Ice Trials of the Korean Research Icebreaker ARAON. Daejeon, Korea: Arctic and Antarctic Research Institute (AARI).

ABS. (2011). Guide for Ice Loads Monitoring Systems. Houston, USA: American Bureau of Shipping.

Lloyd's Register. (2011). FDA ICE Fatigue Induced by Ice Loading, ShipRight Design and construction - Fatigue Design Assesment. London, United Kingdom: Lloyd's Register.

Larson, M., & Kraus, N.C. (1989). SBEACH: Numerical Model for Simulating Storm-Induced Beach Change - Report 1 Empirical Foundation and Model Development (Technicla Report CERC-89-9). Coastal Engineering research center Vicksburg Ms.

Referring to patents:

Righsholder, A.A. (Year). Title of Patent. Patent number, Patent office with country.

Dawoo Shipbulding & Maringe Engineering (DSME). (2013). Distance Length Standardization Method for Preventing Interference at the time of Uploading Cell Guide of Container Ship. Unexamined Patent Publication 1020130044635, Korean Interllectual Property Office.

Referring to websites:

Righsholder, A.A. (Year). Title of webpage. Retrieved Month Year from http://xxxx

International Association of Classification Societies (IACS). (2010a).

Common Structural Rules for Bulk Carriers. Retrieved July 2010 from http://www.iacs-data.org.uk

US Congressional Hearing. (2009). Strategic Importance of the Arctic in Us Policy. Retrieved June 2019 from https://fas.org/irp/arctic.pdf

Dawoo Shipbulding & Maringe Engineering (DSME). (2013). Distance Length Standardization Method for Preventing Interference at the time of Uploading Cell Guide of Container Ship. Retrieved June 2019 from https://patentimages.storage./pdfs/792.pdf

Referring to software:

Righsholder, A.A. (Year). Title of Software. Downloaded Month Year from http://xxxx

Referring to some exceptional cases:
- when authors are missing, institution can replace authors

National Oceanic and Atmospheric Administration (NOAA). (2015). Deep-ocean Assessment and Reporting of Tsunamis (DART). Retrieved December 2019 from https://nctr.pmel.noaa.gov/Dart/

- when dates or years are missing, it is replaced with "n.d."

National Oceanic and Atmospheric Administration (NOAA). (n.d.). Deep-ocean Assessment and Reporting of Tsunamis (DART).

- when more then seven authors, first 6 authors ... last author.

Yeu, T., Choi, H.T., Lee, Y., Chae, J., Lee, Y., Kim, S.S., ... Lee, T.H. (2019). Development of Robot Platform for Autonomous Underwater Intervention. Journal of Ocean Engineering and Technology, 33(2), 168-177. https://doi.org/10.26748/KSOE. 2019.021

Appendix

The appendix is an optional section that can contain details and data supplemental to the main text. For example, explanations of experimental details that would disrupt the flow of the main text, but nonetheless remain crucial to understanding and reproducing the research shown; figures of replicates for experiments of which representative data is shown in the main text can be added here if brief, or as Supplementary data. Mathematical proofs of results not central to the paper can be added as an appendix.

All appendix sections must be cited in the main text. In the appendixes, Figures, Tables, etc. should be labeled starting with 'A', e.g., Fig. A1, Fig. A2, etc.

Examples:
https://doi.org/10.26748/KSOE.2019.022
https://doi.org/10.26748/KSOE.2018.4.32.2.095

Author ORCIDs and Contributions

Author name	ORCID	Contributions
So, Hee	0000-0000-000-00X	①②③
Park, Hye-Il	0000-0000-000-00X	④
Yoo, All	0000-0000-000-00X	⑤
Jung, Jewerly	0000-0000-000-00X	⑤

① Conceived of the presented idea or developed the theory
② Carried out the experiment or collected the data
③ Performed the analytic calculations or numerical simulations
④ Wrote the manuscript
⑤ Supervised the findings of this study

Authors' Information

Requirement for membership

One of the authors who submits a paper or papers should be member of the Korean Society of Ocean Engineers (KSOE), except a case that editorial board provides special admission of submission.

Publication type

Article types include scholarly monographs (original research articles), technical articles (technical reports and data), and review articles. The paper should have not been submitted to other academic journal. When part or whole of a manuscript was already published to conference papers, research reports, and dissertations, then the corresponding author should note it clearly in the manuscript.

Copyright

After published to JOET, the copyright of manuscripts should belong to KSOE. A transfer of copyright (publishing agreement) form can be found in submission website (http://www.joet.org).

Manuscript submission

Manuscript should be submitted through the on-line submission website (http://www.joet.org). The date that corresponding author submits a paper through on-line website is the official date of submission. Other correspondences can be sent by an email to the Editor in Chief or secretariat. The manuscript must be accompanied by a signed statement that it has been neither published nor currently submitted for publication elsewhere. The manuscript should be written in English or Korean. Ensure that online submission are in a standard word processing format (Hangul or MS Word are accepted). Ensure that graphics are high-resolution. Be sure all necessary files have been uploaded/attached.

Authors' checklist

Please refer to "Authors' Checklist" for details.

Article structure

Manuscript must be edited in the following order: (1) Title, (2) Authors' names and affiliations, (3) Keywords, (4) Abstract, (5) Nomenclature (optional), (6) Introduction, (7) Main body (analyses, tests, results, and discussions), (8) Conclusions, (9) Acknowledgements (optional), (10) References, (11) Appendices (optional).

Abstract

A concise and factual abstract is required. The abstract should state briefly the purpose of the research, the principal results and major conclusions. An abstract should be written in around 300 words. References are not cited in abstract whenever possible. Also, non-standard or uncommon abbreviations should be avoided, but if essential they must be defined at their first mention in the abstract itself.

Keywords

Immediately after the abstract, provide a maximum of 5 or 6 keywords.

Equations

All mathematical equations should be clearly printed/typed using well accepted explanation. Superscripts and subscripts should be typed clearly above or below the base line. Equation numbers should be given in Arabic numerals enclosed in parentheses on the right-hand margin.

Tables

Tables should be numbered consecutively with Arabic numerals. Each table should be fully titled. All tables should be referred to in the texts.

Figures

Figures should be numbered consecutively with Arabic numerals. Each figure should be fully titled. All figures should be referred to in the texts. All the illustrations should be of high quality meeting with the publishing requirement with legible symbols and legends.

References in text

References in texts follow the APA style. Authors can also see how references appear in manuscript text through the 'Template'.

Reference list

Reference list follows the APA style. Authors can see how references should be given in reference section through the 'Template'.

Appendices

The appendix is an optional section that can contain details and data supplemental to the main text. If there is more than an appendix, they should be identified as A, B, C, etc. Formulae and equations in appendices should be given separate numbering: Eq. (A.1), Eq. (A.2), etc.; in a subsequent appendix, Eq. (B.1) and so on. Similarly for tables and figures: Table A.1; Fig. A.1, etc.

Peer reviews

Every manuscript received is circulated to two or more peer reviewers. The author's name and affiliation is disclosed during review process to reviewers. The review process can be repeated till the revision requests are suggested by reviewers.

Revised manuscript

Manuscript reviewed should be revised and submitted with responses to the reviewers' comments in three months. Otherwise, the submission is finished with decision of reject.

Proof reading

The accepted manuscript will be sent for the proof reading for

the consistency of text format and the completeness of references. The manuscript may be revised according to the opinion of the manuscript editor.

Galley proof will be provided as a PDF file to the author. Attention of authors should be directed to the instructions which accompany the galley proof, especially the requirement that all corrections, revisions, and additions be entered on the galley proof. The galley proof with the corrections should be returned to the KSOE Secretariat by e-mail within a week. In principal, substantial changes in an article at this stage may not permitted.

Article processing charge

Payment due

Article processing charge (APC) covers the range of publishing services JOET provides. This includes provision of online tools for editors and authors, article production and hosting, and customer services. Upon editorial acceptance of an article for the regular review service and upon submission of an article for the fast review service, the corresponding author will be notified that payment is due.

APC

The APC up to 6 pages is ₩200,000 (or $200) for the regular review service and ₩550,000 (or $550) for the fast review service. For papers longer than 6 pages, an extra APC of $30 per page is charged. No taxes are included in this charge.

Payment methods

Credit card payment can be made online using a secure payment form as soon as the manuscript has been editorially accepted. We will we send a receipt by email once payment has been processed. Please note that payment by credit card carries a surcharge of 10% of the total APC.

Invoice payment is due within 7 days of the manuscript receiving editorial acceptance. Receipts are available on request.

Authors' Checklist

The following list will be useful during the final checking of an article prior to sending it to Journal of Ocean Engineering and Technology for review. Please submit this checklist to the KSOE when you submit your article.

< Editing checklist >

☐ I checked my manuscript has been 'spell-checked' and 'grammar-checked'.
나의 원고에 오타 및 문법적 오류가 있는지 확인하였습니다.

☐ One author has been designated as the corresponding author with contact details such as
  - E-mail address
  - Phone numbers
저자 중 한명의 저자는 교신저자로 지정되었으며, 다음의 연락처가 표기되었습니다.
  - 이메일 주소
  - 전화 번호

☐ I checked abstract 1) stated briefly the purpose of the research, the principal results and major conclusions, 2) was written in around 300 words, and 3) did not contain references (but if essential, then cite the author(s) and year(s)).
나는 초록이 1) 연구의 목적, 주요 결과 및 결론을 포함하고 있음을 확인하였으며, 2) 300단어 내외의 단어로 구성되었음을 확인하였으며, 3) 참고문헌을 포함하고 있지 않음을 확인하였습니다 (꼭 필요시 참고문헌 삽입 가능).

☐ I provided 5 or 6 keywords.
나는 5-6개의 키워드를 사용하였습니다.

☐ I checked manuscript consisted of as follow: (1) Title, (2) Authors' names and affiliations, (3) Keywords, (4) Abstract, (5) Nomenclature (optional), (6) Introduction, (7) Main body (analyses, tests, results, and discussions), (8) Conclusions, (9) Acknowledgements (optional), (10) References, (11) Appendices (optional).
나는 원고가 다음의 순서로 구성되었음을 확인하였습니다: (1) 제목, (2) 저자명/소속기관, (3) 키워드, (4) 초록, (5) 기호 (옵션), (6) 서론, (7) 본문 (해석, 실험, 결과, 검토), (8) 결론, (9) 후기 (옵션), (10) 참고문헌, (11) 부록.

☐ I confirmed that I used clear pictures to make every picture legible.
나는 모든 그림이 가독될 수 있도록 선명한 그림을 사용하였음을 확인하였습니다.

☐ I checked all table and figure captions were written in English.
나는 원고의 모든 표 제목과 그림 제목은 영문으로 작성되었음을 확인하였습니다.

☐ I checked all table and figure numbered consecutively in accordance with their appearance in the text.
나는 본문에서 나타나는 순서대로 표 번호 및 그림 번호가 지정되었음을 확인하였습니다.

☐ I checked abbreviations were defined at their first mention there and used with consistency throughout the article.
나는 영문 약자를 원고의 첫 번째 사용에서 정의하였으며, 이후 원고에서는 동일한 약자를 사용하였음을 확인하였습니다.

☐ I checked that references were in the correct format for the journal (See 'Authors' Information' for details).
나는 모든 참고문헌이 본 저널의 참고문헌 표기법(저자 가이드 참조)에 따라서 작성되었음을 확인하였습니다.

☐ I checked all references mentioned in the Reference list were cited in the text, and vice versa.
나는 'References'에 존재하는 모든 참고문헌은 원고 본문에서 언급되었으며, 반대로 원고 본문에 언급된 모든 참고문헌은 'References'에 표기되었음을 확인하였습니다.

☐ I checked I used the international system units (SI) or SI-equivalent engineering units.
나는 SI 단위계 또는 공학적으로 인정되어지는 단위계를 사용하였음을 확인하였습니다.

< Ethical checklist >

☐ I checked the work described has not been published previously (except in the form of an abstract or as a part of a published lecture or academic thesis).
나는 본 원고의 내용이 초록, 단행본, 학위논문 등을 제외한 타 저널 등에 게재된 사실이 없음을 확인하였습니다.

☐ I checked when the work described has been published previously in other proceedings without copyright, it has clearly noted in the text.
나는 본 원고의 내용이 판권이 없는 프로시딩에 게재되었던 경우 이를 원고에서 명시하였음을 확인하였습니다.

☐ I checked permission has been obtained for use of copyrighted material from other sources including the Web.
나는 웹을 포함하여 판권이 있는 자료의 사용 허가를 득했습니다.

☐ I have processed Plasgiarism Prevention Check through reliable web sites such as www.kci.go.kr, http://www.ithenticate.com/, or https://www.copykiller.org/ for my submission.
나는 논문 표절 유사도 검사를 마친 후 투고하였습니다.

☐ I agree that final decision for my final manuscript can be changed according to results of Plasgiarism Prevention Check by JOET administrator.
나의 최종본 논문에 대한 JOET 자체적인 논문 표절 유사도 검토 결과에 따라 최종 판정이 변경될 수 있다는 사실에 동의합니다.

☐ I checked one author at least is member of the Korean Society of Ocean Engineers.
나는 저자 중 1인 이상이 한국해양공학회의 회원임을 확인하였습니다.

☐ I agreed all policies related to 'Ethical Code of Research' and 'Research and Publication Ethics' of the Korean Society of Ocean Engineers.
나는 연구출판정책과 연구윤리규정을 확인했으며, 준수할 것을 서약합니다.

☐ I agreed to transfer copyright to the publisher as part of a journal publishing agreement and this article will not be published elsewhere including electronically in the same form, in English or in any other language, without the written consent of the copyright-holder.
나는 한국해양공학회지의 저작권 정책에 동의하며, 저작권 위임동의서를 제출하겠습니다.

☐ I have read and agree to the terms of Authors' Checklist.
나는 저자 체크리스트 모든 조항을 검토하였으며, 모든 조항에 동의합니다.

Title of article   :

Date of submission   : DD/MM/YYYY

Corresponding author :   signature

Email address   :

※ E-mail this with your signature to ksoehj@ksoe.or.kr

Publishing Agreement

ARTICLE DETAILS

Title of article :

Corresponding author :

E-mail address :

DOI : https://doi.org/10.26748/KSOE.2XXX.XXX

YOUR STATUS

I am one author signing on behalf of all co-authors of the manuscript.

ASSIGNMENT OF COPYRIGHT

I hereby assign to the Korean Society of Ocean Engineers, the copyright in the manuscript identified above and any tables, illustrations or other material submitted for publication as part of the manuscript (the "Article"). This assignment of rights means that I have granted to Korean Society of Ocean Engineers the exclusive right to publish and reproduce the Article, or any part of the Article, in print, electronic and all other media (whether now known or later developed), in any form, in all languages, throughout the world, for the full term of copyright, and the right to license others to do the same, effective when the Article is accepted for publication. This includes the right to enforce the rights granted hereunder against third parties.

SCHOLARLY COMMUNICATION RIGHTS

I understand that no rights in patents, trademarks or other intellectual property rights are transferred to the Journal owner. As the author of the Article, I understand that I shall have: (i) the same rights to reuse the Article as those allowed to third party users of the Article under the CC-BY-NC License, as well as (ii) the right to use the Article in a subsequent compilation of my works or to extend the Article to book length form, to include the Article in a thesis or dissertation, or otherwise to use or re-use portions or excerpts in other works, for both commercial and non-commercial purposes. Except for such uses, I understand that the assignment of copyright to the Journal owner gives the Journal owner the exclusive right to make or sub-license commercial use.

USER RIGHTS

The publisher will apply the Creative Commons Attribution-Noncommercial Works 4.0 International License (CC-BY-NC) to the Article where it publishes the Article in the journal on its online platforms on an Open Access basis.
The CC-BY-NC license allows users to copy and distribute the Article, provided this is not done for commercial purposes and further does not permit distribution of the Article if it is changed or edited in any way, and provided the user gives appropriate credit (with a link to the formal publication through the relevant DOI), provides a link to the license, and that the licensor is not represented as endorsing the use made of the work. The full details of the license are available at http://creativecommons.org/licenses/by-nc/4.0/legalcode.

REVERSION OF RIGHTS

Articles may sometimes be accepted for publication but later rejected in the publication process, even in some cases after public posting in "Articles in Press" form, in which case all rights will revert to the author.

☑ **I have read and agree to the terms of the Journal Publishing Agreement.**

Corresponding author:

name   signature

※ E-mail this with your signature to ksoehj@ksoe.or.kr (Papers will not be published unless this form is signed and returned)

Ethical Codes of Research

All members of The Korean Society of Ocean Engineers, by observing the following codes of conduct and regulations regarding research in the field, will contribute to the development of ocean engineering and the security and prosperity of the society and the nation, thus holding our honesty, reputation and authority in the highest standards.

A. Foundational Spirit

1. We make a contribution to mutual prosperity of mankind through ocean development, using the knowledge and technique in the field of ocean engineering.
2. We contribute to fostering the good spirit of citizenship by conducting responsible research.
3. We make efforts to enhance our authority and competitiveness as experts in ocean engineering.

B. Fundamental Canons

1. We consider the public security and welfare as a top priority and conform to the principle of sustainable use of ocean in conducting our research.
2. We promote professional development through performing proper research and provide young researchers with the opportunities to develop professionally.
3. We respect the public values such as honesty, accuracy, efficiency and objectivity in offering services such as providing expertise or disclosing research results.
4. We do not have unfair competitions with others and solve problems with objective information and processes when there is a clash of interests.
5. We raise common issues only through objective and fair methods.

C. Practical Platforms

1. We consider the public security and welfare as a top priority and conform to the principle of sustainable use of ocean in conducting our research.
 (a) We must acknowledge the fact that the life, security, health and welfare of the public have an absolute reliance over our products such as structures, equipments and machines that are given thought to and made into decision by engineers.
 (b) We must not propose or approve research plans which cause harm to the public health and welfare.
 (c) We must conform to the principle of sustainable use of ocean to enhance the quality of the public life and endeavor to improve the ocean environment.

2. We promote professional development through performing proper research and provide young researchers with the opportunities to develop professionally.

 (a) As we build our career, we must continue to acquire new knowledge and promote intellectual development by keeping track of research results, organizing research methods and raising necessary issues voluntarily.
 (b) We must be thoroughly honest to the contributions from cooperators, competitors and predecessors and utilize them for our professional development.
 (c) We, as administrators, must supervise young researchers in a fair manner and, as their advisors, must assist them sincerely to grow into socially recognized members.

3. We respect the public values such as honesty, accuracy, efficiency and objectivity in offering services such as providing expertise or disclosing research results.
 (a) When we offer service under our responsibility that involves providing professional knowledge, we must act according to professionalism as a commissioner, trying to prevent waste of resources and reporting objective facts, trustworthy data and accurate research results.
 (b) We prohibit any fraudulent acts in conducting research such as fabrications, forgeries and plagiarism.
 (c) We must admit our mistakes or errors when they are verified and must not try to justify them by distorting facts or data.

4. We do not have unfair competitions with others and solve problems with objective information and processes when there is a clash of interests.
 (a) We must not distort the professional, academical qualifications of ourselves and coworkers. We must not fabricate or exaggerate our positions or authorities of the past achievements.
 (b) Our papers must contain facts and no exaggeration that are contributed to media sources. When publishing a paper or a report which involves multiple researchers, we must allocate authors based on their levels of contributions and mention every person and institution that is concerned and provided assistance.
 (c) We must not criticise others' achievements in an irresponsible manner by intentionally distorting their professional reputation, prospects and character in both direct and indirect ways.
 (d) When a clash of interests occur, we must organize a committee composed of authoritative experts in the field and fairly solve the problem based on objective facts and data.

5. We raise common issues only through objective and fair methods.
 (a) We must be thoroughly objective and honest when submitting expert reports or policy proposals and include relevant, sufficient and appropriate information.
 (b) When addressing public issues through open debates or forums, we must provide opinions based on objective facts

and data and must not cause harm to the public interest by making groundless argument or being involved in private interests with others.

(c) We must be honest when explaining our business and its advantages, and must not try to meet our interests by damaging professional honor and coordination with coworkers.

6. All members of The Korean Society of Ocean Engineers must abide by the ethical codes of research stated above.

D. The Scope of Manuscript

1. Manuscripts include papers, technical reports and commentaries, and papers must be the ones that are not released in other journals.
2. "Journals" are the ones that have an appropriate screening of submitted theses and that are published on a regular basis.
3. All manuscripts other than the ones stated in the previous clause can be submitted such as conference papers, research reports, diploma papers and academic articles, provided that their sources are stated according to the 3rd clause of The Regulations on Paper Submission in The Journal of the Korean Society of Ocean Engineers.

E. The Definitions and Types of Fraudulent Acts in Research

1. "Fraudulent acts in research" include all affairs that violates ethical codes of research: fabrications, forgeries, plagiarism, overlapping publications and unfair marking of writers which may occur in every phase of research process, such as in a proposal, conducting, a report or presentation of research results.
2. "Fabrication and forgeries" refers to an act of distorting the content or outcome of research by making up false data or results.
3. "Plagiarism" refers to an act of unfairly employing all research results, such as others' publications, research proposals, ideas, hypotheses and theories, without a fair approval or quotation.
4. "Overlapping publications" refers to two writings published in different media sources that are totally identical in their contents or share the major contents. It is also the case of overlapping publication where the paper published later contains a slightly different viewpoint, yet contains the same or slightly different analysis on the same data from the previous paper.
5. "Unfair marking of writers" refers to an act of unfairly gaining reputation by pretending to be a real author of a paper without any participation in research.
6. Fraudulent acts also include a behavior of intentionally disturbing investigations regarding assumed misconducts in research or inflicting an injury on an informant.
7. "Other fraudulent acts in research" refers to all affairs that are generally accepted as the violations to ethical codes of research in the academia.

F. Screening System, Processing Criteria and Procedure

1. Screening System
(a) Authors must submit a "consent form of delegation of copyright" which necessitates an author's confirmation on

any violations to ethical codes of research.

(b) When inspectors raise question on any violations to ethical codes of research, The Committee of Ethical Codes of Research determines its/their compliance to the regulations after examining all materials concerned and giving the contributor a chance to defend him/herself.

(c) When any violations to ethical codes of research are found while screening or editing (after the insertion of a paper in an academic magazine), The Committee of Ethical Codes of Research determines its/their compliance to the regulations after giving the contributor a chance to defend him/herself.

(d) When any violations to ethical codes of research are called into question after a paper is published, The Committee of Ethical Codes of Research determines its/their compliance to the regulations after giving the contributor a chance to defend him/herself.

2. Processing Criteria
(a) All processing criteria regarding fraudulent acts in research follow the regulations and detailed rules for operation of The Committee of Ethical Codes of Research of this society.

3. Processing Procedure
(a) When any affair is determined as a violation to the ethical codes of research in the phase of submission or screening, The Editing Commission should report it to The Committee of Ethical Codes of Research.

(b) When any affair is determined as a violation to the ethical codes of research after the insertions of a paper in an academic magazine, The Committee of Ethical Codes of Research should immediately cancel its publication and notify the cancellation to the author/s

G. Ethical codes of Editing

1. The editor must a strong sense of ethics regarding the codes of conduct in research and in publication. Also, he/she must not have any personal interests with others in the process of edition.
2. The editor must thoroughly keep security in all matters related to the contribution of manuscripts, screening and publication.
3. The editor must be well-informed about the violations to ethical codes of research and make a neutral and impersonal judgement when he/she found any violations.

Supplementary Provisions

1. Regulations stated above are enacted after 1 Nov. 2008. For the manuscripts contributed in academic magazines before 1, Nov. 2008, the 3rd clause in "D" is not applied. Also, they are not interpreted as violations to the ethical codes of research even if they did not stated their source in the journal of this society.
2. Also, for the papers applicable to the clause "D" or "E", the writer/s can take measures such as "cancellation of a paper" based on their judgement, or "rejection of screening" if the paper is under screening.

Research and Publication Ethics

Authorship of the paper

Authorship should be limited to those who have made a significant contribution to the conception, design, execution, or interpretation of the reported study. All those who have made significant contributions should be listed as co-authors. Where there are others who have participated in certain substantive aspects of the research project, they should be acknowledged or listed as contributors.

The corresponding author should ensure that all appropriate co-authors and no inappropriate co-authors are included on the paper, and that all co-authors have seen and approved the final version of the paper and have agreed to its submission for publication.

Hazards and human or animal subjects

If the work involves chemicals, procedures or equipment that have any unusual hazards inherent in their use, the author must clearly identify these in the manuscript. If the work involves the use of animal or human subjects, the author should ensure that the manuscript contains a statement that all procedures were performed in compliance with relevant laws and institutional guidelines and that the appropriate institutional committee(s) has approved them. Authors should include a statement in the manuscript that informed consent was obtained for experimentation with human subjects. The privacy rights of human subjects must always be observed.

Ensure correct use of the terms sex (when reporting biological factors) and gender (identity, psychosocial or cultural factors), and, unless inappropriate, report the sex and/or gender of study participants, the sex of animals or cells, and describe the methods used to determine sex and gender. If the study was done involving an exclusive population, for example in only one sex, authors should justify why, except in obvious cases. Authors should define how they determined race or ethnicity and justify their relevance

Fundamental errors in published works

When an author discovers a significant error or inaccuracy in his/her own published work, it is the author's obligation to promptly notify the journal editor or publisher and cooperate with the editor to retract or correct the paper. If the editor or the publisher learns from a third party that a published work contains a significant error, it is the obligation of the author to promptly retract or correct the paper or provide evidence to the editor of the correctness of the original paper.

The Korean Society of Ocean Engineers